

Simulations of Gravitational Microlensing

A thesis submitted to The University of Manchester for the degree of
Doctor of Philosophy
in the Faculty of Engineering and Physical Sciences

2011

Matthew T. Penny
School of Physics and Astronomy

Contents

List of figures	7
List of tables	10
Abstract	13
Declaration	14
Copyright statement	15
Acknowledgements	17
The author	19
Supporting publications	20
1 Gravitational microlensing: basic theory	21
1.1 Introduction	21
1.2 The single lens	22
1.3 Binary lenses	29
1.3.1 The lens equation	29
1.3.2 Critical curves and caustics	32
1.3.3 Lightcurves	35
2 Microlensing observations and simulations	39
2.1 Microlensing observations	39
2.1.1 The probability of microlensing	39
2.1.2 Microlensing surveys	41

2.1.3	Complications	44
2.2	Microlensing simulations	49
2.2.1	Requirements of a microlensing simulation	49
2.2.2	Applications of microlensing simulations	52
3	Orbital motion in microlenses	55
3.1	Introduction	57
3.2	Orbital motion in a binary microlens	59
3.3	Simulating a high-cadence microlensing survey	60
3.3.1	The Galactic model	61
3.3.2	The microlensing events	63
3.3.3	Simulation of photometry	65
3.4	Measuring orbital motion	68
3.4.1	Fitting with the single-lens model	69
3.4.2	Fitting with the binary-lens model	69
3.4.3	Fitting caustic-crossing events	72
3.4.4	Classification of events	74
3.5	Results	77
3.5.1	What fraction of events show orbital motion?	77
3.5.2	What affects the detectability of orbital motion?	82
3.5.3	Are there two classes of orbital motion event?	96
3.6	Summary and discussion	109
3.6.1	Limitations of the study	110
3.6.2	Comparison with observations	112
3.6.3	Future prospects	114
4	Rapidly-rotating lenses	117
4.1	Introduction	118
4.2	What is a rapidly-rotating lens?	120
4.2.1	What happens to the images?	123

4.3	Are RRLs detectable?	126
4.3.1	An analytical approach	126
4.3.2	A numerical approach	129
4.3.3	How many RRL events will we detect?	137
4.4	Estimating RRL parameters	143
4.5	Measuring RRL masses	150
4.6	Additional factors affecting RRL detectability	153
4.6.1	Blending	154
4.6.2	Finite-source effects	154
4.6.3	Inclination and eccentricity	156
4.6.4	Parallax	158
4.7	Discussion and conclusion	158
5	<i>MaBμLS and its application to <i>Euclid</i></i>	161
5.1	Introduction	161
5.1.1	Planet formation and evolution	162
5.1.2	Planetary microlensing	166
5.1.3	Infrared microlensing from space	167
5.1.4	<i>Euclid</i>	168
5.2	<i>MaBμLS</i>	169
5.2.1	The Besançon Galactic model	170
5.2.2	The microlensing events	175
5.2.3	<i>Euclid</i> observing strategy	176
5.2.4	Photometry	177
5.2.5	Planet detections	184
5.3	Expected yields	185
5.3.1	The M_p - a diagram	193
5.3.2	The host-star populations	196
5.4	Discussion	197

5.4.1	The Besançon model	198
5.4.2	Systematics	199
5.4.3	Planet mass measurements	200
5.4.4	Survey optimization	201
6	Summary and future work	203
6.1	Future work	205
6.2	Wider impact	207
A	On the choice of detection criteria	209
	References	217

Word count: < 72 000 words.

List of figures

1.1	Lens geometry	23
1.2	Lightcurves and source trajectories of a single lens	28
1.3	Critical curves and caustics	33
1.4	A non-caustic-crossing binary-lens lightcurve	36
1.5	A caustic-crossing binary-lens lightcurve	37
3.1	Simulated timescale distribution	63
3.2	Example of a lightcurve with extended coverage	67
3.3	Example of a lightcurve fitted using non-adjacent caustic crossings	73
3.4	Examples of lightcurves narrowly failing different cuts	77
3.5	Orbital motion detection efficiency plotted against $ u_0 $	83
3.6	Orbital motion detection efficiency plotted against t_E	85
3.7	Orbital motion detection efficiency plotted against s_0 and a	87
3.8	Orbital motion detection efficiency plotted against q	89
3.9	Orbital motion detection efficiency plotted against M_1	90
3.10	Orbital motion detection efficiency plotted against D_1	91
3.11	Orbital motion detection efficiency plotted against T	92
3.12	Orbital motion detection efficiency plotted against I_b	93
3.13	Orbital motion detection efficiency plotted against f_s	94
3.14	Orbital motion detection efficiency plotted against i	95
3.15	Orbital motion detection efficiency plotted against R_T	96
3.16	Orbital motion detection efficiency plotted against R_v	97

3.17	Plot of q against s_0 for orbital motion events	99
3.18	Plot of $ u_0 $ against s_0 for orbital motion events	100
3.19	Examples of separational-type orbital motion events	102
3.20	Examples of rotational-type orbital motion events	105
4.1	The magnification pattern of a close-topology microlens	121
4.2	The lightcurve of an RRL	122
4.3	Image lightcurves of an RRL	125
4.4	Analytical RRL detectability map in the a - M plane	129
4.5	Numerical RRL detectability map in the a - M plane	131
4.6	Detectability maps for various source velocities and lens distances	132
4.8	Detectability maps for various mass ratios	137
4.9	Simulated RRL timescale distribution	142
4.10	RRL parametrization	144
4.11	Relationship between lightcurve features and RRL parameters	147
4.12	RRL mass-distance relations	151
4.13	The effect of blending on photometric thresholds	153
4.14	RRL lightcurve with finite-source effects	155
4.15	Lightcurves of RRLs with different orbital inclination	157
5.1	Planet mass–semimajor axis diagram	164
5.2	Example of a simulated <i>Euclid</i> image	182
5.3	Lightcurve of the event Figure 5.2	184
5.4	Example lightcurves	186
5.5	Expected planet yield for <i>Euclid</i>	189
5.6	Planet yield for empirical mass functions	191
5.7	Sensitivity of <i>Euclid</i> in the M_p - a plane	194
5.8	Planet yield as a function of a	195
5.9	Planet yield plotted against lens and source distance	196

A.1 Example of a low- $\Delta\chi^2$ planet detection 213

A.2 Another example of a low- $\Delta\chi^2$ planet detection 214

A.3 Parameter estimates for $\Delta\chi^2 = 100$ events 215

A.4 Example of a large- $\Delta\chi^2$ planet detection 216

List of tables

3.1	Summary of results for planetary lenses	79
3.2	Summary of the results for stellar-binary lenses	79
3.3	Binary and orbital motion detection efficiencies	80
3.4	Microlensing parameters for the example lightcurves	101
3.5	Physical parameters for the example lightcurves	108
5.1	Parameters of the <i>Euclid</i> telescope	179
5.2	Parameters of the <i>Euclid</i> detectors	180

The University of Manchester

ABSTRACT OF THESIS submitted by Matthew T. Penny
for the Degree of Doctor of Philosophy and entitled
Simulations of Gravitational Microlensing. December 2011

Gravitational microlensing occurs when a massive lens (typically a star) deflects light from a more distant source, creating two unresolvable images that are magnified. The effect is transient due to the motions of the lens and source, and the changing magnification gives rise to a characteristic lightcurve. If the lensing object is a binary star or planetary system, more images are created and the lightcurve becomes more complicated. Detection of these lightcurve features allows the lens companion's presence to be inferred.

Orbital motion of the binary lens can be detected in some microlensing events, but the expected fraction of events which show orbital motion has not been known previously. We use simulations of orbiting-lens microlensing events to determine the fraction of binary-lens events that are expected to show orbital motion. We also use the simulations to investigate the factors that affect this detectability.

Following the discovery of some rapidly-rotating lenses in the simulations, we investigate the conditions necessary to detect lenses that undergo a complete orbit during a microlensing event. We find that such events are detectable and that they should occur at a low but detectable rate. We also derive approximate expressions to estimate the lens parameters, including the period, from the lightcurve. Measurement of the orbital period can in some cases allow the lens mass to be measured.

Finally we develop a comprehensive microlensing simulator, *MaB μ LS*, that uses the output of the Besançon Galaxy model to produce synthetic images of Galactic starfields. Microlensing events are added to the images and photometry of their lightcurves simulated. We apply these simulations to a proposed microlensing survey by the *Euclid* space mission to estimate its planet detection yield.

Declaration

I declare that no portion of the work referred to in the thesis has been submitted in support of an application for another degree or qualification of this or any other university or other institute of learning.

Copyright statement

- (i) The author of this thesis (including any appendices and/or schedules to this thesis) owns certain copyright or related rights in it (the “Copyright”) and s/he has given The University of Manchester certain rights to use such Copyright, including for administrative purposes.
- (ii) Copies of this thesis, either in full or in extracts and whether in hard or electronic copy, may be made **only** in accordance with the Copyright, Designs and Patents Act 1988 (as amended) and regulations issued under it or, where appropriate, in accordance with licensing agreements which the University has from time to time. This page must form part of any such copies made.
- (iii) The ownership of certain Copyright, patents, designs, trade marks and other intellectual property (the “Intellectual Property”) and any reproductions of copyright works in the thesis, for example graphs and tables (“Reproductions”), which may be described in this thesis, may not be owned by the author and may be owned by third parties. Such Intellectual Property and Reproductions cannot and must not be made available for use without the prior written permission of the owner(s) of the relevant Intellectual Property and/or Reproductions.
- (iv) Further information on the conditions under which disclosure, publication and commercialization of this thesis, the Copyright and any Intellectual Property and/or Reproductions described in it may take place is available in the University IP Policy (see <http://www.campus.manchester.ac.uk/medialibrary/policies/intellectual-property.pdf>), in any relevant Thesis restriction declarations deposited in the University Library, The University Library’s regulations (see <http://www.manchester.ac.uk/library/aboutus/regulations>) and in The University’s policy on presentation of Theses.

Now think about this for a minute: we've been looking out of telescopes for 300 years; we've been sending probes out into space, and we have never seen anything as beautiful as what we see when we walk out the front door.

Alan Bean,
Apollo 12 astronaut and artist

Acknowledgements

First I would like to thank my supervisors Shude Mao and Eamonn Kerins for all the advice and help they have given me during this Ph.D., and the numerous interesting discussions I have had with them.

Next, I would like to thank my parents (Jane and Tim), grandparents (Christine, Halket, Bett and George) and all my other family members for their many years of love and support; they have helped to nurture my passion for astronomy with books, telescopes and encouragement. I'd also like to thank my partner Clare for her love, support, patience and encouragement, especially at times when it felt like I would never get work finished.

I owe a great deal of thanks to those who have helped with the preparation of this thesis, firstly referees (one anonymous, the other Andy Gould) for their helpful advice that has greatly improved the scientific content in these pages, and secondly those who have helped with proof reading (Michael Bareford, Clare Dodd and Alex Bladon). Clare and Alex I am particularly indebted to, not only for their speedy service, when requested, but also for their ability to survive an avalanche of commas.

It is a pleasure to acknowledge all the people with whom I have had interesting discussions over time, or have helped me in some way. There are far too many to list, but here is my attempt: fellow students (Sarah Bryan, Dandan Xu, Alan Duffy, Dave Jones, Rieul Gendron, Scot Hickinbottom, Leo Huckvale), academics and researchers at JBCA (Nick Rattenbury, Anita Richards, Iain McDonald, Tim O'Brien, Cees Bassa, Philippa Browning, Malcolm Gray, Albert Zijlstra, Ian Morison), fellow MiNDSTeP members (Markus Hundertmark, Christine Liebig, Kennet Harpsøe, Martin Dominik) and those in the field of microlensing and the general astronomical community (Scott Gaudi, Martin Smith, Jean-Philippe Beaulieu, Annie Robin, Keith Horne, Uffe Gråe Jorgensen, Colin Snodgrass, Jin An, Nan Li, Jan Skowron, Szymon Kozłowski, Pavel Kroupa, Mark Cropper, Gregor Seidel). My sincerest apologies to those I have missed

out.

I would also like to thank those in support roles who have helped me during this Ph.D.: Angela Linton and Tom Wise for their help with various administrative tasks, and Ant Holloway and Bob Dickson for their management of the computer systems at JBCA. Their continuing battle against faulty air conditioning units, and their timely rehousing of cluster computers in times of crisis has made much of the work presented here possible. I am indebted to those who have devoted large amounts of time to the development of tools such as the ADS, arXiv, L^AT_EX, and much of the software I use, and also to all those who post solutions to technical problems on internet forums, their collective wisdom has saved me uncountable hours of time.

Finally, I am grateful for the financial support of the STFC, without which I could not have done this Ph.D., and also the support of the Deytheur Educational Trust.

The author

The author grew up in Mid Wales, where he attended Carreghofa County Primary School and Llanfyllin High School. He studied for an M.Phys. (Hons) Physics degree at the University of Manchester from 2004–2008. In September 2008 he began studying for a Ph.D. at the Jodrell Bank Centre for Astrophysics (JBCA) at the University of Manchester. The results of that work are presented in this thesis.

Supporting publications

Detectability of orbital motion in stellar binary and planetary microlenses

M. T. Penny, S. Mao and E. Kerins, *MNRAS*, 412:607–626, 2011.

Rapidly rotating lenses: repeating features in the light curves of short-period binary microlenses

M. T. Penny, E. Kerins and S. Mao, *MNRAS*, 417:2216–2229, 2011.

MaB μ LS: the Manchester-Besançon microLensing Simulator and its application to the *Euclid* mission

M. T. Penny, E. Kerins, N. J. Rattenbury, J.-P. Beaulieu, A. C. Robin and S. Mao, to be submitted.

1

Gravitational microlensing: basic theory

1.1 Introduction

Gravitational microlensing occurs when the mass of an object bends and magnifies the light from a more distant star passing almost directly behind it. This chance alignment is transient, and the relative motions of the background source and foreground lens give rise to a recognizable lightcurve as the apparent brightness of the source changes. The presence of additional masses in the lensing system, such as stellar or planetary companions, can cause a diverse range of more complicated lightcurves, whose features can be used to infer the presence and properties of the companions. Microlensing simulations can be used to aid the design of microlensing experiments and provide insight into complex aspects of microlensing phenomena. Simulations also play a vital role in the interpretation of microlensing surveys.

This thesis describes several pieces of work where microlensing simulations have been used to better understand complex microlensing phenomena or to judge the performance of a proposed microlensing survey. The structure of the work is as follows. In this first chapter, the basic theory of gravitational microlensing, by both single masses

and binary systems, is introduced. Chapter 2 describes how microlensing events are observed and how microlensing surveys can be simulated. Chapter 3 describes the development and results of a simulation investigating the effects of orbital motion in binary microlenses. Chapter 4 develops the theory of ‘rapidly-rotating lenses’ and uses simulations to estimate the occurrence rate of microlensing events involving such lenses. Chapter 5 describes the development of the first planetary microlensing simulator to use a population synthesis Galactic model, and applies the simulations to a planetary microlensing survey by the proposed *Euclid* space mission.

1.2 The single lens

We begin by examining the simplest case of microlensing: microlensing by a single point mass. The topics covered in this section and the next have been the subject of many reviews (Paczynski 1996; Wambsganss 2006; Mao 2008; Gaudi 2010, to name a few). Unless otherwise referenced, we refer the reader to these articles here, in order to avoid repetitive referencing.

Although first derived by Einstein (1936), and expanded on by Tikhov (1938), the derivation of the properties of a single point-mass lens were perhaps most clearly and concisely described, independently and simultaneously, by Liebes (1964) and Refsdal (1964). They were also the first to quantitatively estimate microlensing event rates (see Section 2.1.1), based on knowledge of the Galaxy at that time. However, it was Paczynski (1986) who proposed microlensing as a method to search for dark matter in the form of MACHOs,¹ that finally provided the justification to begin massive searches for microlensing. Shortly after the first microlensing surveys began, Mao and Paczynski (1991) and Gould and Loeb (1992) showed that microlensing could be used to detect planets orbiting lens stars.

Einstein (1915) derived the deflection angle of a light ray in a gravitational field of

¹MAssive Compact Halo Objects

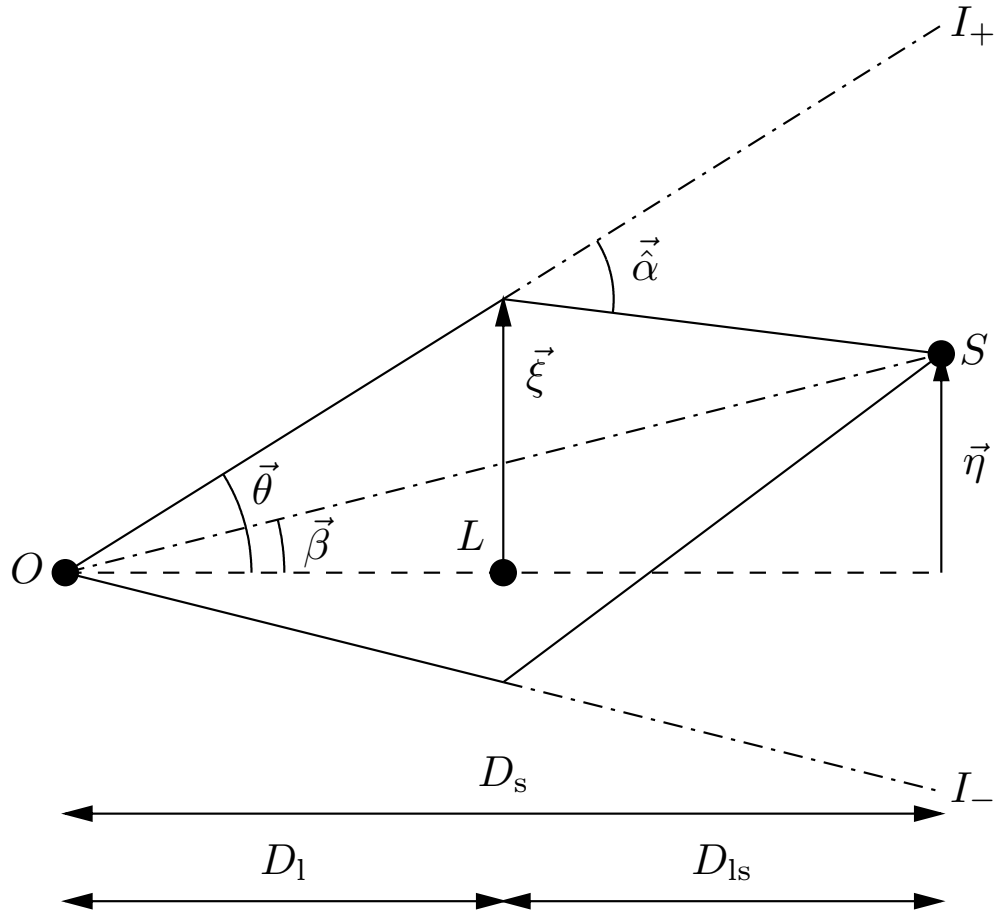


Figure 1.1 – The geometry of light paths through a gravitational lens. Light leaves the source S and passes the lens L to reach the observer O , appearing as two images (I_+ and I_-). The two-dimensional angle vector $\vec{\beta}$ is the true position of the source on the sky, measured relative to the origin, which we assume to be the position of the lens. $\vec{\theta}$ is the apparent position of an image and $\vec{\alpha}$ is the deflection angle of passing light. $\vec{\xi} = \vec{\theta}D_1$ and $\vec{\eta} = \vec{\beta}D_s$ are the projected distance vectors in the plane of the sky of the lens and source, respectively, and D_1 and D_s are the distance from the observer to the lens and source, respectively; D_{ls} is the distance between the lens and source.

a point mass M to be

$$\vec{\alpha} = \frac{4GM}{c^2} \frac{\vec{\xi}}{\xi^2}, \quad (1.1)$$

where $\vec{\xi}$ is the two-dimensional displacement vector² of the light ray from the mass at their closest approach (in the plane perpendicular to the line of sight to the lens), and G and c are the gravitational constant and speed of light, respectively. Using the geometry shown in Figure 1.1, and assuming small angles, Einstein (1936) derived expressions for the image positions and magnifications of a single lens. Figure 1.1 shows light rays emitted by a source S at distance D_s deflected by a massive deflector L (the lens) at distance D_l , so that they reach an observer O . We choose the origin of our sky coordinate system to coincide with the lens. In the absence of deflection, the source would be separated from the lens by the angle $\vec{\beta}$, a two dimensional vector on the sky. Light rays that reach the observer pass the lens with a displacement $\vec{\xi}$ and so the observer sees an image I at the angle $\vec{\theta} = \vec{\xi}/D_l$. The physical projected displacement of the source from the origin is $\vec{\eta} = \vec{\beta}D_s$.

Using simple geometry, and assuming small angles, we can write down the relationship between the undeflected source position and the image position, known as the lens equation

$$\vec{\eta} = \frac{D_s}{D_l} \vec{\xi} - D_{ls} \vec{\alpha}, \quad (1.2)$$

where D_{ls} is the distance between the lens and source. This can be rewritten in terms of the angles $\vec{\beta}$ and $\vec{\theta}$ as

$$\vec{\beta} = \vec{\theta} - \frac{4GM}{c^2} \frac{D_{ls}}{D_l D_s} \frac{\vec{\theta}}{\theta^2}, \quad (1.3)$$

by dividing through by D_s . Defining the angular Einstein radius as

$$\theta_E = \sqrt{\frac{4GM}{c^2} \frac{D_{ls}}{D_l D_s}}, \quad (1.4)$$

and dividing Equation 1.3 by θ_E , we obtain the normalized lens equation

$$\vec{u} = \vec{r} - \frac{\vec{r}}{r^2}, \quad (1.5)$$

²For the single point-mass lens, the lensing potential is axisymmetric and the vector notation can be dropped, but we retain it as it is necessary for the later treatment of binary lenses.

where $\vec{u} = \vec{\beta}/\theta_E$ and $\vec{r} = \vec{\theta}/\theta_E$ are the vector positions of the source and images, respectively, with magnitudes normalized to θ_E . It can immediately be seen that if $\theta \gg \theta_E$ then $u \rightarrow r$ and the effect of the lens will be negligible. Therefore θ_E defines the angular separation scale over which lensing effects are important. In this work we will consider the lensing effects of stars on other stars in the Galaxy, so in the typical units of Solar masses and kpc

$$\theta_E = 2.85 \text{ mas} \left(\frac{M}{M_\odot} \right)^{1/2} \left(\frac{1-x}{x} \right)^{1/2} \left(\frac{D_s}{\text{kpc}} \right)^{-1/2}, \quad (1.6)$$

where we have defined the fractional lens distance $x = D_l/D_s$. At the position of the lens, the physical scale of θ_E is

$$r_E = D_l \theta_E = 2.85 \text{ AU} \left(\frac{M}{M_\odot} \right)^{1/2} [x(1-x)]^{1/2} \left(\frac{D_s}{\text{kpc}} \right)^{1/2}, \quad (1.7)$$

the physical Einstein radius.

The lens equation can be used to determine the undeflected source position given the position of an image, but often we are interested in the inverse problem: finding the image positions given the source position. As the source, lens and observer all lie in the same plane, due to symmetry, so must the images, and we may drop the vector notation. The lens equation for a single lens is then

$$u = r - \frac{1}{r}. \quad (1.8)$$

This is easily rearranged into a quadratic and solved, yielding two solutions

$$r_\pm = \frac{u \pm \sqrt{u^2 + 4}}{2}, \quad (1.9)$$

corresponding to two images: one, the major image at $r_+ > 1$, outside the Einstein radius, and the other, the minor image at $-1 < r_- < 0$, inside the Einstein radius and on the opposite side of the lens. The images are separated by $|r_+ - r_-| \sim 2$ when $u \lesssim 1$ (an angle $\sim 6 \text{ mas}/\sqrt{D_s/\text{kpc}}$), implying that the images cannot be resolved by optical telescopes for typical microlensing events in the Galaxy.

If the images cannot be resolved, then the only way that microlensing can be detected is if it magnifies the source star.³ The magnification of the source can be calculated by considering the lensing of a small annular segment of thickness du and width $ud\phi$ at the position of the source (u, ϕ) in polar coordinates. The source segment is lensed into two annular image segments, with the same angular width and thickness dr_{\pm} . The magnification μ_{\pm} of each image is given by the ratio of the image to source areas

$$\mu_{\pm} = \frac{r_{\pm} d\phi dr_{\pm}}{ud\phi du} \quad (1.10)$$

$$= \frac{u \pm \sqrt{u^2 + 4}}{2u} \frac{dr_{\pm}}{du} \quad (1.11)$$

$$= \frac{1}{2} \left(1 \pm \frac{u^2 + 2}{u \sqrt{u^2 + 4}} \right). \quad (1.12)$$

The second non-constant term always has a magnitude greater than one, so the major image has a magnification μ_{+} , which is always positive and greater than one.⁴ Similarly, the minor image always has a negative magnification $\mu_{-} < 0$, so the image is inverted and may be either magnified or demagnified. We are unable to resolve the images, but as gravitational lensing conserves surface brightness (Schneider et al. 1992), the total absolute magnification μ is an observable quantity

$$\mu \equiv |\mu_{+}| + |\mu_{-}| = \mu_{+} - \mu_{-} \quad (1.13)$$

$$= \frac{u^2 + 2}{u \sqrt{u^2 + 4}}. \quad (1.14)$$

³This is not strictly true, as the lens may cause significant shifts to the light centroid of the source, even when the source is not significantly magnified (Hog et al. 1995; Walker 1995; Dominik and Sahu 2000). Such centroid shifts can be measured to accuracies of small fractions of a pixel if the point spread function is well sampled. We do not consider such astrometric microlensing effects in this thesis, so do not discuss them further.

⁴The sign of the magnification indicates its parity. A positive parity image is not inverted, while a negative parity image is inverted. The magnitude of the magnification indicates whether an image is magnified or demagnified. A magnified image has magnification $|\mu| > 1$ and so is larger than the unlensed source, while a demagnified image has magnification $|\mu| < 1$ and is smaller than the unlensed source.

Unless otherwise noted, all further references to the magnification should be taken to mean the total absolute magnification.

The magnification of a point-mass lens has the following important properties:

- the magnification is always greater than or equal to one,
- the magnification scales as u^{-1} for $u \ll 1$,
- the magnification diverges as u tends to zero,
- the magnification scales as $1 + 2u^{-4}$ for $u \gg 1$,
- the magnification tends to one as u tends to infinity.

So, a lensed source is never demagnified and as a source approaches perfect alignment its magnification diverges. This is obviously unphysical, and we discuss how real lenses behave when perfectly aligned in Section 2.1.3.

The components of the systems we consider (source stars, lenses and the observer on Earth) are all in motion relative to each other, so their alignment is transient. The timescale over which a source will be lensed is the time taken for the source to move relative to the observer-lens line of sight by an angular distance equal to the angular Einstein radius. This is the Einstein radius crossing timescale t_E , which we shall simply call the microlensing, event or Einstein timescale. If we assume the source, lens and observer are all in rectilinear motion

$$t_E = \frac{\theta_E}{\mu_{\text{rel}}} = \frac{r_E}{v_t}, \quad (1.15)$$

where μ_{rel} is the relative proper motion between the lens and source, and v_t is the relative lens-source transverse velocity measured at the lens. Typical velocities within the Galaxy are $\sim 200 \text{ km s}^{-1}$, so in the standard units

$$t_E = 49.4 \text{d} \left(\frac{M}{M_\odot} \right)^{1/2} [x(1-x)]^{1/2} \left(\frac{D_s}{\text{kpc}} \right)^{1/2} \left(\frac{v_t}{100 \text{km s}^{-1}} \right)^{-1}. \quad (1.16)$$

Microlensing will therefore cause a temporary brightening of an otherwise constant background source over the course of a month or so. If we assume the source travels

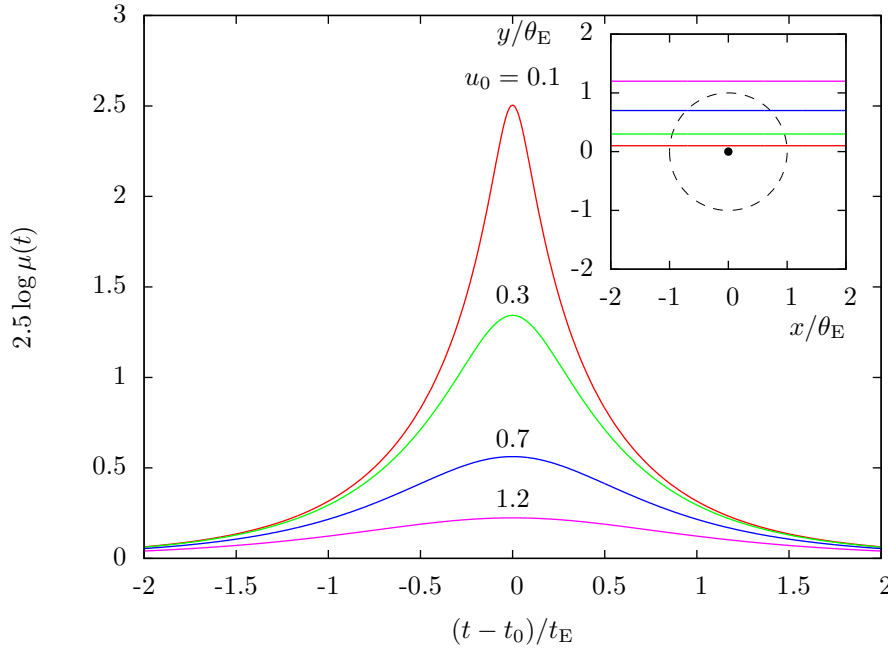


Figure 1.2 – Lightcurves and source trajectories of a single lens. Lightcurves (Equation 1.18) of single lenses with different values of the impact parameter u_0 are shown in different colours. The inset shows the source trajectories for the lightcurves in the main plot. The dashed line shows the Einstein ring, while the point shows the position of the lens.

in a straight line, relative to the lens, then the source-lens separation as a function of time in our normalized units will be

$$u(t) = \sqrt{u_0^2 + \left(\frac{t - t_0}{t_E}\right)^2}, \quad (1.17)$$

where t_0 is the time of lens-source closest approach and u_0 is the minimum lens-source separation, in units of the Einstein radius. The magnification of the source as a function of time is then found by substituting $u(t)$ into Equation 1.14

$$\mu(t) = \frac{u(t)^2 + 2}{u(t) \sqrt{u(t)^2 + 4}}. \quad (1.18)$$

This is the so-called Paczyński lightcurve (Paczynski 1986).

Figure 1.2 shows several examples of the Paczyński lightcurve with different values of u_0 . The effect of the timescale t_E is only to stretch the lightcurve in time, while t_0 shifts the lightcurve in time. The lightcurve is symmetric about a single peak, and is

constant far from the peak. This is in contrast to other astrophysical variable sources, which may have asymmetric lightcurves with constant baselines (e.g., Supernovae, Novae), continuous periodic variability (e.g., variable stars such as Cepheids and RR Lyrae), or repeating episodes of variability (e.g., cataclysmic variables). It should be noted that the only parameter of a single-lens lightcurve that is physically interesting is the timescale t_E . The other parameters t_0 and u_0 reflect the random timing and alignment of the microlensing event. This means that all the information that we would like to know about the lens (its mass, distance and velocity) is constrained by just one parameter. It is therefore impossible to determine these quantities uniquely without additional information. This is known as the microlensing degeneracy, and we shall discuss how it can be broken in the next chapter.

1.3 Binary lenses

A large fraction of stars are not isolated, but part of binary or multiple star systems (Duquennoy and Mayor 1991; Raghavan et al. 2010) or planetary systems (Cumming et al. 2008; Johnson et al. 2010; Sumi et al. 2010; Howard et al. 2011; Mayor et al. 2011). In this section we derive the properties of microlensing by binary lenses. As microlensing is sensitive to mass and not light, planetary-mass bodies can also affect the lightcurve.

1.3.1 The lens equation

In the previous section we saw how the lens equation of a single lens can be derived directly from the lensing geometry, provided one knows the form of the deflection angle. Derivation of the multiple point-mass lens equation is equally straight forward. Equation 1.1 can be generalized for a mass M_i , not necessarily at the origin, that deflects a light ray by an angle

$$\vec{\alpha}_i = \frac{4GM_i}{c^2} \frac{\vec{\xi} - \vec{\xi}_i}{|\vec{\xi} - \vec{\xi}_i|^2}, \quad (1.19)$$

where $\vec{\xi} - \vec{\xi}_i$ is the two-dimensional ray-lens displacement vector ($\vec{\xi}$ is the ray position and $\vec{\xi}_i$ the position of the point-mass lens i). The total deflection that a ray experiences is simply the sum of all deflections from N point-mass lenses (Bourassa et al. 1973)

$$\vec{\alpha} = \sum_{i=1}^N \vec{\alpha}_i. \quad (1.20)$$

We can then write the lens equation for an N point-mass lens as

$$\vec{\beta} = \vec{\xi} - \theta_E^2 \sum_{i=1}^N m_i \frac{\vec{\xi} - \vec{\xi}_i}{|\vec{\xi} - \vec{\xi}_i|^2}, \quad (1.21)$$

where for convenience we have chosen to define the lens equation in terms of the Einstein radius of the total lens mass M , and where $m_i = M_i/M$, the ratio of mass i to the total mass. This equation can then be normalized in the same way as Equation 1.3

$$z_s = z - \sum_{i=1}^N \frac{m_i}{\bar{z} - \bar{z}_i}, \quad (1.22)$$

where we have switched to a complex notation first used by Bourassa et al. (1973) and first applied to microlensing by Witt (1990). The two dimensional vectors ($\vec{\xi} = (x, y)$ etc.) are replaced with complex numbers ($z = x + iy$ etc.) and crucially the vector inverse, e.g., $\vec{\xi}/|\vec{\xi}|^2$, is greatly simplified by replacing it with a complex division, $1/\bar{z}$, where the bar represents complex conjugation. As a binary lens is the most complex lens considered in the thesis, we do not pursue a solution of the general N -point-mass lens equation, though similar steps to those we will take for the binary lens can be used to derive the result for larger values of N (e.g., Rhie 2002).

The binary point-mass lens was first considered in detail by Schneider and Weiss (1986), and most of the results in the remainder of this section follow from that work. However, before beginning, it is helpful to describe the standard parametrization of a binary lens. While not axisymmetric like the single lens, the binary lens does possess a reflectional symmetry axis (the binary axis), which passes through the two lens components. Without loss of generality, we can define a reference frame with its origin somewhere along the binary axis, such that the lens positions z_1 and z_2 are real. There

are many good choices for the position of the origin, depending on the problem at hand. As we will study orbital motion of the binary lens in subsequent chapters, the lens centre of mass is the obvious choice of origin. It is now possible to completely parametrize the binary lens with two parameters: the mass ratio $q \equiv M_2/M_1 = m_2/m_1$, which completely specifies the component masses, as we have normalized relative to the total mass; and the projected separation $s \equiv |z_2 - z_1|$, which completely specifies the position of the lenses relative to their centre of mass. We will use the terms primary and secondary lens to refer to the more and less massive lens components respectively. It is s and q that are the observables of a binary lens. Unless additional information is available, the microlensing degeneracy and projection of the orbit prevents s and q being converted into the physical quantities that we would like to know: the companion mass and the orbital radius.

From Equation 1.22, and substituting in our definition of the mass ratio, the lens equation can be written

$$z = z_s + \left(\frac{m_1}{\bar{z} - \bar{z}_1} + \frac{m_2}{\bar{z} - \bar{z}_2} \right), \quad (1.23)$$

where $m_1 = 1/(1 + q)$, $m_2 = q/(1 + q)$ and $|z_2 - z_1| = s$. Again, we would like to know the image positions given the source position, so we must solve the lens equation. However, as z and \bar{z} are linearly independent,⁵ we have one equation with two unknowns. We can eliminate \bar{z} by taking the complex conjugate of Equation 1.23

$$\bar{z} = \bar{z}_s + \left(\frac{m_1}{z - z_1} + \frac{m_2}{z - z_2} \right), \quad (1.24)$$

to yield an expression for \bar{z} that can be substituted back into Equation 1.23. The lens equation can then be rearranged into a fifth order polynomial, which, in general must be solved numerically. The polynomial order implies there must be five solutions, however, not every solution to the polynomial is a solution to the lens equation and each solution found must be checked. In fact, there are always either three or five solutions to the binary-lens equation (Schneider and Weiss 1986); as we shall see below, this has important implications for binary-lens lightcurves.

⁵This can be seen by constructing the quantities $\frac{1}{2}(z + \bar{z}) = \text{Re}(z)$ and $\frac{1}{2}(z - \bar{z}) = \text{Im}(z)$.

Just as for a single lens, the magnification of the images is the ratio of their area to the area of the source. An infinitesimal area element on the source plane d^2S_s is related to one on the image plane d^2S_1 by

$$d^2S_s = |\mathbf{J}|d^2S_1, \quad (1.25)$$

where \mathbf{J} is the Jacobian of the lens equation

$$\mathbf{J} = \frac{\partial(z_s, \bar{z}_s)}{\partial(z, \bar{z})}. \quad (1.26)$$

The magnification of an image i of a point source is therefore

$$A_i = \frac{1}{|\mathbf{J}|} = \frac{1}{J}, \quad (1.27)$$

the inverse of the Jacobian determinant, evaluated at the position of the image. It is straightforward to differentiate the lens equation to obtain

$$\begin{aligned} J &= \frac{\partial z_s}{\partial z} \frac{\partial \bar{z}_s}{\partial \bar{z}} - \frac{\partial z_s}{\partial \bar{z}} \frac{\partial \bar{z}_s}{\partial z} \\ &= 1 - \left| \frac{m_1}{(z - z_1)^2} + \frac{m_2}{(z - z_2)^2} \right|^2. \end{aligned} \quad (1.28)$$

Similar to the single lens, images may have positive or negative parity, and the total magnification is the sum of the absolute magnification of all images

$$A \equiv \sum_i^{N_{\text{images}}} |A_i|. \quad (1.29)$$

1.3.2 Critical curves and caustics

Before proceeding to plot lightcurves of a binary lens, it is important to pause and examine the Jacobian a little more closely. It can be seen that J may equal zero, when the terms within the modulus brackets lie on the unit circle. When this occurs, the magnification of an image becomes infinite. We can find the points where this occurs by setting $J = 0$ to yield

$$\left| \frac{m_1}{(z - z_1)^2} + \frac{m_2}{(z - z_2)^2} \right|^2 = 1, \quad (1.30)$$

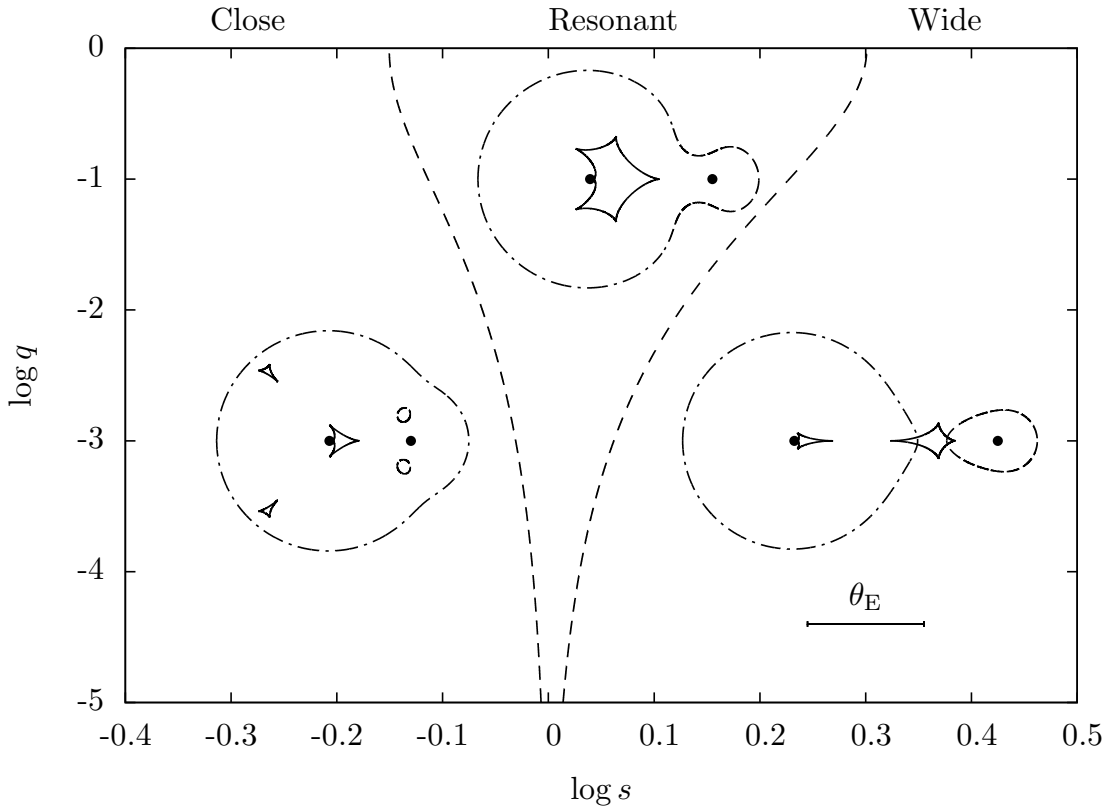


Figure 1.3 – Example critical curves and caustics of each of the three topologies: close, resonant and wide. Dashed lines mark the boundaries between the topologies, plotted on the separation-mass ratio (s - q) plane. Dot-dash lines show critical curves, while solid lines show caustics and dots show the position of the lenses, the more massive lens on the left. All the critical curves and caustics are plotted on the same scale, shown by the scale bar with length θ_E . The mass ratio of each lens is $q = 0.1$, while the close lens has a separation $s = 0.7$, the resonant $s = 1.05$ and the wide $s = 1.75$. Figure design based on a similar figure by Cassan (2008).

which becomes

$$\frac{m_1}{(z - z_1)^2} + \frac{m_2}{(z - z_2)^2} = e^{i\phi}, \quad (1.31)$$

which can be solved for z by rearranging into to a fourth order polynomial. This equation can be solved, usually numerically, for any given value of the parameter ϕ , to yield four solutions. When ϕ is run over $0 \rightarrow 2\pi$, the four solutions join to form smooth, closed curves, called critical curves. The magnification of images on these

curves diverges. The positions on the source plane that give rise to critical images can be found by mapping the critical curves back to the source plane using the lens equation. These curves are called caustics, and are formed of smooth, so-called fold curves, which meet at sharp ‘cusps’. Figure 1.3 shows examples of critical curves and caustics.

The critical curves, being locations where $J = 0$, separate regions of opposite image parity. The caustics separate regions of the source plane with different numbers of images: for a binary lens, outside the caustics the source is lensed into three images, while inside it is lensed into five (Schneider and Weiss 1986). As a source enters (or leaves) a caustic, two images of opposite parity are created (destroyed) at the critical curve. This behaviour causes large discontinuities in the lightcurves of binary lenses (see Section 1.3.3 below).

Schneider and Weiss (1986) showed that the number of caustics, their size, and their shape, is determined only by the mass ratio q and projected separation s of the lens. They found that there were only three possible caustic configurations for a binary lens. These *topologies*, called close, resonant and wide, have three, one, and two disjoint caustics, respectively. Erdl and Schneider (1993) found analytic expressions for the lines in the s - q plane that divide the different topologies:

$$s_c^8 = \frac{(1+q)^2}{27q}(1-s_c^4)^3, \quad (1.32)$$

divides regions of close and resonant topology, and

$$s_w^2 = \frac{(1+q^{1/3})^3}{1+q}, \quad (1.33)$$

divides regions of resonant and wide topology. Figure 1.3 shows examples of each configuration, as well as the lines that separate them. At these lines the multiple caustics of the close and wide topologies merge to form the single resonant caustic. The caustic that lies close to the primary lens in both close and wide topologies is often referred to as the central caustic, while the other caustics are known as secondary or planetary caustics.

1.3.3 Lightcurves

The lightcurve of a binary-microlensing event can be found by again assuming that the source moves along a straight trajectory. As the lens is no longer axisymmetric, we must specify the angle of the source trajectory α , relative to the binary axis, along with the impact parameter u_0 , relative to our chosen origin. The additional three parameters (s , q and α) result in significantly more variety in the lightcurves of binary lenses compared to single lenses (Mao and Paczyński 1991). It is difficult to summarize this variety, but Figures 1.4 and 1.5 show two example lightcurves for the same binary lens. In Figure 1.4 the source does not cross a caustic, while in Figure 1.5 it does. In general, binary-lens lightcurves are asymmetric and may have one or more peaks. In many cases the binary lightcurve can resemble that of a single lens, with only small deviations from the Paczyński form, or it may have large deviations localized to a small section of the lightcurve. Such deviations can be missed, either through low signal-to-noise photometry or sparse sampling of the lightcurve; for example, the lightcurve in Figure 1.4 could be mistaken for a single-lens lightcurve if the photometry was only accurate to ~ 0.1 magnitudes and the lightcurve was not densely sampled.

The strongest features in binary lightcurves are associated with caustics, and a great deal of work has gone into characterizing their features and effects.⁶ When a source enters (or leaves) a caustic, two additional, highly-magnified images are created (or destroyed) causing a large, sharp increase (decrease) in the total magnification. A source that enters a caustic must also leave it, so caustic crossings cause strong U-shaped features in binary lightcurves, as can be seen in Figure 1.5. Even passage close to a caustic can cause strong lightcurve features, especially passage near a cusp. Unless the lightcurve sampling is very sparse, caustic-induced features can usually be detected even with very poor photometry. Therefore, the probability of detecting the binary nature of the lens is closely approximated by the probability of the source

⁶See for example Witt and Mao (1995), Dominik (1999), Bozza (1999), Bozza (2000a), Bozza (2000b), Han et al. (2000), Gaudi and Petters (2002a), Gaudi and Petters (2002b), An (2005), Chung et al. (2005), Han (2006), Chung (2009), Chung and Lee (2011).

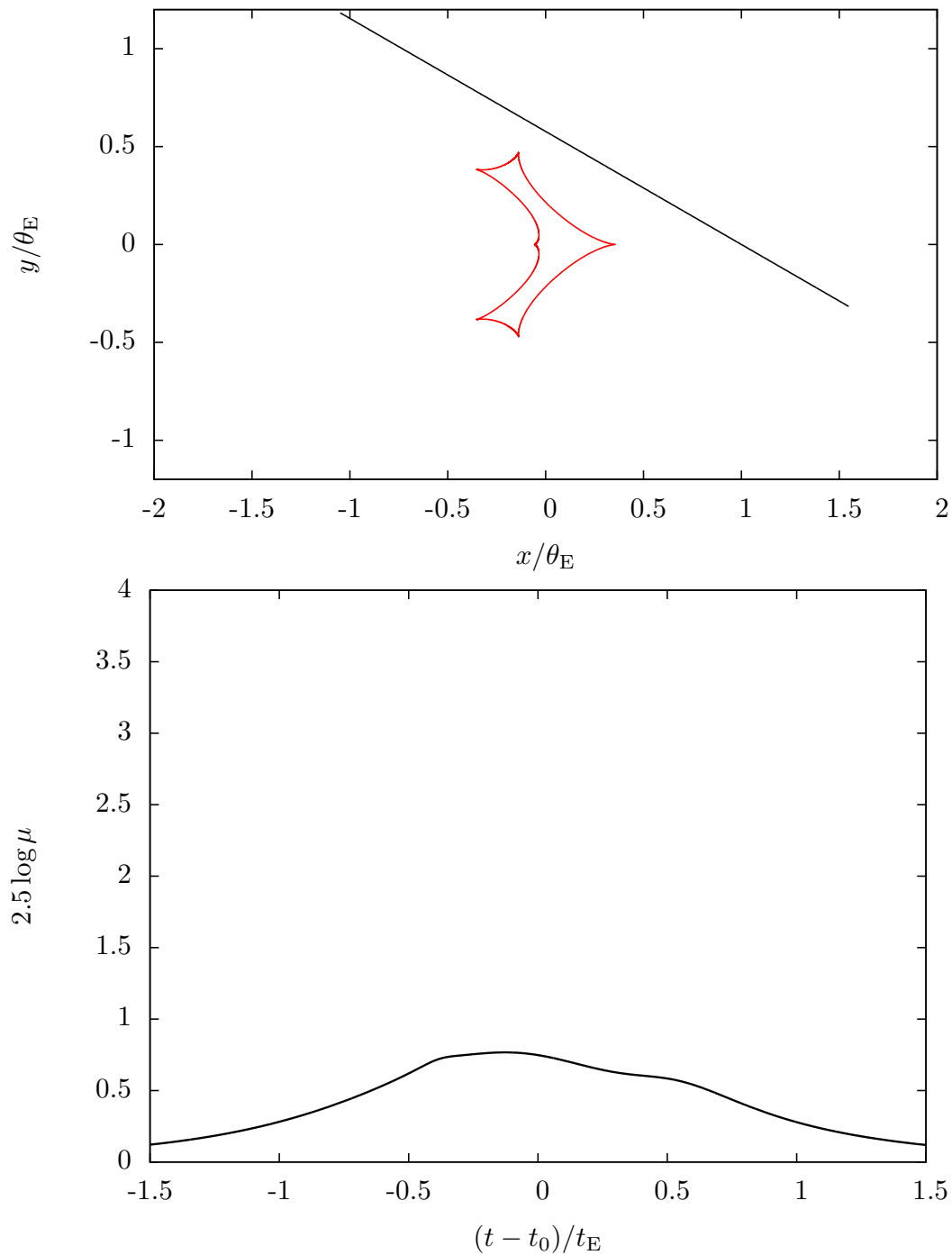


Figure 1.4 – Example of a non-caustic-crossing microlensing lightcurve (lower panel) caused by a binary lens with projected separation $s = 0.9$ and mass ratio $q = 0.1$. The upper panel shows the caustic in red and the source trajectory, moving from left to right, in black. The impact parameter is $u_0 = -0.5$ and the trajectory angle is $\alpha = 240^\circ$.

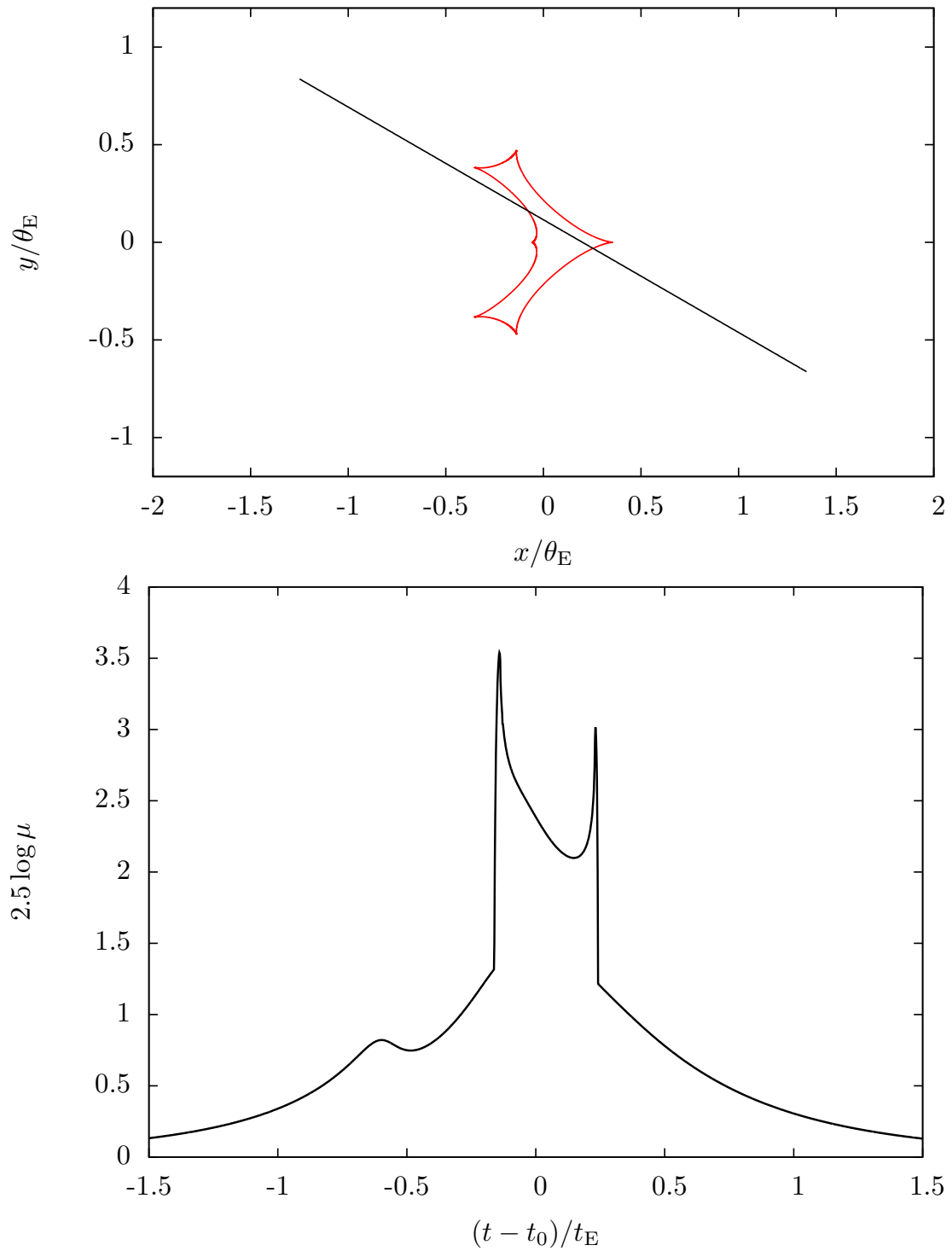


Figure 1.5 – Example of a caustic-crossing microlensing lightcurve. The event is identical to that shown in Figure 1.4, but for the impact parameter, which for this event is $u_0 = -0.1$.

encountering a caustic, which is roughly proportional to the caustic size.

The caustics are largest when the mass ratio q is close to one, and when the separation s is close to one (Schneider and Weiss 1986). For small mass ratios (i.e., planetary lenses) the caustic size decreases roughly as $q^{1/2}$ for planetary caustics and roughly as q for central caustics (Bozza 1999; Han 2006). The shallow scaling of the planetary caustic size means that planetary caustics are still detectable with mass ratios $q \sim 10^{-6}$, i.e., of the order of the Earth-Sun mass ratio. As s becomes large, the size of the planetary caustic scales approximately as s^{-2} , while, as s becomes small it scales as s^3 (Han 2006); the size of the central caustic scales approximately as $(s + s^{-1})^{-2}$ when s is either large or small (Chung et al. 2005). The strong scaling of the planetary caustic size leads to the concept of a *lensing zone*, a range of separations surrounding $s = 1$, over which the size of the planetary caustic is largest and detection of a planet is most likely (Gould and Loeb 1992). This zone is typically considered to extend over the range $0.6 < s < 1.6$ (Wambsganss 1997; Griest and Safizadeh 1998; Han 2009b).

2

Microlensing observations and simulations

Having discussed the basic theory of microlensing in Chapter 1, we now focus on the more practical aspects of observing and simulating microlensing. After a brief theoretical detour to calculate the expected number of microlensing events, the first section describes the strategies and equipment that microlensing surveys employ, before discussing some of the complications associated with real events that were not covered in the first chapter. The second section introduces microlensing simulations, detailing the various aspects that should be considered when building a simulation, and briefly reviews some of the ways microlensing simulations have been used in the past.

2.1 Microlensing observations

2.1.1 The probability of microlensing

The probability that any given source is currently being microlensed is closely related to the microlensing optical depth to that source. The optical depth is the cross section of all lenses lying between the observer and the source, and is chosen to be the area enclosed by the Einstein radius of each lens. Therefore the optical depth to a source at

D_s is

$$\tau = \frac{1}{\delta A} \int_0^{D_s} \delta A dD_1 n(D_1) \pi r_E^2, \quad (2.1)$$

(Vietri and Ostriker 1983), where $\delta A dD_1$ is an infinitesimal volume element along the line of sight to the source, with δA representing a small area perpendicular to the line of sight and $n(D_1)$ is the number density of lenses along the line of sight at distance D_1 . When the number density is replaced by the mass density of lenses $\rho(D_1)$, the dependence of r_E on the individual lens masses cancels out, and τ can be written

$$\tau = \int_0^{D_s} \frac{4\pi G \rho(D_1) D_1 (D_s - D_1)}{c^2 D_s} dD_1. \quad (2.2)$$

The probability that a given source is being microlensed is

$$P = 1 - e^{-\tau}. \quad (2.3)$$

When τ is small, $P \simeq \tau$, which is the case for Galactic microlensing. To get an order of magnitude estimate of the optical depth, we can assume that the mass density of stars is constant, with its local value $0.1 M_\odot \text{pc}^{-3}$; for a source at the distance of the Galactic centre $R_0 = 8 \text{ kpc}$, the optical depth is therefore $\tau \approx 6 \times 10^{-7}$. Observations, as well as estimates of the optical depth calculated using more realistic Galactic models, suggest larger values of $\tau \approx 1\text{--}5 \times 10^{-6}$ (Bissantz et al. 1997; Han and Gould 2003; Hamadache et al. 2006; Popowski et al. 2005; Sumi et al. 2003; Kozłowski 2007; Sumi et al. 2006; Kerins et al. 2009, ordered by the optical depth estimates).

The microlensing event rate, the rate at which new microlensing events occur, is closely related to the optical depth. The rate at which microlensing events occur for a given source is

$$\gamma = \frac{2\tau}{\pi \langle t_E \rangle}. \quad (2.4)$$

where $\langle t_E \rangle$ is the event timescale averaged over the distribution of lens distances, masses and relative lens-source velocities. The total event rate Γ is

$$\Gamma = \sum^{N_s} \frac{2 \tau(D_s)}{\pi \langle t_E \rangle}, \quad (2.5)$$

where N_s is the number of monitored sources. Adopting a value of $\langle t_E \rangle \approx 20$ d, yields a total event rate

$$\Gamma \approx 12 \text{yr}^{-1} \frac{\tau}{10^{-6}} \frac{N_s}{10^6}. \quad (2.6)$$

It is therefore necessary to monitor millions of stars to have a reasonable chance of detecting a microlensing event.

2.1.2 Microlensing surveys

The primary aim of most current microlensing surveys is to detect extrasolar planets. The probability of a planet causing a detectable signature in any given microlensing event is small, $\sim 10^{-2}$ (e.g., Mao and Paczyński 1991; Gould and Loeb 1992; Bennett and Rhie 1996). This implies that in order to have a reasonable chance of detecting a planet, hundreds of microlensing events must be monitored. With microlensing event rates $\Gamma \sim 10$ events per year per million stars, a survey must monitor $\sim 10^8$ stars in order to have a reasonable chance of detecting a planet (once factors that affect the detection efficiency are taken into account). A typical microlensing event has a timescale $t_E \sim 20$ d, so to detect and characterize such events requires approximately nightly photometry. However, planetary signatures are of a much shorter duration (from a few hours to a few days), so in order to fully characterize the complex lightcurve shapes, photometry with a cadence¹ of 5–30 min is necessary. These requirements dictate to every aspect of microlensing observations: the source stars that are targeted, the frequency of observations, and the telescopes and instrumentation that are used.

In order to maximize the numbers of source stars observed, microlensing surveys target the areas of sky with the highest surface density of stars. Within the Galaxy these are regions of low extinction towards the Galactic bulge and inner disc, while externally the Magellanic Clouds and the Andromeda Galaxy are common targets. Even in the Galactic bulge where the density of identifiable stars reaches $\sim 800 \text{ arcmin}^{-2}$ (e.g., Sumi 2004), surveys must monitor tens to hundreds of square degrees to observe

¹Observing frequency.

enough microlensing events. From the ground the stellar density in these fields is at the confusion limit and often many stars are blended within the same point spread function (PSF; see Section 2.1.3 for details of the effect of blending on lightcurves). Accurate time-series photometry in these confusion limited fields requires the use of difference image analysis (DIA, Tomaney and Crofts 1996; Alard and Lupton 1998; Alard 2000; Woźniak 2000; Bramich 2008) or PSF fitting (Stetson 1987; Schechter et al. 1993), each of which works best when the PSF is well sampled, i.e., there are many pixels within a seeing disc. This requires a pixel-scale ~ 0.3 arcsec for the best observing sites. Large CCD chips typically have a few million pixels and thus cover ~ 100 arcmin² of sky. Of the order of 300 pointings are then required to cover the requisite survey area, which if 5 minutes per field is allowed for image exposure and overheads, implies a cadence of roughly one image every few nights. The usable field of view of the telescope may be significantly bigger than that of a CCD chip, and if so the focal plane can be tiled with an array of CCDs to increase the cadence. For example, the OGLE-III survey used an eight-chip mosaic CCD imager with 0.34 deg² total field of view to allow a cadence of roughly one image per night (Udalski 2003).

As previously explained, nightly cadence is sufficient to detect microlensing events, but not to detect and characterize the signatures of planetary microlensing. Traditionally, follow-up observations have been necessary to achieve a cadence of the order of minutes, with 24 hour coverage. These are carried out by a number of networks (currently PLANET², MicroFUN³, RoboNet⁴ and MiNDSTEP⁵), employing many telescopes with mirror sizes ranging from ~ 2 m down to ~ 30 cm, distributed over six continents in order to provide round-the-clock coverage. They target a limited number of microlensing events that are alerted by the survey teams OGLE⁶ and MOA⁷, and monitor them intensively for planetary signatures. Each employs different selec-

²<http://planet.iap.fr/>

³<http://www.astronomy.ohio-state.edu/microfun/>

⁴<http://robonet.lcogt.net/>

⁵<http://www.mindstep-science.org/>

⁶<http://ogle.astrouw.edu.pl/>

⁷<http://www.phys.canterbury.ac.nz/moa/>

tion and observing strategies in order to maximize the efficiency of their observing resources. For example, MicroFUN, composed mainly of small telescopes operated by amateur observers, targets rare, highly-magnified microlensing events, which have a high sensitivity to planets (e.g., Gould et al. 2010), while PLANET uses larger telescopes to monitor more microlensing events, each with a lower individual sensitivity to planets (e.g., Gaudi et al. 2002). The RoboNet and MiNDSTeP teams use sophisticated computer algorithms to schedule their follow-up observations without introducing human selection biases (Dominik et al. 2008; Tsapras et al. 2009).

The survey-follow-up paradigm is extremely resource intensive, and can severely complicate the analysis of events, especially the statistical analysis of planet detections and non-detections (see e.g., Gould et al. 2010; Dominik et al. 2010). In many ways it is beneficial if the surveys can detect planets without the need for follow-up. This is only effective if the surveys can achieve a cadence of several images per hour. To this end, both OGLE and MOA have recently upgraded their instrumentation: OGLE-IV with a 32 chip mosaic imager with 1.4-deg² total field of view, which observes with a cadence of roughly one image per hour on the densest fields (Udalski 2011), and MOA-II with a 10 chip mosaic with a 2.2-deg² field of view, which observes with a cadence of ~10 min, again on a small number of dense fields (Sako et al. 2008). In the near future they will be joined by KMTNet, a network of three microlensing survey telescopes, each with a 4-deg² field of view, to be sited in Chile, South Africa and Australia, which combined will allow continuous high-cadence survey observations (Kim et al. 2010). Continuous, long-term monitoring will also be possible with AST3, a series of telescopes sited at Dome A, Antarctica (Yuan et al. 2010).

The other option for continuous, high-cadence microlensing surveys is a space telescope. Outside the Earth's atmosphere, such a telescope has a much better resolution than is possible from the ground and so can resolve much fainter stars. A wide-field imager need not observe as many fields to monitor the same number of stars as a ground-based survey and so it is possible to conduct a large-scale, high-cadence survey with only a limited number of fields. Moreover, by monitoring smaller, fainter

source stars, a space-based microlensing survey is sensitive to lower-mass planets (see Chapter 5). There are currently two promising proposals for such missions: ESA's *Euclid* (Beaulieu et al. 2010) and NASA's *WFIRST* (Bennett 2011). In Chapter 5, we simulate a microlensing survey by such a mission.

2.1.3 Complications

We have discussed the basics of microlensing theory and observation, but there are a number of complications that arise when observing actual microlensing events, which may need to be accounted for in their analysis. These complications are caused either by the imperfections of observing systems or by the break-down of our assumptions about the events. While complicating the analysis, it is often the case that these additional effects provide extra, valuable information about the event, in some cases allowing the microlensing degeneracy to be partially or fully broken. Some of the most important effects are introduced below.

Blending

Both the optics of the telescope and the Earth's atmosphere act to smear out the point-like image of a star into a finite disc, the PSF, limiting our ability to resolve details of objects near to each other on the sky. From the ground, the atmosphere is the dominant factor for all but the smallest telescopes and even for the best sites the average full width at half maximum (FWHM) of the PSF is ~ 1 arcsec. From space, without atmospheric distortion, resolution is limited by diffraction, optical imperfections or instrumentation.

In the crowded star fields necessary for microlensing, it is often the case that more than one star falls within the same seeing disc, so that multiple stars are seen as a single object (known as the blend, Di Stefano and Esin 1995; Woźniak and Paczyński 1997; Smith et al. 2007). Should one of the stars contributing to the blend be the source of a microlensing event, the apparent magnification of the blend will be less than the actual

magnification of the source. Blending may also make an event appear to have a shorter timescale, as small magnifications in the wings of the event will be less apparent. Similarly, small changes in magnification due to lens binarity may also be washed out, possibly concealing the binary nature of the lens. If the stars that make up the blend have a different colour to the source, then as the microlensing event proceeds the colour of the blend will change (Kamionkowski 1995; Buchalter et al. 1996).

The problem of blending is eased significantly by using DIA (see Section 2.1.2), which subtracts flux that is constant in time, leaving only flux that has varied between images. But even with DIA, uncertainty remains as to what fraction of the subtracted, constant, flux the unlensed source is responsible for. This leads to a degeneracy between the unlensed source flux, the impact parameter and event timescale when fitting models to microlensing data. While generally a nuisance, blending can sometimes be welcome. If it is the lens star that causes the blending, it may be possible to infer the lens mass and distance from its colour and magnitude once the source and lens have separated (Alcock et al. 2001a; Kozłowski et al. 2007). This is especially useful in planetary microlensing events because it allows the planet mass and projected separation to be expressed in physical rather than relative units (Bennett et al. 2007).

Finite sources

The theoretically infinite magnification of a point source, by either a single or binary lens, is obviously unphysical. This divergence of the magnification is a result of our approximation of geometrical optics, and it would be necessary to treat lensing with wave optics in order to properly calculate the magnification of a true point source near a caustic (e.g. Ohanian 1983). However, well before the wave optics regime is reached, our approximation of a point source breaks down: real microlensing sources are stars, with finite angular extent. Although the angular radius of a star θ_* is usually small compared to the angular Einstein radius ($\theta_*/\theta_E \sim 10^{-3-4}$), near a caustic or the centre of a single lens, the magnification can change drastically over a such a small scale. This can lead to one part of the star being significantly more magnified than another

and to calculate the apparent magnification of the source, it is necessary to integrate the product of the point-source magnification and star's intensity profile over the face of the star (Gould 1994b; Witt and Mao 1994; Nemiroff and Wickramasinghe 1994).

While significantly increasing the computational complexity of microlensing calculations, for both single⁸ and binary lenses,⁹ finite-source effects also allow the measurement of several useful quantities. When finite-source effects are measurable in a lightcurve it is possible to measure the time taken for the source to move by one source radius, t_* . The ratio of the angular source radius to the angular Einstein radius is then simply $\rho_* = t_*/t_E$. From the source star's colour and magnitude, we can estimate its angular radius θ_* , allowing the measurement of $\theta_E = \theta_*/\rho_*$ (Nemiroff and Wickramasinghe 1994). From Equation 1.15, this also implies a measurement of the magnitude of the relative lens-source proper motion μ_{rel} ¹⁰ (Gould 1994b; Nemiroff and Wickramasinghe 1994). Measurement of θ_E partially breaks the microlensing degeneracy, and allows a mass-distance relation to be defined

$$M = \frac{1}{\kappa} \frac{x}{1-x} \left(\frac{\theta_E}{\text{mas}} \right)^2 \left(\frac{D_s}{\text{kpc}} \right), \quad (2.7)$$

where $\kappa = 8.144 \text{mas}/M_\odot$ (see e.g., Gould 2000a), x is again the fractional lens distance, and the source distance D_s is assumed to be known, at least approximately.

Parallax

In calculating the lightcurve previously, we have assumed that the source, lens and observer each travel at a constant velocity. This may be a reasonable assumption for stars

⁸See, e.g., Gould (1994b), Witt and Mao (1994) and Lee et al. (2009)

⁹See, e.g., Schramm and Kayser (1987), Wambsganss et al. (1992), Dominik (1995), Bennett and Rhie (1996), Gould and Gaucherel (1997), Dong et al. (2006), Dominik (2007), Pejcha and Heyrovský (2009), Gould (2008), Bennett (2010), Bozza (2010)

¹⁰Not to be confused with the magnification μ . This proper motion is actually the instantaneous geocentric proper motion, rather than the more useful heliocentric or barycentric proper motion. Conversion requires that the direction and not just the magnitude of the proper motion be known. This can be found by measuring microlens parallax or directly detecting the lens once it has separated from the source.

moving in the Galactic potential, but an observer on Earth is constantly accelerating as the Earth orbits the Sun. It will be important to consider this acceleration if the microlensing event has a duration which is a significant fraction of the Earth's orbital period and if the projection of the Einstein radius from the source to the observer plane (the back-projected Einstein radius)

$$\tilde{r}_E = \frac{r_E}{1-x}, \quad (2.8)$$

is of the order of 1 AU (Gould 1992). This may well be the case if the lens is close to the observer. The effect, known as microlensing orbital parallax, causes a modulation of the standard microlensing lightcurve as the source velocity appears to have an additional varying component due to the Earth's motion. A related effect, often referred to as space-based parallax occurs if two observers simultaneously observe a microlensing event from two different locations, with separations of the order of \tilde{r}_E ; in this case each observer sees a slightly different microlensing event due to their different viewing angles (Refsdal 1966; Gould 1992, 1994a). In extreme cases, such as high-magnification events and caustic crossings, a terrestrial parallax effect is observable due to the differing locations of observers on the Earth (Hardy and Walker 1995; Gould and Andronov 1999).

In each case, if such effects are present in the lightcurve, it is possible to measure the microlensing parallax

$$\vec{\pi}_E = \frac{\text{AU}}{\tilde{r}_E} \vec{e}_{\mu_{\text{rel}}}, \quad (2.9)$$

which is the inverse of the back projected Einstein radius (see e.g., Gould 2000a); the microlensing parallax is a vector quantity, with direction parallel to the relative lens-source proper motion vector ($\vec{e}_{\mu_{\text{rel}}}$ is a unit vector in this direction). Combining Equations 2.8 and 2.9 it is possible to construct a mass-distance relation (e.g., Alcock et al. 1995)

$$M = \frac{1}{\kappa} \left(\frac{\text{AU}}{\pi_E} \right)^2 \frac{1-x}{x} \left(\frac{D_s}{\text{kpc}} \right)^{-1}. \quad (2.10)$$

Mass measurements

As we have seen, measurements of finite-source effects or parallax allow additional constraints to be placed on the lens mass and distance. Should it be possible to measure both effects in the same event, it is possible to completely solve the event for the lens mass and distance. The constraints of Equations 2.7 and 2.10 can be combined and solved for the mass and distance (e.g., Gould 2000a)

$$M = \frac{\theta_E}{\kappa\pi_E}, \quad (2.11)$$

$$\pi_l = \pi_E\theta_E + \pi_s, \quad (2.12)$$

where $\pi_l = \text{AU}/D_l$ and $\pi_s = \text{AU}/D_s$ are the parallax of the lens and source, respectively. Additionally, it is possible to measure θ_E by directly imaging the lens once it has separated from the source after the microlensing event. From this the relative proper motion of the lens and source μ_{rel} can be measured, and combined with Equation 1.15 to determine θ_E . This, however, requires that the lens is bright enough to be detectable.

Other complications

Additional lightcurve complications can arise if the source is a binary system. If both components are luminous, and their separation is of the order of the angular Einstein radius, then both stars will be microlensed by differing amounts, and the resulting lightcurve will be the superposition of two separate microlensing lightcurves (Griest and Hu 1992). A binary source will also undergo orbital motion, which can cause effects similar to the parallax effects of the Earth's orbit, whether the second component is luminous or not, provided it is massive (Cherepashchuk et al. 1995; Han and Gould 1997; Paczyński 1997; Rahvar and Dominik 2009). Such effects are called *xallarap*, being the mirror of parallax effects in the source plane.

Should the lens be a binary, its components also undergo orbital motion. This motion, as we shall discuss in Chapter 3, causes significantly more complicated effects than orbital motion of the source or observer. Binary-lens lightcurves can also be

complicated by the presence of additional lens components, such as distant perturbing masses (Bozza 2000a), multiplanet systems (Gaudi et al. 1998; Han et al. 2001; Gaudi et al. 2008), or extrasolar moons (Bennett and Rhie 2002; Han and Han 2002; Han 2008; Liebig and Wambsganss 2010).

2.2 Microlensing simulations

The aim of most microlensing observations is to learn, not about the physics of microlensing, but about the objects that are involved in the microlensing events. The observed distribution of events results from a complex combination of the underlying population of sources and lenses, together with the observing systems and strategies used. It is therefore very difficult to predict the outcome or understand the results of any microlensing experiment without simulating it. In this section we outline the various ingredients that go into microlensing simulations and review some of the previous work where microlensing simulations have played an important role.

2.2.1 Requirements of a microlensing simulation

While the goals of microlensing simulations may vary, we often want to know what the results of a microlensing survey are likely to be. For example, if we are searching for planets, we would like to know how many planets a survey will discover and how their properties relate to the underlying population. To answer these questions to a reasonable degree, our simulations must model the survey equipment and strategy, as well as the distributions of lenses and sources. The relative importance of each component may not be the same from simulation to simulation, but some choice of each must be made. For example, if comparing the relative merits of two proposed telescopes, it will be necessary to accurately model the telescopes and their observing strategies, but the details of the source and lens populations may not be too important, so long as they are roughly representative of those that will be observed. In this section

we describe the different components of a microlensing simulation.

The Galactic distribution of sources and lenses

In a simulation, the Galactic distribution of sources and lenses (e.g., their distance, kinematic, luminosity and mass distributions) will be governed by a Galactic model. This need not be the same model for each component (lenses and sources) or even each quantity (mass, distance etc.). These fundamental source and lens properties are drawn from the Galactic model in order to determine the Einstein radius and timescale of each event, which determine the relative rate at which simulated events occur

$$\gamma \propto r_E v_t. \quad (2.13)$$

If we are interested only in relative rates (as in Chapter 3) we need only select simulated events with probabilities proportional to this relative rate. However, if we wish to compute absolute event rates (as in Chapters 4 and 5) we must normalize to the overall microlensing event rate Γ , computed either from our Galactic model or from empirical estimates.

Source and lens parameters

The next elements of the simulation to consider are the properties of the sources and lenses. Examples of these properties include the semimajor axis and mass ratio of binary lenses. These properties are not fundamental, as for example, a simulation of single-lens events will not need to worry about binary mass ratios. It will often be the case that if these properties are included in the simulation they will have a uniform or logarithmic distribution in order to be used as an independent variable. The line is somewhat fuzzy between a parameter belonging to the Galactic model or to the source or lens, especially for quantities such as the lens mass.

Observing system and strategy

A model of the observing system and its observing strategy must be included. The model should produce simulated observations which resemble the observations conducted by real observatories with similar photometric uncertainties and time sampling. This can either be achieved using a model (as we do in the following chapters) or by using the actual data that has been produced by surveys and injecting simulated events into this data (e.g., Alcock et al. 2000b; Afonso et al. 2003).

Detection criteria

The detection criteria are used to select a (hopefully clean) sample of events of interest from the data of a survey. An ideal set of detection criteria will pass all the events of interest, while rejecting both non detections and false positive events without rejecting any false negatives. This is difficult to achieve in practise. The burden of proof is significantly reduced for a simulation compared to an experiment because all the inputs and the parent population are fully known. However, a simulation should try to recreate the stringent detection criteria of an experiment as closely as possible, or risk being too optimistic.

Common types of detection criteria include:

- a $\Delta\chi^2$ cut – this is used to assess the relative likelihood models that do and do not include a feature of interest, for example a planetary-lens model and a single-lens model. The value of $\Delta\chi^2$ indicates the significance of a detection over a non-detection, with larger values indicating higher significance. For more details see Appendix A, which discusses $\Delta\chi^2$ thresholds in the context of the work presented in Chapter 5.
- a reliability cut – if a data set contains outliers, then a $\Delta\chi^2$ cut may pass events that are caused by a single outlier data point. These false positives can usually be rejected by requiring that several consecutive data points also show signs of the signal of interest.

The question of detection criteria is often turned on its head by asking the question: with what efficiency does the experiment select events for the sample? The detection efficiency of an experiment is the product of the experimental sensitivity and the detection criteria. By applying a chosen set of detection criteria to simulated events injected into experimental data, the survey detection efficiency can be evaluated. It is then possible to estimate the underlying population of events by taking the observed sample of events and dividing through by the detection efficiency.

Blending

Blending does not fit easily into any of the simulation components described so far. Strictly it is a purely instrumental effect (it is caused by the telescope optics and the atmosphere above it). However, it can be easily parametrized as a constant term added to the lightcurve, suggesting that it could be included as a source parameter. In reality though, it is strongly dependent on the stellar crowding (the domain of the Galactic model). A proper treatment of blending requires the combination of the Galactic model with the observing system model. We do this in each subsequent chapter, but only in Chapter 5 do we treat blending in a manner that is consistent with our Galactic model.

2.2.2 Applications of microlensing simulations

Large numbers of microlensing simulations have been performed, predicting the results of surveys, investigating new phenomena, or supplementing the analysis of experimental results. Often, depending on the nature of the work, full simulations as described above are not performed, but one or more simulation components are used.

Many surveys have used simulations to evaluate their detection efficiency: the fraction of microlensing events that will be positively identified in the data. Only with knowledge of the detection efficiency, is it possible to infer the properties of the parent distribution from the observed distribution. To do this, the MACHO, EROS and OGLE collaborations have conducted extensive simulations, injecting a large number of sim-

ulated microlensing events into real data, either at the image level (e.g., Alcock et al. 2000b, 2001b; Sumi et al. 2003; Wyrzykowski et al. 2009, 2011) or at the photometry level (Afonso et al. 2003; Hamadache et al. 2006; Tisserand et al. 2007). These semi-simulated data were then analyzed with the same processing pipelines that analyzed the real data. Knowing the events that were input, the detection efficiency of the experiments can then be determined by comparing the number of events that survive selection cuts to the number of input events. These simulations do not require a Galactic model as the aim is to find the detection efficiency as a function of the parameter t_E , the only observable parameter that is determined by the Galactic model for single-lens events (ignoring parallax etc.). A similar process can be carried out to calculate planetary detection efficiencies (Gaudi and Sackett 2000; Gaudi et al. 2002; Gould et al. 2010).

Various simulations of planetary microlensing have been used to advocate microlensing planet searches. Early works (e.g., Mao and Paczyński 1991; Gould and Loeb 1992; Bolatto and Falco 1994; Bennett and Rhie 1996), did not carry out full simulations, but instead integrated over relatively simple Galactic models and parameter distributions, using semi-analytic detection criteria¹¹ and averaging over uninteresting parameters. Full simulations that include models of observations and more realistic detection criteria have followed (e.g., Peale 1997, 2001; Bennett and Rhie 2002, Gaudi et al., unpublished), arguing the case for ground- and space-based planetary microlensing surveys; the work presented in Chapter 5 follows in this tradition. It should be noted that, while not being as realistic as the full simulations, semi-analytic integrations are often more general, as full simulations strictly only apply to the observational set-up that they model. In practice however, it may be more accurate to extrapolate the results of a full simulation to a different set-up than it is to extrapolate semi-analytic results.

Simulations have also been used to investigate newly discovered or poorly understood effects in microlensing. Examples include simulations of parallax effects (Buchal-

¹¹For example, rather than simulating data to calculate the $\Delta\chi^2$ of a detection, it is possible to estimate the $\Delta\chi^2$ contribution of data points that are taken at a constant rate over an event.

ter and Kamionkowski 1997), high-magnification events (Griest and Safizadeh 1998; Rattenbury et al. 2002), blending (Sumi et al. 2006; Smith et al. 2007) and extrasolar moons (Han and Han 2002; Liebig and Wambsganss 2010). The work presented in the following two chapters provide two more examples, with simulations being used to explore the effects of orbital motion in Chapter 3 and to estimate the rate of occurrence of an extreme form of orbital motion event in Chapter 4.

3

The detectability of orbital motion in microlenses¹

Kepler's laws of orbital motion have proved invaluable throughout all areas of astronomy and astrophysics, enabling the measurement of celestial masses from astrometry and the timing of orbiting bodies. Microlensing is no exception. Detection of lens orbital motion in a binary microlensing event can be especially valuable, as it can enable the deprojection of the binary orbit. This potentially allows the semimajor axis, inclination and eccentricity of the orbit to be constrained as opposed to just the instantaneous projected separation of the lens components that is usually measured (Bennett et al. 2010). However, in many microlensing events it is very difficult to recover orbital information about the lens. This is because the binary microlensing effect only depends on projected quantities, but also because of a mismatch between microlensing and orbital timescales (Dominik 1998b), the former typically being a factor ~ 100 shorter than the latter. While the probability of detecting orbital motion is low, in a small number of binary microlensing events the precise timing allowed by caustic-crossing features has helped to overcome the mismatch in timescales (e.g., Albrow et al. 2000; An et al. 2002; Gaudi et al. 2008), allowing the effects of orbital motion to be detected in both

¹The work presented in this chapter has been published as M. T. Penny, S. Mao, and E. Kerins, *MNRAS*, 412:607-626, 2011.

stellar-binary and planetary microlensing events.

Whilst past detections show that it is possible to detect lens orbital motion, it is not known how frequently we can expect such detections. In this chapter we attempt to quantify the detectability of orbital motion. We do this by simulating binary microlensing events with orbiting lenses, instead of static lenses as is usually assumed in more general microlensing studies. We simulate the observations of a near future survey and fit these observations with static binary-lens models to determine when a detection can be claimed. To obtain the numbers necessary for a statistical sample, we automated the fitting process. In order to be confident of our results from this procedure, we repeated the process with a control sample of static binary lenses, taking care to ensure that the fitting of the two samples was conducted in a fair way. While computational constraints prevent us from including finite-source effects in our lightcurves, our results allow us for the first time to estimate the fraction of events with detectable orbital motion. We also use the simulations to investigate the factors that affect the detectability of orbital motion. By looking at some example detections, we show that to a certain extent the orbital motion effects that are detectable fall into one of two classes: *separational* or *rotational*, as suggested by Gaudi (2009). Separational-class events are caused by the rapid deformation of a resonant caustic due to inclination or eccentricity, and show large changes to the lightcurve over a short period of time. Rotational-class events are caused by the slow rotation of the lens, and show subtle effects over the whole lightcurve.

The structure of the chapter is as follows. In Section 3.1 we review some of the previous work on orbital motion effects in microlensing and in Section 3.2, we outline how orbital motion can affect microlensing lightcurves. Section 3.3 describes our simulations of microlensing events and Section 3.4 describes how we measure the effects of orbital motion. In Section 3.5, we present the results of the simulations. We draw conclusions and discuss the results in Section 3.6.

3.1 Introduction

If the components of a binary microlens are gravitationally bound, they will orbit each other and their projected orientation will change as a microlensing event progresses. As the magnification pattern produced by a binary lens is not rotationally symmetric, the change in orientation may be detectable in the lightcurve of the event. If the orbit is inclined relative to the line of sight, then the projected separation of the lens components will also evolve, causing changes in the structure of the magnification pattern, which again may be detectable. In a small fraction of binary microlensing events we can expect to see the effects of this orbital motion in their lightcurves. If orbital motion can be detected in a microlens it can provide constraints on the mass of the lens, and information about the binary orbit. While it is possible to measure the mass of a binary lens by measuring a combination of other higher-order effects, as discussed in the previous chapter, the only way to deproject the binary orbit and measure the semimajor axis is to measure the orbital motion.

To date, six binary microlensing events have shown strong evidence of orbital motion in the lens system. The first, MACHO-97-BLG-41, was a stellar-mass binary. Modelling of the event was able to measure the change in the projected angle and separation of the binary in the time between two caustic encounters, but was unable to constrain the orbital parameters (Albrow et al. 2000). The second event, EROS-BLG-2000-5, had very good lightcurve coverage, which allowed the measurement of the rates of change of the binary's projected separation and angle; these measurements were then used to obtain a lower limit of the orbit's semimajor axis and an upper limit on the combined effect of inclination and eccentricity (An et al. 2002). The third and fourth examples, OGLE-2003-BLG-267 and OGLE-2003-BLG-291, both seem to show orbital motion effects (Jaroszynski et al. 2005). However, only OGLE survey data was used in their analysis, without follow-up measurements, so the lightcurve coverage was not ideal. Combined with parallax measurement, the masses of both binary lenses were constrained, but no constraints could be placed on the orbits (Jaroszynski

et al. 2005). In each of these four cases, the ratio of the component masses is large (near unity), indicative of the lens systems being binary stars; however, orbital motion has recently been measured in two events involving planetary-mass secondaries.

OGLE-2006-BLG-109 was an event involving a triple lens, with analogues of Jupiter and Saturn orbiting an $\sim 0.5-M_{\odot}$ star (Gaudi et al. 2008). The lightcurve of the event had extremely good coverage and showed multiple features, allowing the orbital motion of the Saturn analogue to be detected. The detection of orbital motion was so strong that the semimajor axes of both planets could be tightly constrained (Gaudi et al. 2008). A more complete analysis of the event, incorporating measurements of the lens flux and orbital-stability constraints, carried out by Bennett et al. (2010), tightly constrained four out of six Keplerian orbital parameters of the Saturn analogue, and weakly constrained a fifth. The planet OGLE-2005-BLG-071Lb is an ~ 4 Jupiter-mass planet orbiting an $\sim 0.5-M_{\odot}$ star (Udalski et al. 2005). Measurements of the orbital motion in this event have allowed some constraints to be placed on the planet's orbit (Dong et al. 2009b). In all six events other higher-order effects have also been detected, most notably microlens parallax and finite-source effects, which are detected in all the events, and in each case allow the measurement of the lens mass.

Despite these detections, there has been relatively little theoretical work on orbital motion in microlensing, likely due to the traditional assumption that the effects of orbital motion on a binary-microlens lightcurve will be small and in most cases negligible (e.g., Mao and Paczyński 1991; Gould and Loeb 1992). The problem was first considered in detail by Dominik (1998b), who concluded that in most microlensing events the effects of lens orbital motion were likely to be small, though in some cases, lightcurves could be dramatically different. Dominik (1998b) points out that the effect is most likely to be seen in long-duration binary microlensing events with small projected binary separations. Ioka, Nishi, and Kan-Ya (1999) also studied the problem and noted that the effect of binary-lens rotation is likely to be important in self-lensing events in the Magellanic clouds. Rattenbury et al. (2002) showed that orbital motion could affect the planetary signatures seen in high-magnification events.

The six microlensing events that display orbital motion make up a significant fraction of the few tens of large-mass-ratio binary microlensing events² that have been modelled (e.g., Alcock et al. 2000a; Jaroszynski 2002; Jaroszynski et al. 2004, 2006; Skowron et al. 2007), which begins to shed doubt on the previous conclusion that lens orbital motion is likely to be unimportant in most binary events. The two planetary events constitute approximately 15 percent of the entire published microlensing planet population. These observations motivate us to revisit the question: how likely are we to see lens orbital motion in a microlensing event? This question is made especially pertinent in the context of the next generation of ground- and space-based high-cadence microlensing surveys, which will make the dense, largely-continuous lightcurve coverage of EROS-BLG-2000-5 and OGLE-2006-BLG-109 the norm rather than the exception. The aim of this chapter is to estimate the fraction of stellar-binary and planetary microlensing events where orbital motion is detectable, and to investigate the factors that affect the detectability. To do this, we simulate a large number of microlensing events caused by orbiting binary lenses.

3.2 Orbital motion in a binary microlens

The lightcurve of a microlensing event can be considered as a one-dimensional probe by the source of the two-dimensional magnification pattern produced by the lens (Wambsganss 1997). The magnification pattern of a single lens is rotationally symmetric about the position of the lens, but the magnification pattern of a binary lens is more complicated, containing strong caustic structures that exhibit a reflectional symmetry about the binary axis (the axis connecting the lens components; Schneider and Weiss 1986). However, far away from the caustics the magnification pattern can resemble that of a single lens.

As the lens components orbit each other, their position angle and their projected

²We will refer to binary lenses with mass ratios $q > 0.01$ as stellar binaries, and those with $q < 0.01$ as planetary.

separation can change. These changes cause changes in the orientation and structure of the magnification pattern respectively. It is clear, however, that only if the source traverses regions of the magnification pattern that differ significantly from that of a single lens, will it be possible to detect these effects of orbital motion. For the effects to be measurable, the lightcurve of the event must be affected in a significant way that is not reproducible by a static binary-lens model. It is also possible to detect the effect of orbital motion by showing that a static model is less physically plausible than an orbiting model, but this will usually require further information about the event, such as an independent constraint on the lens mass.

The effects of orbital motion on a lightcurve can also be mimicked by other higher-order effects, especially parallax and xallarap. Parallax effects are caused by the motion of the Earth about the Sun and cause the source to take an apparently curved path through the magnification pattern (e.g., Smith, Mao, and Paczyński 2003). In the case of xallarap, the source travels along a curved path through the magnification pattern as a result of binary orbital motion in the source system (Griest and Hu 1992; Paczyński 1997; Dominik 1998b; Rahvar and Dominik 2009). These curved paths can look very similar to those taken by the source in the rotating binary-lens centre-of-mass frame and hence it can sometimes be difficult to identify the true cause of the effect.

3.3 Simulating a high-cadence microlensing survey

The aims of this study are:

- to determine the fraction of microlensing events that will be affected by orbital motion, as will be observed by next-generation microlensing surveys, and
- to investigate the factors that affect the detectability of orbital motion, to aid the targeting of such events without resorting to exhaustive modelling efforts.

To achieve the first goal, the various factors that go into the observation of a microlensing event should be simulated: accurate modelling of the observing setup, the

distributions of planetary and stellar-binary lens systems, and the distribution of the sources and lenses throughout the Galaxy. To achieve the second goal we must simplify the parameter space we investigate, as far as possible without removing essential elements from the model, so as to allow a clear interpretation of the results.

To balance these somewhat contradictory requirements we choose to accurately simulate ideal photometry and use a semi-realistic model of the Galaxy, while investigating a logarithmic distribution of companion masses and separations. This allows us to use our simulations to gain a good order of magnitude estimate of the results expected from future surveys, whilst simultaneously investigating the factors that have the largest impact on the detection of orbital motion over a relatively uniform parameter space.

3.3.1 The Galactic model

To simulate the kinematic and distance distributions of the source and lens populations, we assume a simplistic bulge and disc model of the Galaxy. We assume all sources are located in the bulge, at a fixed distance $D_s = R_0 = 8$ kpc, in the direction of Baade’s Window, where R_0 is the distance to the Galactic centre. The lens distances are distributed according to the stellar density distribution of Model II of Binney and Tremaine (2008), which consists of a thin and a thick exponential disc and an oblate spheroidal bulge with a truncated power-law density distribution. The kinematics of our Galactic model are based on that of Han and Gould (1995b) who describe the kinematics of a stellar disc and a barred bulge. The distribution of transverse lens-source relative velocities, dn/dv_t , is dependent on the observer’s velocity, and the velocity distributions of the lens and source populations. The observer is assumed to follow the Galactic rotation at the position of the Sun and therefore has a velocity $(v_{O,\ell}, v_{O,b}) = (225.2, 7.2)$ km s⁻¹ in the direction of Galactic coordinates (ℓ, b) , once the Solar peculiar velocity is included. The source and lens are assumed to follow the Galactic rotation with an additional random component. In the directions ℓ and b ,

their velocities have the form

$$v_\ell = v_{\text{rot}} + v_{\text{rand},\ell}, \quad v_b = v_{\text{rand},b}, \quad (3.1)$$

where v_{rot} is the rotational component of the velocity, and $v_{\text{rand},\ell}$ and $v_{\text{rand},b}$ are random velocities in the directions ℓ and b , respectively. The rotation curve of the bulge is assumed to be flat beyond a distance of 1 kpc from the Galactic centre, and that of a solid body within 1 kpc. Therefore, the rotational velocity component, v_{rot} , for bulge stars is

$$v_{\text{rot}} = \begin{cases} v_{\text{max}} \left(\frac{R}{\text{kpc}} \right) & \text{if } R < 1 \text{ kpc} \\ v_{\text{max}} & \text{if } R \geq 1 \text{ kpc,} \end{cases} \quad (3.2)$$

where $v_{\text{max}} = 100 \text{ km s}^{-1}$ is the maximum rotational velocity of the bulge and $R = \sqrt{X^2 + Y^2}$, where (X, Y, Z) is a Galactocentric coordinate system with the X -axis increasing towards the observer and the Z -axis pointing out of the Galactic plane. For the disc, $v_{\text{rot}} = 200 \text{ km s}^{-1}$. The random velocity components are assumed to follow Gaussian distributions, with dispersions taken from Han and Gould (1995a). These dispersions are $(\sigma_\ell, \sigma_b) = (30, 20) \text{ km s}^{-1}$ for the disc and $(\sigma_X, \sigma_Y, \sigma_Z) = (110, 82.5, 66.3) \text{ km s}^{-1}$ for the bulge. From these quantities, the relative transverse velocity of the source v_t (the quantity we are interested in) can be calculated from the relative velocities in the ℓ and b directions, v_ℓ and v_b , respectively, as

$$v_t = \sqrt{v_\ell^2 + v_b^2}, \quad (3.3)$$

where (e.g., Han and Gould 1995b)

$$v_{\ell,b} = (v_l - v_o)_{\ell,b} + x(v_o - v_s)_{\ell,b}, \quad (3.4)$$

and v_o, v_l and v_s are the observer, lens and source velocities respectively, in the directions ℓ and b .

The final distribution of lens distances and velocities takes into account the dependence of the event rate $\Gamma \propto v_t \sqrt{x(1-x)}$ on the distribution of each parameter. While the kinematic and density distributions are produced from different Galactic models,

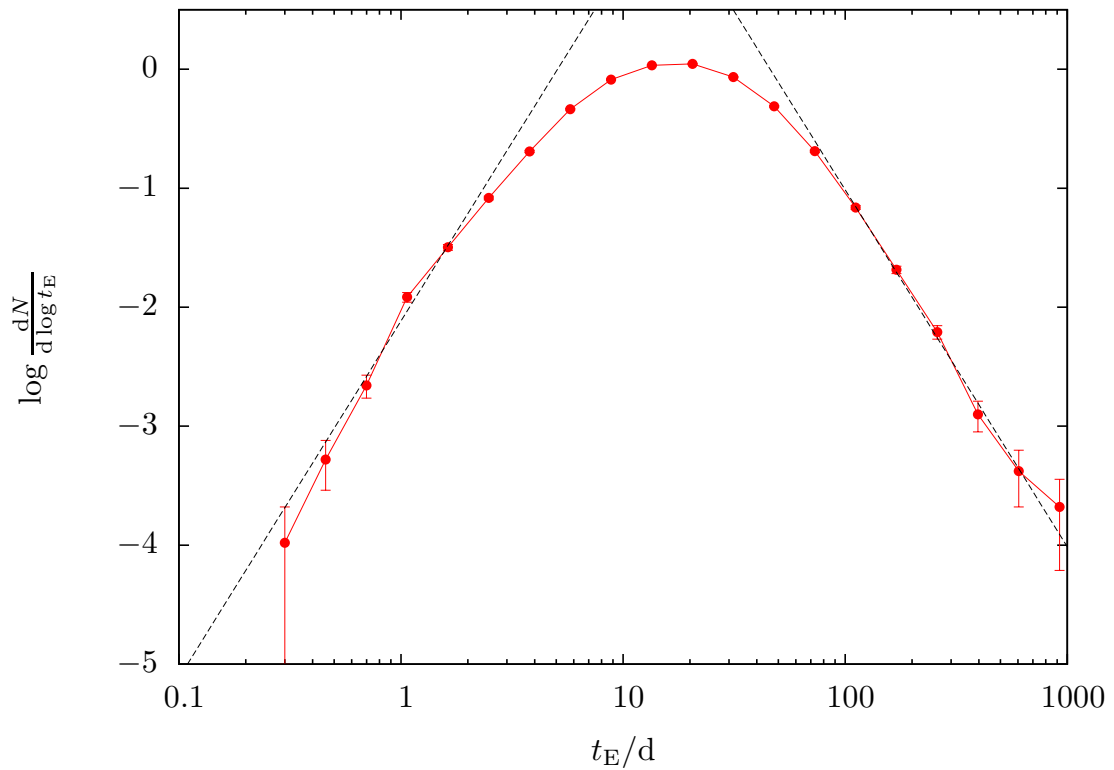


Figure 3.1 – The Einstein timescale distribution for $\sim 50\,000$ simulated events. The solid line and data points show the simulated data, and the dashed lines show lines of slope 3 and -3 , the expected asymptotic behaviour of the distribution.

they qualitatively reproduce the observed Einstein timescale distribution, shown in Figure 3.1, including its asymptotic behaviour (Mao and Paczyński 1996).

3.3.2 The microlensing events

Blending

When observing a microlensing event, it is often the case that the light of the source being magnified is blended with that of nearby stars in the field (Di Stefano and Esin 1995). The amount of blending can be quantified by a blending fraction f_s , which we define to be the fraction of the total flux of the observed blend that the source

contributes when unmagnified, such that the time dependent magnitude of the blend is

$$I(t) = I_b - 2.5 \log[f_s A(t) + (1 - f_s)], \quad (3.5)$$

where I_b is the baseline magnitude of the observed blend when the source is unmagnified and $A(t)$ is the magnification caused by the lens.

The distribution of baseline magnitudes and blending fractions is drawn from simulations of blending effects by Smith et al. (2007) who perform photometry on mock images of typical Galactic bulge fields with high stellar density. Specifically, we calculate the blending fraction and baseline magnitude for each event from the input and output magnitudes of source stars drawn from their simulation with 1.05-arcsec seeing and input stellar density of 133.1 stars arcmin⁻² down to a magnitude of $I = 17$, before any detection efficiency cuts are made to the catalogue. As the phenomenon of negative blending (the source apparently contributing a fraction $f_s > 1$ to the total flux of the blend; Park et al. 2004; Smith et al. 2007) is poorly understood, we only include sources with moderate negative blending, requiring that $f_s < 1.2$.

The mock images are produced by Smith et al. (2007) using the method of Sumi et al. (2006), drawing stars from the Hubble Space Telescope I -band luminosity function of Holtzman et al. (1998), adjusted to account for denser fields and brighter stars using OGLE data. Extinction was accounted for using the extinction maps of Sumi (2004) and the baseline magnitudes were measured using the standard OGLE pipeline based on *DOPHOT* (Schechter et al. 1993). Full details of the method are given by Smith et al. (2007), and references therein.

Lenses and sources

The lens systems are composed of a primary of mass M_1 and secondary of mass M_2 . The primary's mass is drawn from a broken power-law distribution,

$$\frac{dn}{dM_1} \propto M_1^{(\alpha+0.5)}; \quad \alpha = \begin{cases} -1.3 & M_1 \leq m_{\text{break}} \\ -2.0 & M_1 > m_{\text{break}}, \end{cases} \quad (3.6)$$

matching that of Gould (2000b), though with a slightly lower break mass ($m_{\text{break}} = 0.5M_{\odot}$) and with lower and upper limits of $0.05M_{\odot}$ and $1.2M_{\odot}$, respectively. The addition of 0.5 to the power-law index is to account for the dependence of the microlensing event rate on the mass of the lens. We do not include a population of stellar remnant lenses, such as white dwarfs, neutron stars and black holes. The mass ratio q of the secondary to the primary is drawn from a logarithmic distribution, with limits $10^{-2} \leq q < 1$ for stellar-binary lenses and $10^{-5} \leq q < 10^{-2}$ for planetary lenses. Note that for lower-mass primaries, the distribution of stellar-binary mass ratios includes secondaries with masses as low as $\sim 5M_{\text{Jupiter}}$, i.e., well into the planetary-mass regime. The lower limit of the planetary mass ratio distribution implies a secondary of ~ 1 Earth mass for a $0.3M_{\odot}$ primary.

The components of the lens orbit their combined centre of mass in Keplerian orbits, of semimajor axis a , distributed logarithmically (e.g., Abt 1983) over the range $a = 0.1\text{--}20$ AU. These orbits are inclined to the line of sight, with inclination angles distributed uniformly. For stellar binaries we performed two sets of simulations, one with zero eccentricity e and another with bound, eccentric orbits with eccentricities distributed uniformly over $0 \leq e < 1$.

The source trajectories were parametrized by the angle of the source trajectory relative to the binary axis α_0 , at the time of closest approach t_0 , and the impact parameter u_0 , the projected source-lens separation in units of Einstein radii at t_0 . We set $t_0 = 0$, for simplicity, and α_0 and u_0 were distributed uniformly over the ranges $0 \leq \alpha_0 < 2\pi$ and $-1.5 \leq u_0 < 1.5$ respectively.

3.3.3 Simulation of photometry

In the hunt for planets, the proposed next generation of ground-based microlensing surveys will consist of a (potentially homogeneous) network of telescopes located throughout the southern hemisphere such that the target fields in the Galactic bulge can be monitored continuously during the times when the bulge is observable. The

telescopes will have diameters between 1.3–2.0 m and fields of view 1.4–4.0 deg². They will operate at a cadence of approximately 10 min and are expected to discover several thousand microlensing events per year. An example is KMTNet, a network of three identical 1.6-m telescopes due to enter operation in 2014 (Kim et al. 2010). Such surveys can operate effectively without the need for intensive follow-up observations due to their high cadence and continuous coverage. However, it is likely that the survey/follow-up observing paradigm will persist, with low-cadence surveys monitoring far larger areas of sky. High-cadence surveys should begin operating near the middle of the decade (~2015), and will likely be followed by space-based microlensing surveys. However space-based surveys will not begin before roughly the end of the decade, and so this work concentrates on ground-based surveys.

Unfortunately, the effects of the weather amongst other things make completely continuous, high-cadence observations unachievable in reality. Rather than including complicated models of these effects, we instead choose a simpler prescription. Each event is monitored with continuous photometry at a reduced cadence of 30 min. These observations are performed by telescopes with 1.3-m effective diameter observing in the *I*-band. For each exposure of 120 s the seeing is chosen from a lognormal distribution with mean 1.2 arcsec and standard deviation 0.25 arcsec, and a background flux distributed as

$$F = 8500 \text{ LN}(1.5, 0.4) \text{ photon arcsec}^{-2}, \quad (3.7)$$

which is integrated over a seeing disc, and where $\text{LN}(\mu, \sigma)$ is a lognormal distribution with mean μ and standard deviation σ . New values of seeing and background flux are chosen for each observation. A lower limit on the photometric accuracy is imposed by adding a Gaussian noise component, with dispersion 0.3 percent, to the photon counts, which are calculated by assuming 10 photon m⁻² s⁻¹ reaches the observer from a $I = 22$ source.

To ensure that all the features of a lightcurve are covered and that there is a good balance between the baseline, peak and features of the lightcurve when fitting (see the next section), the lightcurve is monitored continuously over the times $-5t_E \leq t - t_0 <$

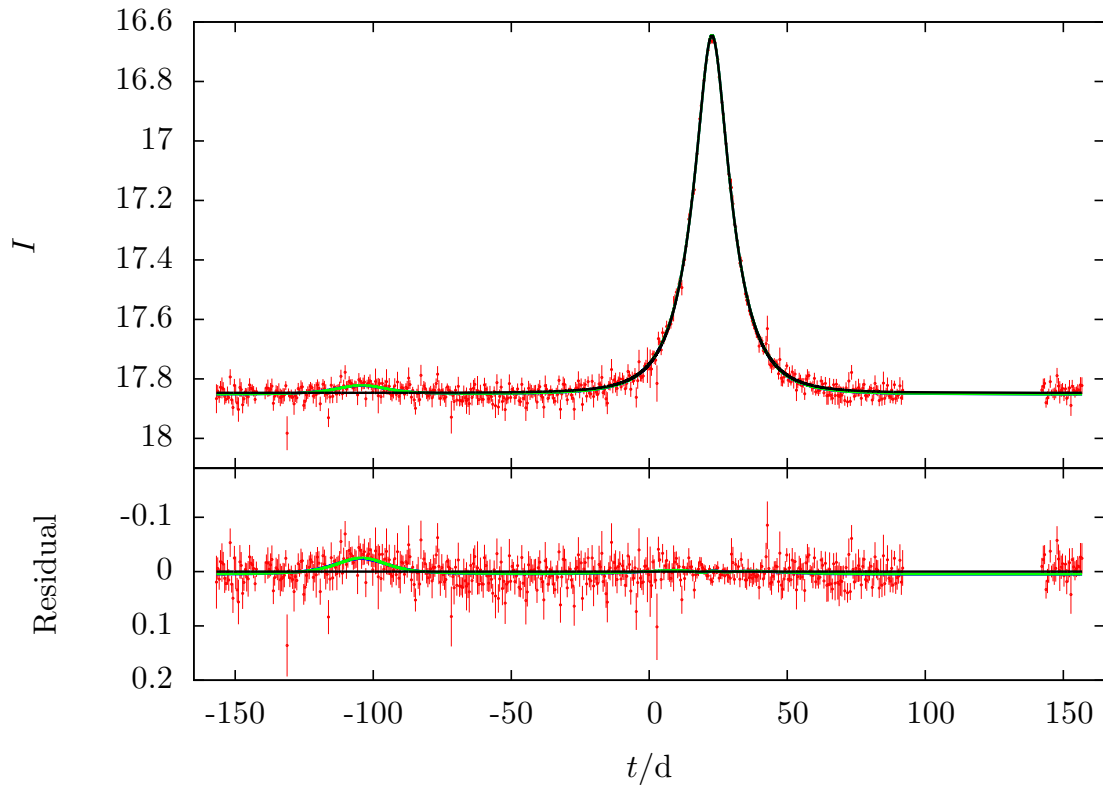


Figure 3.2 – An example lightcurve from the simulations that required coverage to be extended to cover a feature far from the lightcurve peak. The upper panel shows the lightcurve (I -band magnitude) and the lower panel shows the Paczyński residual (I -band residuals from the single-lens fit). The red points show the simulated data points with error bars, and black, green and blue lines are the best-fitting Paczyński model, the best-fitting static-binary model and the true orbital motion model (largely hidden below the green static model curve), respectively. Only 1 in 24 data points are shown for clarity. The lightcurve shown is for that of an event by a stellar-binary lens with $q = 0.22$, $s \approx 8.6$ and $t_E = 14.9$ d. Usually, only data points that cover the inner $5t_E$ are used, apart from some data points used to constrain the baseline magnitude (cf. the lightcurve for times $t > 0$ d); however additional data points are used to fully cover the additional lightcurve feature down to the baseline (cf. the lightcurve for $t < 0$ d). Further details for the event can be found in Tables 3.1 and 3.2.

$5t_E$, and over $10.5t_E \leq |t - t_0| < 9.5t_E$ to sample the baseline. To ensure that all features are covered, if the magnification of the source rises above $A \geq A_{\text{thresh}} = 1.0062$, the coverage is extended so as to be continuous within one Einstein timescale of the feature and continuous between the feature and $t = t_0$. Figure 3.2 shows an example of a lightcurve where coverage had to be extended.

3.4 Measuring orbital motion

Ultimately, we are interested in finding the fraction of binary microlensing events that show signs of orbital motion. This requires that we classify the events we simulate into those binary events that do show orbital motion, those that do not, and events that do not show binary signatures. This classification can be made, based on how well single-lens and static-lens models fit the simulated data. We first fit each simulated event with a single-lens model. Those events which are poorly fit by the single-lens model, we then fit with a static binary-lens model.

To evaluate the effectiveness of each stage of the fitting process, we also simulate a control sample. For the single-lens model fitting, the control is a sample of simulated single-lens events, and similarly for the static-lens model fitting the control is a sample of simulated static binary-lens events. Using these controls we can evaluate what fraction of events that are poorly fit are due to orbital motion and what fraction are due to a failure of the fitting routines. We can then correct our results for these false positives.

We simulate $\sim 100\,000$ lightcurves, of which nearly 3000 are detected as binary lenses. Such a large number of events requires that we develop a fully automated-fitting pipeline that requires no human supervision. The pipeline for single-lens models is relatively straight forward, due to the simple nature of the single-lens lightcurve. The problem at hand is complicated significantly by the requirement that we treat a control sample of static lenses in the same way as we do the orbiting lenses. Were we not to do this, the two methods that we present below could be significantly simplified.

3.4.1 Fitting with the single-lens model

The single-lens model has five parameters: the time of closest approach t_0^P , the event timescale t_E^P , the impact parameter u_0^P , the baseline magnitude I_b^P and the blending fraction f_s^P . We perform a χ^2 minimization using the MINUIT routine from CERNLIB (James and Roos 1975), with all parameters free; all parameters are unconstrained, except for f_s^P , which is constrained to be within $0.0 < f_s^P < 1.2$. For each event, we perform seven single-lens fits, with different initial blending fractions, $f_s^P = 0.05, 0.2, 0.4, 0.6, 0.8, 1.0$ and 1.2 . For each fit, the initial guesses for each parameter are:

- $t_0^P = 0$,
- the timescale is the true timescale,
- the baseline magnitude is taken to be the magnitude of the first data point on the lightcurve, and
- the impact parameter is chosen such that, at $t = t_0^P$, the magnitude of the event is that of the brightest data point.

This prescription works well for events which are well modelled by a single-lens model, but not so well for events with strong binary features or events which are heavily blended and barely rise above the baseline. We expect events with strong binary features to be poorly modelled, but we do not want to include the heavily blended events in our sample of binary-lens events. We therefore eliminate heavily blended events before performing the fitting, so that only the events that the single-lens model fails to fit are ones that show genuine signs of lens binarity. This cut is described in the next section.

3.4.2 Fitting with the binary-lens model

To fit the binary-lens lightcurves, we found it necessary to split the events into caustic-crossing events and non-caustic-crossing events and to fit each category using a different parametrization. The non-caustic-crossing events are fitted with a standard

parametrization, with a reference frame centred on the primary lens.³ The parameters are:

- the time of closest approach to the lens primary t_0^S ,
- the event timescale t_E^S ,
- the impact parameter between the lens primary and the source u_0^S ,
- the angle of the source trajectory to the binary axis α_0^S ,
- the logarithm of the projected binary separation $\log s^S$,
- the logarithm of the normalized secondary mass $\log m_2^S$,
- the baseline magnitude I_b^S , and
- the blending fraction f_s^S .

For brevity we introduce the vector notation

$$\vec{p}^S = (t_0^S, t_E^S, u_0^S, \alpha_0^S, \log s^S, \log m_2^S, I_b^S, f_s^S), \quad (3.8)$$

to represent the parameter set of the standard binary parametrization.

Because of the number of lightcurves necessary to obtain a good statistical sample, a full search of the entire binary-lens parameter space is not computationally feasible, we perform just one minimization per lightcurve. We must therefore pay special attention to the choice of initial guesses we use, first so as to maximize the chance of finding a good minimum, and second so as to treat the fitting of the static-binary events comparably to the orbiting-binary events. The static-binary simulations are drawn from the same distributions as the orbiting-binary simulations, the only difference being that the lens is frozen in the state it would be in at $t = t_0$.

³This frame was chosen because it can be difficult to fit wide binary lenses using the centre-of-mass frame.

As we have simulated the microlensing events, we already have a perfect knowledge of the lensing systems and we can use this knowledge to obtain a good set of initial guesses. We note that at a given time, the state of an orbiting-binary lens can be described by a static-binary model. We can therefore describe our lens at time t using the time dependent parameter set

$$\vec{p}(t) = (t_0, t_E, u_0, \alpha_0(t), s(t), q, I_b, f_s), \quad (3.9)$$

where we have used the centre-of-mass reference frame. Note that only two of the parameters are time-dependent and so we can use the true values of the constant parameters as initial guesses, having applied the appropriate coordinate transformations.⁴ However, we are still left with the problem of choosing the guesses of α_0^S and s^S . We could choose $\alpha_0(t_0)$ and $s(t_0)$, but this would bias the fitting success probability unfairly towards static-binary events, i.e., the initial guess would be the actual model used to simulate the data, guaranteeing a good fit.

Instead, we choose to use $s(t_f)$ and $\alpha_0(t_f)$, where t_f is the time of a feature in the lightcurve. We define a feature simply as any maximum in the lightcurve, or a maximum or minimum in the Paczyński residual (the residual of the true lightcurve with respect to the best-fitting single-lens model) with $|I - I_{\text{Pac}}| > 0.1$, where I is the I -band magnitude of the true model, and I_{Pac} the I -band magnitude of the best-fitting Paczyński model. As there is in general more than one feature, we choose the feature that gives the best $\chi^2(\vec{p}(t_f))$. If the initial guesses for fits to static-binary lightcurves are chosen in the same way (as if the binary were orbiting) then the initial guesses for static lenses should be worse than for orbiting lenses. This is because, at the time of the chosen feature the true orbiting-lens magnification will exactly match the magnification of the initial guess static model. In reality, for $t_f \approx t_0$ there will likely be a bias in favour of static lenses and for $t_f \neq t_0$ there will be a bias in favour orbiting lenses, but we do not believe this will affect results significantly. To fit the events, we

⁴In the reference frame of \vec{p}^S , t_0 and u_0 would also be time dependent as the origin (the primary mass) is not fixed.

again use the MINUIT minimizer, allowing all parameters to vary. All parameters are unconstrained, except for f_s^S , which is constrained to the range $0 < f_s^S < 1.2$.

The binary-lens fitting procedure can be summarized as follows:

1. find the lightcurve features (peaks in the lightcurve and peaks and troughs in the residuals)
2. find the static model with the best χ^2 from the orbiting model frozen at the time of the feature
3. perform a MINUIT minimization starting at this point.

3.4.3 Fitting caustic-crossing events

While the method just described is suitable for events which showed smooth binary features, it is not always suitable for those events which exhibit caustic crossings. For these events, in addition to fitting with the standard parametrization, we also used the alternative parametrization of Cassan (2008). This replaces the parameters specifying the source trajectory $(t_0^S, t_E^S, u_0^S, \alpha_0^S)$, with parameters that better reflect the sharp caustic-crossing features of the lightcurve $(t_{\text{en}}^C, t_{\text{ex}}^C, l_{\text{en}}^C, l_{\text{ex}}^C)$ the times of a caustic entry and exit and the positions of the entry and exit on the caustic, respectively; l_{en}^C and l_{ex}^C are defined to be the chord length along the caustic, normalized such that $0 \leq l_{\text{en}}^C < 2$ and $0 \leq l_{\text{ex}}^C < 2$. Full details of the parametrization can be found in Cassan (2008). The parameter set we use for caustic-crossing events is therefore

$$\vec{p}^C = (t_{\text{en}}^C, t_{\text{ex}}^C, l_{\text{en}}^C, l_{\text{ex}}^C, \log s^C, \log q^C, l_b^C, f_s^C), \quad (3.10)$$

where the parameter $\log m_2^S$ has been replaced by $\log q^C$ as a matter of preference; the two parameters are related by $m_2^S = q^C / (1 + q^C)$.

The accurate calculation of the l_{en}^C and l_{ex}^C parameters is quite computationally expensive, compared to the calculation of a lightcurve, and needs to be repeated each time s or q changes. Also, despite the improved parametrization, the χ^2 surface is still

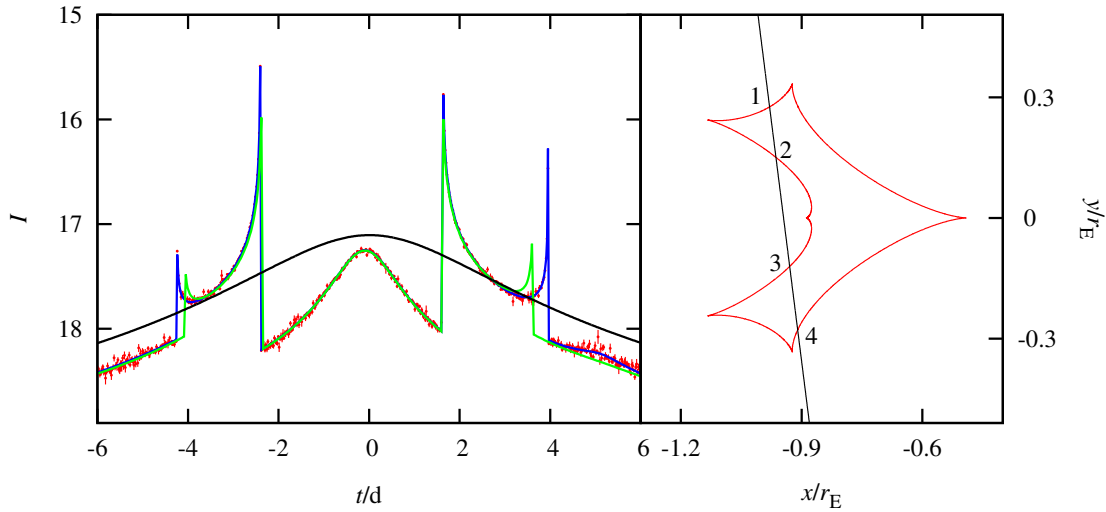


Figure 3.3 – Example lightcurve and caustic map of an event where a non-adjacent caustic entry–exit pair was chosen for fitting with the Cassan (2008) parametrization. The lightcurve is shown in the left-hand panel, where red points show the simulated data, the blue line is the true model and the green line is the static-binary model. The right-hand panel shows a map of the caustic of the static-binary model, plotted in red, and the source trajectory, plotted in black. The numbers indicate the order of the caustic crossings. The static model has been adjusted by hand to better show the two fixed and two free caustic crossings. Further details for the event can be found in Tables 3.1 and 3.2.

very complicated, especially in the $l_{\text{en}}^{\text{C}}-l_{\text{ex}}^{\text{C}}$ plane, containing many local minima. For these reasons we pursue a multi-stage minimization process:

1. We begin by conducting a grid search over the entire $l_{\text{en}}^{\text{C}}-l_{\text{ex}}^{\text{C}}$ plane, with 128×128 points spaced evenly in l_{en}^{C} and l_{ex}^{C} , and with all other parameters, including the caustic-crossing times, fixed at their true values, except for $\log s^{\text{C}}$. We fix $\log s^{\text{C}}$ at a random value chosen from the range $\Delta \log s^{\text{C}} = 1.5[\log s(t_{\text{ex}}) - \log s(t_{\text{en}})]$ or $\Delta \log s^{\text{C}} = 0.015$, whichever is greater, centred on the midpoint of $\log s$ between the caustic crossings, where $s(t_{\text{en}})$ and $s(t_{\text{ex}})$ are the projected separations at the caustic entry and exit times, respectively. The range of $\Delta \log s^{\text{C}}$ is truncated, if necessary, to ensure that it only covers the caustic topologies at the time of the crossings. For the static lenses, $\log s^{\text{C}}$ is chosen from a uniform distribution with

the same range as if the lens were orbiting.

2. The grid search is then refined by performing a second 128×128 grid search over a box of side length $1/32$ about the grid point with the lowest χ^2 .
3. Five more pairs of low- and high-resolution grid searches ($2 \times 128 \times 128$ grid points for each pair) are performed with different random values of $\log s^C$. In cases where there are multiple caustic crossings, different pairs of caustic crossings are used to define $(t_{\text{en}}^C, t_{\text{ex}}^C, l_{\text{en}}^C, l_{\text{ex}}^C)$ for each grid search. Figure 3.3 shows an example lightcurve where the first caustic exit defines $(t_{\text{en}}^C, l_{\text{en}}^C)$ and the second caustic entry defines $(t_{\text{ex}}^C, l_{\text{ex}}^C)$.
4. The next stage of the fitting simply polishes the model from the best-fitting grid point by performing a MINUIT minimization starting from this point over just the parameters l_{en}^C and l_{ex}^C , with all other parameters fixed.
5. In the final stage of the fitting, all parameters except for t_{en}^C and t_{ex}^C are allowed to vary in a further MINUIT minimization. Again, all parameters are unconstrained, except for f_s^C , which is constrained to the range $0 < f_s^C < 1.2$.

We found that at all stages of the minimization for caustic-crossing events, the minimization performed better when the first and last data points inside the caustic crossing were not considered in the fit. This is because, with the high-cadence observations that we simulate, the point source is typically very close to the inside of the fold caustic, and hence is magnified by many orders of magnitude. This leads to unrealistic photometry in two ways: firstly, in a real detector, saturation would become a problem, and secondly, a real, finite, source would not be magnified in such an extreme way.

3.4.4 Classification of events

With the modelling procedures in place, we now describe the classification of the events. The aim is to determine the orbital motion detection efficiency: the fraction

of binary-lens events that show orbital motion signatures. To do this we not only need to define how orbital motion events are classified, but also how binary events are classified, too. Events are classified by applying a series of cuts to the full sample of simulated events. Examples of events that narrowly miss each cut will be shown in Figure 3.4.

The classification is performed by a series of cuts based on the χ^2 results of the fitting described in the last section. The first cut, the variability cut, removes events that do not show significant variability. This is done without fitting by comparing the χ^2 values of the simulated data relative to the true model, χ_{OM}^2 , and relative to a constant lightcurve with no variability at the true baseline magnitude, χ_{b}^2 . We exclude events that do not satisfy

$$\frac{\Delta\chi_{\text{b}}^2}{n_{\text{obs}}} \equiv \frac{\chi_{\text{b}}^2 - \chi_{\text{OM}}^2}{n_{\text{obs}}} > 0.3, \quad (3.11)$$

where n_{obs} is the number of observations.

The second cut is used to classify events into single-lens-like events and binary-lens events;⁵ i.e., events that do not and do exhibit binary-lens features in their lightcurves, respectively. Using the results of the single-lens modelling, χ_{Pac}^2 , the χ^2 of the simulated data with respect to the single-lens model, we define events that satisfy

$$\Delta\chi_{\text{Pac}}^2 \equiv \chi_{\text{Pac}}^2 - \chi_{\text{OM}}^2 > 200, \quad (3.12)$$

to be binary events, and those that do not to be single events. This corresponds to a detection of a deviation from the single lens at a level of $\sim 14\sigma$. Binary events can then be further split into caustic-crossing events and smooth events. We define a caustic-crossing event as one where at least one data point is measured when the source is inside a caustic.⁶

The final cut is based on the result of lightcurve fitting with binary models. Events that satisfy

$$\Delta\chi_{\text{S}}^2 \equiv \chi_{\text{S}}^2 - \chi_{\text{OM}}^2 > 200, \quad (3.13)$$

⁵For brevity, single-lens events from here on.

⁶The removal of data points in the fitting process does not affect the classification.

are classified as events that exhibit orbital motion (orbital motion events) and those that do not are classified as static events, where χ_S^2 is taken to be the χ^2 of the best-fitting static-binary model. For smooth events, this is the χ^2 of the best-fitting standard binary model; for caustic-crossing events it is the χ^2 of the better fitting of the Cassan (2008) caustic-crossing model or the standard binary model. In the case of the caustic-crossing events, the data points removed from the lightcurve do not contribute to χ_{OM}^2 .

With these classifications in place, we can now define the binary detection efficiency and the orbital motion detection efficiency. The binary detection efficiency is the fraction of detectable microlensing events that show binary signatures

$$\epsilon_{BS} \equiv \frac{N_{BS}}{N_{ml}}, \quad (3.14)$$

where N_{ml} is the number of events satisfying $\Delta\chi_b^2/n_{obs} > 0.3$ and N_{BS} is the number of events satisfying $\Delta\chi_{Pac}^2 > 200$. The orbital motion detection efficiency is the fraction of binary events that show orbital motion signatures

$$\epsilon_{OM} \equiv \frac{N_{OM}}{N_{BS}}, \quad (3.15)$$

where N_{OM} is the number of events satisfying $\Delta\chi_S^2 > 200$.

To be confident of our results, we must quantify the effectiveness of the modelling prescriptions we use. We can do this by measuring the rate of false positives in our samples. To measure these rates, we simulate both single-lens events and static-binary events, drawn from the same distributions as the orbiting-lens events. These events then go through the same fitting procedure as the orbiting-lens events and are subject to the same cuts. The binary-lens false-positive rate ϵ_{BS}^{single} is therefore the fraction of detectable single-lens microlensing events that survive the $\Delta\chi_{Pac}^2 > 200$ cut and the orbital motion false-positive rate ϵ_{OM}^{static} is the fraction of static-binary events that survive the $\Delta\chi_S^2 > 200$ cut. Figure 3.4 shows some lightcurves from the simulations, which were slightly below the threshold for each cut.

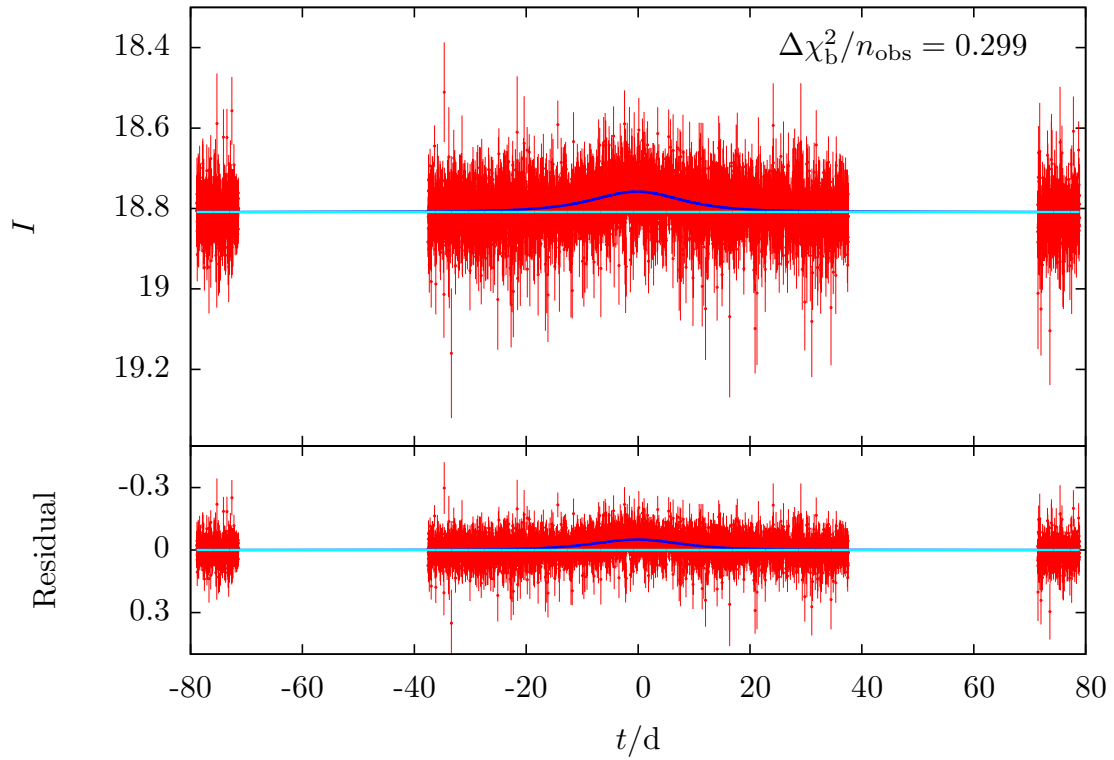


Figure 3.4 – Example lightcurves of three events that narrowly failed one of the classification cuts (continued on the following page). The lightcurve above failed the $\frac{\Delta\chi_b^2}{n_{\text{obs}}} \equiv \frac{\chi_b^2 - \chi_{\text{OM}}^2}{n_{\text{obs}}} > 0.3$ cut, while the top and bottom lightcurves in the continued figure failed the $\Delta\chi_{\text{Pac}}^2 \equiv \chi_{\text{Pac}}^2 - \chi_{\text{OM}}^2 > 200$ and $\Delta\chi_S^2 \equiv \chi_S^2 - \chi_{\text{OM}}^2 > 200$ cuts, respectively. The latter two lightcurves show only the central portion of the lightcurve without the data used to constrain the baseline. The upper panel of each subplot shows the lightcurve, and the lower panel the residual with respect to the appropriate model for the cut, that is, the constant baseline model, the best-fitting Paczyński model and the best-fitting static-binary model in the top, middle and lower subplots, respectively. Colour coding is the same as in Figure 3.2 and the cyan line in the top subplot shows the constant baseline ‘model’. Further details for the events can be found in Tables 3.1 and 3.2.

3.5 Results

3.5.1 What fraction of events show orbital motion?

We begin by presenting and analyzing the results of the simulations as a whole, calculating the fraction of microlensing events in which we expect to see orbital motion

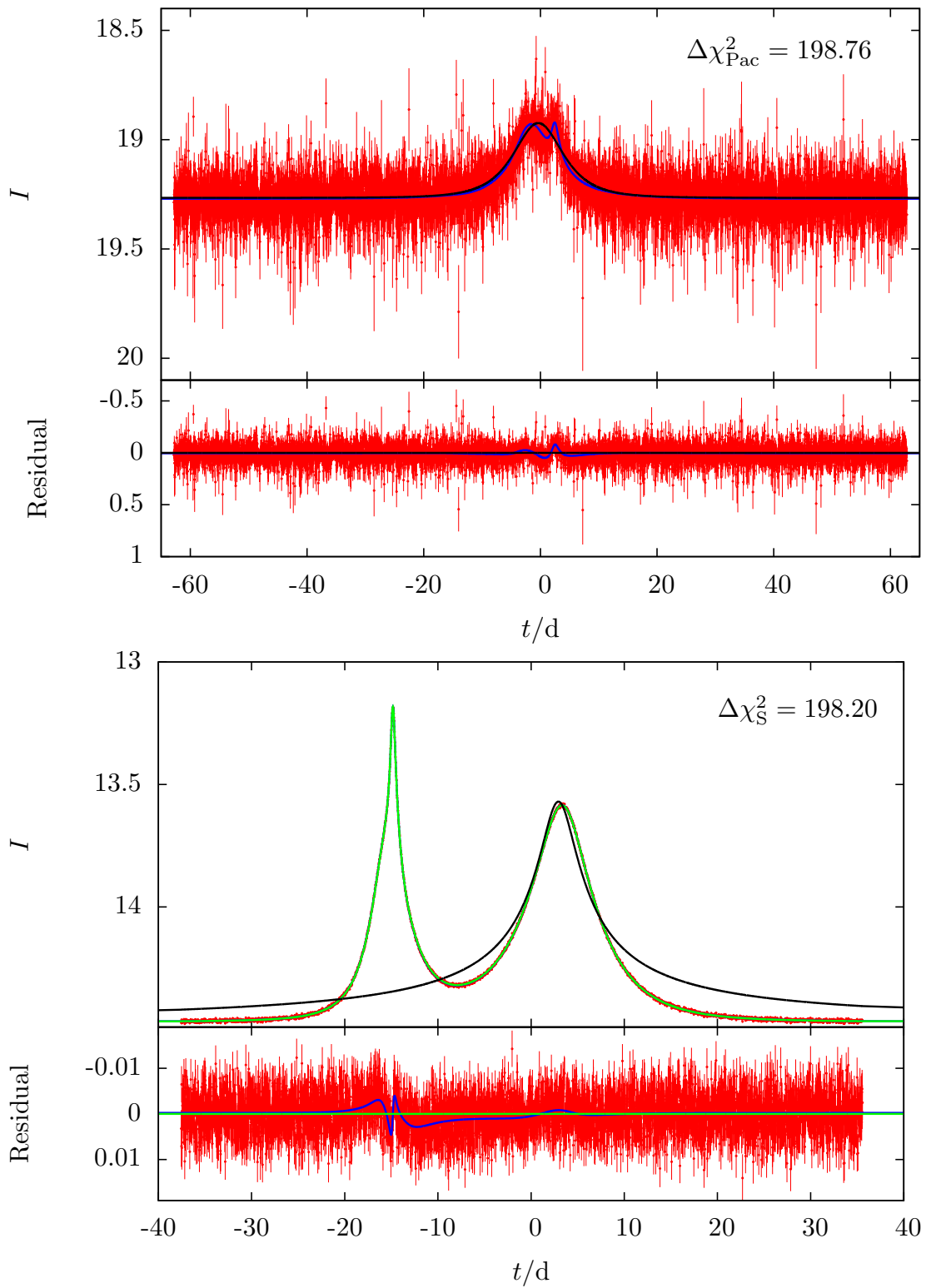


Figure 3.4 – Continued

Table 3.1 – Summary of the results for planetary lenses.

Orbit	static	circular
Single	48511	49226
Binary	1364	1366
Caustic	410	449
Caustic static	397	414
Caustic orbital motion	7	35
Smooth	954	917
Smooth static	931	883
Smooth orbital motion	23	34

Table 3.2 – Summary of the results for stellar-binary lenses.

Orbit	static	circular	eccentric
Single	4151	4046	4153
Binary	1413	1424	1385
Caustic	641	635	613
Caustic static	608	538	550
Caustic orbital motion	25	86	61
Smooth	772	789	772
Smooth static	764	743	729
Smooth orbital motion	8	46	43

events. Tables 3.1 and 3.2 summarize the results of the cuts described in the previous section, for planetary and stellar-binary events, respectively. It should be noted that in a small number of caustic-crossing events, the fitting procedure failed; these events have been excluded from the analysis of the orbital motion detection efficiency, but not from the analysis of the binary detection efficiency. These events are included in the Binary and Caustic rows of Tables 3.1 and 3.2, but not in the others.

Table 3.3 – Binary and orbital motion detection efficiencies.

Orbit		circular	eccentric
$q < 0.01$	ϵ_{BS}	0.0772 ± 0.0014	–
$q < 0.01$ Caustic	ϵ_{OM}	0.061 ± 0.010	–
$q < 0.01$ Smooth	ϵ_{OM}	0.0130 ± 0.0055	–
$q < 0.01$ All	ϵ_{OM}	0.029 ± 0.005	–
$q \geq 0.01$	ϵ_{BS}	0.260 ± 0.004	0.251 ± 0.004
$q \geq 0.01$ Caustic	ϵ_{OM}	0.098 ± 0.011	0.060 ± 0.010
$q \geq 0.01$ Smooth	ϵ_{OM}	0.048 ± 0.006	0.045 ± 0.006
$q \geq 0.01$ All	ϵ_{OM}	0.070 ± 0.006	0.052 ± 0.006

Table 3.3 shows the binary detection efficiency and orbital motion detection efficiency for both planetary and stellar-binary lenses. It should be noted that the binary detection efficiency will be larger than for microlensing events with finite sources, as the effect of the finite source will be to smooth out sharper lightcurve features, and usually reduce the amplitude of deviations from the single-lens model. This means that ϵ_{BS} for planetary lenses is likely a significant overestimate; however, for stellar-binary lenses the result is likely to be more realistic, as stellar-binary lightcurve features tend to be stronger and have longer durations. The detection efficiencies presented have been corrected for systematic false positives from each fitting stage by subtracting the measured false-positive rates $\epsilon_{\text{BS}}^{\text{single}}$ and $\epsilon_{\text{OM}}^{\text{static}}$ from the detection efficiencies measured for orbiting lenses. From a simulation of 10^4 single lenses with no false positives, we measured $\epsilon_{\text{BS}}^{\text{single}} = 0_{-0}^{+4.7 \times 10^{-5}}$, where the error quoted is a statistical $1-\sigma$ confidence limit, calculated using Wilson’s score method (Wilson 1927; Newcombe 1998b). To calculate the errors on the corrected detection efficiencies shown in Table 3.3, and on those we present in the next section, we use Wilson’s score method adapted for the difference of two proportions (Newcombe 1998a, method 10). For planetary events, we measured false-positive rates of $\epsilon_{\text{OM}}^{\text{static}} = 0.0241_{-0.0032}^{+0.0036}$ for smooth events and $\epsilon_{\text{OM}}^{\text{static}} = 0.0173_{-0.0039}^{+0.0050}$

for caustic-crossing events. For stellar-binary events we measured $\epsilon_{\text{OM}}^{\text{static}} = 0.0104^{+0.0028}_{-0.0022}$ for smooth events and $\epsilon_{\text{OM}}^{\text{static}} = 0.0395^{+0.0056}_{-0.0050}$ for caustic-crossing events. The overall orbital motion detection efficiencies were calculated as a weighted average of the detection efficiencies for smooth and caustic-crossing events, once corrected for false positives.

While in many cases we may not be able to say whether or not a lightcurve in our simulations definitively shows orbital motion signatures (due to the relatively high rates of false-positive detections), there is a clearly detected excess of detections in the circular- and eccentric-orbit simulations relative to the static ones. The significance of this excess is above $3\text{-}\sigma$ (Poisson noise) for both binary and planetary caustic-crossing events and smooth binary events. However, detection of the excess is only marginal in smooth planetary events.

Interestingly, there appears to be a discrepancy in the orbital motion detection efficiencies for stellar-binary caustic-crossing events, between the circular- and eccentric-orbit simulations: $\epsilon_{\text{OM}} = 0.098 \pm 0.011$ for circular orbits and $\epsilon_{\text{OM}} = 0.060 \pm 0.010$ for eccentric orbits. However, the same static-orbit simulation results were used to calculate the corrected orbital motion efficiencies for both circular and eccentric orbits, which means that the measurements are not independent. Also, the eccentricity of the orbits allows the projected separation to take a wider range of values than the circular orbits, which means the false-positive rate measured with the same distribution for circular orbits is likely an overestimate for eccentric orbits; for caustic-crossing events, the majority of false positives are caused by events with resonant caustic topology (see Figure 3.17 later in this section). We therefore believe the discrepancy to be caused largely due to a combination of a relatively large statistical fluctuation in the number of eccentric-orbit events that do show orbital motion, and an overestimate of the false-positive rate for eccentric orbits.

3.5.2 What affects the detectability of orbital motion?

We now investigate the effects that various system parameters have on the detectability of orbital motion. We look at the dependence of the orbital motion detectability on both the standard microlensing parameters and the physical orbital parameters, and compare them where appropriate. We conducted two sets of simulations, one with circular orbits and one with eccentric orbits. Both data sets are in good agreement, so we only present the results for events with circular orbits.

The impact parameter

We begin by looking at the dependence on the impact parameter u_0 , the sole parameter that determines the maximum magnification of a single-lens microlensing event $A_{\max} = (u_0^2 + 2)/(u_0 \sqrt{u_0^2 + 4})$. For all binary lenses, except wide stellar binaries, the central caustic is located near to the centre of mass and so u_0 determines whether or not the source will encounter this caustic. Figure 3.5 plots the orbital motion detection efficiency and the number of orbital motion detections against $|u_0|$. The results are presented separately for caustic-crossing and smooth events, respectively. The orbital motion detection efficiency results have been corrected for false positives by subtracting the false positive rate in each bin. The number of detections are displayed uncorrected, together with the number of detections in the static-orbit simulations. Note that the orbital motion detection efficiency we plot can be negative due to statistical fluctuations; when it is, the measurement should be considered to be consistent with zero.

The plots of orbital motion detection efficiency (from here on, detection efficiency) against $|u_0|$ for caustic-crossing events show much the same trends for both planetary and stellar-binary lenses. There is a significant detection efficiency for high-magnification (low- $|u_0|$) events only, with no caustic-crossing planetary detections for $|u_0| \gtrsim 0.6$ and only a few for stellar binaries. This is due to the location of central and resonant caustics close to the center of mass, which can only be crossed in events with small $|u_0|$. Consequently, for the events with larger $|u_0|$, the source can only cross

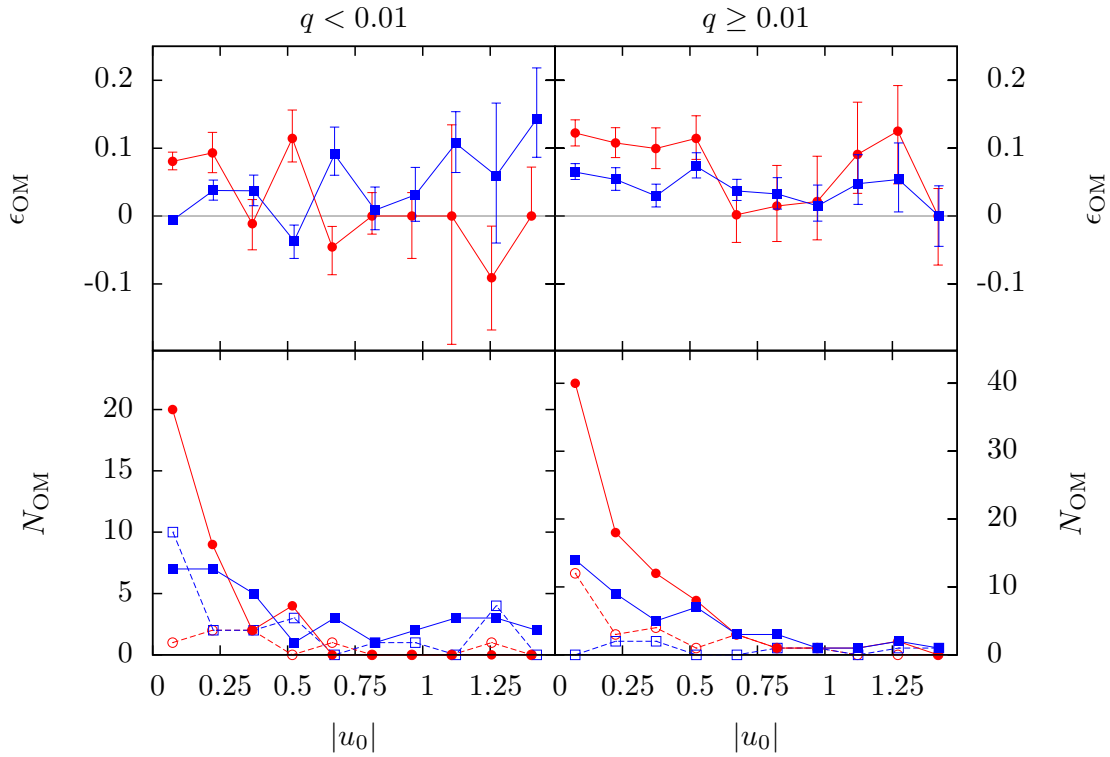


Figure 3.5 – Plot of the orbital motion detection efficiency, corrected for systematic false positives (top panels), and the absolute number of orbital motion detections in the simulations (lower panels), against the impact parameter $|u_0|$. Results are shown for lenses with planetary mass ratios (left-hand panels) and stellar-binary mass ratios (right-hand panels). Red lines with filled squares show the results for caustic-crossing events and blue lines with filled circles show the results for smooth events. In the upper panels a line marks zero orbital motion detection efficiency. All events had circular orbits, and in the lower panels results are shown for events where the lens components were in orbit (solid lines, filled points) and where they were held static for the calculation of the false-positive rate (dashed lines, open points). Events have been binned into bins of equal width, and points plotted at the centre of the bin. Note that in the lower panels the scales are different and that a factor of ~ 9 more planetary events were simulated than stellar-binary events.

weaker secondary caustics. In wide binaries these secondary caustics will typically move slowly, and in close binaries the secondary caustics are typically very small and are rarely crossed. The secondary caustics of close stellar binaries are significantly larger and stronger than those of planetary lenses, and so are more likely to be crossed by the source. Being larger, the caustic also has a longer time in which to change due to orbital motion as the source crosses it. Both factors lead to the small but significant detection efficiency for $|u_0| \gtrsim 0.6$ in stellar caustic-crossing events.

For smooth events, the planetary and stellar-binary lenses show weak but opposing trends, with the efficiency increasing slightly as $|u_0|$ increases for planetary events and decreasing slightly as $|u_0|$ increases for stellar-binary events. This indicates that the impact parameter only plays a small role in orbital motion detectability for smooth lightcurves. Note, however, that for both smooth and caustic-crossing events, the number of orbital motion detections, as opposed to the detection efficiency, is a strong function of $|u_0|$, peaking at small values due to the dependence of the binary detection efficiency on the impact parameter.

The event timescale

Figure 3.6 plots the detection efficiency against the event timescale t_E . All classes of binary event (planetary or stellar-binary, smooth or caustic-crossing) show a strong detection efficiency dependence on the event timescale. The reason for this dependence is simply because a longer timescale allows the lens to complete a larger fraction of its orbit. This means there can be a larger change in the magnification pattern during the course of any binary-lens features. In the case of planetary lenses, it seems that a timescale of greater than ~ 10 d is necessary for caustic-crossing events to show detectable orbital motion, and slightly longer for smooth events. Caustic-crossing events show larger detection efficiency than smooth events, even at shorter timescales. This is likely due to the high accuracy with which caustic-crossing times and the lightcurve shape around caustic crossings can be measured. In the case of OGLE-2006-BLG-109, this has allowed the orbital motion of the lens to be measured from data covering just

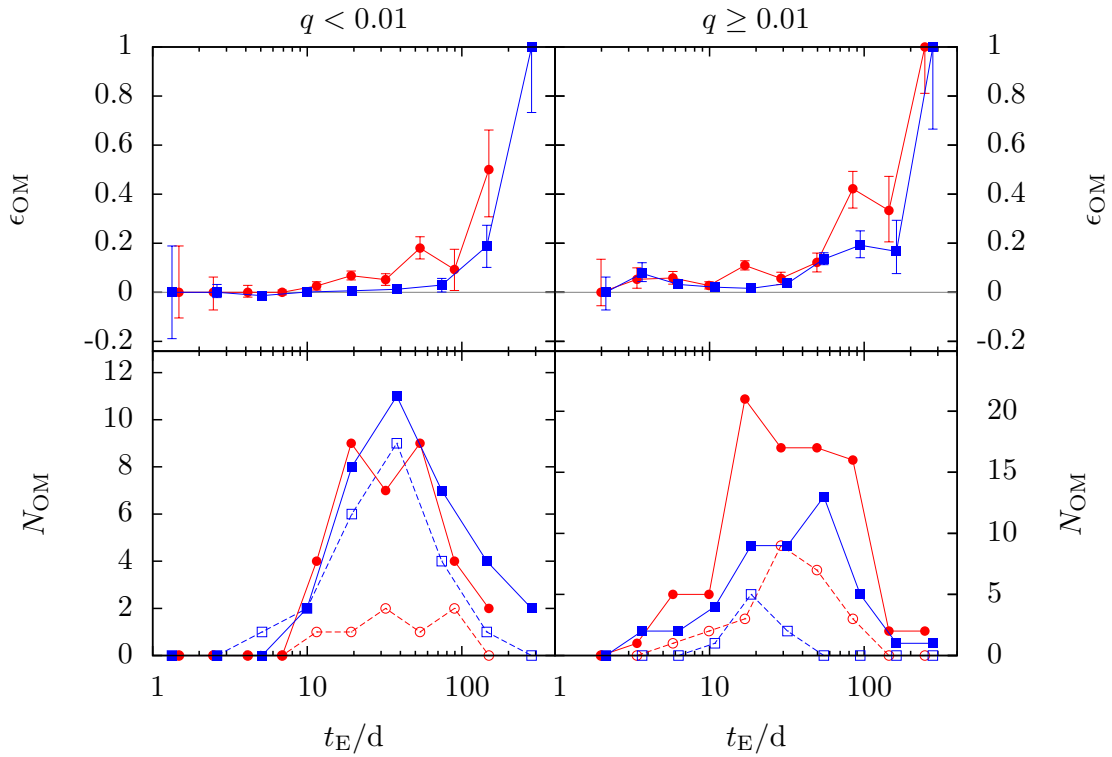


Figure 3.6 – As Figure 3.5, but plotted against the event timescale t_E .

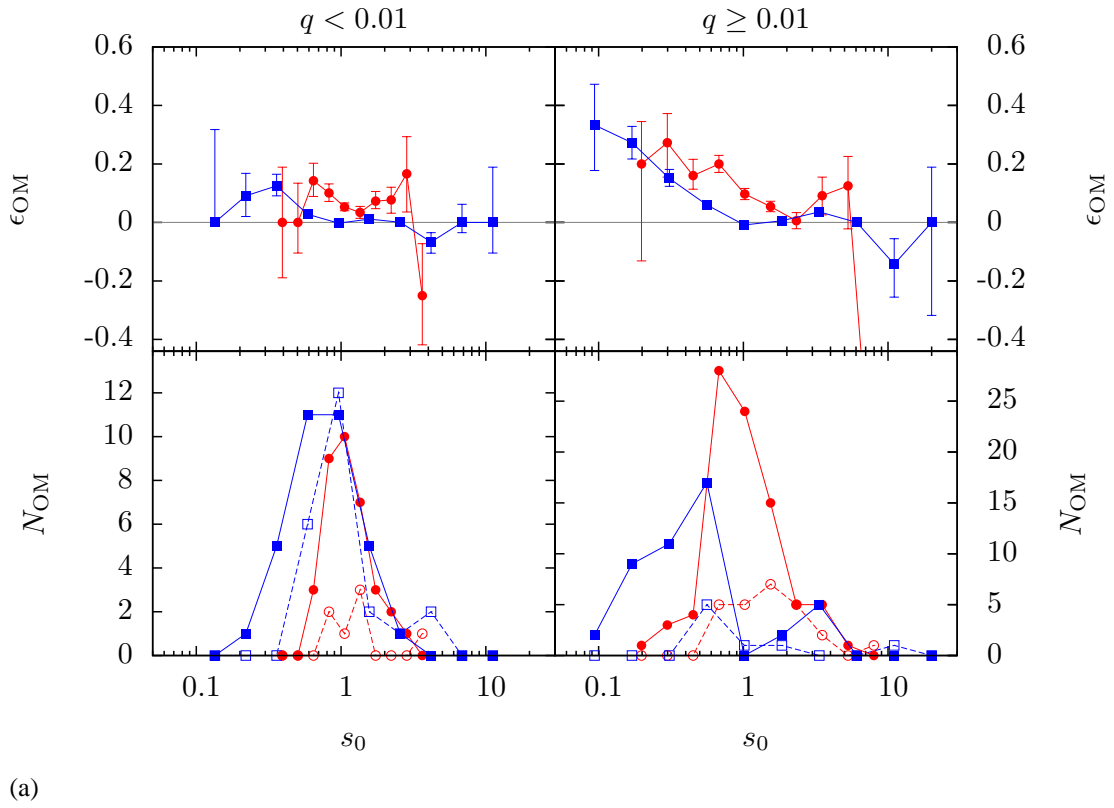
~ 0.2 percent of the orbit (Gaudi et al. 2008; Bennett et al. 2010). Smooth events in contrast, require a much larger fraction of the orbit to cause significantly detectable changes in the lightcurve and hence require a longer timescale to achieve the same detection efficiency. However, typically it is possible for smooth features to cover a much larger fraction of the lightcurve than caustic-crossing features, lessening the effect of this discrepancy.

For stellar-binary lenses, orbital motion features can be detected effectively over almost the entire range of timescales that we simulated, though with a low efficiency for timescales below ~ 40 d for smooth events and ~ 10 d for caustic-crossing events. For events with timescales over ~ 100 d, the detection efficiency reaches ~ 20 percent for smooth events and ~ 40 percent for caustic-crossing events. The detection efficiencies are similar for planetary events. The majority of planetary and stellar-binary events showing orbital motion have timescales of around ~ 10 – 40 d,

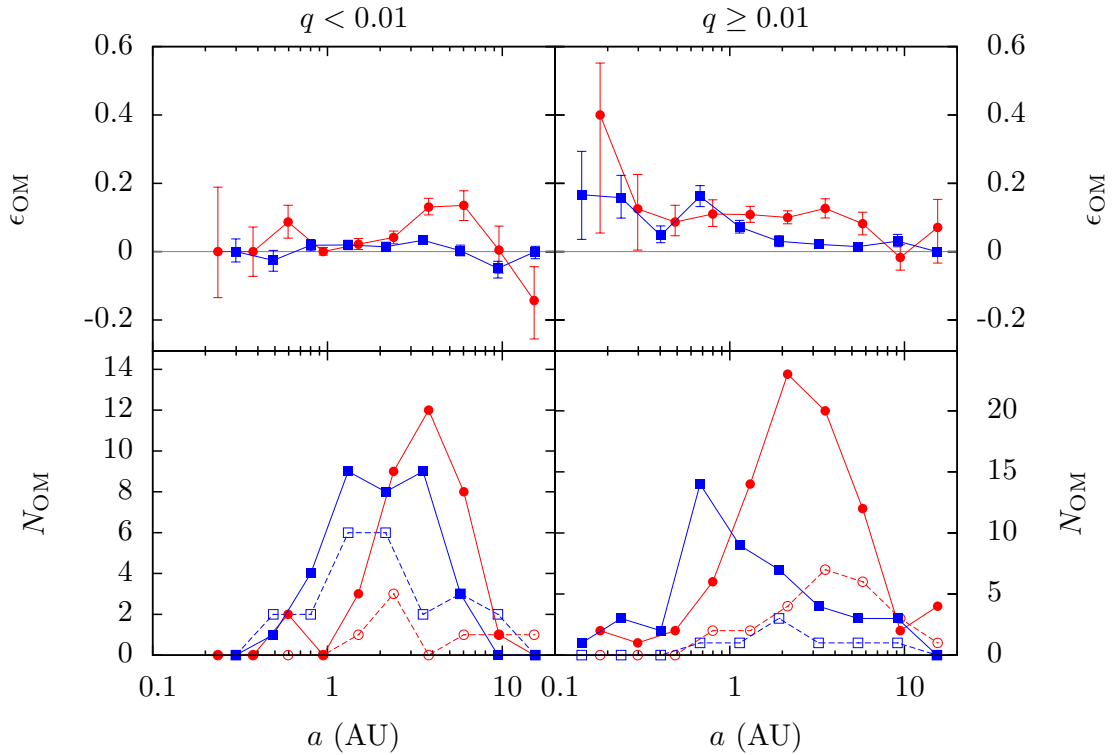
with few events at larger t_E due to the steep t_E^{-3} distribution at large timescales (Mao and Paczyński 1996). However, the strong dependence of ϵ_{OM} on timescale means that the slope of the high- t_E tail of the distribution of orbital motion events is much shallower than t_E^{-3} .

The projected separation and semimajor axis

The plots of detection efficiency against projected separation s_0 and semimajor axis a (shown in Figure 3.7) tell largely the same story. The detection efficiency in stellar binaries has a significant inverse dependence on both s_0 and a , as would be expected from the dependence of the orbital velocity on the semimajor axis. However, the behaviour for planetary lenses is less intuitive: for caustic-crossing events, there is a significant peak in the detection efficiency at $a \sim 4$ AU, and a peak/shoulder at $s_0 \sim 2$. There is a second peak in ϵ_{OM} with s_0 . The two peaks occur at values of s_0 where the boundaries between caustic topologies occur for the highest mass ratio planets. It is at these boundaries that the caustics deform most rapidly, for small changes in projected separation $d(\log s)$. The peak in ϵ_{OM} against a at $a \sim 4$ AU for caustic-crossing planetary events is accompanied by a hint of a peak at small values of a . The peak at $a \sim 4$ AU can be explained by considering the typical scale of the Einstein ring and by considering the trend of ϵ_{OM} with the event timescale. The typical size of the Einstein ring for a microlensing event is 2–3 AU, but as seen in Figure 3.6, orbital motion effects typically occur in events with larger timescales. As the timescale is correlated with the Einstein ring size and caustic-crossing events typically occur in systems with $s_0 \sim 1$, the peak orbital motion detection efficiency occurs at a semimajor axis slightly above the typical Einstein ring size, at $a \sim 4$ AU. The increase in orbital velocity as a decreases likely causes the second weaker peak in ϵ_{OM} at smaller a . Little can be said about the trend of ϵ_{OM} with a for smooth planetary events, due to the small number of events and the distribution of Einstein radius sizes, the latter serving to smear out any obvious trends. However, when plotted against s_0 , ϵ_{OM} does increase towards smaller values of s_0 as would be expected from orbital-velocity considerations.



(a)



(b)

Figure 3.7 – As Figure 3.5, but plotted against s_0 , the lens separation at time t_0 , above, and the semimajor axis a , below.

Returning to the caustic-crossing stellar-binary events, ϵ_{OM} flattens off as a increases to ~ 4 AU, before dropping to zero. This flattening likely has the same cause as the peak for planetary caustic-crossing events. We see the more intuitive inverse trend in stellar binaries because of the stronger and larger magnification pattern features that they exhibit, and the larger range of s over which the caustics have a significant size. This results in a distribution of events over a and s_0 that is broader and somewhat less peaked than for planetary events (see the lower panels of the plots in Figure 3.7). This allows the inverse relationship between orbital velocity and semimajor axis to have a greater influence on the trend in the orbital motion detection efficiency. We note that the reason we see such a complicated relationship between ϵ_{OM} and a and s_0 , but not for example between ϵ_{OM} and t_E , is that the factors that affect the timescale (lens mass, source velocity) all act monotonically to affect the detection efficiency, whereas the caustic size and strength is a strongly peaked function of s_0 and a .

The mass ratio

Figure 3.8 plots the detection efficiency against the mass ratio q . Treating both planetary and stellar-binary lenses together, there is a trend of increasing detection efficiency with increasing q , for both smooth and caustic-crossing events. However, for caustic-crossing events, this increase is very shallow, with a factor of $\lesssim 3$ increase over three decades in q , from $\log q \approx -3$ to $\log q = 0$. For smooth events, there is a stronger trend, with the detection efficiency being effectively zero for $\log q \lesssim -3.5$, while rising from ~ 1 percent to ~ 10 percent over the range $-3.5 \lesssim \log q < 0$. These shallow dependencies are somewhat unexpected in relation to the stronger $q^{0.5}$ dependence of the binary detection efficiency, which derives directly from the dependence of caustic size on q (Han 2006). However, the orbital detection efficiency effectively divides through by this dependence (unlike the curves of the number of orbital motion detections, which show a strong dependence on q), to leave a very shallow orbital motion detection efficiency curve. The other effect that q has on the lightcurve features is to make them stronger as q increases. In caustic-crossing events, the caustic features are

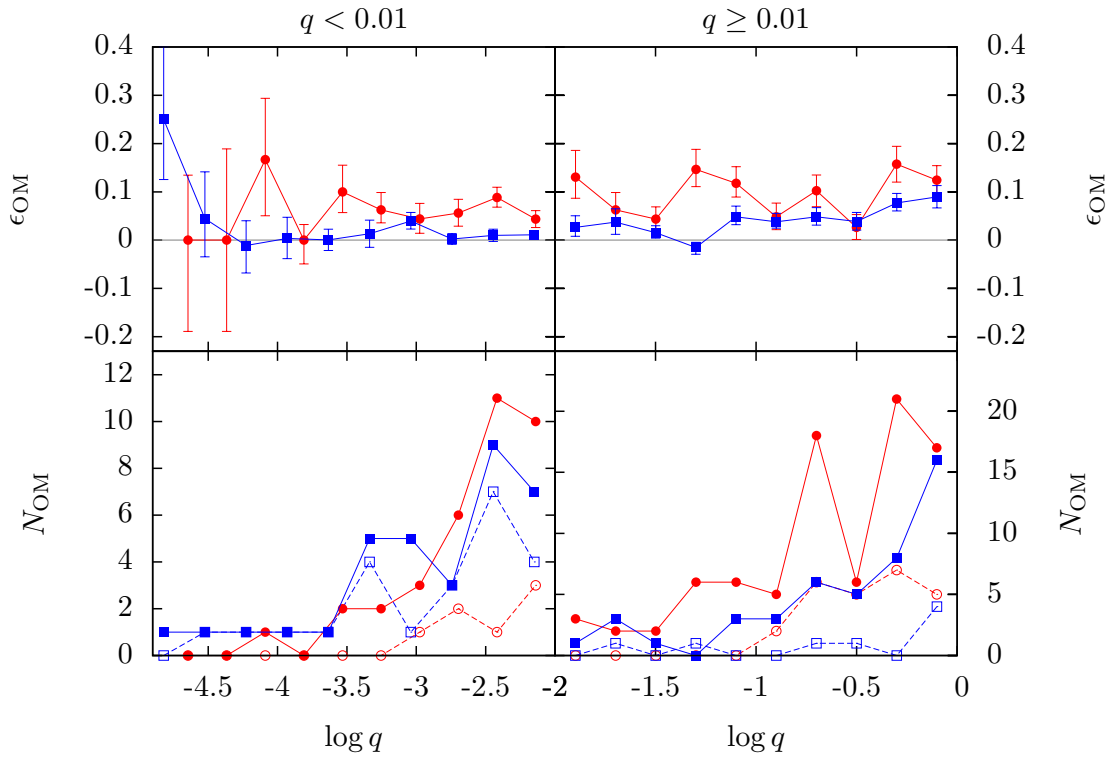


Figure 3.8 – As Figure 3.5, but plotted against the mass ratio q .

usually strong, independent of the value of q , and hence the caustic-crossing events curve is shallower than the curve for smooth events, for which the dependence of the feature strength on q is much more important.

The lens mass and distance

Figure 3.9 shows the detection efficiency plotted against the primary-lens mass. The dependence is as expected for both mass ratio regimes and for both types of binary event, increasing as the mass of the primary increases. The trend is strongest in smooth, stellar-binary events.

Figure 3.10 plots the detection efficiency against the lens distance. In all cases, a trend of increasing detection efficiency with decreasing lens distance is seen, though caustic-crossing events suffer from small number statistics at low values of D_1/D_s . Note however, that the number of orbital motion detections peaks at $D_1/D_s \sim 0.7$ due

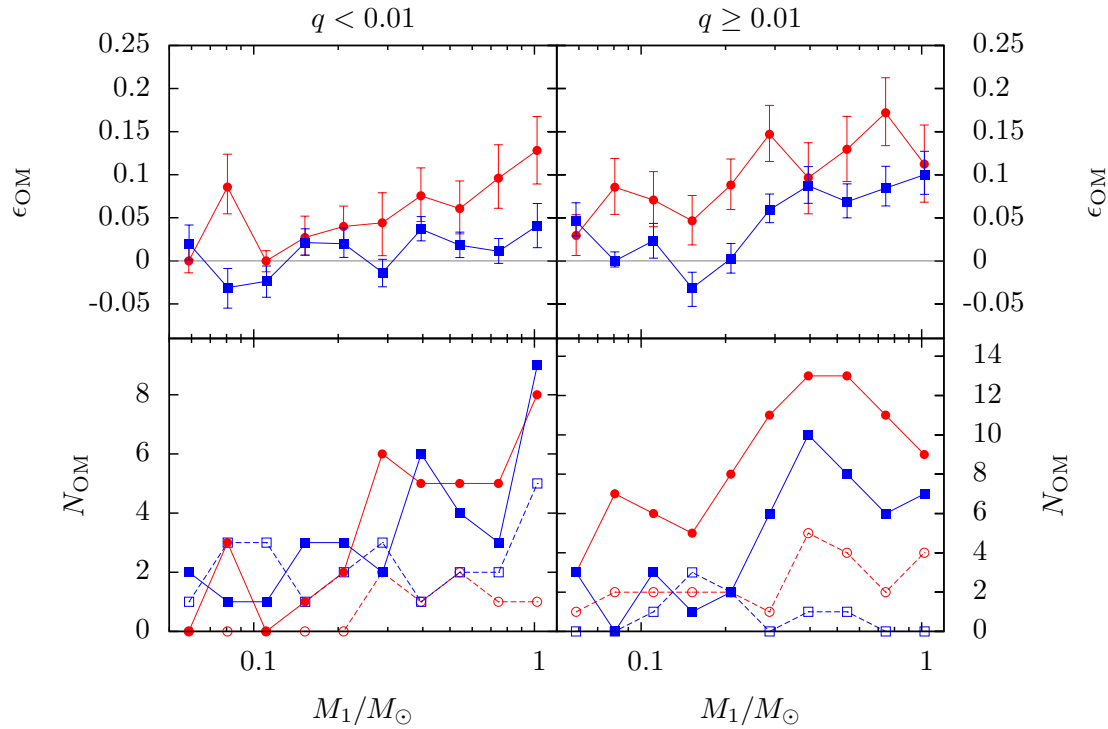


Figure 3.9 – As Figure 3.5, but plotted against the primary lens mass M_1 .

to the Galactic distribution of lenses.

The orbital period

Figure 3.11 shows the detection efficiency plotted against the orbital period. Both types of stellar-binary event show a significant inverse trend. At large periods, planetary caustic-crossing events show a peak and stellar caustic-crossing events a flattening. These features correspond directly to similar features in the curves of ϵ_{OM} with a and will have the same cause: a strong dependence of the caustics on the projection of the semimajor axis.

The baseline magnitude and blending

Figures 3.12 and 3.13 plot the detection efficiency against the baseline magnitude I_b and blending fraction f_s , respectively. For our purposes, the primary effect of both pa-

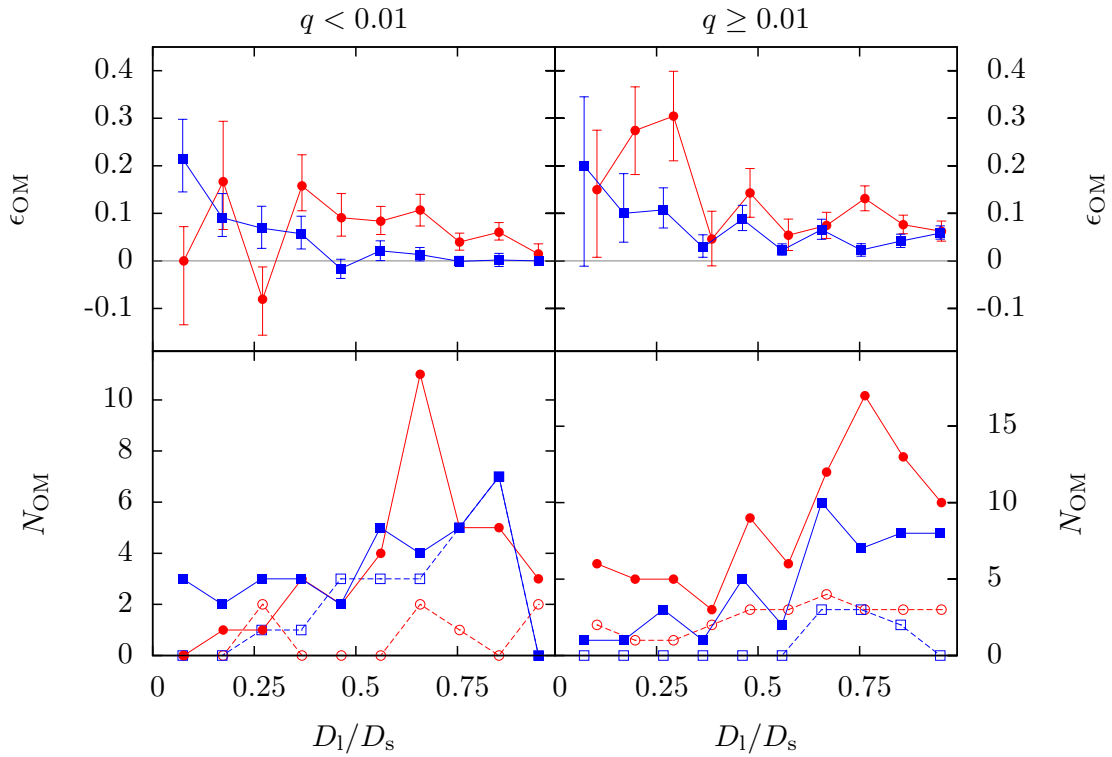


Figure 3.10 – As Figure 3.5, but plotted against the lens distance D_1 .

rameters is to affect the accuracy with which microlensing variations can be measured in the lightcurve. For a fixed observing setup, the baseline magnitude determines the photometric accuracy, which should lead to a trend of increasing detection efficiency with decreasing magnitude. This is seen to a certain extent in all cases, but events with brighter baselines may suffer significantly from blending if it is not the event source that is bright, but a blend.

Blending determines the relative strength of features in the lightcurve and as such has a much more significant effect on the detection of smooth binary features, which have a continuous range of shapes and sizes. This is compared to the effect on caustic crossings, which are typically sharp and very strong. Noting that we define the blending fraction to be the fraction of baseline flux contributed by the source, it is no surprise that smooth stellar-binary events show a significant increase in orbital motion detection efficiency with blending fraction. This is less obvious in planetary lenses,

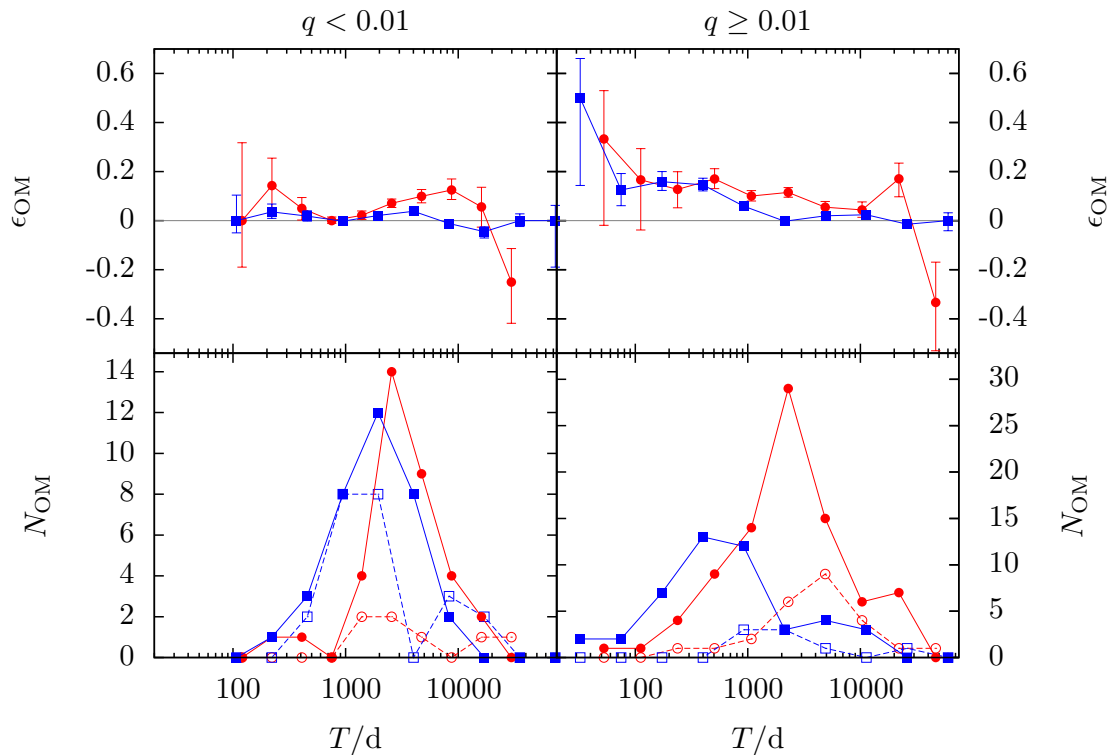


Figure 3.11 – As Figure 3.5, but plotted against the orbital period T .

likely because the smooth lightcurve features of planetary lenses are often very weak and difficult to detect even without the hindrance of the blending, and would not permit the measurement of higher-order effects for any value of blending fraction. It is more surprising perhaps, that caustic-crossing events show a significant dependence on blending. In the simulations, all caustic-crossing events had detectable binary features, regardless of blending. The observed trend then implies that, at least in some orbital motion detections in caustic-crossing events, the additional smooth features in the lightcurve (such as peaks and shoulders due to cusp approaches outside the caustic and features due to fold caustic approaches within the caustic) play an important role in the detection of orbital motion. Some of these smoother features in caustic-crossing lightcurves can be seen in lightcurves (a) and (e) shown in Figure 3.19.

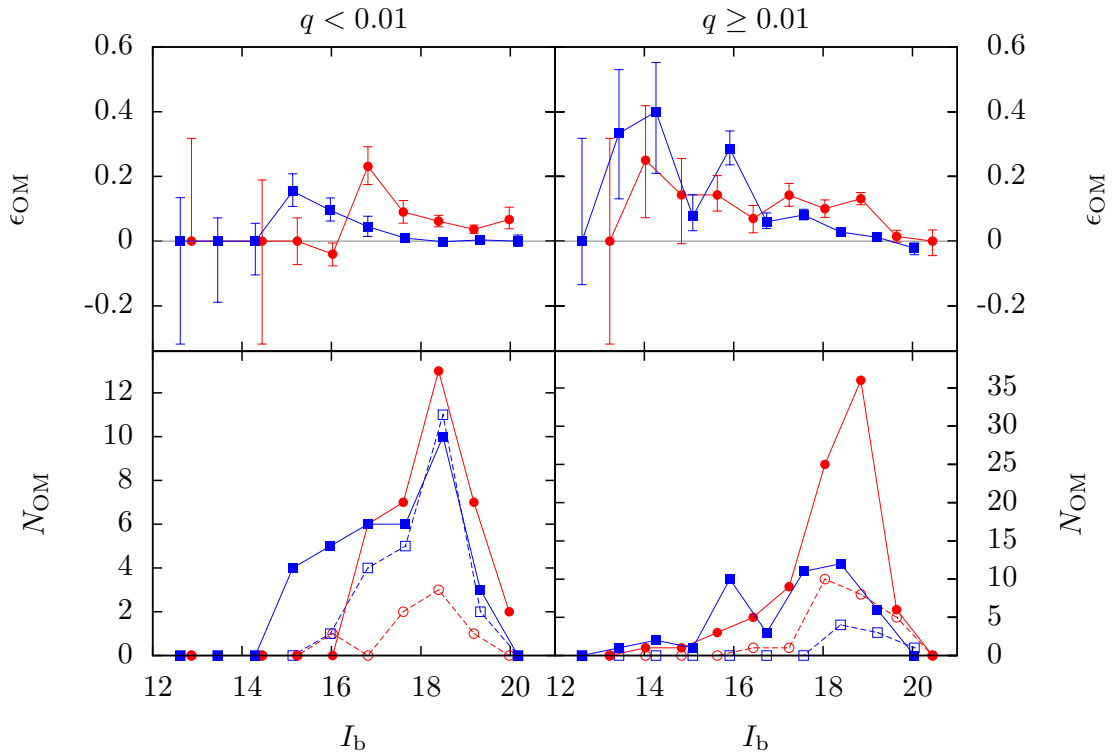


Figure 3.12 – As Figure 3.5, but plotted against the baseline magnitude I_b .

The orbital inclination

Figure 3.14 plots the detection efficiency against inclination. There is little evidence for any significant dependence on inclination, either for caustic-crossing events or for smooth planetary events. There is however, a stronger trend for smooth stellar-binary events, the detection efficiency decreasing as the inclination increases. This would be expected in systems where $a/r_E \lesssim s_c$, near the boundary between close and resonant caustic topologies, where a reduction in the projected separation due to inclination would reduce the size of the caustics and reduce the detectability of both binary features and orbital motion signatures. Unfortunately, due to the similar effects of inclination and eccentricity on the projected orbit, the data from the eccentric-orbit simulations did not show any dependence of ϵ_{OM} with eccentricity. This however implies that the effects of eccentricity on the orbital motion detection efficiency are not likely to be significantly stronger than those of inclination.

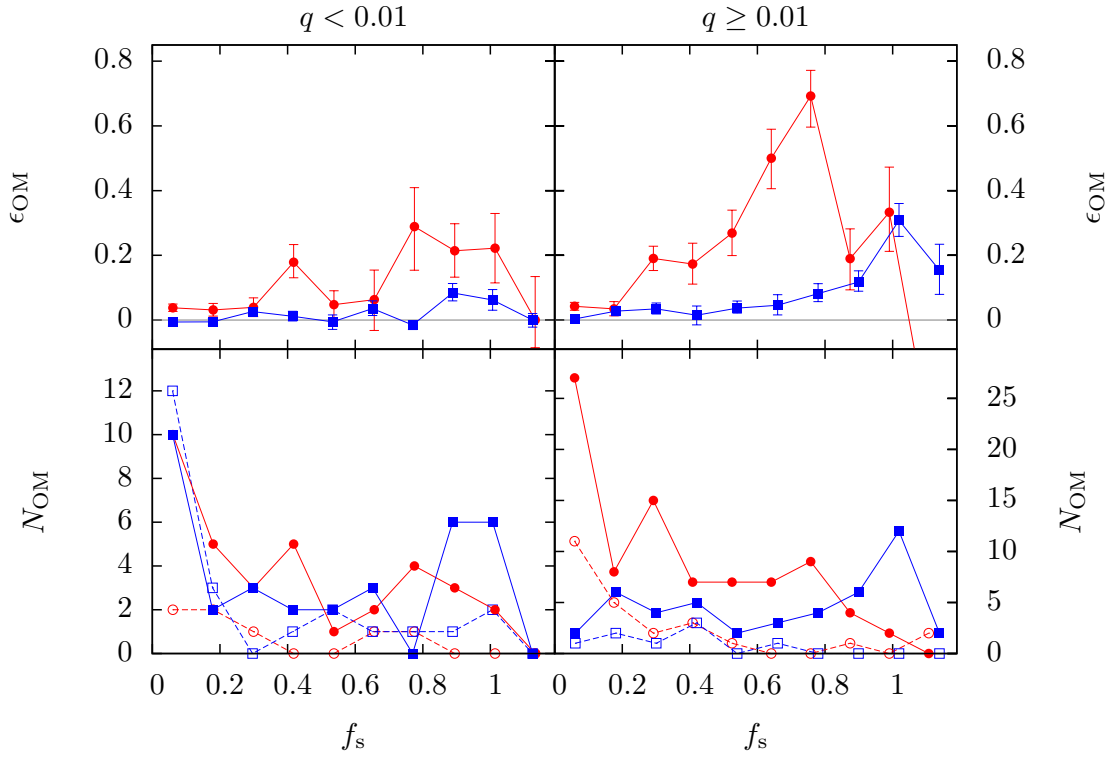


Figure 3.13 – As Figure 3.5, but plotted against the fraction of baseline flux associated with the source f_s .

Timescale and velocity ratios

It is important not just to consider the system parameters in isolation, but also their combined effects on the orbital motion detection efficiency. For example, Dominik (1998b) introduced two dimensionless ratios to describe the magnitude of orbital motion effects on a binary lens:

$$R_T = \frac{t_E}{T}, \quad (3.16)$$

the ratio of timescales, and

$$R_v = \frac{v_{\text{circ}}}{v_t}, \quad (3.17)$$

the ratio of velocities, where $v_{\text{circ}} = a/2\pi T$ is the circular velocity of the orbit. These ratios attempt to encapsulate the most important factors that determine if an event will show orbital motion features. Figures 3.15 and 3.16 plot the detection efficiency against R_T and R_v , respectively. Both ratios prove to be good descriptors of the orbital

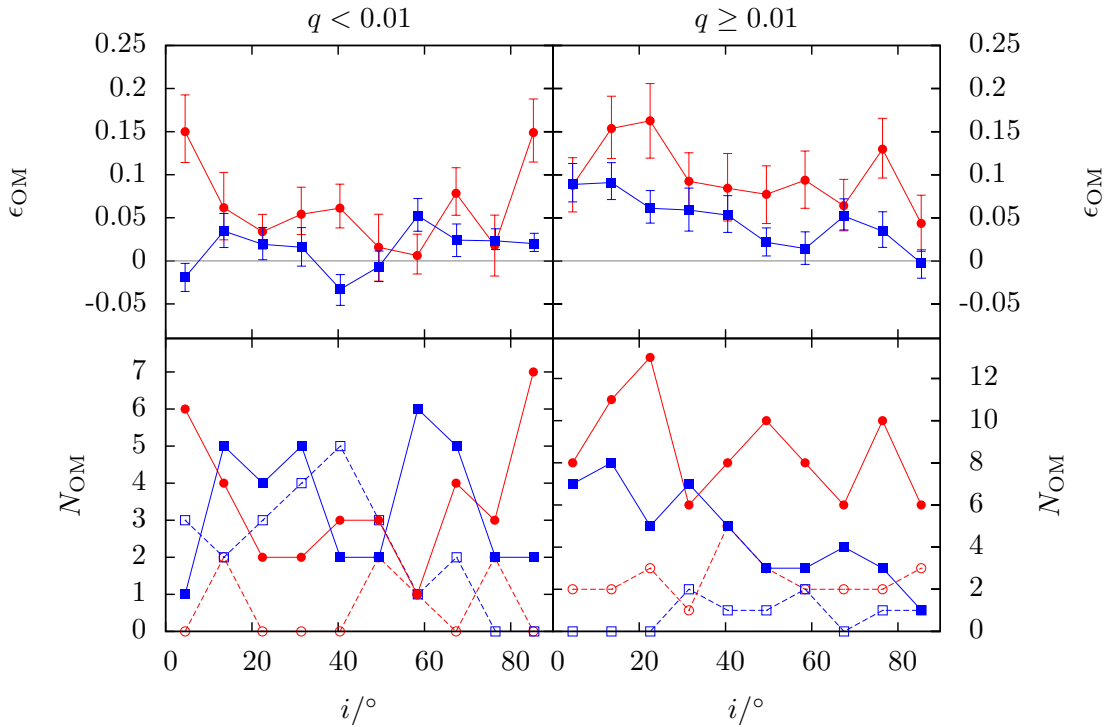


Figure 3.14 – As Figure 3.5, but plotted against the orbital inclination i .

motion detection efficiency, with ϵ_{OM} showing strong increasing trends as R_{T} and R_{v} increase. This trend occurs across all mass ratios and lightcurve types, though with a lower significance in planetary events. It would even seem that in the case of smooth events, there exists a threshold value of the ratios, below which the orbital motion detection efficiency is negligible. For the ratio of timescales, the threshold is $\log R_{\text{T}} \approx -2$ for both planetary and stellar-binary lenses, while for the ratio of velocities the value appears to be more dependent on the mass ratio, taking values of $\log R_{\text{v}} \approx -2.5$ for planetary lenses and $\log R_{\text{v}} \approx -2.75$ for stellar-binary lenses. There may be similar thresholds for caustic-crossing events at smaller values of R_{T} and R_{v} , but this is not clear due to the small number of simulated events with very low R_{T} and R_{v} .

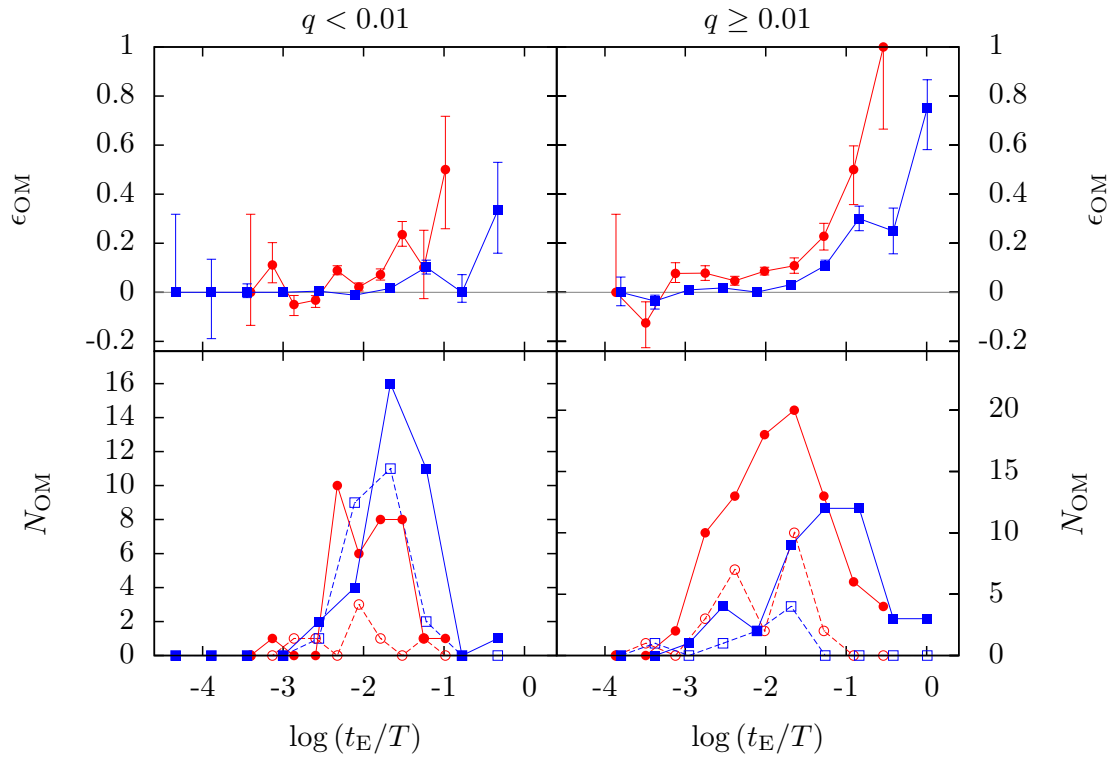


Figure 3.15 – As Figure 3.5, but plotted against the ratio of microlensing to orbital timescales $R_T = t_E/T$.

3.5.3 Are there two classes of orbital motion event?

Gaudi (2009) has suggested that orbital motion can affect the lightcurves of microlensing events in two ways. In the first scenario, the orbital motion effects are dominated by rotation in the lens, as the orientation of the binary axis changes during the time between two widely-separated lightcurve features. The second type of effect is due to changes in the projected separation over the course of a single lightcurve feature, such as a resonant caustic crossing. In this section we will describe the typical features of each type of event before investigating to what extent orbital motion events can be classified in such a way.

Gaudi (2009) describes the *separational* class of event as typically occurring in archetypal binary microlenses with resonant caustic crossings. If the binary's orbit is inclined, the projected separation of the lenses changes, causing a stretching or com-

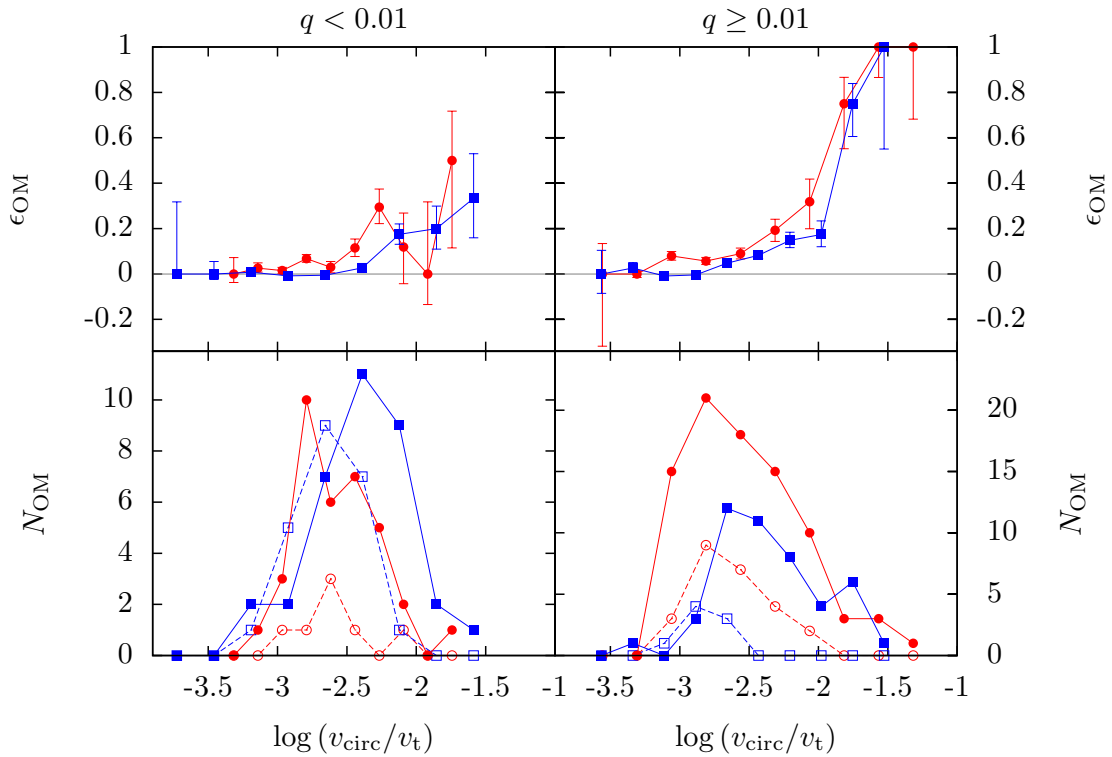


Figure 3.16 – As Figure 3.5, but plotted against the ratio of orbital and source velocities $R_v = v_{\text{circ}}/v_t$.

pression of the resonant caustic. If the projected separation is close to a boundary between caustic topologies, $s \sim s_c$ or $s \sim s_w$, the changes in the caustic structure can be very rapid. If the microlensing event occurs while these changes are happening, and the source crosses or passes close to the caustics, there is a very good chance of detecting the orbital motion. As a whole though, the changes in caustic structure during the caustic-crossing timescale will be fairly small, e.g., the difference in caustic-crossing time between the static lens and the orbiting lens may be of the order of minutes to hours (cf. the orbital period of several years). It is only the extremely high accuracy with which caustic crossings can be measured and timed that facilitates the high orbital motion detection probability. These changes to the caustic shape will often be more significant than the changes in orientation of the caustic due to rotation, and so we class them as separational orbital motion effects.

Gaudi (2009) described the *rotational* class of event as occurring when a source encounters two disjoint caustics of a typically close-topology lens. In the time between the two caustic encounters, which are separated by a time $\Delta t \sim t_E$, the lens components have time to rotate and show detectable signatures of orbital motion. We extend the class by considering the important effect to be the long baseline over which binary-lensing features can be detected. If binary-lens features are detectable across a significant fraction of the lightcurve, then a significant amount of rotation can occur in the lens while the features are detectable. Such large-scale features occur in both stellar-binary and planetary magnification patterns. They include regions of excess magnification that stretch between the central and secondary caustics in stellar-binary lenses and regions of relative demagnification in planetary lenses. If lenses with such features rotate rapidly, then the source may encounter them in such a way that a static-lens interpretation of the lightcurve features is not possible, and lens rotation must be invoked.

Is there evidence of two classes in the distribution of orbital motion events?

We begin by looking for evidence of two classes of event in the locations of the orbital motion events in the s_0 - q plane. Figure 3.17 plots q against s_0 for all events with detected binary signatures. It is immediately clear that caustic-crossing and smooth orbital motion events reside in different regions of the s_0 - q plane, with virtually all events within the intermediate topology regime being caustic crossing. Almost all smooth orbital motion events are located in the close-topology region. This broadly reflects the underlying pattern for all binary events and is not in itself evidence of two classes of orbital motion events, but is instead a result of different caustic sizes in the different caustic topologies.

Another feature of the plot is the clustering of caustic-crossing orbital motion events near the boundary of the close and intermediate topologies. It is close to the topology boundaries that the changes in projected separation cause the largest changes in the caustics. It is, however, difficult to attribute this clustering to faster caustic mo-

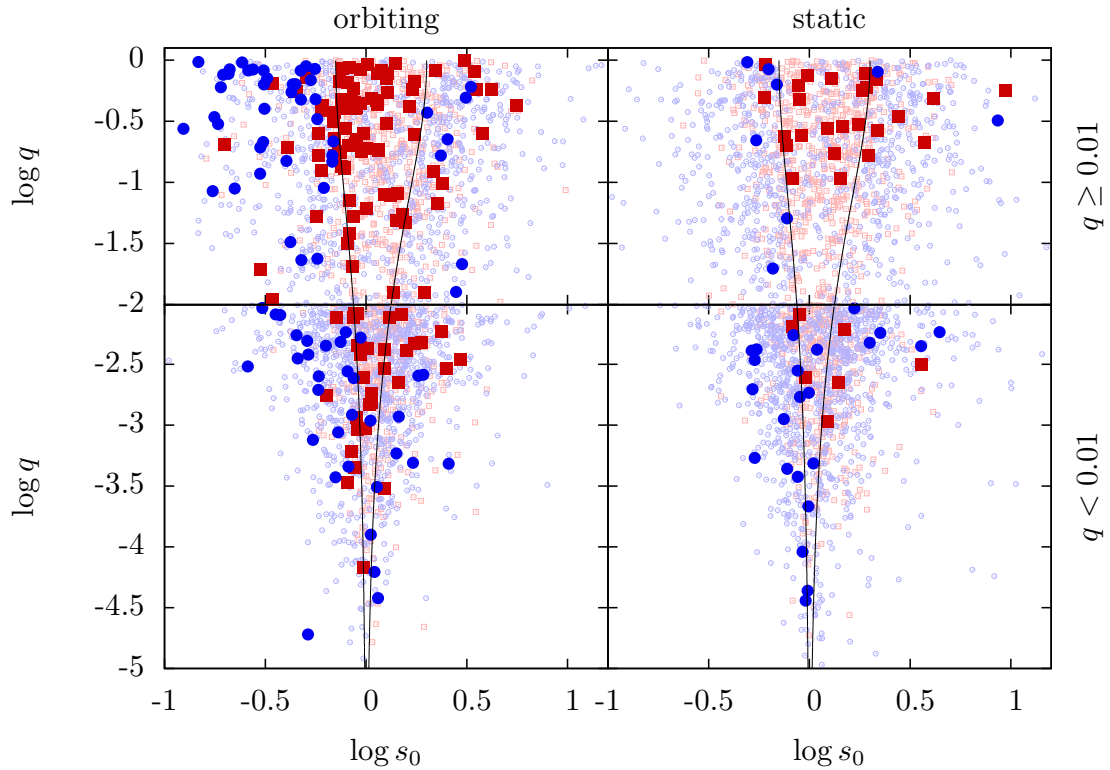


Figure 3.17 – Scatter plot of q against s_0 for microlensing events with detectable binary signatures. Caustic-crossing events are plotted with red squares, and smooth events with blue circles. Events classified as orbital motion events are plotted with larger, darker, filled points and those classified as static with smaller, lighter, open points. The black lines show the positions of the caustic topology boundaries.

tions due to separational changes, as orbital velocity is inversely correlated with s_0 , and so there should be more orbital motion events at smaller values of s_0 in any case. In support of the existence of a separational class, there is a hint of clustering against the resonant-wide boundary. However, the caustic size peaks at both topology boundaries, as the single resonant caustic stretches before splitting apart into central and secondary caustics, possibly meaning that simply the increased size of the caustics causes the increased density of detections.

Figure 3.18 plots the impact parameter against s_0 and is very useful in separating different kinds of binary event, especially for planetary lenses. The events follow a dis-

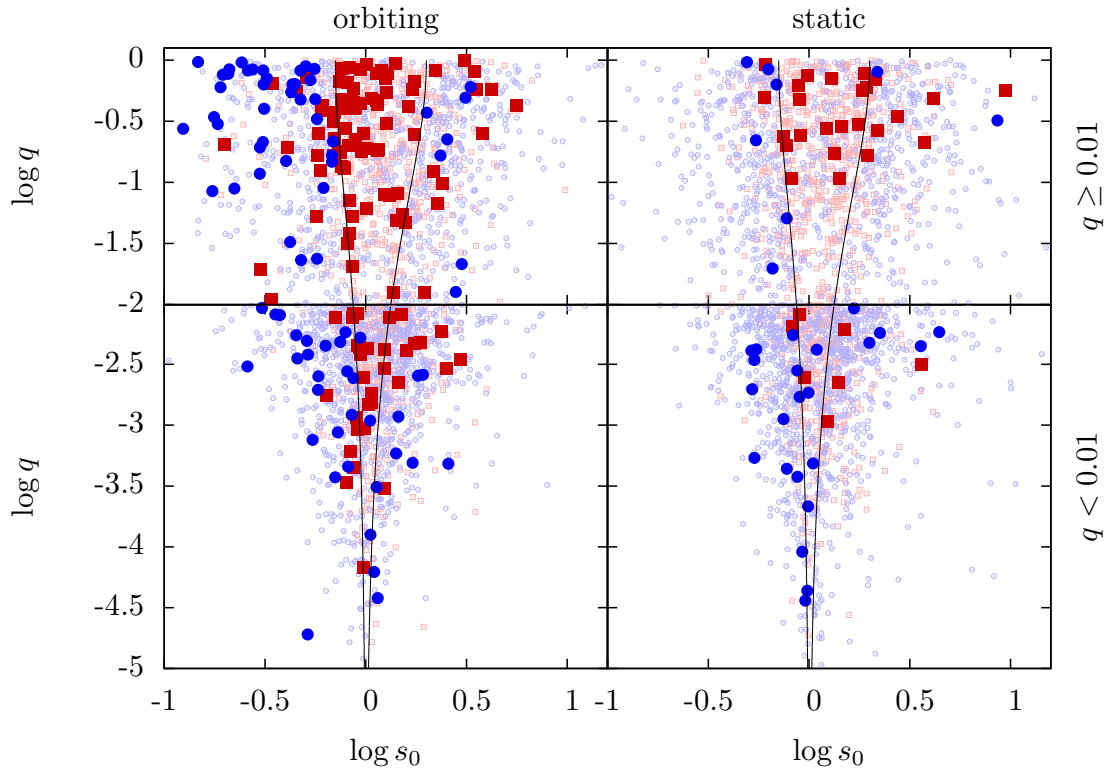


Figure 3.18 – As Figure 3.17, but showing $|u_0|$ plotted against s_0 .

tinctive pattern, with a large clump of events centred at $|u_0| \sim 0$ and $\log s_0 \sim 0$, which consists of high-magnification events that encounter the central or resonant caustic. At very small $|u_0|$, this clump extends over a significant range in s_0 , but narrows as $|u_0|$ increases to its narrowest point at $|u_0| \sim 0.3$ (or at larger $|u_0|$ for stellar binaries), corresponding to the maximum size of the region affected by resonant caustics. As $|u_0|$ increases, the plot shows a distinctive ‘V’ shape, with no binary signatures being detected for events with $s_0 \sim 0$. This ‘V’ shape arises as in events with larger $|u_0|$, the source passes through regions of the magnification pattern that can only contain secondary caustics, and does not enter the regions containing central or resonant caustics. In other words, the binary features in lenses with $s_0 \sim 1$ only occur in regions of the magnification pattern that the sources with large $|u_0|$ do not probe.

The events which occur on the branch with large $|u_0|$ and large s_0 are caused by wide-topology lenses, and therefore involve only a single secondary-caustic encounter.

Table 3.4 – Microlensing parameters for the example lightcurves.

Figure	Orbit [†]	u_0	$\alpha_0/^\circ$	s_0	q	t_E/d	I_b	f_s
3.2	C	0.48	307	8.64	0.22	14.9	17.9	1.04
3.3	S	-0.091	186	0.95	0.054	14.7	19.2	0.59
3.4tl [‡]	C	1.43	315	5.23	0.030	7.5	18.8	0.41
3.4tr [‡]	C	-0.16	155	0.61	0.14	12.6	19.3	0.082
3.4bl [‡]	C	0.37	255	2.92	0.21	6.9	14.5	0.93
3.19a	C	-0.011	255	1.06	0.0016	26.2	17.1	0.19
3.19b	C	-0.024	285	1.31	0.0076	132.2	18.7	0.067
3.19c	C	-0.071	81	1.04	0.0015	12.2	19.6	0.71
3.19d	C	0.22	265	0.87	0.00045	65.7	18.0	0.38
3.19e	C	0.16	169	0.94	0.0038	26.3	17.3	0.15
3.19f	E	-0.20	16	0.55	0.49	14.8	17.3	0.073
3.20a	C	0.15	52	0.57	0.33	54.6	18.6	0.67
3.20b	C	0.033	69	0.45	0.56	88.3	18.2	0.72
3.20c	C	-0.56	353	0.18	0.30	49.3	16.0	1.04
3.20d	C	-0.076	245	2.38	0.0059	9.0	20.0	1.04
3.20e	E	-0.33	163	0.34	0.29	82.4	15.3	0.96
3.20f	E	0.21	77	0.79	0.29	24.3	18.7	0.20

[†]C–circular orbit, S–static orbit, E–eccentric orbit

[‡]tl–top left, tr–top right, bl–bottom left

The rotation of these lenses is typically very slow, and over the short duration of the binary features (typically of the order of a day), the lens completes only a very small fraction of its orbit. This points towards separational changes being the dominant effect in the detection of orbital motion features in events on this branch, even with the enhancement of rotational velocity due to the longer solid body ‘lever arm’.

The events that occur on the branch with large $|u_0|$ and small s_0 are largely smooth events, with the occasional caustic-crossing event. The smooth events are likely caused by the source crossing the large cusp extensions that occur in close-binary lenses, suggesting that they will belong to the rotational class of events.

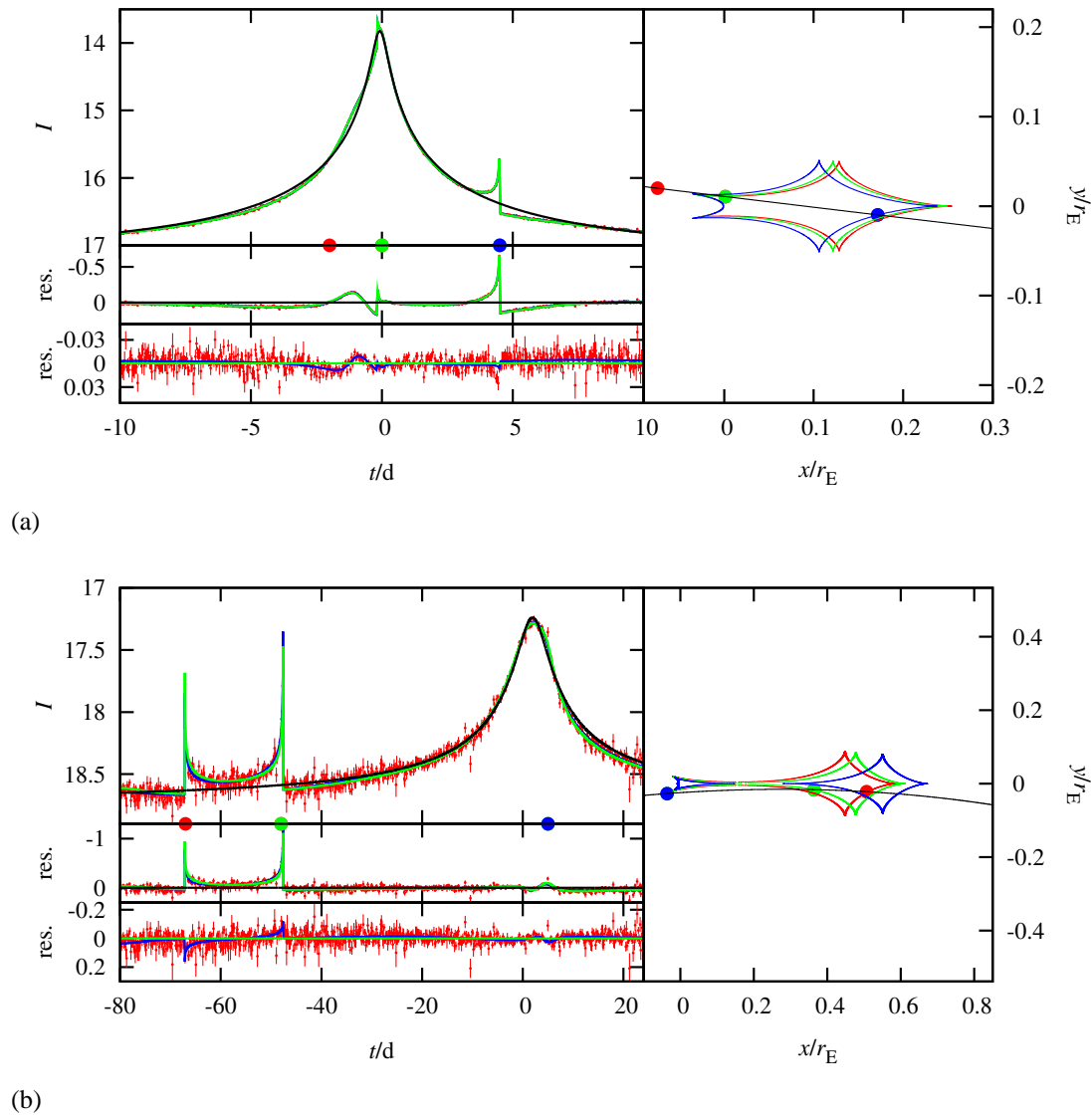


Figure 3.19 – Example lightcurves of simulated events affected by separational-type orbital motion effects. In each subfigure, the left-hand panels show the lightcurve, its residual with respect to the best-fitting Paczyński model and its residual with respect to the best-fitting static-binary model, from top to bottom, respectively. Simulated data are shown in red, the Paczyński model is shown in black, the static-binary model is shown in green and the true model is shown in blue. The right-hand panel shows the caustics at various times and the source trajectory in the frame of reference rotating with the projected binary axis. The source trajectory is plotted in black, and the caustics are colour coded according to the time. Coloured points on the lightcurve panel show the time at which the caustic was in the state shown and the coloured points on the source trajectory show the position of the source at this time. The parameters of the microlensing events can be found in Tables 3.1 and 3.2.

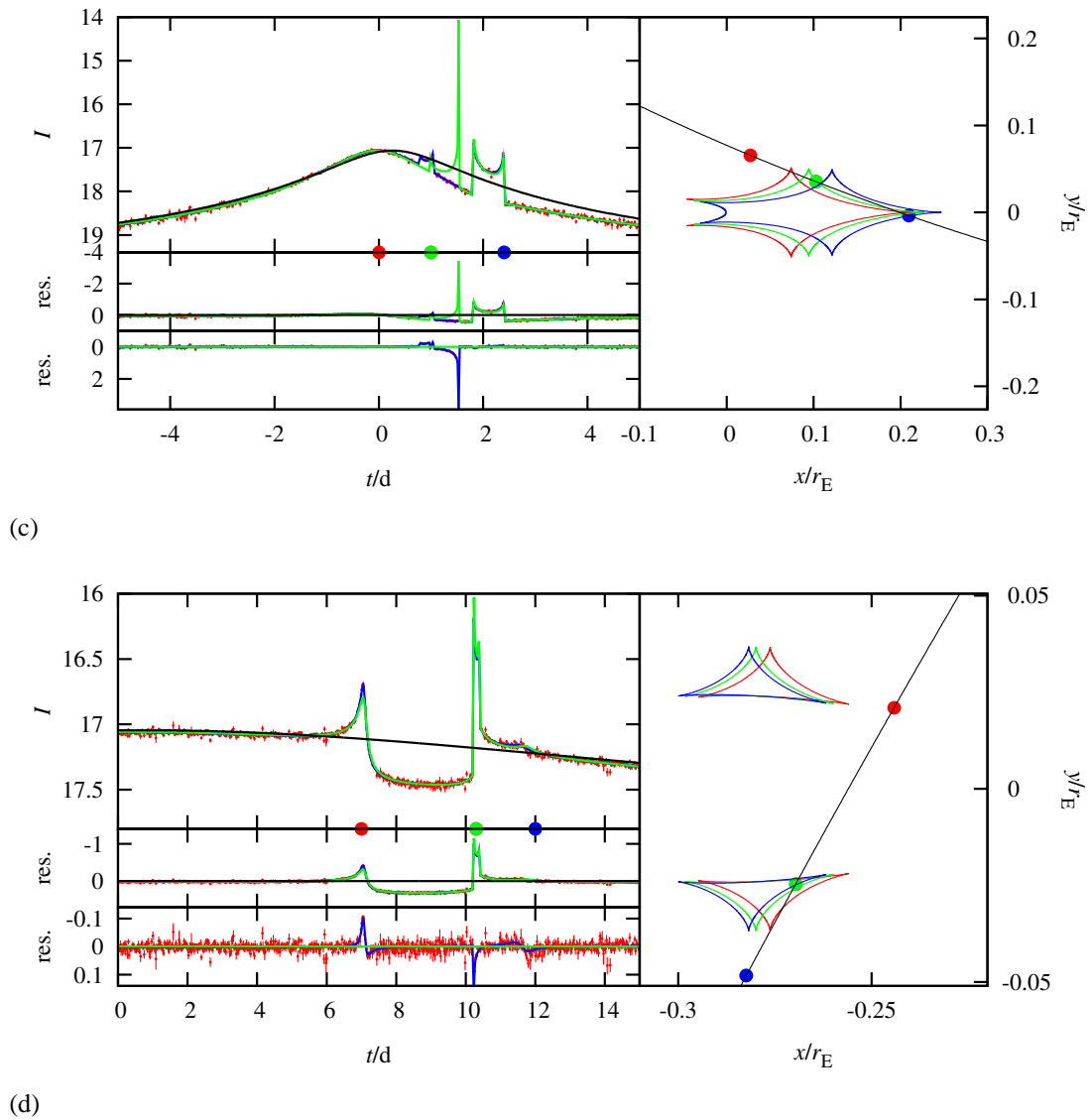


Figure 3.19 – Continued

Evidence for two classes of orbital motion event by example

Unfortunately, it is difficult to attribute the cause of any one grouping of orbital motion events in Figures 3.17 and 3.18 to either the rotational or the separational class, partly because both types of motion will affect each event to some extent. Despite this, it is possible to classify many individual events as either a separational or rotational event. Figures 3.19 and 3.20 show example lightcurves of both classes of orbital motion event,

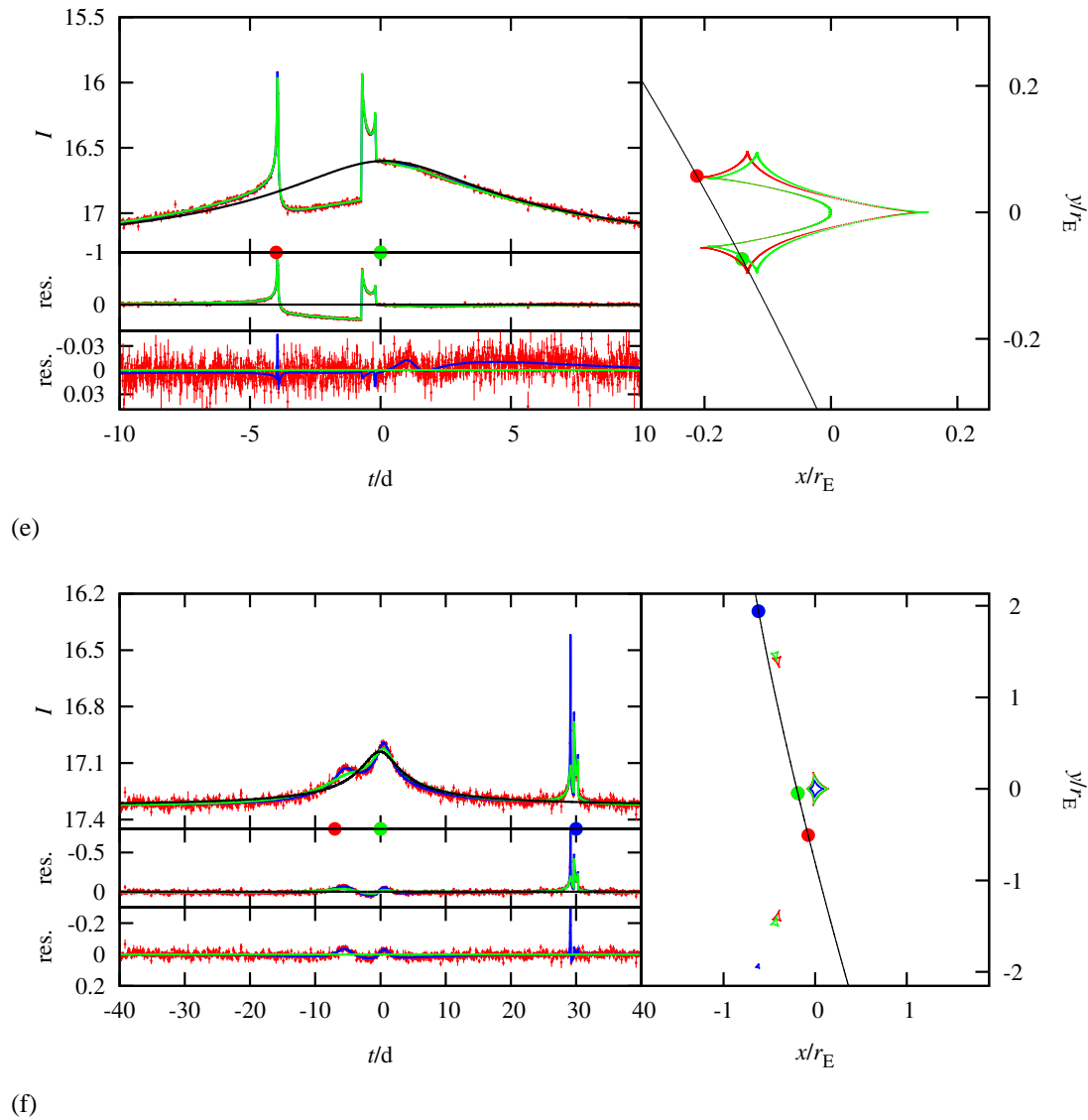


Figure 3.19 – Continued

separational and rotational, respectively. The plots show the lightcurves and residuals in the left-hand panels, together with a map of the source trajectory and caustic motions in the right-hand panels. The source trajectory and caustics are shown in the frame of reference that rotates with the binary axis, with its origin at the centre of mass. In this frame, rotation of the lens causes the source trajectory to appear curved, while changes in lens separation cause the caustics to change shape and move. Note that in event (f)

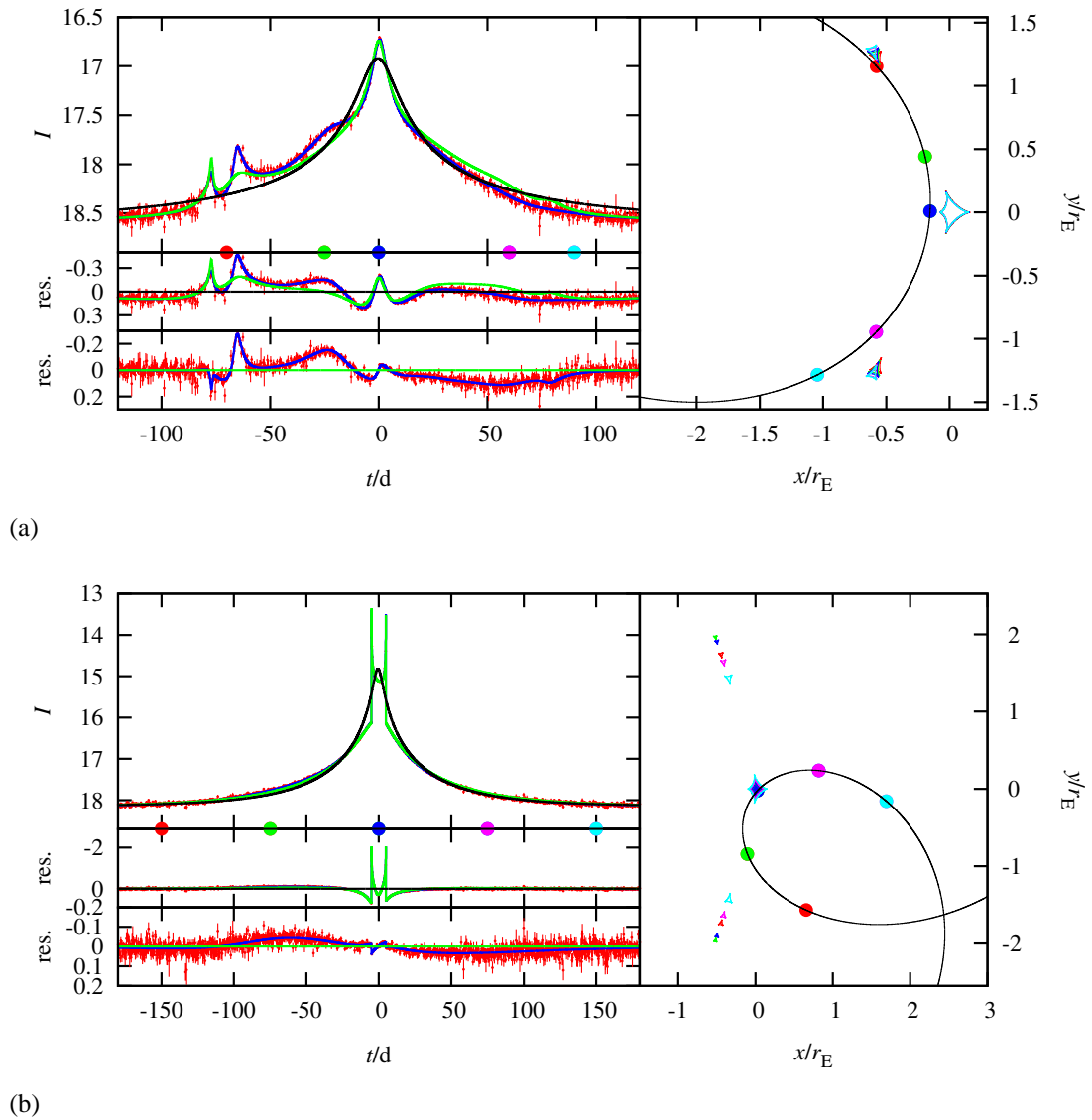


Figure 3.20 – As Figure 3.19, but showing example lightcurves of simulated events affected by rotational-type orbital motion effects.

in Figure 3.19, and events (e) and (f) in Figure 3.20, the lens orbits are eccentric, so that the source does not travel along the shown trajectory at a constant rate.

Figure 3.19 shows examples of separational events. In each example the source trajectory appears relatively straight, indicating that the lens rotates little; however, in each case the caustics move significantly. Events (a), (b), (c) and (e) all involve resonant-caustic crossings and conform well to the picture described by Gaudi (2009).

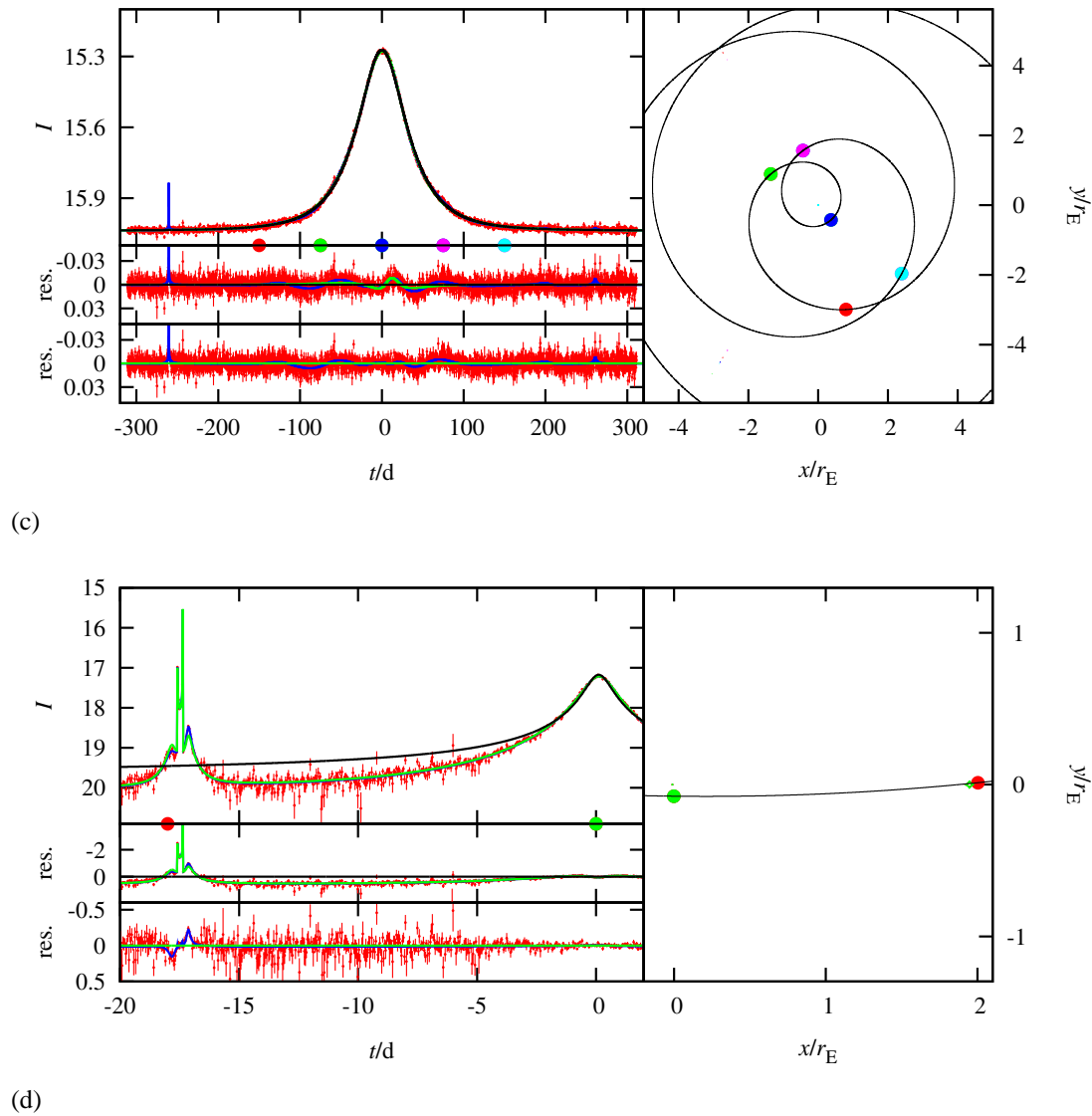


Figure 3.20 – Continued

Event (d) could be described as the encounter of two disjoint caustics, similar to the original description of the rotational class of events by Gaudi (2009), but other than the close topology, the event is remarkably similar to event (e); the source trajectory is slightly curved, but it is clear that separational effects are dominant. At first glance, event (f) would clearly fit into the picture of disjoint caustic encounters, but the source trajectory reveals that rotation plays only a minor role. In this event, a static fit to just

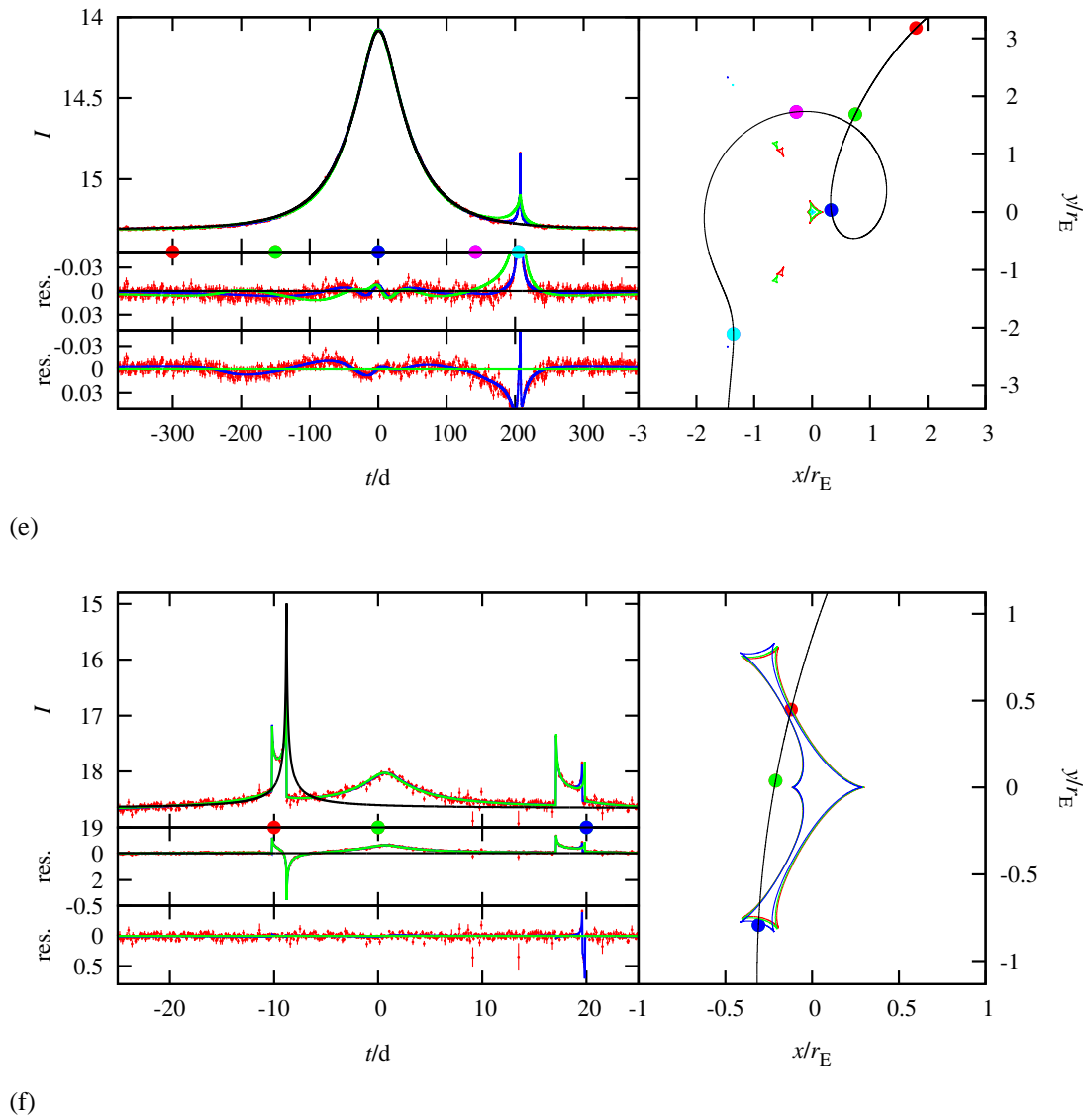


Figure 3.20 – Continued

the features about $t = t_0$ would suggest a close encounter with a large secondary caustic at $t \approx 1.5t_E$, but instead changes in the binary's separation cause the source to not just encounter, but cross a now much smaller secondary caustic at $t \approx 2t_E$.

In contrast to Figure 3.19, the source trajectories in Figure 3.20 show significant curvature. Event (a) fits the description of rotational events by Gaudi (2009), exactly. The source first encounters a secondary caustic, but the rotation of the lens causes the

Table 3.5 – Physical parameters for the example lightcurves.

Figure	Orbit	M_1/M_\odot	M_2	a/AU	T/d	e	$i/^\circ^\ddagger$	$v_t/\text{km s}^{-1}$	D_l/kpc
3.2	C	0.084	$0.018 M_\odot$	10.7	39799	0	214	134.8	5.75
3.3	S	0.70	$0.038 M_\odot$	1.88	1090	0	300	215.7	7.40
3.4tl [‡]	C	0.058	$0.0018 M_\odot$	4.46	14047	0	173	196.3	6.04
3.4tr [‡]	C	0.13	$0.017 M_\odot$	1.22	1298	0	311	183.8	5.95
3.4bl [‡]	C	0.10	$0.021 M_\odot$	3.52	6852	0	112	282.8	6.43
3.19a	C	0.55	$0.89 M_{\text{Jupiter}}$	5.82	6924	0	93	167.3	6.12
3.19b	C	0.75	$6.0 M_{\text{Jupiter}}$	4.32	3767	0	115	39.8	6.01
3.19c	C	0.27	$0.43 M_{\text{Jupiter}}$	0.51	256	0	243	63.2	7.91
3.19d	C	0.89	$0.42 M_{\text{Jupiter}}$	3.83	2899	0	136	88.8	2.13
3.19e	C	1.17	$4.7 M_{\text{Jupiter}}$	3.42	2130	0	56	173.5	7.19
3.19f	E	0.21	$0.10 M_\odot$	0.61	306	0.92	102,216	183.0	6.90
3.20a	C	0.56	$0.18 M_\odot$	1.88	1098	0	16	101.2	2.44
3.20b	C	0.38	$0.21 M_\odot$	1.69	1044	0	40	57.4	2.69
3.20c	C	0.68	$0.20 M_\odot$	0.65	205	0	30	115.8	5.97
3.20d	C	0.65	$4.0 M_{\text{Jupiter}}$	2.70	2005	0	2	218.3	7.75
3.20e	E	0.59	$0.17 M_\odot$	1.35	656	0.77	303,213	68.2	5.56
3.20f	E	0.39	$0.11 M_\odot$	2.14	1609	0.18	2,143	187.0	5.64

[†]For events with eccentric orbits, two values of inclination are quoted, representing inclinations about two orthogonal axes on the sky. The effect of this second inclination is absorbed into the source trajectory for circular orbits.

[‡]tl–top left, tr–top right, bl–bottom left

source to pass the opposite side of the central caustic. Rotation also prevents the source from crossing the magnification excess between the central caustic and the other secondary caustic. During the entire event, separational changes cause only slight changes in the caustics. In event (c), the rotation is more extreme, but the caustics smaller. The binary features are therefore more subtle, being caused by small magnification excesses between the caustics, the secondary caustics being located at $\sim(-3, \pm 4)$ and the central caustic at $\sim(0, 0)$. The rotation of the lens causes the source to cross each excess more than once, and there are several minor deviations visible in the residual

between the static and true model of the event. Event (d), while being caused by a wide lens, which is expected to rotate slowly, is clearly caused by rotation. During the event, there are virtually no separational changes, but the precision with which the secondary caustic-crossing and cusp approach features constrain the source trajectory mean that the very slight rotation, which brings the source closer to the central caustic, is detectable. Events (b) and (e) both show strong signs of rotation in their source trajectories, but separational changes are also important. While we assign them to the rotational class of events, in reality, they may better fit into a third, hybrid class. Event (f) also shows signs of both rotational and separational orbital motion effects, but we assign it to the rotational class, because without rotation the second caustic crossing would be significantly shorter.

We have been able to classify the example events shown in Figures 3.19 and 3.20, demonstrating that the dichotomy suggested by Gaudi (2009) is indeed real. The classification does not so much reflect a physical difference between the two types of event (though we might generally expect separational events to have larger semimajor axis than rotational events), but more a difference in the circumstances of observation (e.g., different orbital inclinations). As is often the case with classifications defined qualitatively, some events are difficult to firmly classify, as they show aspects of both types of orbital motion. These events can be classified into a third, hybrid class of orbital motion events, or perhaps it is more appropriate to say that they belong to both classes.

3.6 Summary and discussion

We have simulated the lightcurves of $\sim 100\,000$ microlensing events caused by stars orbited by a companion star or planet. By fitting simulated data with single-lens and static-binary models we have determined the fraction of these events where the binarity of the lens is detected and we have also estimated the fraction of these events where orbital motion is detected. For an observational set up that resembles a near-future microlensing survey conducted by a global network of telescopes without intensive

follow-up observations, we found that orbital motion was detected in ~ 5 – 10 percent of simulated stellar-binary microlensing events, depending on the characteristics of the event. Similarly, the rate of detection of orbital motion in simulated microlensing events where a planet is detected was ~ 1 – 6 percent.

We investigated the effects of various event parameters on the fraction of events showing orbital motion. orbital motion detection efficiency as a fraction of binary detections was found to depend only weakly on the mass ratio of the binary, but strongly on the event timescale. We found that a significant number of microlensing events showing orbital motion can be classified into one of two classes: those where the dominant cause of orbital motion effects is either the separational motion of the binary due to either inclination or eccentricity, or those where it is the rotational motion of the binary.

Before closing the Chapter, we will now discuss some of the implications of the work presented. We examine some of the limitations of the work, before comparing our simulation results with observations. Finally we look to what can be expected in the future.

3.6.1 Limitations of the study

The questions that we wanted to answer in this work were: what fraction of microlensing events observed by the next-generation microlensing surveys will be affected by orbital motion and what type of events are the effects likely to be seen in? While we do not claim to have fully answered these questions, we do feel that this work represents an important step in that direction. The simulation of the photometry is slightly optimistic, and does not include the effects of weather and the systematic differences in the site conditions and observing systems distributed across the Globe that would make up the network of telescopes needed for a continuous monitoring microlensing survey. The observing setup we simulated is in some respects more like a space-based microlensing telescope than a ground-based network. However, the photometric accu-

racy that we simulated is not too optimistic, and the differences between the static and orbiting simulations show that orbital motion plays a significant role in a significant fraction of microlensing events.

As discussed in Section 3.3, our choice of models will not fully answer the question of how many microlensing events with orbital motion effects will be seen; however, they do provide a good order of magnitude estimate. The binary detection efficiencies we find assume that all stars have a companion, and so must be adjusted accordingly to account for this. For example, current estimates suggest that only ~ 33 percent of stellar systems are binaries (e.g., Lada 2006), so assuming that a next generation microlensing survey detects ~ 2000 events per year, we can expect to see ~ 30 stellar-binary microlensing events showing orbital motion signatures per year. However, the true rate may be higher as the mass ratio distribution that we use for stellar binaries is not realistic; the real distribution is likely to be peaked in the range $0.1 \leq q \leq 1$ (e.g., Duquennoy and Mayor 1991; Raghavan et al. 2010). A similar calculation for planetary lenses, assuming the fraction of stars hosting planets is ~ 0.5 , yields a detection rate of ~ 1.5 caustic-crossing orbital motion events per year. Again, this estimate is affected significantly by our assumptions. Our mass ratio distribution is optimistic (for the detection of orbital motion), as current microlensing results suggest an inverse relation between planet frequency and mass ratio in the regions microlensing is sensitive to (Sumi et al. 2010). This implies our estimates will be optimistic, but we have also assumed there is only one planet per system. Many multiplanet systems have been discovered to date (e.g., Gaudi et al. 2008; Fischer et al. 2008) and they are thought to be common. The microlensing planet detection efficiency in multiplanet systems is increased, as the planets are spread over a range of semimajor axes. This will somewhat compensate for the overestimate due to the incorrect mass ratio distribution.

The major limitation of this work is that finite-source effects are not considered. The finite size of the source acts to smooth out the extreme magnification peaks as a source crosses a caustic, limiting the precision with which magnifications can be measured and caustic crossings timed, and thus plays an important role in orbital motion

detection. However, in most cases, the caustic-entry times can still be timed accurately if the caustic crossing is monitored with high enough cadence. In some cases, the effect may increase the detectability of orbital motion as the source will probe more of the magnification pattern, especially when a source travels approximately parallel to and very close to the inside of a fold caustic, producing additional peaks between the caustic crossings. We cannot quantitatively estimate the effects that finite source size has on the orbital motion detection efficiency, but we do not believe it will significantly affect our order of magnitude estimates. Unfortunately, including finite source sizes in the modelling of a microlensing event increases the required computation time by several orders of magnitude, so the effect could not easily be included in the simulations without significantly reducing the sample size.

3.6.2 Comparison with observations

While our simulations are more representative of future microlensing surveys, it is possible for us to compare the results of our simulations with the results of the current microlensing observations. Current microlensing planet searches using the survey/follow-up strategy routinely achieve a cadence similar to, or better than, that expected for future high-cadence surveys for a small number of microlensing events per year (e.g., Dong et al. 2009a). We can therefore compare the detection efficiency of orbital motion in the events where planets are detected. At the time of writing, there were ten published detections of planets by microlensing (Bond et al. 2004; Udalski et al. 2005; Beaulieu et al. 2006; Gould et al. 2006; Gaudi et al. 2008; Bennett et al. 2008; Dong et al. 2009a; Sumi et al. 2010; Janczak et al. 2010), and of these, seven had high-cadence coverage of a significant proportion of the lightcurve. In two of these events the orbital motion of the planet was detected (Gaudi et al. 2008; Dong et al. 2009b),⁷ leading us to estimate an orbital motion detection efficiency of $\sim 0.29_{-0.10}^{+0.13}$ percent.

⁷While the orbital motion of the Jupiter analogue was not detected in the OGLE-2006-BLG-109 system, the planet itself would still have been detected in the absence of the Saturn analogue, so it contributes to the denominator of the detection efficiency, but not to the numerator.

This efficiency is larger than we find in our simulations. However, the orbital motion effects in the OGLE-2005-BLG-71 event are very subtle, and improve the fit by $\Delta\chi^2_S \ll 200$ (Udalski et al. 2005; Dong et al. 2009b),⁸ meaning that it would not be classed as a detection in our simulations; this reduces the comparable detection efficiency estimate to $0.14^{+0.11}_{-0.07}$. Our estimate of 0.06 ± 0.01 for planetary caustic-crossing events is roughly consistent with this rate. It should be noted that this figure could be biased as events showing orbital motion signatures will take significantly longer to analyse. Unfortunately a similar estimate for stellar-binary lenses is not so simple as they are usually not followed-up to the same degree that planetary events are, either in terms of observations or modelling.

We have identified two different classes of orbital motion event so it is natural to try to classify the orbital motion events that have already been seen. The orbital motion detected in OGLE-2006-BLG-109 (Gaudi et al. 2008; Bennett et al. 2010) was detected due to deformation of a resonant caustic, so the event can easily be assigned to the class with separational changes. OGLE-2005-BLG-71 (Udalski et al. 2005; Dong et al. 2009b) is harder to classify, as the orbital motion effects observed were very subtle. The event suffers from the well known close-wide degeneracy (Griest and Safizadeh 1998; Dominik 1999), and rather strangely, for the close ($s < 1$) solution, separational changes are more prominent than rotational, and vice versa for the wide ($s > 1$) solution, where we might normally expect the opposite. We therefore do not assign the event to either class. Of the stellar-binary lenses, MACHO-97-BLG-41 (Albrow et al. 2000) was mainly influenced by rotation, and was detected by two disjoint caustic crossings, so is classed as a rotational event. EROS-2000-BLG-5 (An et al. 2002) undoubtedly belongs to the separational class; the caustic structure was resonant with s close to s_w , and changes in separation were measured with high signif-

⁸The overall reduction in χ^2 between the two analyses was much less than 200 when the size of the data sets and differing degrees of freedom were accounted for. The full analysis by Dong et al. (2009b) included higher-order effects not included in the original Udalski et al. (2005) analysis, some of which had a much larger effect than orbital motion.

icance, while rotational changes were consistent with zero. The final events, OGLE-2003-BLG-267 and OGLE-2003-BLG-291 (Jaroszynski et al. 2005) are not very well constrained, so we do not attempt to classify them.

We finally suggest that the event OGLE-2002-BLG-069 (Kubas et al. 2005) is a strong candidate for showing rotational-type orbital motion effects. The event was modelled successfully by Kubas et al. (2005) without including orbital motion, with a close-binary solution favoured physically and by the modelling. The event had a timescale $t_E \approx 105$ d and binary parameters $s = 0.46$ and $q = 0.58$. The lightcurve was very similar to event (b) shown in Figure 3.20, having a long, well covered central-caustic crossing, with measurements of both caustic entry and exit. The physical lens parameters obtained from the modelling suggest lens masses of $M_1 = 0.51M_\odot$ and $M_2 = 0.30M_\odot$, and a projected separation of ~ 1.7 AU, with a corresponding minimum period of $T \gtrsim 900$ d. The baseline is relatively bright, at $I_b \sim 16.2$, and so subtle magnification deviations could probably be constrained by the data, if they have been covered. The combination of the relatively large timescale ratio $t_E/T \approx 1/9$ and the bright baseline suggest that the lens will complete a substantial part of an orbit during the event (which is significantly magnified for a duration of several event timescales), meaning there is a significant chance that the source will encounter the secondary caustics if they rotate.

3.6.3 Future prospects

Interestingly, our results show that the orbital motion detection efficiency depends only weakly on the mass ratio. In the case of planetary events, caustic-crossing orbital motion detections occur preferentially in high- to moderate-magnification events ($A \gtrsim 5$), while smooth orbital motion detections occur in all but high-magnification events. Our results therefore suggest that the strategy of targeting high-magnification events (Griest and Safizadeh 1998; Han and Kim 2001) should allow caustic-crossing orbital motion events to be detected efficiently. However, the strong dependence of orbital motion

detection efficiency on the event timescale suggests that long-timescale events should also be routinely followed up. While follow-up of these events requires a significant investment of resources from the follow-up teams, like high-magnification events, they are relatively rare. For a given cadence, these events allow a better signal to noise detection of planetary deviations, and also allow more time for the prediction of future features. Long-timescale events are also more likely to show parallax features, allowing constraints to be placed on the lens mass.

High-cadence, continuous-monitoring microlensing surveys will begin operating in the next few years. Already, the MOA-II survey (Hearnshaw et al. 2006; Sako et al. 2008) has been surveying a fraction of its total survey area with a cadence of ~ 10 min for some time, and the OGLE-IV survey (Udalski 2009) has begun operations this year, and should provide significant increases in cadence over OGLE-III. KMTnet, a uniform network of telescopes with near continuous coverage, and operating at a cadence of ~ 10 min should begin operating around 2014; this promises an almost order of magnitude increase in the detection rate of microlensing events, and a similar, if not bigger, increase in the detection rate of planets by microlensing. The uniform nature of the survey network will also make statistical analysis of the planets detected easier, greatly enhancing the work already done in this direction (Sumi et al. 2010; Gould et al. 2010). The work we have presented shows that a significant fraction of the events will show signs of orbital motion, which will significantly complicate the interpretation of future planet detections. However, these complications can be used to provide valuable additional constraints on the lens.

Often overlooked are binary-star microlensing events. The next generation surveys will detect many more binary-star events than planetary events. A large number of these lenses will be located in the Galactic bulge and be composed of low-mass stars, providing an opportunity to study the properties of the bulge binary-star population. Our results show that a significant fraction of these events will show orbital motion signatures, and it is likely that in a significant number of these events it will be possible to measure the masses of the system. It should therefore be possible to

measure the statistics of a population that is difficult to reach by current spectroscopic and astrometric methods due to their low brightness and long periods.

4

Rapidly-rotating lenses: repeating orbital motion features in close binary microlenses¹

In the previous chapter we looked at some of the possible effects of orbital motion on microlensing events. We showed that some of the orbital motion events could be classified as separational events, where the detectable orbital motion signatures were caused by rapid changes to the structure of resonant caustics as a binary moved in an inclined orbit. Alternatively, more gradual orbital rotation across an entire event can give rise to more subtle, yet still detectable, signatures of orbital motion. We showed that the majority of orbital motion events that fall into this second, rotational class are caused by binary lenses with orbits smaller than the Einstein radius. In fact, in Figure 3.20 (c) we show an example of an event with such a close orbit that the lens completes more than one orbit in the time that the source is significantly magnified. In this chapter we investigate in more detail if rapidly-rotating lenses (RRLs) with repeating, detectable features such as this are likely to be common. We also explore what information can be extracted from such lenses.

¹The work presented in this chapter has been published as M. T. Penny, E. Kerins and S. Mao, *MNRAS*, 417:2216-2229, 2011.

We begin in Section 4.1 by reviewing the aspects of microlensing that are relevant to the work in this chapter. In particular we examine the magnification pattern of a close-binary lens and discuss how orbital motion affects this. In Section 4.2 we give a definition of an RRL event and look at what happens to the images during the event. In Section 4.3 we estimate the detectability and the rate at which RRLs occur. In Section 4.4 we describe how physical parameters can be measured from RRL lightcurves, including in some cases the mass and orbital parameters of the RRL. In Section 4.6 we briefly introduce additional factors that can potentially affect the lightcurve and the parameters measured from it. We close the chapter with a discussion in Section 4.7.

4.1 Introduction

The complexities of microlensing lightcurves can be considered as deviations from the single-lens Paczyński form. The deviations may be relatively minor and can cover the entire lightcurve, as in most parallax events (e.g., Smith et al. 2002a), or they can be large and cover only a small fraction of the lightcurve, as in many binary-lens events (e.g., Kubas et al. 2005; Beaulieu et al. 2006). In binary-lens events, these deviations from the single-lens form are caused by a difference in the magnification pattern of the lens. The most prominent features of the binary-lens magnification pattern are caustics, where the magnification of a point source diverges (see Figure 4.1). A source passing over a caustic will show a sharp rise in magnification as it enters the caustic and a sharp fall as it leaves. Other, more smooth magnification pattern features can also be associated with the caustics. For example, just outside the caustics, near the cusps, there are excesses of magnification that cause peaks in the lightcurve (e.g., Pejcha and Heyrovský 2009). Also, between the facing cusps of the central and secondary caustics, there is an ‘arm’ of excess magnification, weaker than the cusp excesses but often still detectable. The significance of these magnification arms will become clear below.

In a binary-lens event, the caustics are largest and usually strongest when the pro-

jected lens separation $s \sim 1$, i.e., when the lens components orbit with semimajor axis a which is similar to the Einstein radius $r_E \sim 2\text{--}3$ AU. At these separations there is only a single, so-called resonant caustic that resides near the lens centre of mass and only rotates slowly. The orbital periods of these lenses are typically $T \sim 1000$ d, much longer than the microlensing event timescale, which for a typical Galactic microlensing event is $t_E \sim 20$ d. The lenses therefore complete only a small fraction of their orbit during the course of the microlensing event and only a fraction of the events are expected to show detectable signs of orbital motion in their lightcurves (see the previous chapter and Gaudi and Gould 1997; Dominik 1998b; Konno and Kojima 1999; Ioka et al. 1999; Rattenbury et al. 2002). Those events where orbital motion is detected are typically separational-type events where the orbital motion detection comes through the deformation of the resonant caustic during a caustic crossing; because the sharp caustic-crossing features on the lightcurve can be precisely timed, the crossings can be used to constrain even small lens motions (Albrow et al. 2000; An et al. 2002; Gaudi et al. 2008; Ryu et al. 2010; Hwang et al. 2010; Skowron et al. 2011; Batista et al. 2011). However, in only two of these events has orbital motion allowed measurements of multiple orbital parameters (Bennett et al. 2010; Skowron et al. 2011). In the rest it was only possible to place relatively weak constraints on the orbits due to the tiny fraction of the orbit that was probed.

Lenses with closer orbital separations have three caustics: one at the centre of mass and two secondary caustics separated from the centre (Schneider and Weiss 1986). The two secondary caustics will move rapidly as the magnification pattern rotates as a solid body. These caustics are smaller than those of resonant binary lenses, meaning it is less likely that the source will encounter them; therefore, the lightcurves of binary lenses with very close orbits will in most cases resemble single lenses. However, in favourable cases the binary-lens lightcurve features are detectable. With close orbits these lenses will have orbital periods much more closely matched to the microlensing timescale. Analogous to observational celestial mechanics, measurements of orbital parameters are much more accurate if observations cover more than a single orbit (e.g., Boden

et al. 2005). Rapidly-rotating lenses with detectable features therefore represent an opportunity to map a complete or nearly-complete orbit of a binary microlens, possibly allowing stronger constraints to be placed on the lens orbital parameters than are possible with resonant, separational-type orbital motion events.

4.2 What is a rapidly-rotating lens?

We define a rapidly-rotating lens (RRL) to be a binary microlens, which, if monitored continuously with suitable photometric accuracy, would guarantee that at least one feature of its magnification pattern would be seen to repeat at least once in its lightcurve due to the lens orbital motion. This implies that the lens completes at least two orbits during the time in which its binary-lensing features are detectable. We choose this definition over the more simple comparison of microlensing and orbital timescales (e.g., $T < t_E$ Dominik 1998b) because without detecting binary features it is impossible to measure the binary's rotation. As mentioned in the previous section, the strength of binary features declines as the orbital separation and period decrease. So simply decreasing the period does not necessarily increase the prospects of detecting a repeated feature. Therefore, an RRL can only result from a compromise between a fast rotation rate and detectable binary-lensing features.

Throughout the chapter we shall focus on close-topology lenses, which have separations $s \lesssim 0.7$ (Schneider and Weiss 1986; Erdl and Schneider 1993), a choice we shall justify in Section 4.3. Figure 4.1 shows the magnification pattern of a close-topology lens and labels a number of features. The structure and features of the magnification pattern depend only on the projected separation of the lens components s , and the mass ratio q (Erdl and Schneider 1993). The most important features of the close magnification pattern are a central caustic, located at the lens centre of mass, and two secondary caustics which lie away from the lens centre. Stretched between the central and secondary caustics are two 'arms' of excess magnification (relative to the magnification that would be caused by a single lens of mass equal to the total binary

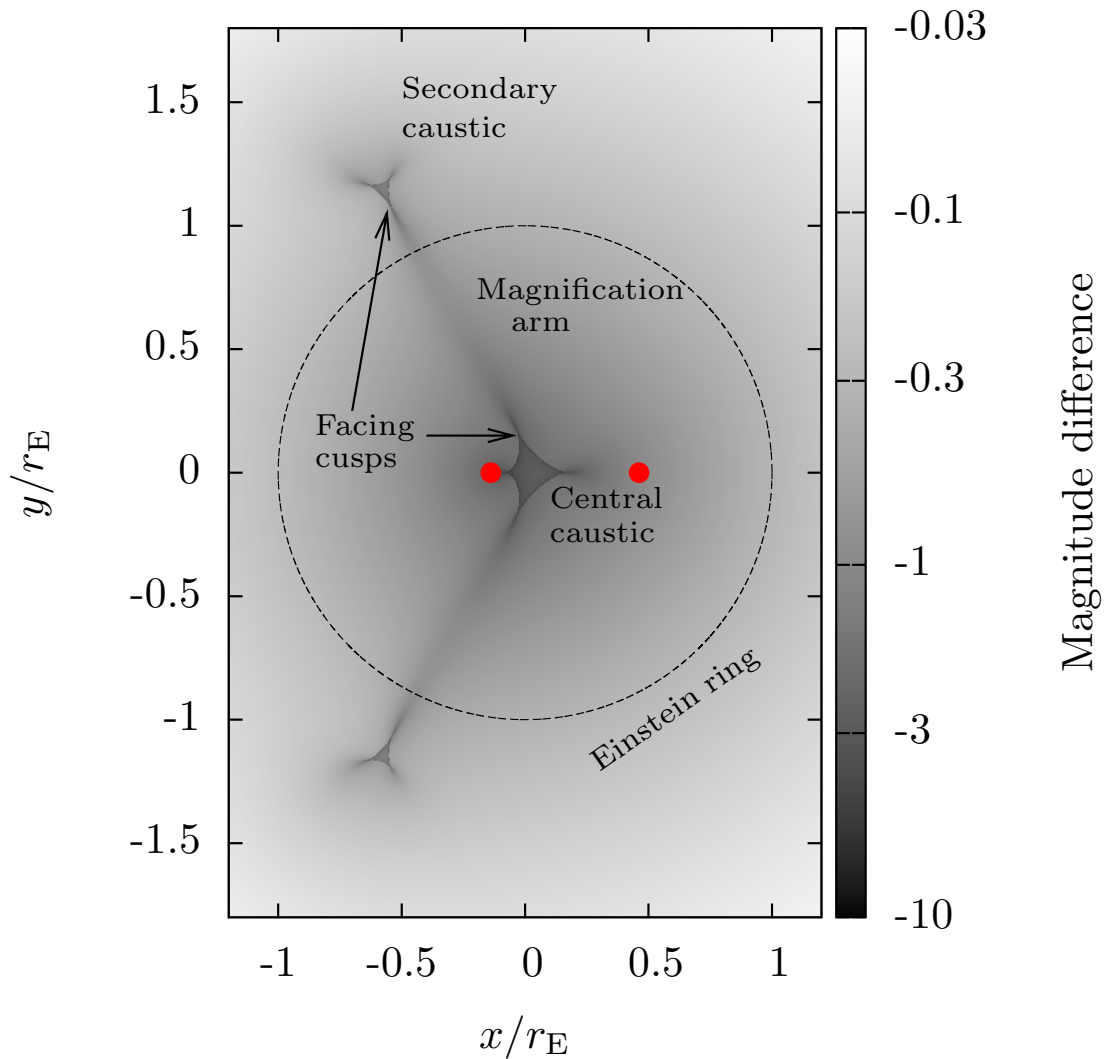


Figure 4.1 – The magnification pattern of a close-topology microlens. The dots denote the lens positions, with the primary lens at negative x . The lens has a mass ratio $q = 0.3$ and projected separation $s = 0.6$. Notable features of the magnification pattern are labelled.

mass). During a microlensing event, a source will travel across the magnification pattern and we will observe the source change in brightness. The form of this lightcurve is determined by the trajectory that the source takes. As the source moves, the magnification pattern will not stay fixed, as the binary will also move in its orbit. Should the lens orbit lie face-on to the line of sight, then the magnification pattern will rotate as the source moves across it. Should the orbit be inclined or eccentric, the structure of the

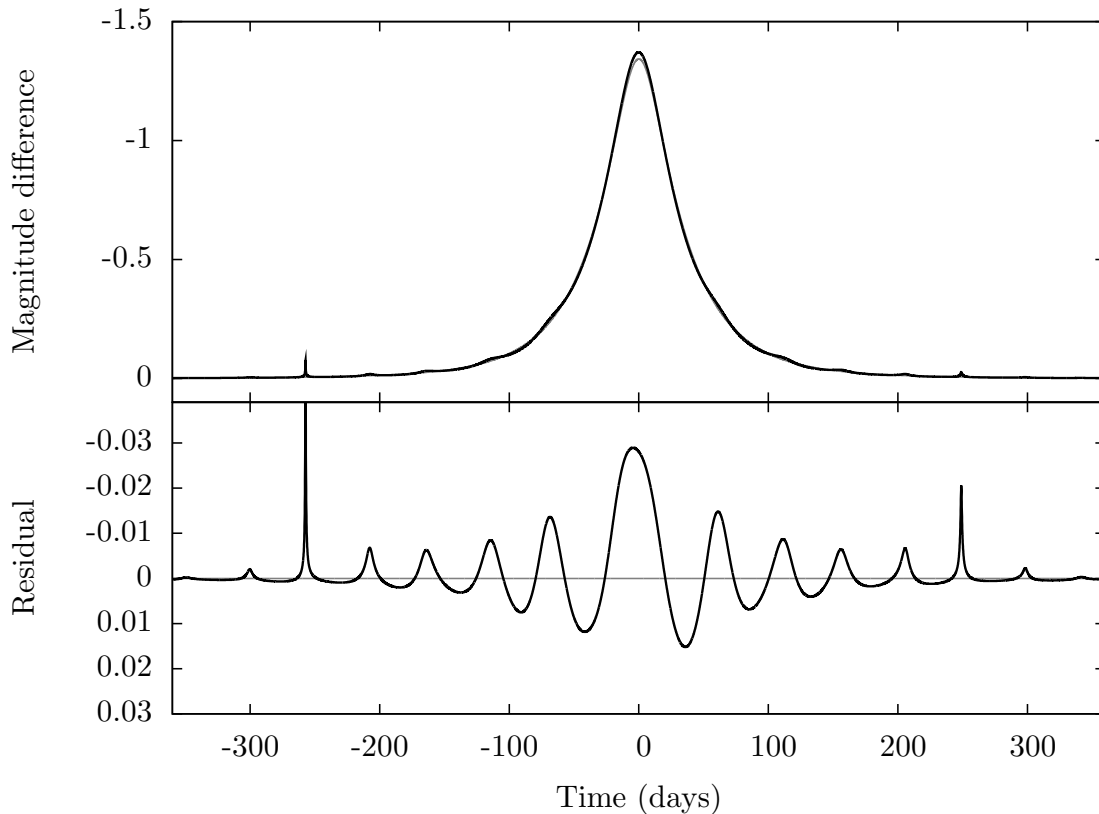


Figure 4.2 – The lightcurve of an RRL. The upper panel shows the RRL lightcurve in black, and the Paczyński lightcurve of a single lens with the same total mass in grey. The lower panel shows the residual with respect to the Paczyński lightcurve. Features due to the magnification arms appear as peaks in the residual, while between them there are relative demagnifications. Large, short-duration spikes occur when the secondary caustic passes close to or over the source. The system has parameters $t_E = 61$ d, $T = 92$ d, $s = 0.23$, $q = 0.8$, $u_0 = 0.3$, $\phi_0 = 1.75$ (see Section 4.4 for definitions of u_0 and ϕ_0).

magnification pattern will also change, as it depends on the projected lens separation s (Schneider and Weiss 1986).

Figure 4.2 shows the lightcurve of an RRL with a similar magnification pattern to that shown in Figure 4.1. It closely resembles the lightcurve of a single lens, the Paczyński lightcurve, but with a quasi-periodic variation over the entire lightcurve that only becomes obvious in the residual that is left once the Paczyński curve is subtracted from the lightcurve. These periodic features correspond to the magnification arms that

extend between the secondary and central caustics, which sweep over the source as the lens rotates. The microlensing timescale of the lightcurve shown is $t_E \approx 60$ d, but it is clear that repeating binary features remain in the lightcurve at a time from peak magnification much greater than this, which corresponds to a source position far outside the Einstein ring. This is because the secondary caustics can lie far outside the Einstein ring, their distance from the lens centre increasing as the binary separation decreases. However, both the size of the secondary caustics, and the strength of the magnification arms connecting them with the central caustic, decrease with decreasing binary separation. We note at this point that, despite the large separation of the secondary caustics, we need not consider relativistic effects of superluminal caustics (Zheng and Gould 2000) as the ratio of the caustic rotational speed to the speed of light in all the cases we will consider is $\sim 10^{-3}$.

4.2.1 What happens to the images?

The image configuration of a point-mass lens consists of two images: a major image, of positive parity and magnification $\mu_+ \geq 1$, outside the Einstein ring and a minor image of negative parity and magnification $\mu_- < 0$, inside the Einstein ring (e.g., Refsdal 1964; Liebes 1964). The addition of a second mass to the lens causes an additional image of negative parity to be produced if the source does not lie within a caustic (Schneider and Weiss 1986). If the lens is far from resonance, i.e., $s \ll 1$ or $s \gg 1$, two of the three images can still be associated with the major and minor images of the single lens, while the new third image is labelled a tertiary image.

It is interesting to study what is happening to each of the three images during the course of an RRL event. Dubath, Gasparini, and Durrer (2007) study the effects of an orbiting close-binary lens on the major image by casting the lensing potential as a time-varying quadrupole. They show that the major image can exhibit significant time-dependent deviations from the single-lens form when it is highly magnified, and go on to calculate the expected rate of events showing such deviations. Unfortunately,

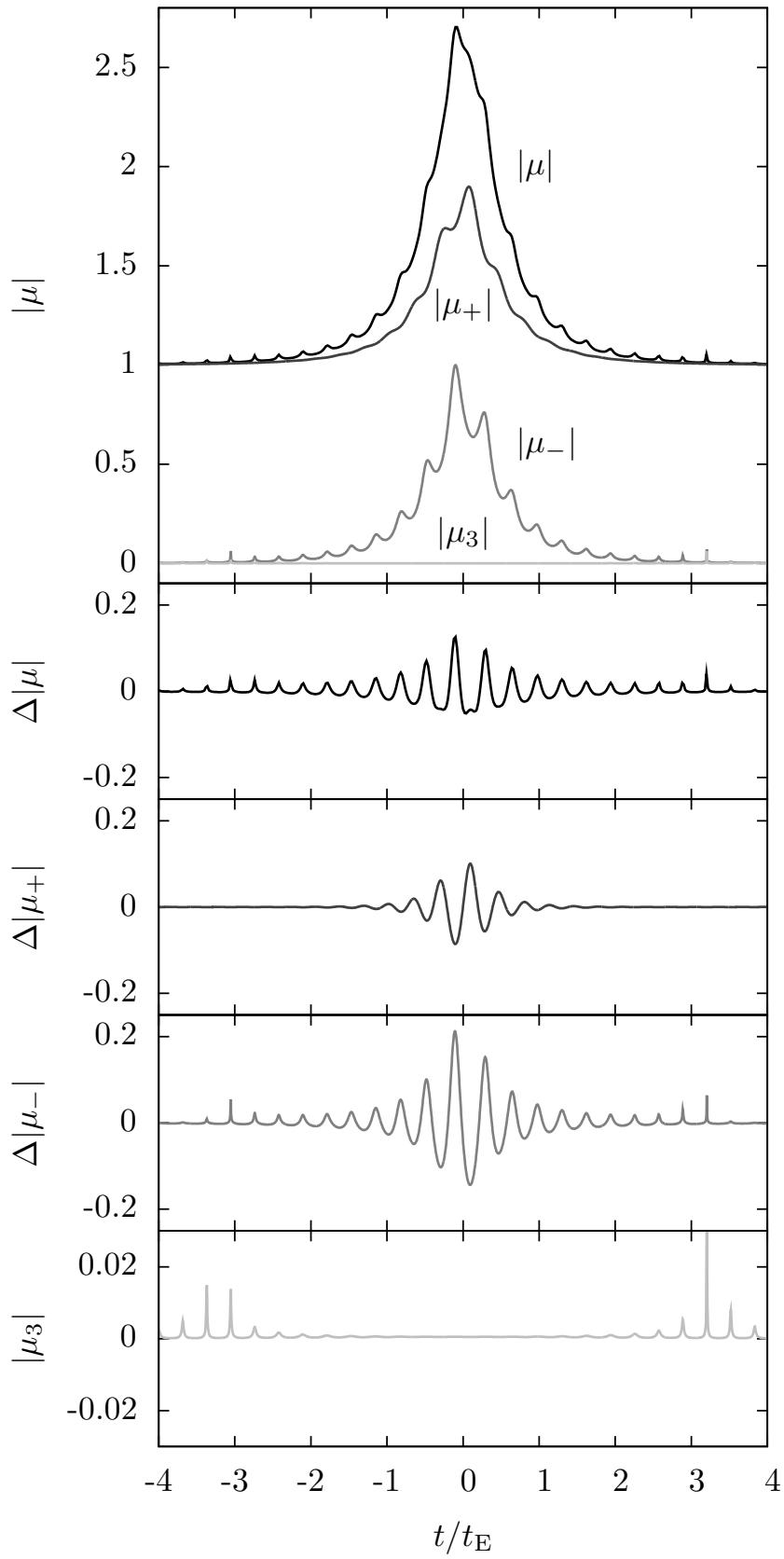


Figure 4.3 – Lightcurves and residuals for each image of a microlensing event with repeating features. The top panel shows the absolute magnification of the combined images ($|\mu|$), and the individual major ($|\mu_+|$), minor ($|\mu_-|$) and tertiary ($|\mu_3|$) images in different shades of grey. The central panels show the absolute magnification residual with respect to the single-lens form for all images combined, the major image and the minor image, going from top to bottom, respectively; the bottom panel shows the absolute magnification of the tertiary image, which has no single-lens counterpart. The event has the didactic, but unrealistic, parameters $u_0 = 0.4$, $s = 0.3$, $q = 1.0$ and $t_E/T = 10$.

they neglect to consider both the tertiary image and the minor image, the latter of which will be magnified by a similar degree to the primary image, as $\mu_+ \gg 1$ and $|\mu_+| - |\mu_-| = 1$ (e.g Refsdal 1964; Liebes 1964).

In the top panel of Figure 4.3 we plot the lightcurves of all three images for an RRL with an unrealistically short period compared to its event timescale. The observable lightcurve ($|\mu|$ against t) clearly exhibits strong repeating features. The lightcurves of the major and minor images ($|\mu_+|$ and $|\mu_-|$, respectively) also show strong features, while the tertiary image lightcurve $|\mu_3|$ is flat and extremely demagnified over most of the event. However, it is more informative to look at the residual lightcurve (the RRL lightcurve minus the single-lens lightcurve of the same total mass) for each image and all images combined, which are shown in the lower panels of Figure 4.3. The tertiary image has no single-lens counterpart, so we just show its lightcurve with an expanded scale.

In the residuals, each image shows a strikingly different pattern of features: the major image is only significantly perturbed from its single lens form when the source is within $\sim r_E$ of the centre of mass, while the minor image shows significant perturbations out to the position of the secondary caustics. It is only when the source is close to the secondary caustics that the tertiary image is magnified significantly. It is interesting to note that the periodic variations in the major and minor image are out of phase and cancel each other to a significant degree around the lightcurve peak where the

amplitude of the major image variations is large. Also, throughout the lightcurve the amplitude of the minor image residual is larger than that of the major image. Both points have implications for the expected rates calculated by Dubath et al. (2007).

Figures 4.2 and 4.3 show that an RRL can clearly exhibit interesting, repeating lightcurve features if the binary period and separation conspire. However, this could be a very rare occurrence, and in order to see if RRL events will be detectable in real microlensing surveys we must consider how their properties, such as the amplitude of the periodic signal, relate to the physical parameters of the lensing system.

4.3 Are RRLs detectable?

In the previous section we defined a criterion for a lens to be an RRL and described the features of an RRL event. In this section we put the definition on a more quantitative basis and investigate whether RRLs will occur amongst the microlensing events that are detected by surveys. To determine if detection is plausible, we investigate the range of physical parameters required to produce a microlensing event with repeating features, first analytically and then numerically. Finally we apply our numerical method to simulated microlensing surveys to estimate the expected rate of RRL detections.

4.3.1 An analytical approach

To see repeating features in a microlensing event, the most fundamental requirement of the system is that the lens completes more than one orbit during the event. The magnification pattern of a binary lens is complicated but the essential features of a close-binary lens can be captured by assuming it to be composed of two straight, radial arms that extend from the centre of mass to the position of the secondary caustics. Under this assumption (and assuming a random initial phase angle) repeating features are guaranteed to be observed if the lens completes two orbits in the time that the source

spends within the radius swept out by the arms. We can write this as an inequality

$$2T < \frac{\pi}{2} u_{\pm} t_E, \quad (4.1)$$

where u_{\pm} is the radial position of the secondary caustics in units of Einstein radii (see Figure 4.10) and the factor of $\pi/2$ is the mean chord length across a unit circle, which accounts for the random impact parameter of source trajectories relative to the lens centre of mass. It should be noted that it is possible for a feature to repeat if the binary completes between one and two orbits, but this requires a coincidence in the timing of the first feature.

Both the orbital period and the Einstein timescale depend on the lens mass, and the period also depends on the lens semimajor axis, so it is possible to write this constraint in terms of M and a . For projected lens separations $s \ll 1$, Bozza (2000b) has derived an analytical approximation for the secondary-caustic positions (see Equation 4.14), which if we keep only the first order terms is

$$u_{\pm}(s, q) \simeq s^{-1}. \quad (4.2)$$

Using the definitions of the Einstein radius and timescale (Equations 1.7 and 1.15) and Kepler's third law, with a little algebra we can then write Equation 4.1 as a constraint on the semimajor axis of the binary

$$a < 4.51 \text{ AU } [x(1-x)]^{2/5} D_s^{2/5} v_t^{-2/5} M^{3/5}, \quad (4.3)$$

where we have assumed a face-on orbit so that $s = a/r_E$, and where M is the total lens mass in Solar masses, D_s the source distance in kpc, $x \equiv D_1/D_s$ is the ratio of lens and source distances and v_t the relative lens-source velocity in km s^{-1} .

While we have an upper limit on the lens semimajor axis, in order for RRL lightcurve features to be detected they must be strong enough to be detectable in the photometry of the microlensing event. This requirement is somewhat ambiguous but as the magnification pattern depends only on s and q and the strength of features decreases with decreasing s , we can assume that, for a given photometric precision and mass ratio,

magnification pattern features will be detectable only when the separation is larger than a certain value, i.e.,

$$s > s_{\text{det}}, \quad (4.4)$$

where s_{det} depends on q and the photometric accuracy. For stellar-binary mass ratios, there will only be a small dependence on q but there will be a strong dependence on the photometric accuracy; however, a value of $s_{\text{det}} = 0.3$ is reasonable (see Section 4.3.2).

We can again write this constraint as a limit on the semimajor axis

$$a > 2.85 \text{ AU } s_{\text{det}} [x(1-x)]^{1/2} D_s^{1/2} M^{1/2}. \quad (4.5)$$

We now have an upper and a lower limit on a , which are dependent on other parameters of the lensing system, the most interesting being the total lens mass. Figure 4.4 shows these constraints on the semimajor axis as a function of mass, for a lens system with $x = 0.75$, $D_s = 8 \text{ kpc}$ and $v_t = 50 \text{ km s}^{-1}$, with values of $s_{\text{det}} = 0.3, 0.2$ and 0.1 . Other than the slow lens-source velocity ($\langle v_t \rangle \approx 200 \text{ km s}^{-1}$ for a bulge microlensing event), these values are typical of a microlensing event towards the Galactic bulge. The plot shows that most of the parameter space is excluded, but thanks to the differing power-law indices on the mass dependence, there is a small range of parameters over which repeating features should be detectable. For the parameters shown, the detectable region opens up at $M \sim 1M_\odot$ and $a \sim 1 \text{ AU}$, and widens to $a = 3.3\text{--}4.4 \text{ AU}$ by $M = 10M_\odot$. The dependence of the limits on other parameters means that the region of detectability will get smaller and move to larger a as the source distance grows; will get larger and move to smaller a and M as the lens moves closer to the source or the observer; and will get smaller as the relative lens-source velocity increases. A small but significant fraction of binary stars will have total masses and semimajor axes in the range of detectability (e.g., Duquennoy and Mayor 1991), and even more if improved photometric accuracy can reduce s_{det} .

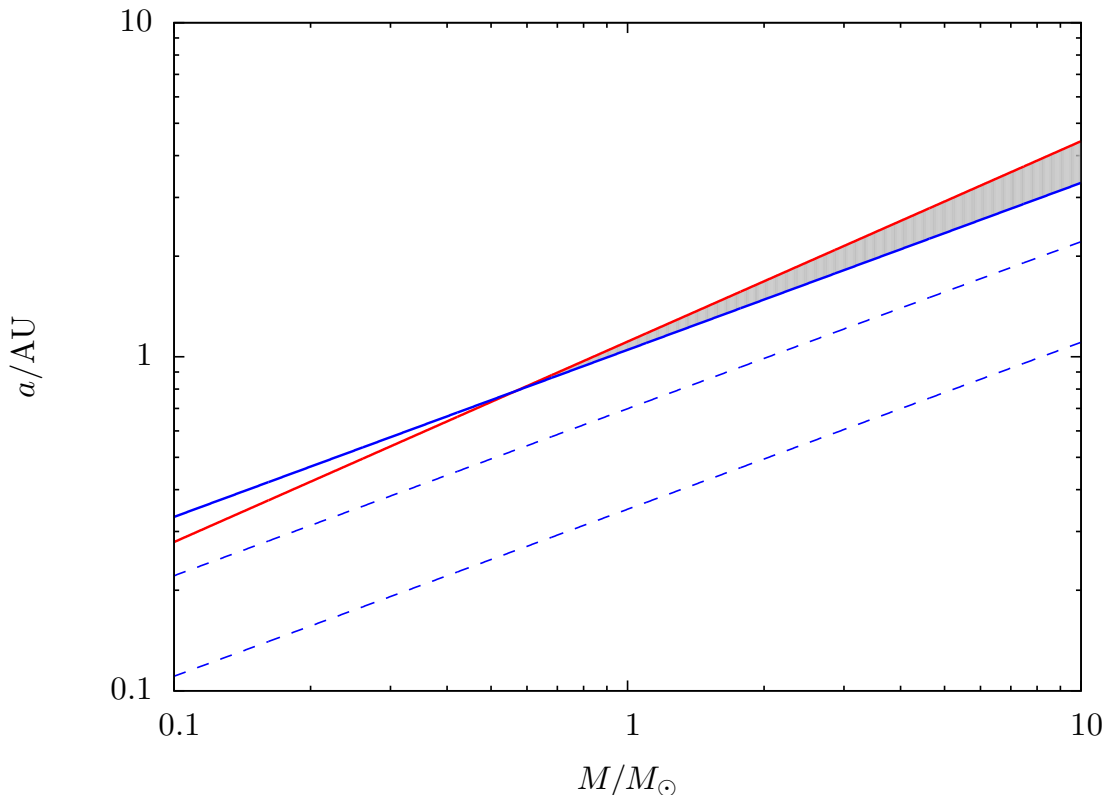


Figure 4.4 – Plot showing the region of the total mass-semimajor axis plane where repeating features are observable. The red line shows the upper limit on a provided by the constraint in Equation 4.3, while blue lines show the lower limit on a provided by the constraint in Equation 4.5, with values of $s_{\text{det}} = 0.3, 0.2$ and 0.1 from top to bottom. The other parameters are set at $x = 0.75$, $D_s = 8$ kpc and $v_t = 50$ km s $^{-1}$. The region where repeating features are detectable for $s_{\text{det}} = 0.3$ is shaded grey.

4.3.2 A numerical approach

In deriving analytical limits on the range of lens parameters we have had to make assumptions about the magnification pattern and strength of features. If we instead proceed numerically, we need not make these assumptions as we can determine precisely the regions of the magnification pattern where features are detectable for any given photometric accuracy. We define a detectability ε that is the probability that, for a given lens system and photometric precision, an RRL with a face-on orbit will exhibit at least one detectable repeating feature in its lightcurve. A feature is said to be

detectable at a radial position u , if the range of magnifications μ over a circle of radius u satisfies

$$\Delta m \equiv 2.5 \log \left[\frac{\mu_{\max}(u)}{\mu_{\min}(u)} \right] \geq \Delta m_{\min}, \quad (4.6)$$

where we have expressed the range of magnifications ($\mu_{\min} \rightarrow \mu_{\max}$) as a magnitude difference Δm and where Δm_{\min} is the photometric detection threshold, which can be taken to mean the typical uncertainty in magnitude on a data point in the baseline of the lightcurve. In calculating ε we average over the random parameters of the source trajectory and phase angle.

We can now test the predictions we made in Section 4.3.1 by comparing them with the numerically calculated detectability. Figure 4.5 plots the numerical detectability ε against total mass M and semimajor axis a for the set of parameters we used for Figure 4.4. At some values of M and a the numerical calculation fails due to loss of precision from catastrophic cancellation in the calculation of the magnification. The analytical upper and lower limits of Equations 4.3 and 4.5 are also shown in the figure, however with $s_{\text{det}} = 0.28$ as opposed to 0.3. It can be seen in the figure that the analytical upper limit of Equation 4.3 agrees very well with the numerical region of detectability, coinciding with the boundary where ε begins to fall from unity as a increases. Equation 4.3, without the factor of 2 that was introduced on the left-hand side of Equation 4.1 to guarantee a repeated feature, also describes well the region where detection becomes possible but is not guaranteed (i.e., $0 < \varepsilon < 1$).

The analytical lower limit, once the parameter s_{det} has been adjusted to 0.28 for a guaranteed repeating feature, also agrees well with the numerical region of detectability. It should be noted however, that the slope of the lower edge of the numerical region is slightly shallower than the analytical lower limit. This becomes more pronounced when the lens gets closer to the source, the total mass increases or the source velocity decreases. This is because the assumption that there are detectable features over the entire magnification pattern within $u < u_{\pm}$ breaks down and the detectable features lie in two disjoint regions: a disc surrounding the central caustic and an annulus containing the secondary caustics. The size of these regions depends on s and so the lower limit

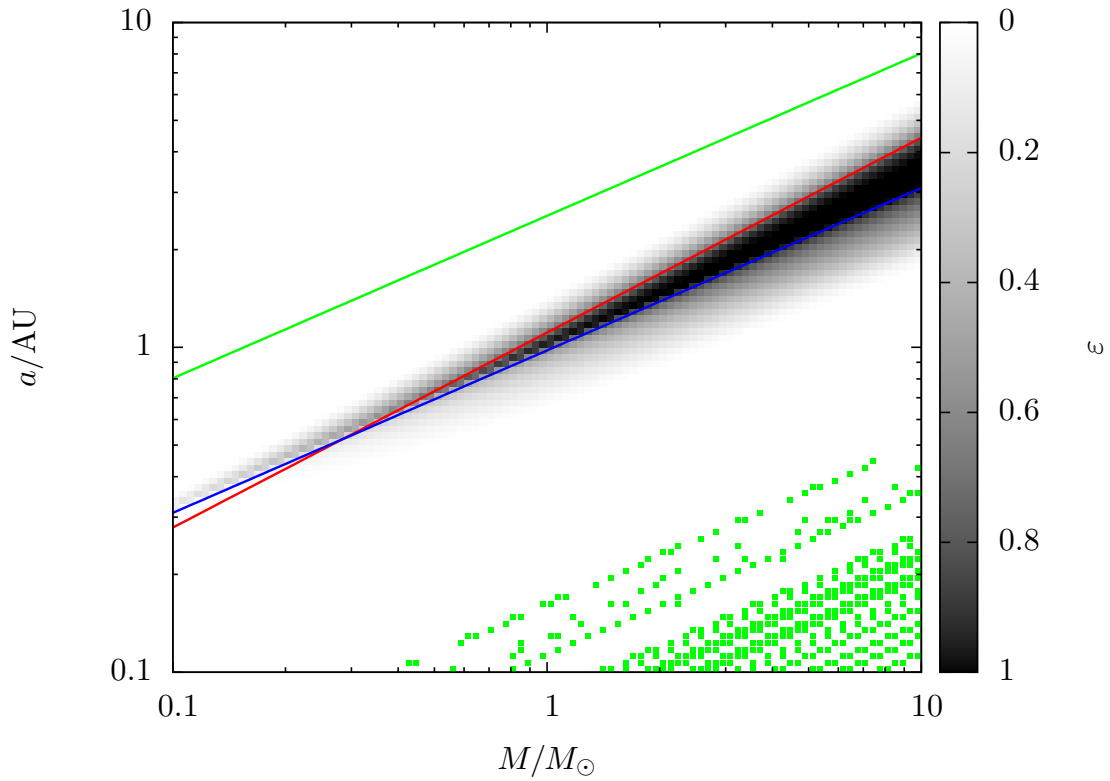


Figure 4.5 – Plot of the average detectability ε (plotted with darkening shades of grey as ε increases) against total lens mass M and semimajor axis a for a lens with mass ratio $q = 0.3$ and a photometric precision $\Delta m_{\min} = 0.01$. The lens and source distances and relative velocity are the same as used in Figure 4.4. The red line is the analytical upper limit of Equation 4.3, while the blue line is the analytical lower limit of Equation 4.5 with a value of $s_{\text{det}} = 0.28$. The green line at the top of the figure marks the boundary between regions of close- and resonant-topology lenses – we only calculate ε for close-topology lenses. The green points lower in the figure mark points where our calculation of ε failed (see text for details).

on a becomes a shallower function of M . This effect is more important in determining the slope of the lower limit on a where $\varepsilon = 0$.

The effects of lens distance and lens-source velocity

Having looked at the role of mass and orbital separation, it is important to investigate how the detectability of repeating features depends on other factors. Figure 4.6 shows

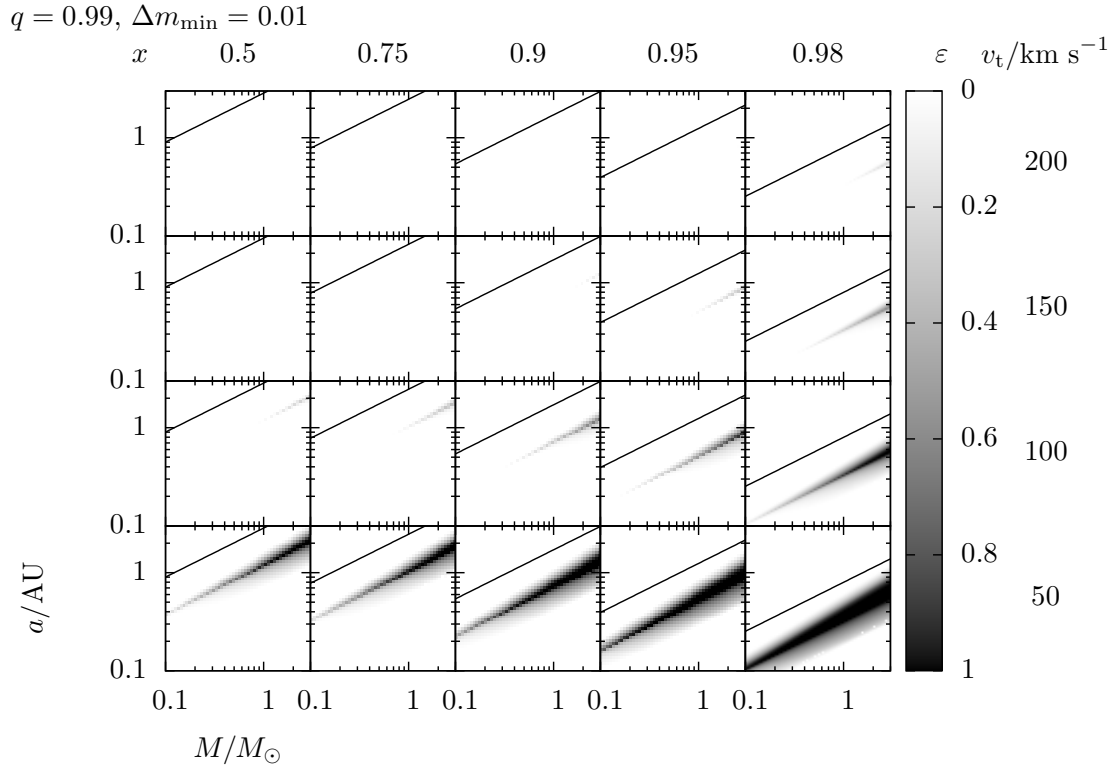


Figure 4.6 – Maps of detectability ε plotted against a and M for a binary of mass ratio $q = 0.99$, photometric threshold $\Delta m_{\min} = 0.01$ and various values of the fractional lens distance $x = D_l/D_s$ and source velocity v_t . Each small panel is essentially the same as the plot in Figure 4.5, but with different parameter values and slightly restricted ranges $M = 0.1\text{--}3M_\odot$ and $a = 0.1\text{--}3\text{ AU}$. Moving from left to right, sub-panels have different fractional lens distances $x = 0.5, 0.75, 0.9, 0.95$ and 0.98 ; the results remain the same under the transformation $x \rightarrow (1 - x)$, i.e., there is reflectional symmetry about $x = 0.5$. Moving from bottom to top, sub-panels have different source velocity $v_t = 50, 100, 150$ and 200 km s^{-1} . The source distance is fixed at $D_s = 8\text{ kpc}$. The black line shows the boundary between close- and resonant-caustic structures, above which we do not plot ε . As in Figure 4.5, there are points where the calculation of ε fails, but these are not shown for clarity as they do not impinge on the regions of detectability.

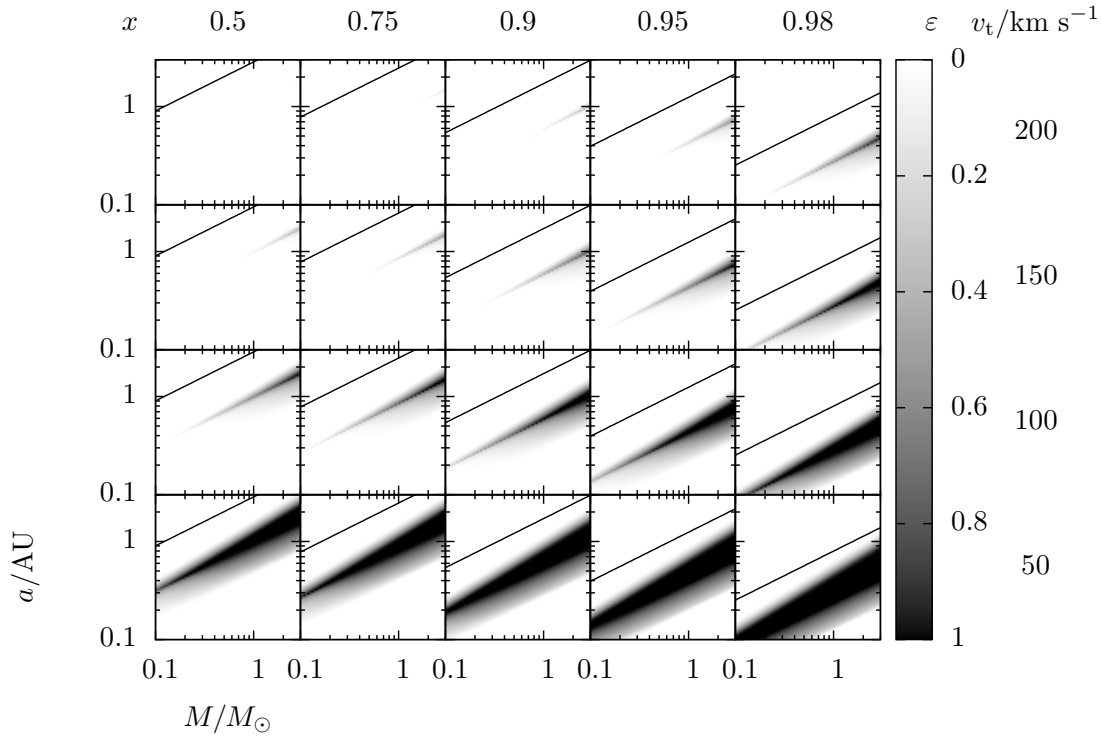
detectability maps similar to that in Figure 4.5, but for a mass ratio $q = 0.99$, photometric precision $\Delta m_{\min} = 0.01$ and various values of the lens distance and source velocity. It is clear that the source velocity has a large effect on the detectability, with large regions of detectability for $v_t = 50 \text{ km s}^{-1}$ at all lens positions, which are reduced drastically for $v_t = 100 \text{ km s}^{-1}$. Once $v_t = 150 \text{ km s}^{-1}$ there is only a tiny region of low detectability for lenses very close to the source (or to the observer, as $x(1-x)$ is symmetric about $x = 0.5$). For $v_t = 200 \text{ km s}^{-1}$ there is only detectability in the most favourable cases of very high photometric accuracy and fractional lens distance. This strong dependence on v_t occurs because the number of orbits completed by the lens decreases as v_t increases (the $v_t^{-2/5}$ term in Equation 4.3) but does not affect the strength of binary features (Equation 4.5 is independent of v_t). In other words, when taking the ratio of the upper and lower limits of a , the v_t term does not cancel at all but all other terms cancel to a degree. Unfortunately, the microlensing event rate peaks at $v_t \sim 200 \text{ km s}^{-1}$, but there is a significant fraction of events with $v_t < 100 \text{ km s}^{-1}$ (e.g., Dominik 2006).

The lens distance does not affect the size of the detectable region as strongly as the source velocity does, as the upper and lower limits of the detectable region scale with $x(1-x)$ as similar power laws (-0.4 and -0.5 respectively). However, this similar scaling does mean that the detectable regions move as x changes, occurring at lower a and increasing in size slightly as $x(1-x)$ decreases. For microlensing events towards the Galactic bulge, the event rate peaks at $x \sim 0.8$ (e.g Dominik 2006), whereas for self lensing in the Magellanic clouds x will be close to unity, $x \approx 0.98$.

The effect of photometric precision

Figure 4.7 plots the detectability for different values of the photometric precision Δm_{\min} . The photometric precision of the observations strongly affects the detectability of repeating features. For $\Delta m_{\min} = 0.005$ and 0.01 we see large regions of detectability for small source velocities and for $\Delta m_{\min} = 0.005$ even some detectability when $v_t = 200 \text{ km s}^{-1}$. As Δm_{\min} increases to 0.02 , the detectable regions shrink signifi-

$q = 0.99, \Delta m_{\min} = 0.005$



$q = 0.99, \Delta m_{\min} = 0.02$

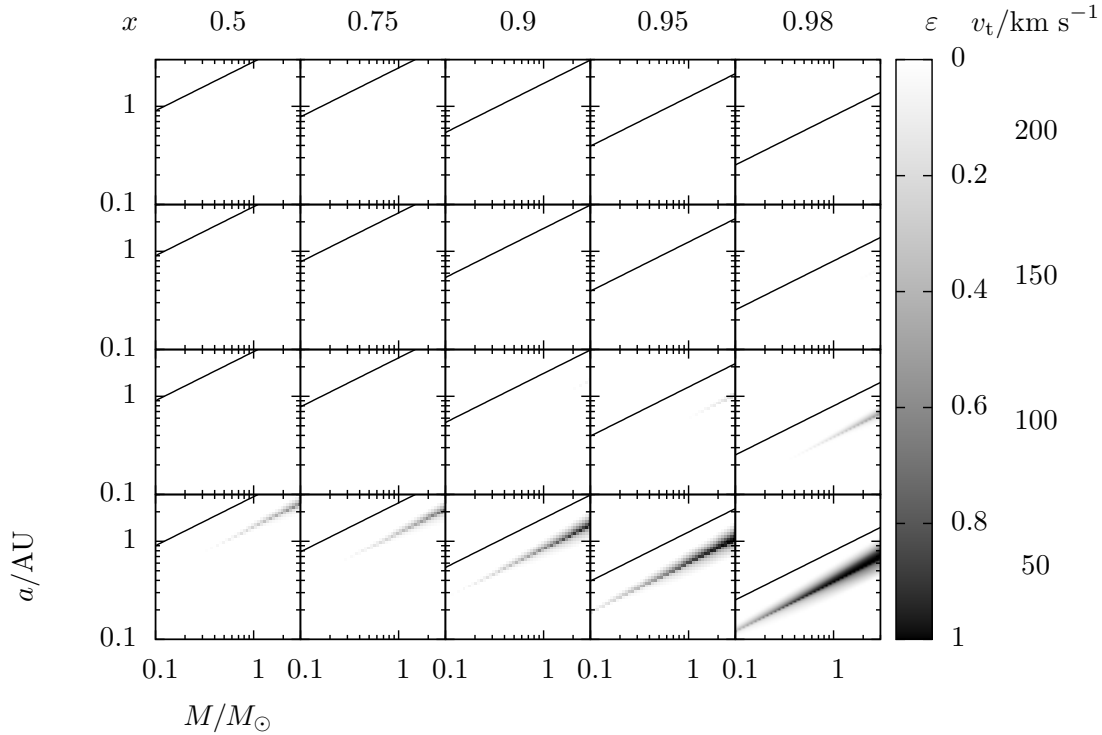


Figure 4.7 – As Figure 4.6, but plotted for three more values of the photometric threshold $\Delta m_{\min} = 0.005$ and 0.02 in the top and bottom figures, respectively, and $\Delta m_{\min} = 0.04$ in the figure continued on the next page.

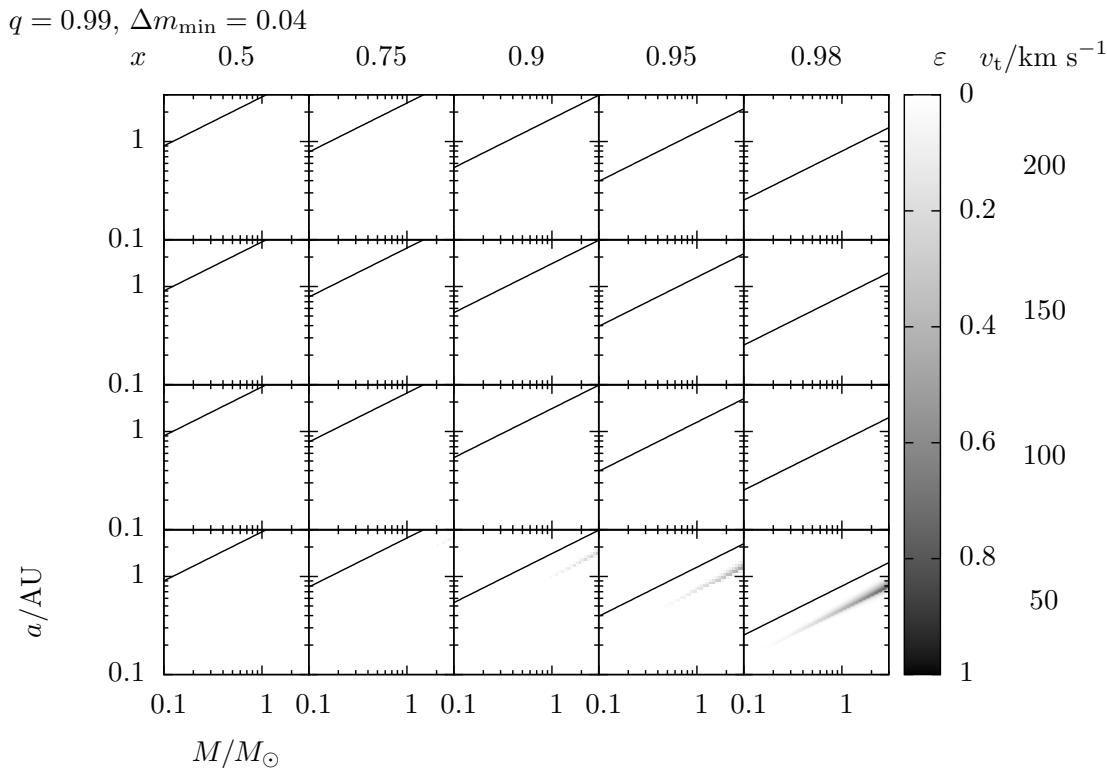


Figure 4.7 – Continued

cantly and all but disappear for $v_t \geq 100 \text{ km s}^{-1}$. For $\Delta m_{\min} = 0.04$ there is virtually no detectability, with only a small chance of detection for the smallest velocities and largest lens distances. Increasing the threshold effectively increases the lower limit of a at which binary features are detectable, while leaving the upper limit unchanged. Therefore, just as with the source velocity, the photometric threshold has a large effect on the size of the detectability region. It should be noted that the detection threshold Δm_{\min} is in fact a combination of the effects of photometric precision and the blending by unrelated starlight, which acts to add a noise component to the measurement of the magnification caused by the lens. The effect of blending is discussed further in Section 4.6.1.

Even in the most favourable case of low photometric threshold, low source velocity and high fractional lens distance, the region of detectability does not reach the boundary between close- and resonant-caustic topologies. This is because, as the pro-

jected separation increases and approaches the close-resonant topology boundary, the secondary caustics move rapidly inwards to merge with the central caustic. This decreases the radial range over which binary features are detectable. At the same time the orbital period will increase rapidly as the semimajor axis increases. These combined effects mean that in order to see repeating features from a lens with resonant topology, an extremely low source velocity is necessary to allow the lens to orbit in the time the source spends near the resonant caustic. Dominik (1998b) computes lightcurves for events with rapidly-rotating resonant caustics, but does not estimate how often such situations will arise.

The effect of the mass ratio

Figure 4.8 shows the same maps as Figure 4.6 but for differing q , and the threshold fixed at $\Delta m_{\min} = 0.01$. The maps for $q = 0.3$ are similar to those for $q = 0.99$ and there is little difference in the size of the region of detectability. However, once q has fallen to 0.1, the size of the detectable region has begun to shrink, such that for higher values of Δm_{\min} (not shown) there is only a very small chance of detection with small source velocities. For lower mass ratios still, there are only very small regions of detectability for $q = 0.03$ and effectively zero detectability for $q = 0.01$. If we take the boundary between brown dwarfs and planets to be at $13M_{\text{Jupiter}}$, there is a very small region of detectability where the secondary lens is a planet, but the apex of the detectable region (where the upper and lower limits meet) occurs close to this boundary regardless of the mass ratio. So, there is little chance of detecting repeating features from a planetary system unless the photometry is very accurate, the lens very close to the source or the source velocity is significantly smaller than 50 km s^{-1} . Such low velocity events are rare but are known to occur, e.g., the event OGLE-1999-BLG-19 had a source velocity $v_t = 12.5 \pm 1.1 \text{ km s}^{-1}$ (Smith et al. 2002b).

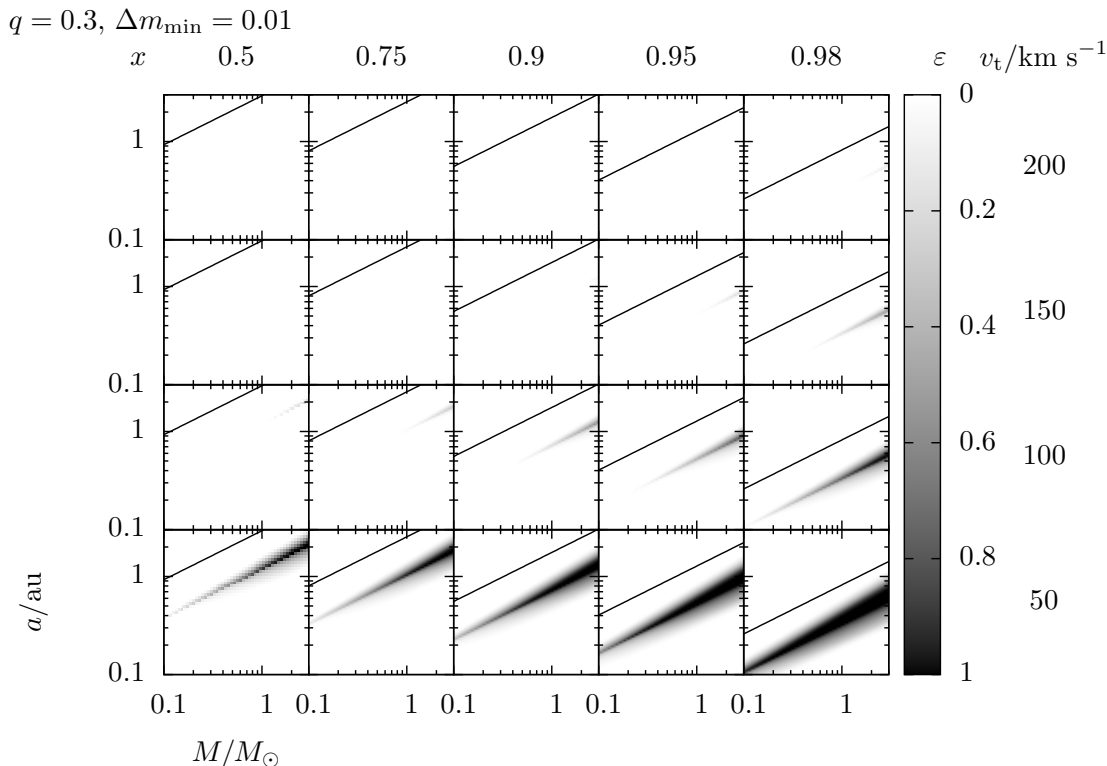


Figure 4.8 – As Figure 4.7, but plotted for differing mass ratios in each grid. Moving from top to bottom (continued on following pages) the detectability is plotted for $q = 0.3, 0.1, 0.03$ and 0.01 . The total mass corresponding to a secondary below the deuterium burning limit $M_{\text{D}} \approx 13M_{\text{Jupiter}}$, is $M < 0.054M_{\odot}$, $M < 0.14M_{\odot}$, $M < 0.43M_{\odot}$ and $M < 1.25M_{\odot}$ respectively for each value of q . The photometric detection threshold in each case is $\Delta m_{\min} = 0.01$.

4.3.3 How many RRL events will we detect?

To estimate the rate of detectable RRL events we conducted a simulation of a space-based H -band microlensing survey, such as *Euclid* (Beaulieu et al. 2010) or *WFIRST* (Bennett 2011), and a ground-based I -band survey, based on OGLE-III (Udalski et al. 1997; Udalski 2003). More details about *Euclid* and *WFIRST* can be found in the next chapter. Using the Besançon population synthesis model of the Galaxy (Robin et al. 2003), including a three dimensional extinction model (Marshall et al. 2006), we produced a catalogue of possible microlensing events following the recipe of Kerins

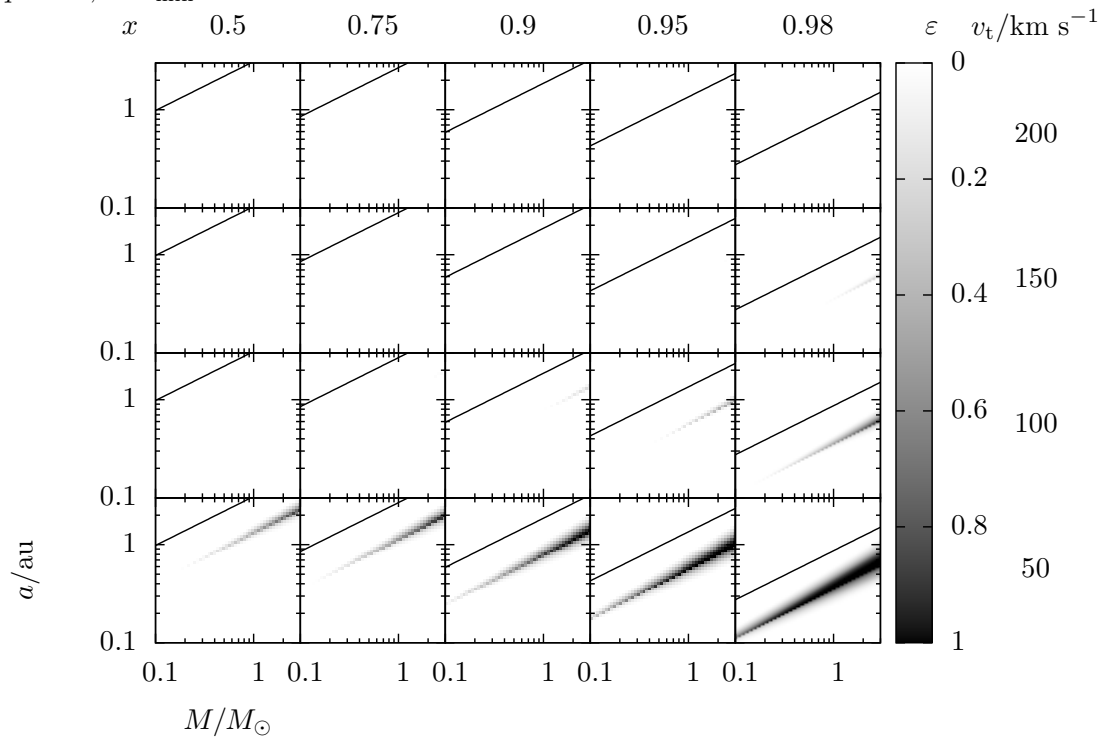
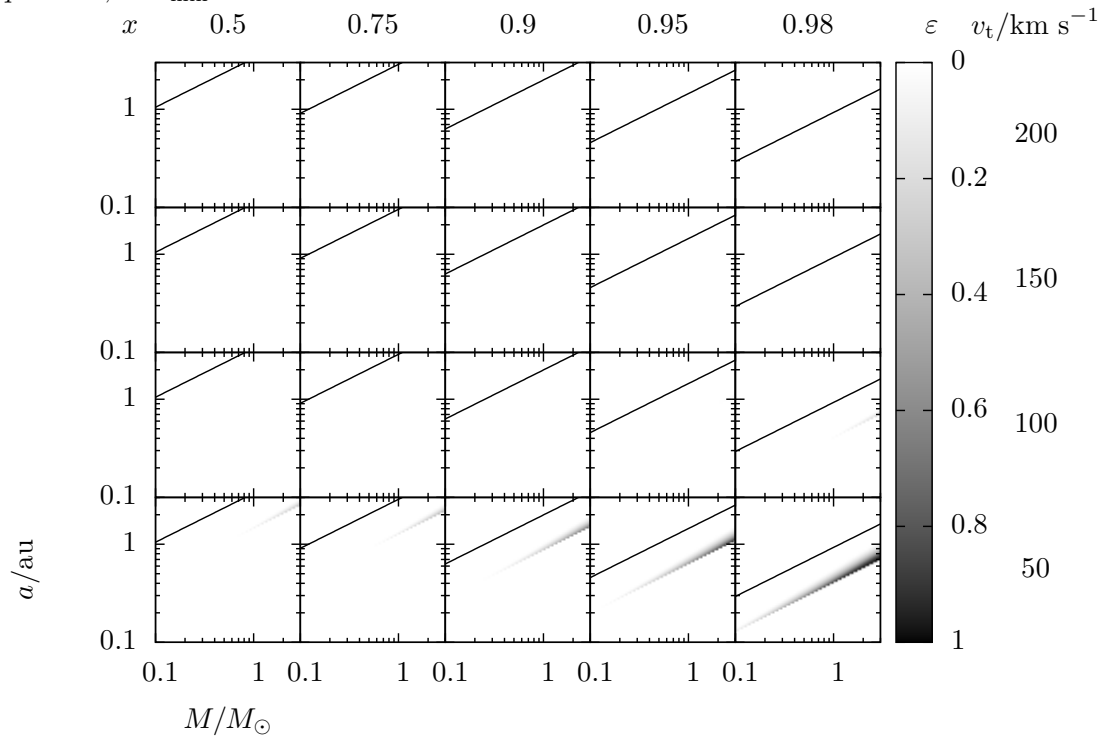
$q = 0.1, \Delta m_{\min} = 0.01$  $q = 0.03, \Delta m_{\min} = 0.01$ 

Figure 4.8 – Continued

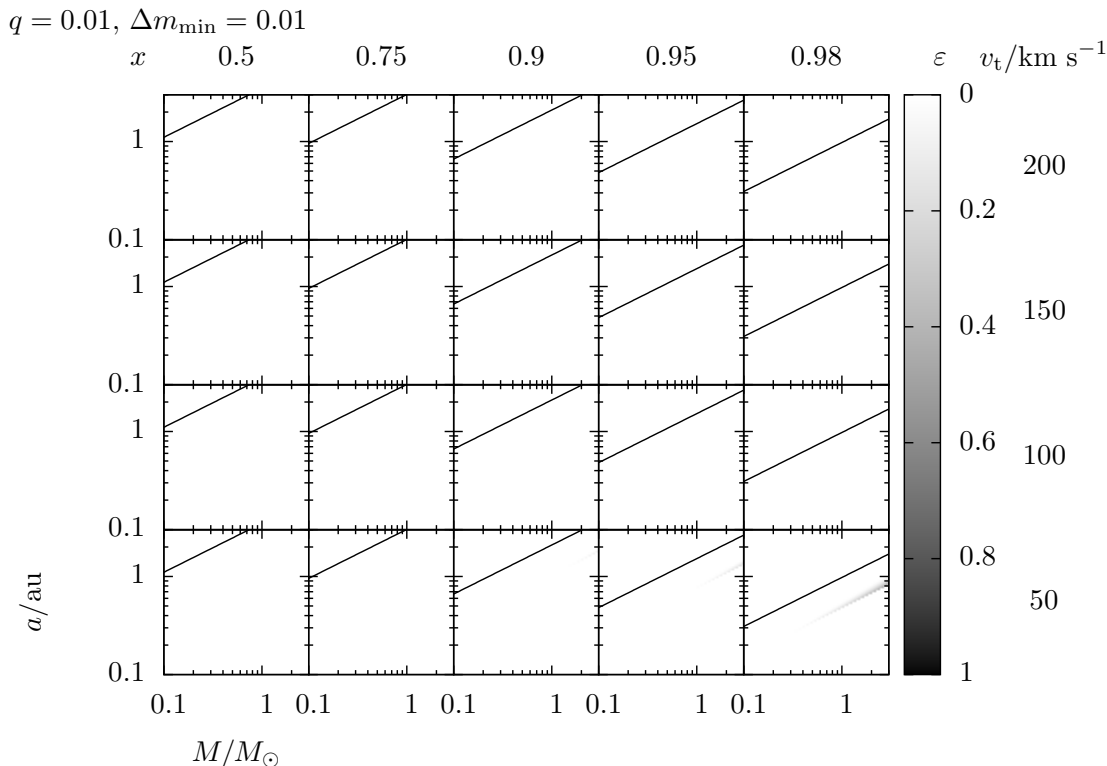


Figure 4.8 – Continued

et al. (2009). Source stars with magnitudes $H_s < 25$ and $I_s < 21$ are drawn from the Besançon model and lensed by stars of any magnitude in the space- and ground-based simulations respectively. The lens mass is split up into two components with a mass ratio q distributed logarithmically in the range $q = 0.1-1$ and orbit with a semimajor axis a distributed logarithmically in the range $a = 0.1-4$ AU. Each event is assigned a weighting $w = 2r_{E}v_l u_{0,\max}$ proportional to its event rate, where $u_{0,\max}$ is the maximum impact parameter that the event could have and its peak single-lens magnification remain detected at 5σ above baseline, taking into account blending. Each event was assigned a blending fraction $f'_s \leq 1$ drawn from the blending distributions of Smith et al. (2007), with source density 131 stars per square arcmin, and seeing 0.7 arcsec and 1.05 arcsec for the space-based and ground-based simulations respectively. This will significantly overestimate the blending effect for the space-based simulation, as the diffraction-limited PSF for a 1-m telescope will have a full width at half maxi-

mum ~ 0.4 arcsec; Smith et al. (2007) do not simulate seeing better than 0.7 arcsec. The final blending suffered by the source f_s also includes flux from the lens, which is obtained from the Besançon model assuming it is a single star. However, the luminosity of binary star with the same total mass as a single star will be less than the single-star luminosity, as luminosity scales roughly as $M^{2.4}$ for low-mass main-sequence stars (Henry and McCarthy 1993, based on V -band mass-luminosity relation for masses $M = 0.18\text{--}0.5M_\odot$). The severity of blending is thus overestimated in both ground- and space-based simulations, much more so for the space-based survey, and as blending has a large effect on the detectability (see Section 4.6.1), the event rates we estimate will be conservative. However, we do not include the effect of orbital inclination, which can decrease the amplitude of lightcurve features slightly (see Section 4.6.3), so this optimistic assumption will likely balance the pessimistic blending we apply. The photometric detection threshold was calculated based approximately on the proposed design of the *Euclid* mission (Euclid payload manager 2009) for the space-based survey and the OGLE-III setup (Udalski et al. 1997) for the ground-based setup. Total event rates are normalized to rates $\Gamma_{\mu L} = 7000 \text{ yr}^{-1}$ for the space-based survey (e.g., Bennett and Rhie 2002) and $\Gamma_{\mu L} = 600 \text{ yr}^{-1}$ for the ground-based survey, corresponding roughly with the rate detected by the OGLE-III survey. The rate of RRL events Γ_{RRL} is taken to be

$$\Gamma_{\text{RRL}} = \frac{\Gamma_{\mu L}}{W} \sum_i w_i \varepsilon_i, \quad (4.7)$$

the normalized sum of the product of ε_i and w_i , the detectability and weight of event i respectively, over all microlensing events, where $W = \sum w_i$ is again summed over all events.

The simulations do not account for the observing strategy and assume that frequent monitoring (a few data points per night or greater) is conducted for a significant fraction of the year (6 months or greater). It is difficult to assess the impact of seasonal observability on the probability of detecting repeating features without performing detailed detection efficiency simulations. To account for this we introduce a factor f_{seas} ,

the fraction of a year spent continuously observing, which is approximately the probability that an individual feature is ‘caught’. We must also account for the fact that not every lens is binary. Raghavan et al. (2010) find that 44 percent of stellar systems are multiple, with mass ratios $q > 0.1$, and of these about 20 percent lie in the appropriate semi-major axis range, so we adopt a binary fraction $f_b \approx 0.1$.

For our entire sample of space-based survey events we find that RRL events make up a fraction $(1.1 \pm 0.2) \times 10^{-3}$ of the total microlensing event rate, which corresponds to an event rate $\Gamma_{\text{RRL}} = (7.8 \pm 1.5)f_{\text{seas}}f_b \text{ yr}^{-1}$. Similarly for the ground-based survey we find that a fraction $(0.5 \pm 0.1) \times 10^{-3}$ of the total microlensing event rate is made up of RRLs, which corresponds to an event rate $\Gamma_{\text{RRL}} = (0.32 \pm 0.06)f_{\text{seas}}f_b \text{ yr}^{-1}$. In all cases the errors are statistical.

Figure 4.9 shows the distribution of microlensing timescales for the detectable RRL events and all microlensing events in the space-based simulation. The results are very similar for the ground-based survey, other than the overall normalization. The distributions do not take into account any timescale dependence on detection efficiency, or the binary fraction. The timescale distribution for RRLs shows a peak at $t_E \sim 200 \text{ d}$, i.e., at timescales a factor of ten longer than the overall microlensing timescale distribution. Even at this timescale, however, detectable RRL events make up less than one percent of the whole. As the timescale increases, the fraction of RRL events increases. Long-timescale events are intrinsically rare, but RRL events make up a significant fraction of all events with these timescales and so such events are good targets to search for RRL signals. Additionally, their long timescales mean that each event is observable for many years and it is possible to obtain dense coverage of the lightcurve with standard survey-mode observations. The timescale distribution for all events agrees well with the expected asymptotic behaviour (Mao and Paczyński 1996), except for the points at very small and large t_E , where small number statistics are in effect.

Various microlensing surveys have targeted the Galactic bulge more or less continuously for roughly twenty years. These survey-mode observations take place over much of the year, so the seasonal observability factor f_{seas} will be close to unity. There

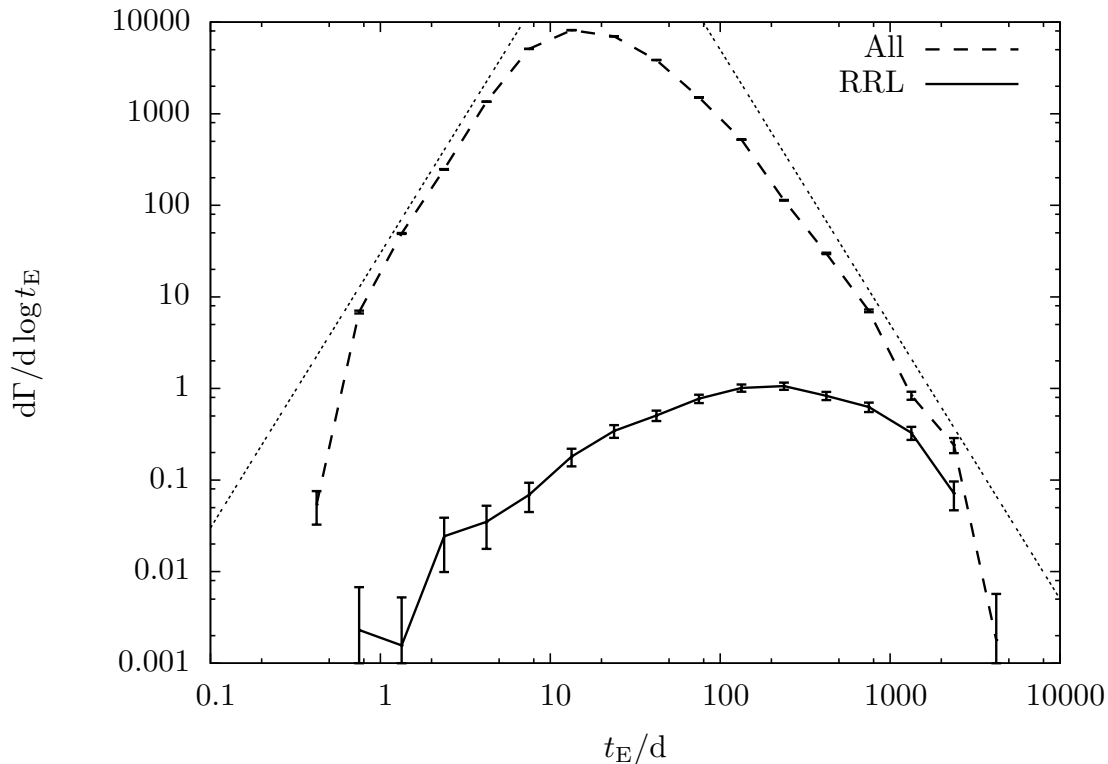


Figure 4.9 – Microlensing timescale distributions for detectable RRL events (solid line) and all microlensing events (dashed line) for the space-based survey. The dot-dashed lines show the expected asymptotic slope of the timescale distribution, with power law indices ± 3 (Mao and Paczyński 1996).

is therefore a good chance that there is of the order of one RRL event in current microlensing data sets. New ground-based microlensing surveys, some already in operation and some due to start in the near future, will increase the overall microlensing event rate significantly, so there is also a reasonable chance of detecting of the order of one RRL event over a timescale ~ 5 yr.

A space-based microlensing survey is proposed for two space missions which would launch at the end of the decade: ESA’s *Euclid* (Beaulieu et al. 2010) and NASA’s *WFIRST* (Bennett 2011). Such a mission may only spend 2–3 months per year performing a microlensing survey, as the majority of observing time would be spent on dark energy surveys. As such the seasonal observability $f_{\text{seas}} \sim 0.2$ factor would be

low, and a high degree of coincidence would be necessary for multiple RRL features to fall within the observing windows. The number of space-based RRL detections is therefore likely to be low in reality. However, a dedicated space-based microlensing survey, possibly as a mission extension to *Euclid* or *WFIRST*, observing the bulge continuously for most of the year would be very likely to detect RRL events.

4.4 Estimating RRL parameters

The lightcurve of a static-binary microlensing event contains information on the lens, which can be found by fitting the lightcurve with a static-binary microlensing model. Similarly, the lightcurve of an RRL contains information about the lens and its orbit. In this section we investigate the information it is possible to extract from RRL lightcurves and how this can be done. More specifically, we derive a number of approximations that relate the parameters of the RRL, including the orbital period, to features of the lightcurve. These approximate parameters can then be used as the initial guesses for a fit to the lightcurve.

The static-binary-lens lightcurve for a point source can be described with a minimum of seven parameters: three to describe the source trajectory, usually an impact parameter u_0 and angle α , and the time of closest approach to the origin t_0 ; one for the lightcurve baseline m_b ; two to describe the lens, the mass ratio q and projected separation s in units of Einstein radii; and finally the Einstein radius crossing time t_E . The coordinate system is usually chosen so that both lenses lie on the x -axis and the origin is the centre of mass; we shall refer to this coordinate system as the *static centre-of-mass system*.

The simplest RRL, with a face-on, circular orbit requires just one additional parameter, the orbital period T , for a total of eight parameters. In contrast, a full Keplerian orbit requires five additional parameters (including the period), bringing the total to thirteen parameters, many of which will be hard to constrain. We demonstrate below that the eight parameters of the face-on, circular model can be well constrained by

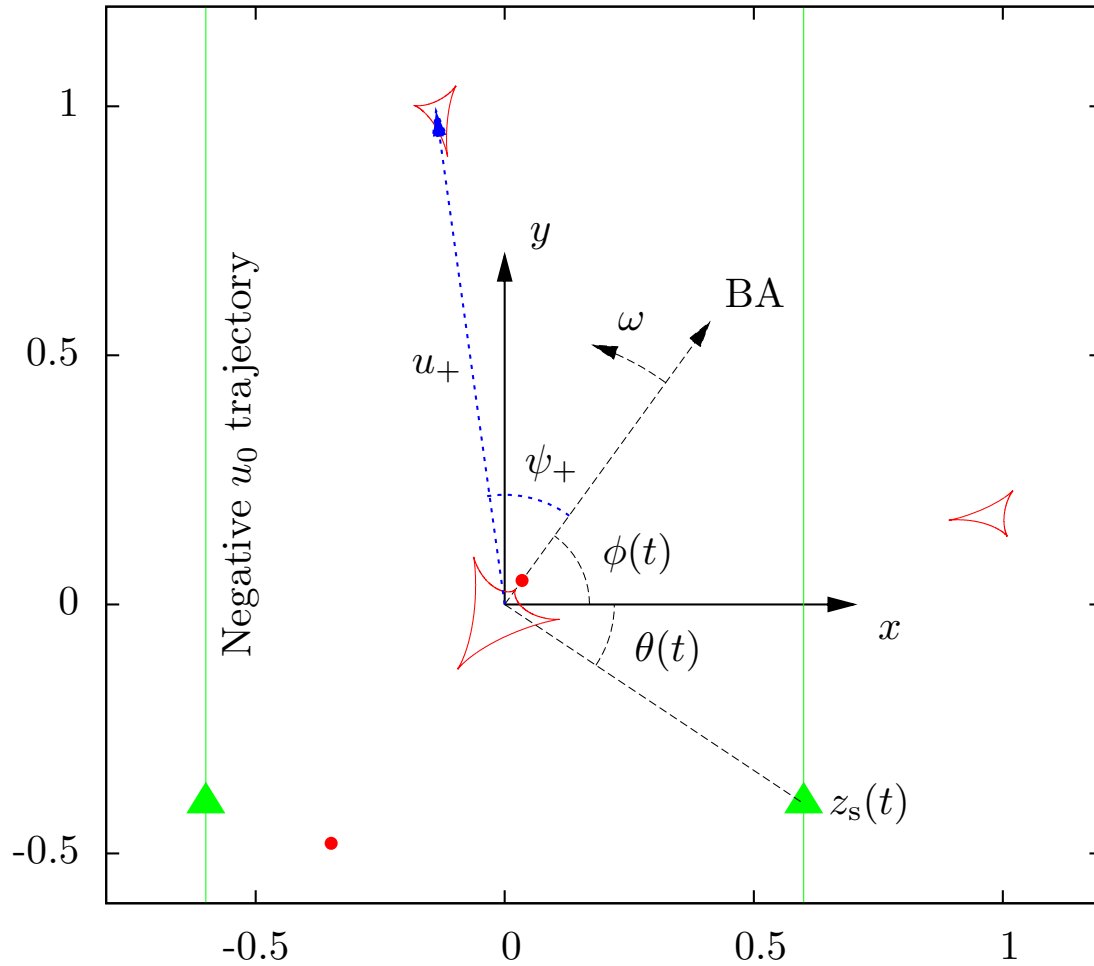


Figure 4.10 – Parametrization of the RRL. Caustics are shown as solid red lines, the lens positions as red circles, with the primary lens in the positive quadrant, and the source trajectory as a solid green line at positive x . The green line at negative x shows the trajectory of a source with negative u_0 (see text for more details). The binary axis (BA), which subtends an angle $\phi(t)$ relative to the fixed x -axis, rotates at a frequency $\omega = 2\pi/T$. (u_+, ψ_+) is the position of one of the secondary caustics in polar coordinates that rotate with the binary axis; similarly, the other caustic is at (u_-, ψ_-) . The blue dotted line shows the Bozza (2000b) approximation to the position of the centre of the secondary caustic (Equation 4.14) for this lens. The lens has the parameters $s = 0.65$ and $q = 0.1$, and lengths are in units of the Einstein radius.

the lightcurve and parameters can effectively be ‘read off’ the lightcurve with only a small amount of algebraic manipulation. It should be possible to use these parameter estimates in a more detailed modelling analysis, either using the face-on, circular model (which will be well constrained should the face-on, circular orbit approximation apply), or as partial constraints for a full Keplerian model. This analysis, which we describe briefly later, can significantly reduce the range of parameters it is necessary to search in order to find the best-fitting event model. In Section 4.6.3 we briefly discuss the effects of orbital inclination and eccentricity on the lightcurves and detectability of RRLs, and in Section 4.6.4 we discuss the effect of parallax on an RRL lightcurve.

We choose a coordinate system fixed with respect to the sky, with its origin the lens centre of mass. As such, the lens components are not fixed. For convenience, we recast the angle $\alpha \rightarrow \phi_0$, where ϕ_0 is the angle subtended by the primary mass relative to the x -axis at time t_0 and we fix the angle of the source trajectory such that the source travels parallel to the y -axis. At time t the source is at the (complex) position

$$z_s(t) = \left(u_0, \frac{t - t_0}{t_E} \right), \quad (4.8)$$

and subtends the angle

$$\theta(t) = \arctan \left(\frac{t - t_0}{u_0 t_E} \right), \quad (4.9)$$

with respect to the x -axis. Similarly, the binary axis, which we define as the line extending from the centre of mass through the primary mass, subtends an angle

$$\phi(t) = \frac{2\pi}{T}(t - t_0) + \phi_0, \quad (4.10)$$

with respect to the x -axis. This parametrization is shown in Figure 4.10. The parametrization differs from that recently proposed by Skowron et al. (2011) for orbiting-binary lenses, which is best suited for binaries with orbits much longer than the microlensing timescale. The Skowron et al. (2011) parametrization is expressed in terms of the 3-dimensional position and velocity of one lens component, as the on-sky position components will be well constrained. The on-sky velocity components may be well constrained and the radial position and velocity are likely to be poorly or not

constrained. However, as we will show, for an RRL it is the orbital period and phase angles that will be well constrained, so it is better to couch the problem in terms of these quantities.

Many of the features in a close-binary-lens magnification pattern are radial, or approximately so. This makes them ideal for measuring the rotation rate of the lens. A feature occurs on the lightcurve when a magnification-pattern feature sweeps over the source. A radial feature that subtends the angle ψ_f relative to the binary axis will occur on the lightcurve when

$$\theta(t) = \phi(t) + \psi_f. \quad (4.11)$$

By solving this equation we can use the timing of repeated features to easily obtain approximate measurements of some of the lens parameters. This means that many of the lens parameters can be ‘read-off’ the lightcurve and it is possible to build an approximate model of the lens quickly, without complex analysis. For such estimations, the most important magnification map features are:

- the magnification arms (shown in Figure 4.1, which extend from the central caustic to the secondary caustics),
- a planetary demagnification (a region of demagnification relative to the single lens) that lies between the secondary caustics, with its minimum lying along the binary axis.

The planetary demagnification feature is only present for lenses with small mass ratios $q \lesssim 0.3$. Both features are complementary, as in equal-mass-ratio binaries the planetary demagnification does not occur, but the magnification arms are strong and very close to radial, while in low-mass-ratio binaries the magnification arms are weaker and less radial, but the demagnification region is strong and always lies at $\psi_f = \pi$.

Figure 4.11 shows a lightcurve where features repeat strongly five times. The first step to estimating RRL parameters is to fit the lightcurve with a Paczyński curve. This is a relatively trivial task and most RRL lightcurves will approximate a Paczyński curve

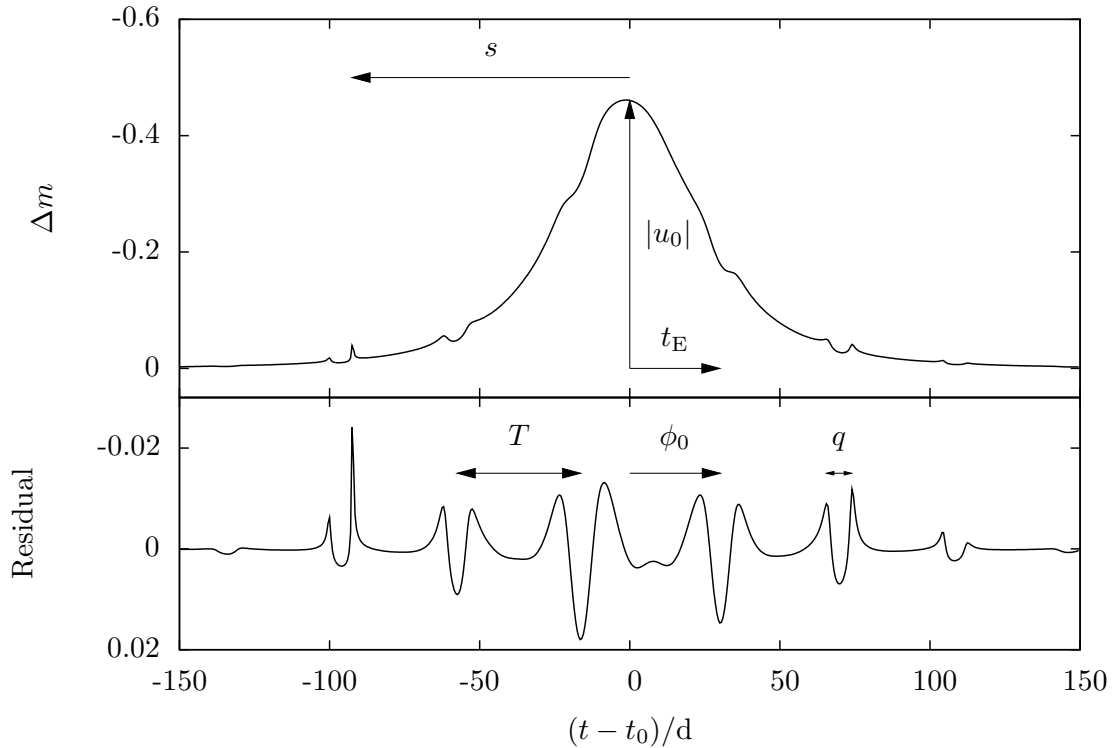


Figure 4.11 – An example lightcurve of an RRL showing how lightcurve features relate to the parameters of the lens. The lens has parameters $t_E = 30$ d, $T = 38$ d, $s = 0.3$, $q = 0.1$, $u_0 = 0.8$, $\phi_0 = 2.14$.

with only small deviations. This fit allows an accurate estimation of the parameters t_0 , t_E and $|u_0|$, the last down to an ambiguity in sign, which corresponds to the source moving upwards and passing the lens centre on its left (positive u_0) or right (negative u_0), having imposed the convention that the lens always rotates anti-clockwise. This Paczyński model completely describes the source trajectory and hence defines the left hand side of Equation 4.11. The orbital period can now be estimated by timing two occurrences of the same magnification-pattern feature. The period is not simply the time elapsed between two features because the source moves during this time. Instead, by solving Equation 4.11 we can find the relation between the period T and the time of two consecutive occurrences of the same magnification-pattern feature at times t_1 and

t_2

$$T = \frac{2\pi}{2\pi + [\theta(t_2) - \theta(t_1)]} (t_2 - t_1), \quad (4.12)$$

where the fraction is the number of orbits the source completes between the two source encounters. The degeneracy in the measurement of the sign of u_0 affects this equation, due to the presence of the $\theta(t)$ terms, but can be resolved if more than one pair of features is available for estimating T , as only one value of u_0 will give consistent estimates of T for different feature pairs.

With an estimate of the period, if we know the angle subtended by a feature on the magnification map ψ_f , we can also estimate the phase angle ϕ_0 , again taking into account the source motion

$$\phi_0 = \theta(t_f) - \psi_f - \frac{2\pi}{T}(t_f - t_0). \quad (4.13)$$

The planetary demagnification region has $\psi_f = 0$, which makes this task simple. However, the demagnification may not be obvious or, if the mass ratio of the lens is high, may not be present. In these cases it is necessary to know ψ_f for the magnification arms. Knowing that they extend from the central caustic (roughly at the centre of mass) to the secondary caustics, we need only know the position of the secondary caustics to estimate ψ_f . Bozza (2000b) has derived analytical approximations for the position and shape of secondary caustics in close lenses with $s \ll 1$, using a series expansion of the Jacobian. He finds that the secondary caustics are located at

$$z_{\pm} \simeq \frac{1}{s(1+q)} \begin{bmatrix} (1-q)(1-s^2) \\ \pm \sqrt{q}(2-s^2) \end{bmatrix}, \quad (4.14)$$

in the static centre-of-mass system. Figure 4.10 shows that this expression is reasonable even when s is quite large. If we assume the magnification arms are radial, we can use Equation 4.14 to approximate the angle of the magnification arms, to second order in s , as

$$\psi_{\pm} \simeq \arctan \left[\frac{\pm \sqrt{q}(2+s^2)}{1-q} \right], \quad (4.15)$$

which is relatively insensitive to the lens separation s . It is useful to note the asymptotic behaviour: $\psi_{\pm} \simeq \pm 2q^{1/2}$ as $q \rightarrow 0$ and $\psi_{\pm} \rightarrow \pm\pi$ as $q \rightarrow 1$. While the dependence of ψ_{\pm}

on q implies an ambiguity in the estimation of ϕ_0 , the corollary is that we can estimate the mass ratio from the timing of features as well. Using the times of consecutive magnification-arm crossings, t_+ and t_- , we have

$$|\psi_{\pm}| = \frac{1}{2} \left| \theta(t_-) - \theta(t_+) - \frac{2\pi}{T} (t_- - t_+) \right|. \quad (4.16)$$

This value can be substituted into Equation 4.13 and Equation 4.15 can then be solved for q .

The remaining parameter that we are interested in is the lens separation s . The angle of features is essentially independent of s , so it is not possible to estimate s by timing features. However, by noting that the magnification pattern becomes essentially featureless beyond the secondary caustics (see Figure 4.1), and that the position of the caustics does depend on s , it is possible to estimate s from the lightcurve. Unfortunately the secondary caustics are very small, and in most events they will not pass directly over the source, so the estimate will not be very accurate. The best estimate of the position of the caustic will be derived from the largest peak due to a magnification arm in the wings of the lightcurve (e.g., the peak at $t \approx -90$ d in Figure 4.11). This will occur when the radial source position approximately coincides with the radial caustic position, so that $|z_s|^2 \approx |z_{\pm}|^2$. Using Equation 4.2, to first order, we can write

$$s \approx \left[u_0^2 + \left(\frac{t_c - t_0}{t_E} \right)^2 \right]^{-1/2}, \quad (4.17)$$

where t_c is the time of the peak due to the caustic.

We have outlined how the parameters of an RRL can be estimated from pairs of feature timings in the case of the simplest RRL. However, in a given event there may be many repetitions and better parameter estimates can be obtained by considering all the lightcurve features simultaneously. For a given magnification pattern and source trajectory it is possible to compute a timing model by finding all possible solutions of Equation 4.11, $\theta(t) = \phi(t) + \psi_f$ for each feature. By extracting the occurrence time of all the lightcurve features it is possible to fit timing models to this timing data. It is also possible to add additional features to this timing model, such as the effects of

inclination and eccentricity by modifying the function $\phi(t)$, or microlensing parallax by modifying $\theta(t)$. This modelling may be significantly faster than a full lightcurve-fitting analysis, especially when additional effects are included, as there is no need to calculate finite-source magnifications. While it will not fully remove the need for lightcurve fitting, it will significantly narrow down the range of parameters over which lightcurve fitting has to search.

4.5 Measuring RRL masses

We have shown that it is possible to estimate the parameters of an RRL lightcurve, but what we would really like is to be able to measure the physical parameters of the lens, most importantly the lens mass and the binary separation in physical units. Compared to a static-binary lens, we have one additional piece of information with which to infer M and a : the orbital period. Dominik (1998b) has shown that by combining the orbital period T and the lens separation s , it is possible to write down a mass-distance relation

$$M = \frac{T^4}{C^6 s^6 x^3 (1-x)^3 D_s^3}, \quad (4.18)$$

which relates the mass to the lens distance through known quantities, assuming the source distance is known from its colour and magnitude; the constant

$C = 2.85 M_\odot^{-1/2} \text{ AU kpc}^{-1/2}$ when the period is measured in years and the source distance in kpc. As we will demonstrate in Section 4.6.3, it is likely that if the orbit is inclined it will be possible to measure the inclination and account for projection, so that the value of s that is measured can be used to obtain a good approximation of a/r_E . This means that as Equation 4.18 has a minimum at $x = 0.5$, we can place a firm lower limit on the mass of the lens, and an upper limit on the semi-major axis.

To improve on the mass-distance relation, an additional piece of information is needed to break the degeneracy. This can be obtained by measuring $\pi_E = \text{AU}(1-x)/r_E$, the microlensing parallax (Gould 1992), or by measuring $\theta_E = r_E/D_1$, the angular Einstein radius, through detection of finite-source effects (Gould 1994b; Nemiroff and

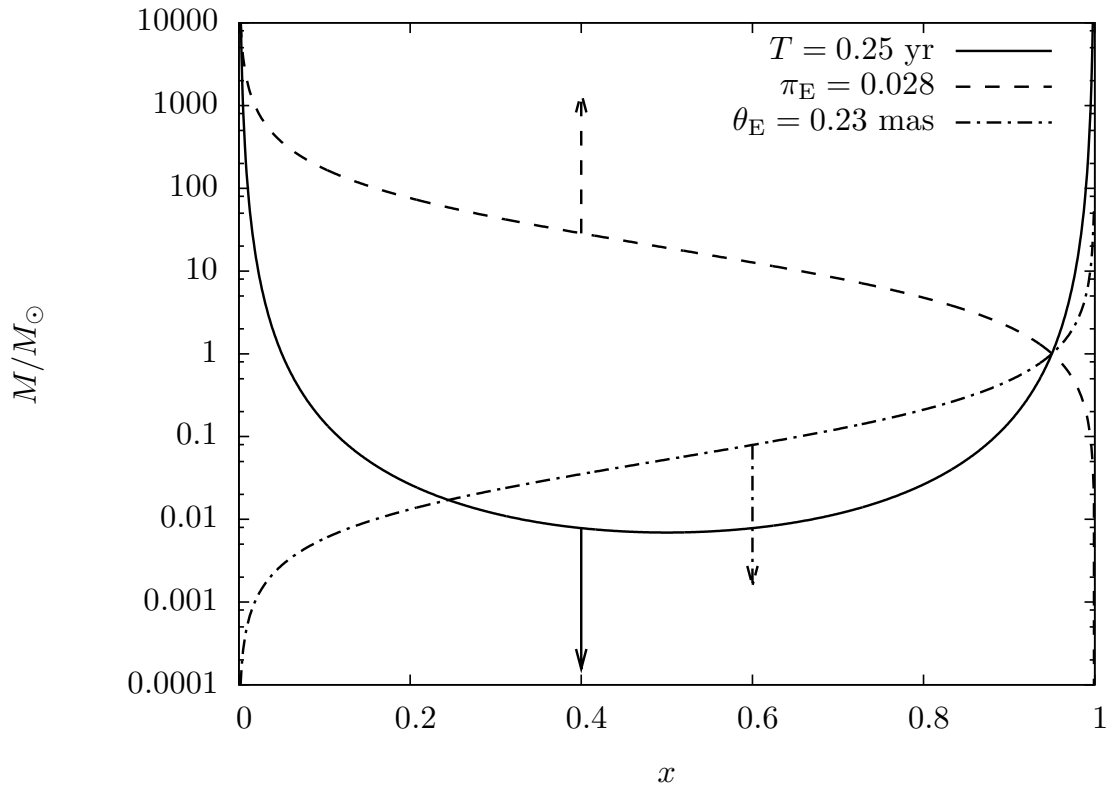


Figure 4.12 – Plot of the various mass-distance relations for the event shown in Figure 4.11, labelled by the parameter measurement that would allow their definition. The arrows point into the region that is *allowed* should only an upper limit on T , π_E or θ_E be available. If the period T is measured along with only one of π_E or θ_E , the mass and distance to the lens can not be determined uniquely, but even a relatively weak upper limit on the other parameter may be sufficient to rule out one possible solution; note however that a lack of finite-source effects places a lower limit on θ_E .

Wickramasinghe 1994; Witt and Mao 1994), or direct detection of the lens once it has separated from the source (Alcock et al. 2001a; Bennett et al. 2006, 2007; Kozłowski et al. 2007). Measurement of either π_E or θ_E allows a second mass-distance relation to be written, for π_E (Gould 1992)

$$M = \frac{\text{AU}^2(1-x)}{C^2 x D_s \pi_E^2}, \quad (4.19)$$

or similarly for θ_E (Gould 1994b; Nemiroff and Wickramasinghe 1994)

$$M = \frac{\theta_E^2 x D_s}{C^2(1-x)}, \quad (4.20)$$

if θ_E is measured in units of mas. One of these relations can then be combined with Equation 4.18 to yield two possible solutions to the mass and distance. This can be seen in Figure 4.12, which plots the mass-distance relations for the event shown in Figure 4.11.² The π_E - and θ_E -lines cross the T -line in two places: once at the true parameter values $x = 0.95$, $M = 1M_\odot$, and once at other values of M and x which are different for each relation. With a measurement of only one of π_E or θ_E it is not possible to uniquely determine the mass and the distance. This is likely to be the case, as finite-source effects are most likely in lenses close to the source, while parallax is most likely in lenses close to the observer. However, even a crude limit on the unmeasured parameter may be enough to rule out one possible solution, e.g., an upper limit on π_E from the lack of parallax effects may allow the solution with smaller x to be ruled out, or a lower limit on θ_E from the lack of finite-source effects may allow the solution with larger x to be ruled out. Direct detection of the lens may require a very long time baseline as RRL features are most detectable in events with low lens-source proper motions. However, RRLs are more likely to be more massive than the average lens (and therefore brighter) and the diffraction limit of 30–40-m class telescopes, such as the Thirty Metre Telescope (TMT),³ the Giant Magellan Telescope (GMT),⁴ or the European Extremely Large Telescope (E-ELT),⁵ may be sufficient to resolve the lens and source in a reasonable time.

²Note that parallax or finite-source effects were not included in the model used to plot the lightcurve.

³<http://www.tmt.org>

⁴<http://www.gmto.org>

⁵<http://www.eso.org/public/teles-instr/e-elt.html>

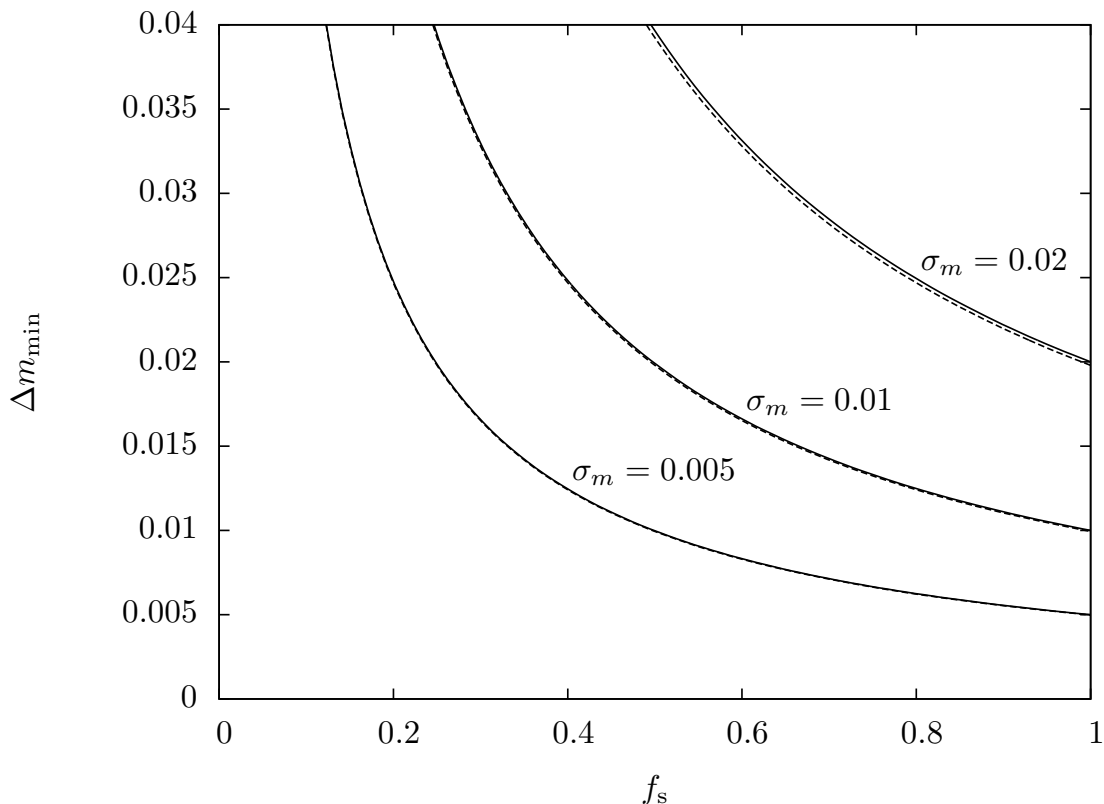


Figure 4.13 – The effect of blending on the photometric detection threshold. The effective threshold Δm_{\min} is plotted against the ratio of source to total blend flux f_s for three values of photometric precision σ_m . The solid lines show the exact value, whereas the dashed line shows the approximation for small σ_m .

4.6 Additional factors affecting RRL detectability

In the preceding sections we have mentioned a number of additional effects that can affect the form of an RRL lightcurve and its detectability. In this section we briefly outline the most important effects and the impact they have on RRL lightcurves and detectability.

4.6.1 Blending

For a given photometric precision σ_m magnitudes, the effective threshold at the event baseline is

$$\Delta m_{\min} = 2.5 \log \left(10^{0.4\sigma_m} - 1 + f_s \right) - 2.5 \log f_s \quad (4.21)$$

$$\simeq 2.5 \log \left(1 + 0.92 \frac{\sigma_m}{f_s} \right), \quad (4.22)$$

where the approximation applies for small σ_m and f_s is the fraction of the total light at baseline contributed by the unlensed source. Figure 4.13 shows this for various values of the photometric threshold. It is clear that only with the most accurate photometry will it be possible to detect RRL features when the blend contributes most of the flux; for less accurate photometry, $\sigma_m \approx 0.02$, even a small amount of blending will significantly affect the detectability of features. The effect of blending decreases as the magnification increases, but we wish to see features over the entire lightcurve and only a small region of the lightcurve will be magnified enough to significantly reduce the effect of blending.

4.6.2 Finite-source effects

Figure 4.14 shows the lightcurve of an RRL lensing a giant source of radius $100R_\odot$, in comparison to the same RRL lensing a point source. The effect of the finite source on the lightcurve is clear, causing a wider, lower peak magnification. Whilst the lens centre of mass transits the source, there is effectively no deviation from the finite-source point-lens lightcurve, except for spikes in the residual at $t \approx \pm 20$ d which are characteristic of a large source crossing a small central caustic (Dong et al. 2009a; Han 2009a). In the wings of the lightcurve there is very little difference between the finite- and point-source lightcurves and most of the features in the residuals have the same amplitude. Only when the source is very close to the secondary caustic is there any deviation from the point-source lightcurve in the wings. The left inset of Figure 4.14 shows that the peak in the finite-source lightcurve at $t \approx -210$ d is slightly broader

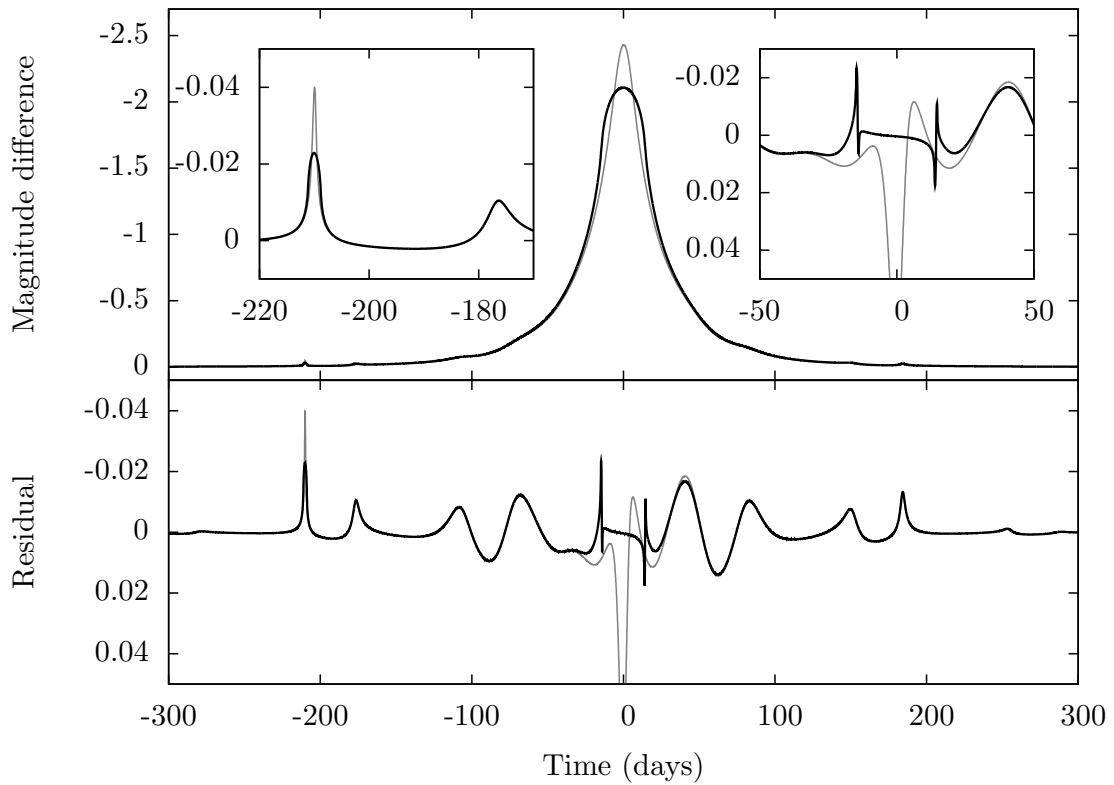


Figure 4.14 – The lightcurve of an RRL lensing a finite source of radius $100R_{\odot}$ (black) compared to the lightcurve of the same RRL lensing a point source (grey). The inset figures show in more detail the residuals when the source is close to the secondary caustic (on the left) and the central caustic (on the right). The lens has a mass $M = 0.8M_{\odot}$, semimajor axis $a = 0.4$ AU, mass ratio $q = 0.3$, fractional lens distance $x = 0.95$, source distance $D_s = 8$ kpc, source velocity $v_t = 50$ km s $^{-1}$, impact parameter $u_0 = 0.1$ and phase angle $\phi_0 = \pi/4$. The ratio of source to Einstein angular radii $\rho_* = \theta_s/\theta_E = 0.28$ is very large. The effects of finite sources are only significant when the source is near the central or secondary caustics.

and about half the amplitude of the point-source lightcurve. Interestingly, this peak, although broadened by the finite-source, is still much narrower than the source crossing time, which determines the width of the central peak. Its width is instead determined by the time taken for the secondary caustic to cross a source diameter.

The example we have shown is very extreme, with a very large source, very close to the lens, and even then the finite-source effects only render binary features undetectable

over a relatively small fraction of the lightcurve. A typical giant source star will be up to a factor of ten smaller, so the part of the lightcurve severely affected by finite-source effects will be correspondingly smaller. As the source has to be transited by the lens centre for finite-source effects to become apparent at the lightcurve peak, the probability of this occurring is also reduced by the same factor. This means that finite-source effects will not affect the detectability of repeating features very much. If finite-source effects are detected in an event, the measurement of the source radius, combined with a measurement of the lens period can be used together to measure the lens mass to a two fold degeneracy (Dominik 1998b).

4.6.3 Inclination and eccentricity

Inclination and eccentricity of the lens orbit will act to make the magnification-pattern motion much more complicated, as changes in the projected lens separation cause the caustics to move and change shape (see, e.g., Figures 3.19 and 3.20). The effects are too complicated to investigate in detail here, but it is worth considering them in brief. For a lens with a given semimajor axis, inclining the orbit should reduce the detectability of features over part of the orbit, as s decreases. Figure 4.15 shows the effect of inclination on the lightcurve of an RRL. It shows that inclination tends to decrease the amplitude of features but does not completely wipe them out, even when the inclination $i = 90^\circ$. In this extreme case, rather than rotating, the secondary caustics move along diagonal lines as the projected separation of the lenses changes, but their angle does not (except for flips by π every half period). Inclination significantly changes the morphology of the lightcurve and can also change the timing of peaks (see, e.g., those at $t \approx -300$ d), which implies that it may be possible to measure the inclination of the lens orbit from the lightcurve.

In contrast to inclination, eccentricity may increase the detectability of features. For a given semimajor axis, eccentricity can both increase and decrease the projected separation. However, Kepler's second law implies that the lens will spend longer at

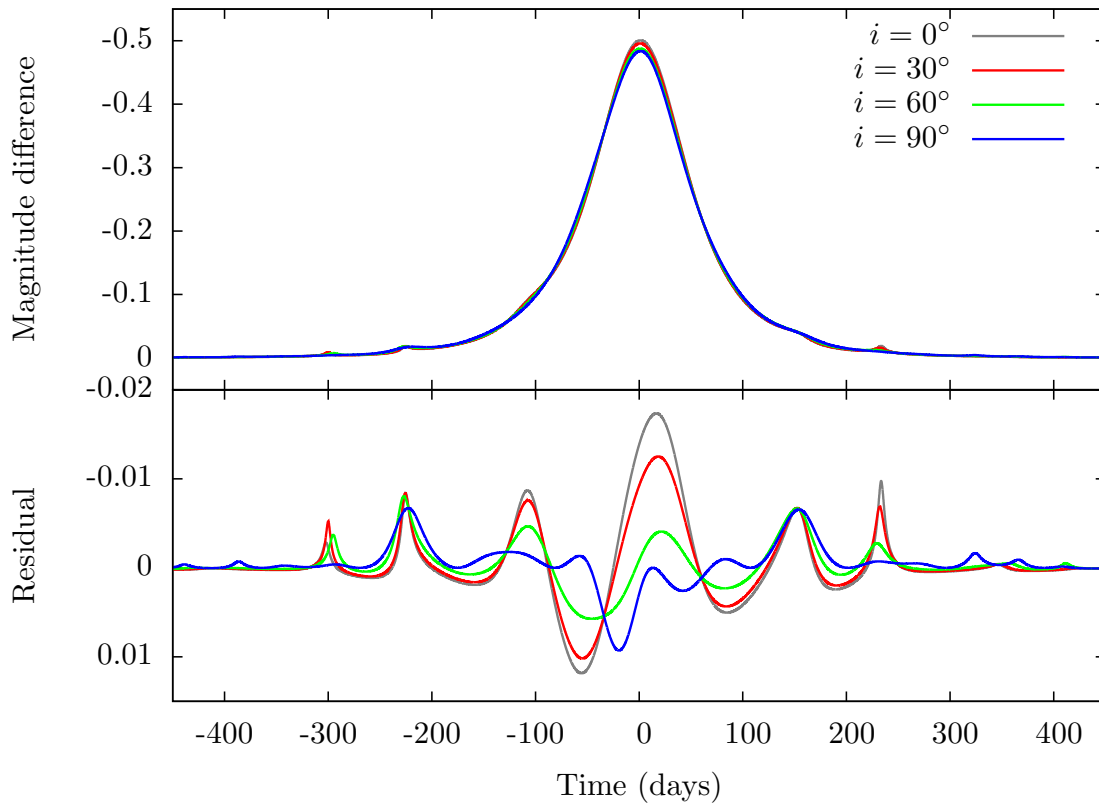


Figure 4.15 – The lightcurves of RRLs with different orbital inclinations relative to the line of sight. For each lightcurve, the lens has mass $M = 0.58M_\odot$, semimajor axis $a = 0.54$ AU, mass ratio $q = 0.52$, fractional lens distance $x = 0.86$, source distance $D_s = 9.5$ kpc, source velocity $v_t = 61$ km s $^{-1}$, impact parameter $u_0 = 0.77$, phase angle $\phi_0 = 4.3$ measured in the plane of the orbit. The orbit was circular, and inclined about the x -axis as defined in Figure 4.10.

larger projected separations (assuming no inclination). As with inclination, eccentricity will also change the lightcurve morphology and timing of features, so it may also be possible to measure the eccentricity of the lens from the lightcurve. Simultaneously including the effects of inclination and eccentricity in the modelling of an RRL event will likely be difficult, as together they require an additional four parameters over the standard RRL parametrization. However, as the angle of magnification-pattern features does not depend strongly on the projected separation, it will be possible to include inclination and eccentricity in the timing analysis proposed in Section 4.4. This may significantly ease the analysis by narrowing down the search space to the range of

parameters compatible with timing measurements.

4.6.4 Parallax

Parallax effects due to the motion of the Earth about the Sun will cause the source to appear to take a curved path through the plane of the sky and will affect the lightcurve of an RRL event. If the magnitude of the parallax effect is small then it will cause only small perturbations to the shape of the lightcurve and the timing of features. Larger effects may cause significant changes to the RRL lightcurve, significantly changing the timing of features, and possibly making them appear less periodic, or adding a stronger annual periodicity to the lightcurve. However, while parallax may significantly complicate the interpretation of an RRL event, it does not affect the magnification map and the detectability of RRL features should remain the same. Moreover, the detection of parallax in an RRL event will allow the lens mass to be measured, at least to a two-fold degeneracy (see Section 4.4). Due to the photometric accuracy required to detect RRLs and the long timescales of the events, the probability of detecting parallax along with RRL features is significant (Buchalter and Kamionkowski 1997).

4.7 Discussion and conclusion

Although the phenomena of microlensing by lenses with rapid orbital motion has been discussed previously in the literature (Dominik 1998b; Zheng and Gould 2000; Dubath et al. 2007), no work so far has properly treated all the factors required to estimate a realistic event rate. In this chapter, we have outlined the theory of RRLs and used it to estimate the range of parameters over which they are detectable and the rate at which they are expected to be observed. We find that RRLs with masses and orbital radii typical of binary stars are detectable and that there is a reasonable chance that they will be detected, either in current microlensing data sets or in ongoing or near-future microlensing surveys.

In calculating these rates we have actually used the relatively stringent criteria of requiring that two or more lightcurve features from the same orbital phase are detected in the lightcurve. If we relax this repetition requirement somewhat, to include lenses that display significant signs of orbital motion (say several degrees rotation per t_E), the event rate will increase significantly, as lenses can then have larger orbits and hence stronger lightcurve features. In the previous chapter we have shown that orbital motion is detectable in a large fraction (~ 15 percent, see Figure 3.11) of binary lenses with detectable binary-lensing features and orbital periods comparable to the microlensing timescale.

We have detailed how the features of an RRL lightcurve can be used to measure its period and potentially measure its mass. Even if features do not repeat, if several features are detectable in the lightcurves of binary-lens events then the techniques we have outlined for timing features and extracting parameter estimates may be of some use in their analysis. Without repeating features, the orbital period may not be constrained as accurately, but it should be possible to place constraints on the lens mass and orbit in many cases.

So far we have neglected to discuss the prospects for positively identifying RRL events from other events which may mimic their features. Periodic features may also be induced by orbital motion in the observer and source planes, or intrinsic variability in the source or a blend star. In the observer plane, the period of orbital parallax effects is well defined and unless the lens has an orbital period similar to 1 yr, it is unlikely the effects will be confused. Even if the orbital period is close to one year, the shape of features in the lightcurve are likely to be different. Orbital effects in the source plane may be more difficult to exclude as the period is not fixed. If there is only a single luminous source (the xallarap case, Paczyński 1997; Han and Gould 1997; Rahvar and Dominik 2009), a timing analysis similar to the one we proposed for the lens can be performed for the source. This analysis should be somewhat easier and more precise for xallarap as there are no complicated features in the magnification pattern. If this timing analysis is insufficient to separate the two cases then the shape of lightcurve

features may differentiate the two interpretations. In the case where both sources are luminous, the lightcurve can take a more complicated shape, which may more closely resemble that of an RRL (e.g., Cherepashchuk et al. 1995; Han and Gould 1997). Even in this case, timing analysis for maxima and minima of the lightcurve should be easier than for RRLs, and full lightcurve modelling starting from timing analysis solutions will likely be able to differentiate the two scenarios. Finally, variability of the source or a blend may also produce similar lightcurve features. If this variability is detectable at baseline, then as long as the baseline is long enough the RRL scenario need not be considered (Wyrzykowski et al. 2006).

It is worth noting that we should naively expect the rate of RRL/significant lens orbital motion events to be similar to the rate of binary-source orbital motion events. This is because the factors that govern their occurrence, such as the ratio of orbital separation to the Einstein ring and the ratio of orbital to microlensing timescales, will have similar distributions in the lens and source populations. Similarly, we would expect the rate of parallax events to be roughly ten times greater than the rate of RRL events with orbital periods ~ 1 yr, as the binary fraction is ~ 0.1 while the observer is always orbiting. It is worth comparing this with the number of reported single-lens parallax events, ~ 20 – 50 (e.g., Poindexter et al. 2005; Smith et al. 2005, and references therein), while ~ 10 events have been successfully fitted with xallarap models (Smith et al. 2003; Poindexter et al. 2005). In contrast, only one binary-lens event has shown significant rotation, MACHO-97-BLG-41 (Albrow et al. 2000). In this event, the lens rotates at $\sim 4^\circ$ per t_E (a low rotation rate compared to RRLs), which is detected thanks to the source crossing the central and one secondary caustic, as opposed to the smaller, smoother, more continuous features of RRLs. It is possible therefore that many events with significant rotational orbital motion signatures have not been modelled or have been interpreted as xallarap events. Thus it is important that any event that is modelled with xallarap also be tested with an orbiting binary-lens model.

5

The Manchester-Besançon microLensing Simulator and its application to the *Euclid* mission¹

5.1 Introduction

In this chapter we return to the central theme of the thesis: simulations. With the recent selection of *Euclid* by ESA (Laureijs et al. 2011) and the top prioritization of *WFIRST* by the “New Worlds, New Horizons” report (Blandford et al. 2010), there is a significant chance that a space-based planetary microlensing survey may be undertaken at the end of the decade. This has produced renewed interest in microlensing simulations, which will be used to optimize any survey before it is launched. This chapter describes the development of a new microlensing simulator, *MaB μ LS*. It is the first simulator to combine a population synthesis Galactic model (the Besançon model Robin et al. 2003) with a comprehensive treatment of multi-band imaging photometry. As a preliminary test of the simulator we apply it to a simulation of the *Euclid* mission.

¹Part of the work presented in this chapter will be submitted for publication as M. T. Penny, E. Kerins, N. J. Rattenbury, J.-P. Beaulieu, A. C. Robin and S. Mao, to be submitted.

We begin the chapter by reviewing the current theories of planet formation and evolution, and how microlensing can be used to test these. We recap the theory of planetary microlensing, discuss how microlensing surveys can be performed from space and introduce the *Euclid* mission. In Section 5.2 we describe the simulator, outlining the major features and explaining some of the design choices. In this section we also describe the Besançon Galactic model, which is used by the simulator. In Section 5.3 we describe the results of the preliminary *Euclid* simulation, before ending with a discussion in Section 5.4.

5.1.1 Planet formation and evolution

The burgeoning list of known exoplanets is revealing huge diversity in the properties and structure of exoplanetary systems. The formation and evolution of planetary systems is still an open question and an area of significant ongoing research. Presently, two formation models are considered plausible: core accretion and disc instability (see D’Angelo et al. 2011, for a review).

In the core accretion scenario (Safronov 1969; Mizuno 1980; Lissauer 1987), planets form out of a thick disc of gas and dust by the gradual build-up of material from dust grains into larger and larger objects through collisions. Once the objects become large enough, they begin to accrete first dust, and then gas, via gravity, a runaway process as the accretion rate increases with mass. Planet growth is halted by the protoplanet clearing its area of the disc or through competition with neighbouring planets (Pollack et al. 1996). Although at the end of the process planet formation is rapid, the initial stages of planet growth are slow, and the whole process takes of the order of a few Myr, with an upper limit imposed by the lifetime of the disc (Pollack et al. 1996). In the core accretion model, terrestrial planets (such as Earth and Mars) can be considered as the cores of planets that fail to reach the mass required for runaway gas accretion, either due to their location in the disc or the influence of other planets nearby that grow more rapidly. The core accretion process is most efficient in a region of enhanced disc den-

sity where water and other hydrogen compounds condense to form ice (Morfill 1985; Stevenson and Lunine 1988). This region (the so-called ice- or snow-line) lies at orbital radii ~ 2 AU and is thought to be where most planets form. This is at the distance that microlensing surveys are most sensitive to planets (see Chapter 1 and Section 5.1.2).

In contrast, in the disc instability model (Kuiper 1951; Cameron 1978; Boss 1997), giant planets form through a gravitational instability in a gaseous disc. Such an instability can cause fragmentation of the disc into clumps, which can collapse under gravity in a rapid process taking ~ 1000 yr. Stellar irradiation and other factors are thought to prevent the growth of instabilities at orbital radii less than a few tens of AU, limiting the effectiveness of disc instabilities to form planets at these distances (see, e.g., D'Angelo et al. 2011). Beyond this, it is likely that disc instability is the only mechanism by which giant planets can form (Boss 2011). In this model, terrestrial planets are still thought to form through a process similar to core accretion (Boss 2006). Disc instability therefore predicts that, unless giant planets migrate inwards from the far disc, microlensing experiments should detect giant planets at large orbital radii, but only low-mass planets in the region of peak microlensing sensitivity.

From the earliest discoveries of Jupiter-mass planets on close-in orbits around normal stars (Mayor and Queloz 1995; Marcy and Butler 1996) it has been clear that the orbital structure of some, if not all, planetary systems must undergo significant evolution (Lin et al. 1996), either during the formation stages or in subsequent planet-planet interactions. Migration of planets during formation, due to interactions with the disc, can cause both inward (Goldreich and Tremaine 1980; Ward 1997) and outward migration (Masset and Snellgrove 2001). Resonant trapping by giant planets can cause other planets to join in with this migration (Snellgrove et al. 2001). More violent planet-planet interactions can result in planets being scattered inwards (Nagasawa et al. 2008), outwards or even being ejected completely from their systems (Veras et al. 2009). Recent microlensing results on the abundance of isolated planetary-mass objects suggest that more than one Jupiter-mass planet per star is potentially ejected in this way (Sumi et al. 2011).

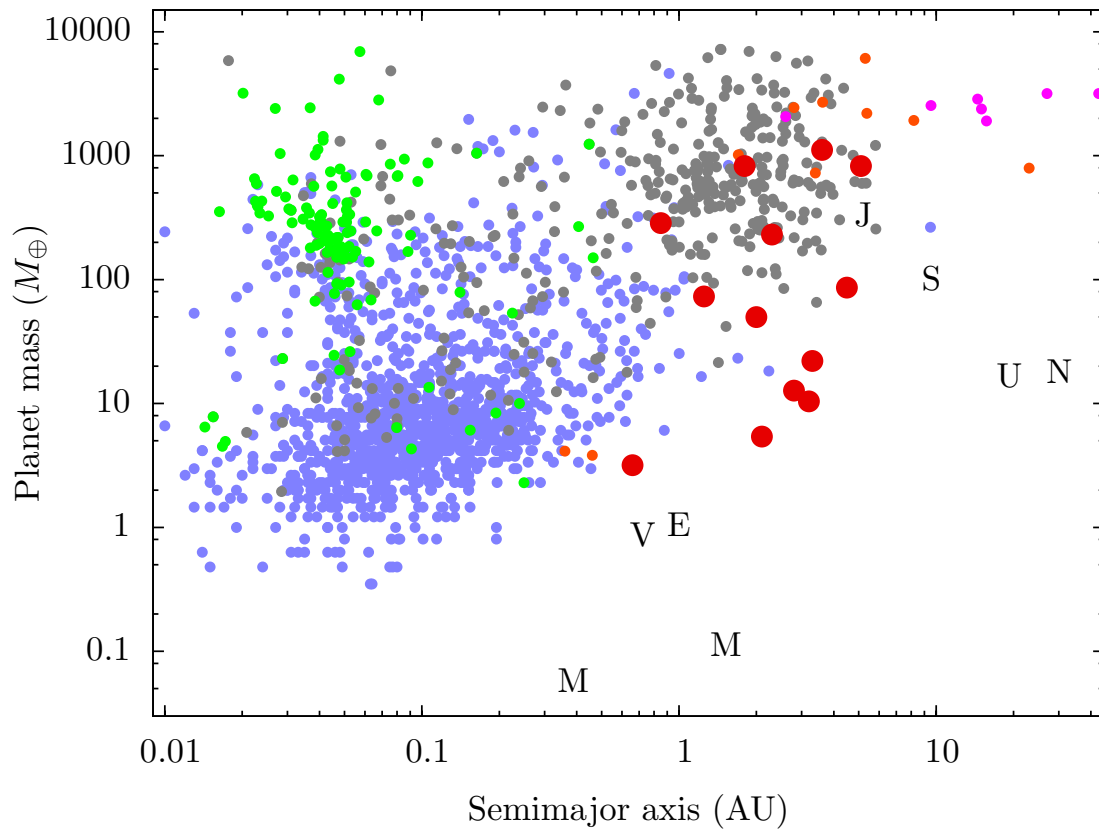


Figure 5.1 – The planet mass–semimajor axis diagram for the known exoplanets (exoplanets.eu as of 17th October 2011, Schneider et al. 2011), together with *Kepler* candidate planets (Borucki et al. 2011), plotted assuming the mass–radius relation used by Lissauer et al. (2011). Some planets have been clipped at smaller and larger semimajor axis. Grey points show planets detected by radial velocities, green by transits, red by microlensing, magenta by direct imaging, orange by timing and light blue points show *Kepler* candidates. Solar System planets are denoted by letters.

The planet mass–semimajor axis diagram

The complex interplay between planet formation and orbital evolution means that the planet mass–semimajor axis diagram (M_p – a diagram, see Figure 5.1 for the plot of the known exoplanets) is a powerful diagnostic for testing planet formation theories (e.g., Ida and Lin 2004; Currie 2009). Planets forming via core accretion will start off at low masses near the centre of the diagram and move upwards as they accrete mass (Mor-

dasini et al. 2009a). Through orbital evolution they will move horizontally on the plot, either smoothly as a result of migration or by discontinuous jumps due to scattering. Similarly, planets formed by disc instability will start at the upper right of the diagram and may move inward through migration or scattering.

While the difference between core-accretion and disc-instability models of planet formation are over the formation mechanism of giant planets, both models will also predict different distributions of low-mass planets. This is because giant planets in the process of formation will consume or disrupt some of the disc material that would otherwise be available to form low-mass planets. Also, giant planets dominate the orbital dynamics of planetary systems, making certain regions of the system dynamically unstable. Low-mass planets are therefore a valuable additional probe of the planet formation progress.

The list of more than 650 known exoplanets (Schneider et al. 2011; Wright et al. 2011) detected through radial velocities (RV), transits, timing, direct imaging and microlensing, together with 1235 candidate planets detected by *Kepler* (Borucki et al. 2011), already shows significant structure in the M_p - a diagram (Udry and Santos 2007). Major features of the diagram are:

- a clump of \sim Jupiter-mass planets at small radii (the so-called hot Jupiters),
- a large population of \sim 10 Earth-mass planets in orbits with semimajor axis $a \approx 0.03$ – 0.5 AU, which could extend further outwards and to lower masses (the so-called hot Neptunes and super Earths, e.g., Mayor et al. 2011),
- a population of giant planets from 1–5 AU,
- a relatively small number of giant planets in large orbits,

as well as several regions between these populations with seemingly fewer planets. It is possible to explain some of these features with either the core accretion model or disc instability model, but currently both models struggle to reproduce all the features of the diagram (e.g., Ida and Lin 2008a; Boss 2011). The region above $a \sim 1$ AU

and below $M_p \sim 50M_\oplus$ is currently inaccessible to RV, transit and direct imaging surveys, and will likely remain so for some time due to the limitations of each survey method. While GAIA astrometry may extend down to $\sim 30M_\oplus$ at ~ 2 AU (Casertano et al. 2008), the only way to detect Earth-mass planets and below at such orbital radii is via microlensing (e.g., Bennett and Rhie 1996).

5.1.2 Planetary microlensing

Microlensing occurs when the light from a distant, background source passes near enough to an intervening mass, the lens, to be deflected by its gravitational field (Einstein 1936). A single lens forms two unresolvable images, on opposite sides of the lens, separated by an angle $\sim 2\theta_E$, where $\theta_E \sim 0.5$ mas is the angular Einstein radius (Liebes 1964). At the distance of the lens, typically $\sim 6\text{--}8$ kpc, this corresponds to a physical Einstein radius r_E , which is of the order of $2\text{--}3$ AU. As the source, lens and observer move, the images move and their magnification changes, resulting in a characteristic lightcurve, which brightens and fades symmetrically over a timescale ~ 20 d (Paczynski 1986). Each of the characteristic scales of a microlensing event (the angular and physical Einstein radii, and the event timescale) scale as the square root of the lensing mass. However, the amplitude of the lightcurve is independent of mass, depending only on the impact parameter u_0 , the closest projected approach between the source and lens in units of θ_E .

Should the lensing object be a star with a planetary system, and if the light from the source star passes near to one of the planets, then the gravitational field of the planet will itself perturb the image and therefore the lightcurve (Mao and Paczyński 1991; Gould and Loeb 1992). The timescale of this perturbation will scale as the square root of the planet mass, lasting typically of the order of a day for Jupiter-mass planets (Gould and Loeb 1992) and of the order of hours for Earth-mass planets (Bennett and Rhie 1996). Similarly, the probability of a perturbation occurring scales roughly as the square root of the planet mass, or more strictly, as the square root of the planet-host

mass ratio q (Gould and Loeb 1992). This shallow sensitivity curve makes microlensing ideal for detecting low-mass planets. The scaling breaks down at \lesssim Mars mass, where finite-source effects begin to wash-out planetary signatures, even for main-sequence source stars (Bennett and Rhie 2002). The sensitivity of microlensing to planets is largest at projected semimajor axis $a_{\perp} \sim r_E \sim 2$ AU, where the microlensing images are most likely to be perturbed (Wambsganss 1997; Griest and Safizadeh 1998), but the sensitivity extends inwards to orbits with $a_{\perp} \sim 0.5$ AU, and outwards to infinity, through sensitivity to free-floating planets (Han et al. 2004; Sumi et al. 2011).

5.1.3 Infrared microlensing from space

Microlensing is a very rare phenomenon. Any given source star is microlensed at most once every $\sim 10^5$ years (Paczynski 1986; Griest 1991) and the probability of a planetary signature in each event is ~ 1 percent (Mao and Paczynski 1991; Gould and Loeb 1992). Therefore, in order to detect a statistically significant sample of planets, it is necessary to monitor $\sim 10^8$ stars with a cadence short enough to characterize planetary perturbations lasting \sim hours (Tytler 1996). Due to its high stellar density and optical depth, the Galactic bulge is the best target. Towards the bulge, extinction is a significant problem in the optical, but from the ground is balanced by an equally problematic sky background in the infrared. From the ground, the extreme stellar crowding and arcsecond-scale seeing, mean that only the giant star population can be properly resolved (Bennett 2004). Therefore, in order to monitor enough source stars, ground-based surveys must regularly observe ~ 100 deg² (Tytler 1996). Current and future ground-based surveys (e.g., MOA-II, OGLE-IV, KMTNet, AST3, see Chapter 2) with wide-field imagers will achieve suitable cadence over a large-enough area to routinely detect large numbers of giant planets (should they exist in sufficient abundance), but will not be able to monitor enough stars at the high-cadence necessary to detect Earth-mass planets at a reasonable rate. For this reason, targeted follow-up of promising microlensing events by large networks of small telescopes is used to achieve high ca-

dence and continuous event coverage (see, e.g., Gould et al. 2010), and push the sensitivity of ground-based microlensing firmly into the super-Earth regime (Beaulieu et al. 2006; Bennett et al. 2008). However, the follow-up networks only have the capacity to observe ~ 100 events per year or less with suitable cadence or coverage (Peale 2003). This is sufficient to probe the mass function down to $\sim 5\text{--}10M_{\oplus}$, and possibly the semi-major axis distribution of planets above $\sim 50M_{\oplus}$, but is unlikely to provide more than isolated detections below these masses (Peale 2003; Bennett 2004; Dominik 2011).

Observations from space are able to overcome many of the problems facing ground-based observers. A space telescope has better resolution due to the lack of atmosphere and also a lower sky background, especially in the infrared. This means that with appropriate instrumentation, a space telescope can resolve main-sequence sources in the bulge and monitor the required $\sim 10^8$ sources over a much smaller area. This in turn allows high-cadence observations on a small number of fields (Bennett and Rhie 2002; Bennett 2004). The fundamental requirements of a space telescope for a microlensing survey are a wide field of view ($\gtrsim 0.5 \text{ deg}^2$), with a small pixel scale. In order to minimize the effect of extinction towards the Galactic bulge, it must observe in the near infrared. The telescope must also have a large enough collecting area to allow high-precision photometry of main-sequence bulge stars in short exposure times. These are almost exactly the same requirements as the type of telescope required to study dark energy via a survey for weak gravitational lensing, baryon acoustic oscillations or supernovae, each of which requires deep, high-resolution near-infrared images over a wide field. Such synergy has long been recognized (Bennett and Rhie 2002).

5.1.4 *Euclid*

Euclid is an ESA M-class mission to investigate the nature of the accelerating universe and dark matter (Laureijs et al. 2011). It will do this through measurements of weak gravitational lensing (the small distortions to high-redshift galaxy images due to gravitational lensing by the intervening mass distribution of the universe) and baryon acous-

tic oscillations (the clustering of galaxies on scales set by the decoupling of baryons and relativistic matter in the early universe). *Euclid* will use a 1.2-m Korsch telescope with a high-resolution optical imager (*VIS*) and a near infrared imaging spectrometer (*NISP*), operating simultaneously to perform a 15 000-deg² wide survey and 40-deg² deep survey over six years to measure galaxy shapes and photometric and spectroscopic redshifts. *VIS* will observe with a wide optical band-pass covering *R*, *I* and *Z*, and *NISP* will have available three infrared filters: *Y*, *J* and *H*. The spacecraft design and survey strategy of *Euclid* means that for two months per year it cannot observe its target fields and must observe within the Galaxy. A planetary microlensing survey can utilize this available time (Beaulieu et al. 2010) and such a survey has been included as an additional science programme in the *Euclid* Definition Study Report (Laureijs et al. 2011, hereafter *Euclid* red book).

Similar to *Euclid* is a proposed American mission, the Wide-Field InfraRed Survey Telescope (*WFIRST*, Green et al. 2011). It too will probe the nature of dark energy, but unlike *Euclid*, a 500-day microlensing survey is one of its primary science objectives.

5.2 The Manchester-Besançon microLensing Simulator (*MaB μ LS*)

We have designed the Manchester-Besançon microLensing Simulator (*MaB μ LS* – pronounced *may-buls*) to perform detailed simulations of multi-component microlensing surveys, involving telescopes on the ground and in space, operating with different observing strategies. Ultimately, we aim to use the simulator to perform the following:

- feasibility studies and figure of merit calculations for proposed microlensing surveys,
- optimization of observing strategies for current and future surveys,
- model-dependent detection efficiency calculations for survey data.

Though in this chapter we only consider planetary microlensing, the simulator is an all-purpose simulator, applicable to any Galactic microlensing phenomena.

MaB μ LS is the first microlensing simulator to use a combination of a population synthesis Galactic model with a realistic treatment of imaging photometry. This means that every aspect of the simulation, including the event rate calculations, blending and photometry are simulated self-consistently. The modular approach that we have taken means that the type of events studied can be ‘switched-out’ easily, probably making *MaB μ LS* the most versatile microlensing simulator developed to date.

As described in Section 2.2, several key ingredients are needed in order to simulate any microlensing survey. A simulator must draw its simulated events from a Galactic model and distributions of the event parameters. It must simulate the observations of the survey, and finally, it must also simulate the detection criteria used to select its sample of events. It is also necessary to make a choice as to the complexity of the microlensing model used to simulate events. For example, is the lens composed of a single mass or multiple components? Are higher-order effects such as parallax and orbital motion included? In the rest of this section we will discuss both how *MaB μ LS* implements each component of the simulation and the choice of parameters we use in the simulation of the *Euclid* microlensing survey. Unless stated otherwise, we have taken the survey parameters from the *Euclid* red book.

5.2.1 The Besançon Galactic model

MaB μ LS has been built with the intention of drawing microlensing events from the Besançon model (Robin and Creze 1986; Robin et al. 2003), a population synthesis model of the Galaxy, though in principle *MaB μ LS* can use any Galactic model that can produce similar outputs to that of the Besançon model.

The Besançon model (Robin and Creze 1986; Robin et al. 2003) is a population synthesis model designed to model Galactic formation, structure and evolution using constraints from observational data such as star counts and kinematics. It contains four

stellar populations, a spheroid (stellar halo), a barred bulge, and thin and thick discs. The stars of each population are formed from gas, assuming a star formation history and initial mass function (IMF). The stars then evolve along evolutionary tracks to reach their present-day state (Haywood et al. 1997). The evolutionary model determines the distribution of stellar parameters, which are converted to colours and magnitudes using stellar atmosphere models. The spatio-kinematic distribution of the disc stars is determined by integration of a self-consistent gravitational model using the Poisson and Boltzmann equations. Finally, the observed colours and magnitudes are determined using a three-dimensional dust model (Marshall et al. 2006). A limited number of model parameters are then optimized to reproduce observed star counts and kinematics. The output of the model is a list of stars with known properties that are selected by colour and magnitude in small fields surrounding a chosen line-of-sight.

The Besançon model is in constant development (e.g., Robin et al. 2011, submitted). In this work we use version 1106 of the Besançon model, though an updated version of the model has been released since. In subsequent models, the properties of the bar (see below) change significantly from those we use here.

The stellar halo

The stellar halo is modelled as being formed by a single burst of star formation at 14 Gyr, with metallicity $[\text{Fe}/\text{H}] = -1.78$. It has a triaxial velocity distribution with dispersions $(\sigma_U, \sigma_V, \sigma_W) = (131, 106, 85) \text{ km s}^{-1}$. Its density is small near the Galactic center and so contributes only marginally to the optical depth and microlensing event rate.

The bulge

The bulge, altered from that used by Kerins et al. (2009), consists of a boxy triaxial distribution, similar to that described by Picaud and Robin (2004), but with a Gaussian density law as opposed to a Freudenreich (1998) sech^2 law (Robin et al. 2011). The

major axis of the triaxial structure lies at an angle of 12.5° relative to the Sun–Galactic centre line of sight and has scale lengths $(X, Y, Z) = (1.63, 0.51, 0.39)$ kpc, where the X direction is parallel to the major axis and the X and Y axes lie in the Galactic plane. This is truncated at a Galactocentric radius of 2.67 kpc. The bulge rotates as a solid body with a speed $40 \text{ km s}^{-1} \text{ kpc}^{-1}$. The velocity dispersions in the bulge along the axes defined above are $(113, 115, 100) \text{ km s}^{-1}$. The central stellar mass density of the bulge, excluding the central black hole and clusters, is $19.6 \times 10^9 M_\odot \text{ kpc}^{-3}$.

Embedded within the bulge is also an elongated bar (Robin et al. 2011). However, in the version of the model we use here, its density is smaller by $\sim 10^{-4}$ times that of the bulge, so we do not describe it further.

The stellar population of the bulge is assumed to form in a single burst 7.9 Gyr ago (Picaud and Robin 2004), following Girardi et al. (2002). The bulge IMF (dN/dM) scales as M^{-1} below $0.7 M_\odot$ and follows a Salpeter slope above this. The population has a mean metallicity $[\text{Fe}/\text{H}] = 0.0$ with dispersion 0.2 and no metallicity gradient. The stellar luminosities are calculated using Padova isochrones (Girardi et al. 2002).

The thick disc

The thick disc is modelled by a single burst of star formation at 11 Gyr. Its properties have been constrained using star counts by Reylé and Robin (2001). The thick disc contributes only marginally to the microlensing event rate, so we do not describe it in detail. Its parameters are described by Robin et al. (2003).

The thin disc

The thin disc is assumed to have an age of 10 Gyr, over which star formation occurs at a constant rate. Stars are formed with a two-slope IMF that scales as a power-law $M^{-1.6}$ below $1 M_\odot$ and M^{-3} above, based on the Hipparchos luminosity function (e.g., Haywood et al. 1997), with updates described by Robin et al. (2003). Stars below $1 M_\odot$ follow the evolutionary tracks of Vandenberg et al. (2006), while those above

follow Schaller et al. (1992) tracks. The thin disc follows an Einasto (1979) density profile with a central hole. The density normalization, kinematics and metallicity distribution of the disc depend on stellar age, with seven age ranges defined, whose parameters are given by Robin et al. (2003). The Solar velocity is $(U_{\odot}, V_{\odot}, W_{\odot}) = (10.3, 6.3, 5.9)$ km s⁻¹, with respect to the local standard of rest $V_{\text{LSR}} = 226$ km s⁻¹. The disc has a scale length 2.36 kpc, and the hole has a scale length 1.31 kpc, except for the youngest disc component which has disc and hole scale lengths of 5 kpc and 3 kpc, respectively. The disc is truncated at 14.0 kpc. The scale height of the disc is computed self-consistently using the Galactic potential via the Boltzmann equation as described by Bienayme et al. (1987). Also modelled in the disc are its warp and flare (Reyl   et al. 2009).

Extinction

Extinction is computed using a three-dimensional dust distribution model of the inner Galaxy ($|\ell| < 100^\circ$, $|b| < 10^\circ$), built by Marshall et al. (2006) from analysis of 2MASS data (Cutri et al. 2003) using the Besan  on model. Marshall et al. (2006) did this by comparing observed, reddened stars to unreddened simulated stars drawn from the Besan  on model. From this the extinction as a function of distance along a given line of sight is computed by minimizing χ^2 between observed and simulated $J - K_s$ colour distributions. The resulting map has a ~ 15 -arcmin resolution in ℓ and b , and a distance resolution ~ 0.1 – 0.5 kpc, resulting from a compromise between angular and distance resolution.

Other components

The Besan  on model also takes account of other Galactic components, including the mass due to the dark matter halo and interstellar medium. The details of these components are given by Robin et al. (2003). White dwarfs are included in the model separately to normal stars, with separate densities and luminosity functions determined

from observational constraints (Robin et al. 2003, and references therein). The evolutionary tracks and atmosphere models of Bergeron et al. (1995) and Chabrier (1999) are used to compute their colours and magnitudes.

Microensing with the Besançon model

Following the method of Kerins et al. (2009), *MaB μ LS* uses two star lists output by the Besançon simulation to construct catalogues of possible microlensing events and calculate their properties. The first list, the source list, is drawn from the Besançon model using a single magnitude cut in the primary observing band of the survey. A second list, the lens list, is drawn from the model without a magnitude cut. Both source and lens lists are truncated at a distance of 15 kpc to improve the statistics of nearer lenses and sources that are much more likely to be lensed/lensing.

Overall microlensing event rates are calculated along multiple lines of sight, with spacings set by the resolution of the Marshall et al. (2006) dust map. The total rate due to each pair of source and lens lists, about the line-of-sight (ℓ, b) , is

$$\Gamma(\ell, b) = \frac{\Omega_{\text{los}}}{\delta\Omega_s} \sum^{\text{Sources}} \left(\frac{1}{\delta\Omega_l} \sum_{D_l < D_s}^{\text{Lenses}} 2\theta_E \mu_{\text{rel}} \right), \quad (5.1)$$

where Ω_{los} is the solid angle covered by a dust-map resolution-element, and $\delta\Omega_s$ and $\delta\Omega_l$ are the solid angles over which the source and lens catalogues are selected, respectively. The rate is calculated over the all possible source-lens pairs to minimize the noise of counting statistics. The inner sum over the lenses is related to the optical depth integral of Equation 2.1, which is a line integral over physical quantities (in this case $r_E v_t$, the product of the physical Einstein radius and the relative lens-source velocity). However, the lens catalogue is selected from a beam and so the quantities must be weighted by a factor $1/D_l^2$ to counteract the increasing volume of an element along the beam; the integrand then becomes $\theta_E \mu_{\text{rel}}$, the angular counterparts of r_E and v_t , where μ_{rel} is the relative lens-source proper motion. The total event rates are then stored for later use.

To simulate microlensing, *MaB μ LS* draws sources and lenses from their respective lists with replacement, requiring the source be more distant than the lens. From the source and lens parameters, the Einstein radius and timescale are computed, as well as the rate weighting assigned to the event

$$\gamma = u_{0\max} \theta_E \mu_{\text{rel}}, \quad (5.2)$$

where $u_{0\max}$ is the maximum impact parameter of the event; how $u_{0\max}$ is determined is discussed in the following sections. Events are simulated and those that pass the detection criteria are flagged. The rate of detections in a given dust-map element is the sum of the weights of detected events normalized to the sum of the rate weightings for all the simulated events – this is essentially a detection efficiency. The detection efficiency is then multiplied by the total line-of-sight rate computed in Equation 5.1 to yield the expected detection rate for $0.25 \times 0.25 \text{ deg}^2$, the size of the dust-map element. These rates are then summed over all the dust-map elements to yield the total simulation event rate.

5.2.2 The microlensing events

MaB μ LS uses user-supplied functions to compute microlensing lightcurves including any effects that the user wants to model. For this work we modelled only planetary lens systems composed of a single planet orbiting a single host star. As we want to investigate the planet detection capability of *Euclid* as a function of planet mass M_p and semimajor axis a , we chose to simulate systems with various fixed values of planetary mass and semimajor axis distributed logarithmically in the range $0.03 < a < 30 \text{ AU}$. We assume a circular planetary orbit that is inclined randomly to the line of sight. The orbital phase at the time of the event is again random; at this stage we do not model the effects of orbital motion in the lens. The impact parameter and angle of the source trajectory are distributed randomly, with the impact parameter in the range $u_0 = 0$ – $u_{0\max}$.

The maximum impact parameter $u_{0\max}$ is chosen such that, if the lens were single, the total flux at the event peak (of the magnified source and any nearby blend) would be at least a factor of 0.0125 larger than the total flux at baseline, regardless of whether such an increase is observable.² So, if the source is heavily blended in the primary band, the minimum peak magnification required is larger, and $u_{0\max}$ consequently smaller. This condition is necessary to ensure that time is not spent simulating microlensing events that would never be detected, but comes at the cost of missing some fraction of planet detections where the primary lensing event would not be seen, but lensing by a planet would be. These missed events would be classified as isolated or free-floating planet detections, which can be simulated separately with *MaB μ LS*. We do not simulate free-floating planets observed by *Euclid* here, but will do so in the near future.

The planetary microlensing lightcurves are computed assuming that the source has a uniform intensity profile (in other words, no limb darkening). The finite-source magnification is computed using the hexadecapole approximation when finite-source effects are small (Pejcha and Heyrovský 2009; Gould 2008) and the contouring method when they are not (Gould and Gaucherel 1997; Dominik 1998a). Finite-source effects are accounted for in single-lens lightcurve calculations using the method of Witt and Mao (1994). When fitting lightcurves with the single-lens model, we use a finite-source single-lens model if the impact parameter $u_0 < 2\rho_*$, where ρ_* is the ratio of angular source radius to the angular Einstein radius. Otherwise the point-source single-lens model is used.

5.2.3 *Euclid* observing strategy

The observing strategy governs the way that each telescope and instrument observe the survey fields, including the exposure times, stacking and dithering of images, and visit

²This corresponds to $u_{0\max} = 3$ for an unblended source. The calculation is done in the primary observing pass-band.

patterns. *MaB μ LS* allows fine control of the time budget through user-defined observing sequences, taking account of the time required for dithering and readout between the images of a stack, and allowing for differing amounts of dead-time between each new field pointing. For ground-based observatories, down-time due to bad weather, or any other cause, is included through nightly bad weather probabilities, and observations are only simulated after astronomical twilight and when the moon is not too close a target field.

For the *Euclid* simulation, we assume that most of the observations will be taken in the primary observing band, while colour information will be obtained by one observation of each field every 12 hours in each of the three auxiliary bands. While *Euclid*'s *VIS* and *NISP* instruments are designed to image simultaneously, we assume that only one instrument images at any one time, in order to be conservative. This also allows for the possibility that the down-link bandwidth is not sufficient to download simultaneous imaging data.

In order to achieve a cadence of less than 20 min, the survey we simulate targets 3 fields of $\sim 0.5 \text{ deg}^2$ with a total exposure of 270 s per pointing, split into stacks of 3 (*Y*- and *J*-band) or 5 (*H*-band) exposures with *NISP*. We assume that there is 5 s of dead time between the exposures of a stack. The *VIS* instrument observations consist of a single 540-s exposure. We assume a slew and settle time of 85 s, according to a space-craft design using reaction wheels (*Euclid* red book). We assume that any readout, filter wheel rotation and data down-link is performed during slewing. Some of these parameters are summarized in Tables 5.1 and 5.2 below. We simulate a survey by *Euclid* of 300 days, spread over 5 years in seasons lasting 60 days.

5.2.4 Photometry

MaB μ LS simulates optimal crowded field photometry (CFP) by simulating images of crowded fields and counting flux in a small aperture centred on the source. We subtract the background, assuming it to be perfectly known. While aperture photometry

performs poorly in real CFP applications, the main reason for this is the lack of good measurements of the background in crowded fields. By assuming a perfectly known background, we are effectively simulating the performance of PSF fitting (Stetson 1987; Schechter et al. 1993) or difference imaging analysis (DIA) photometry (Alard 2000; Woźniak 2000; Bramich 2008), both of which fit for the background over a large area of the image. The possible optimism of the background subtraction should be offset by the remaining deficiencies of standard aperture photometry, which remains sub-optimal even if the background is perfectly known. For example, photometric scatter can be reduced by using an optimized aperture (Naylor 1998) or by PSF fitting (Schechter et al. 1993). The latter technique should be especially effective for data from *Euclid*'s VIS instrument, as weak lensing measurements require that the PSF be extremely well characterized over the entire instrument field of view (*Euclid* red book).

MaB μ LS can also include the effect of systematic photometry errors to a limited degree. One such source of systematic errors is sub-pixel pointing errors, which can be significant in under-sampled images. The sub-pixel shifts can be added to the simulated images at each epoch or the size of the error bar estimated from ideal simulations. However, the inclusion of these errors is optional, as they can be corrected for with accurate pointing data; we do not include them in the *Euclid* simulations, assuming that accurate telemetry will be available. We assume that errors due to small movements of the telescope during exposures (jitter) are accounted for in the PSF. Other possible sources of systematic errors can be added to the photometric error simply as a fractional error in quadrature. We assume a fractional systematic error of 0.003.

The simulated images themselves are constructed using star lists from the Besançon model. Stars are added to each image and kept track of so that they can be added to images of the same source taken with different filters, instruments or telescopes. In this way we account for blending in a manner that is fully consistent across all bands and instruments. In fact, several star lists are used for each field; each list covers a different set of non-overlapping magnitude ranges in order to minimize the effects of small-number statistics on rarer bright stars. The stars are added using either a user-

Table 5.1 – Parameters of the *Euclid* telescope. All parameter values have been drawn from the *Euclid* red book.

<i>Telescope parameters</i>	
Diameter (m)	1.2
Central blockage (m)	0.4
Slew + settle time (s)	85

defined PSF function or a numerical PSF model, each of which is integrated over the detector pixels. As the star lists used to generate images cover all magnitudes, they take account of the diffuse background due to unresolved stars. A background due to other diffuse sources, such as zodiacal light and night-sky brightness, is also added and can be varied between exposures. Finally, light due to the source and lens stars is added. Time series photometry is performed by repeatedly replacing the variable source in each new image.

The number counts that are recorded by the detector in a given pixel are determined by a set of detector parameters, all of which are user-defined. These parameters are listed in Table 5.2, where their values for the various *Euclid* instruments and bands are also listed. We note the following about the parameters listed in the table:

- The zero-point is the AB magnitude of a point source, which would cause one count s^{-1} in the detector, after all telescope and instrument inefficiencies have been accounted for. The *Euclid* zero-points assume end-of-life instrument performance (M. Cropper, G. Seidel, private communication).
- We distinguish between dark current and thermal background. The dark current is the rate of counts induced by thermal sources *within the detector pixels*, and is independent of the observing band. The thermal background is the count rate due to thermal photons emitted by all components of the spacecraft that hit the detector.

Table 5.2 – Parameters of the *Euclid* detectors. Unless footnoted, all parameter values have been drawn from the *Euclid* red book. Where necessary parameters are explained in the text.

Detector parameters

Instrument	VIS		NISIP	
	RIZ	Y	J	H
Size (pixels)	24k \times 24k		8k \times 8k	
Pixel scale (arcsec)	0.1		0.3	
PSF FWHM (arcsec)	0.18	0.3*	0.36*	0.45*
Bias level (e ⁻)	380 [†]		380 [†]	
Full well depth (e ⁻)	2 ¹⁶		2 ¹⁶	
Zero-point (ABmag)	25.58*	24.25**	24.29**	24.92**
Readout noise (e ⁻)	4.5	7.5*	7.5*	9.1*
Thermal background (e ⁻ s ⁻¹)	0	0.26	0.02	0.02
Dark current (e ⁻ s ⁻¹)	0.00056 [◊]		0.1*	
Systematic error	0.003 [†]		0.003 [†]	
Diffuse background (ABmag arcsec ⁻²)	21.5 [‡]	21.3 [‡]	21.3 [‡]	21.4 [‡]
Exposure time (s)	540	90	90	54
Images per stack	1	3	3	5
Readout time (s)	< 85		5 [†]	

*Schweitzer et al. (2010). The readout noise depends on the number of non-destructive reads; see text for further details.

[†]Assumed in this work.

*M. Cropper, private communication.

**G. Seidel, private communication.

[◊]CCD203-82 data sheet, issue 2, 2007. e2v technologies, Elmsford, NY, USA.

[‡]Calculated based on field locations, taking values for the zodiacal background from Leinert et al. (1998), and assuming an extra 0.2 magnitudes from other sources such as scattered light.

- For the *Euclid* simulations, we assume that the diffuse background is due primarily to zodiacal light but that there is also an additional diffuse background with 20 percent of the intensity of the zodiacal light, which accounts for all other sources of diffuse background. The zodiacal light background is calculated for each band using data given by Leinert et al. (1998).
- The *VIS RIZ*- and *NISP Y*-bands are not included in the Besançon model, so we assume that the AB magnitude of a star in the *RIZ*-band is the average of its *R* and *I* AB magnitudes, and similarly we assume that the *Y*-band magnitude is the average of *I* and *J*.

Should a pixel within the photometry aperture saturate, the data point is flagged and is not included in the subsequent analysis. We do not yet include the effects of cosmic rays in the images, but will in future versions of *MaB μ LS*. For the *Euclid* simulations, cosmic rays will only significantly affect observations with the *VIS* instrument, because the *NISP* instrument, made up of infrared arrays, will use up-the-ramp fitting with non-destructive reads (Fixsen et al. 2000) to reduce readout noise and correct detector nonlinearities (Schweitzer et al. 2010; Beletic et al. 2008). As a consequence of the multiple reads, up-the-ramp fitting mitigates against data loss due to cosmic rays and saturation. In order to ensure conservatism, we assume data with saturated pixels is lost completely. Currently we simulate the *NISP* instrument as a conventional CCD, but with variable read-noise determined by a fundamental read-noise ($13 e^-$) and the number of non-destructive reads during an exposure, which we assume occur at a constant rate of once every ~ 5 s (Schweitzer et al. 2010). A more realistic simulation of the performance of imaging photometry with up-the-ramp fitting will be included in a future version of the simulator. We do not simulate the more complicated effects of charge smearing (see, e.g., Cropper et al. 2010) and ghosts from bright stars.

For the *Euclid* simulations we use numerical PSFs computed for each instrument and each band. The *NISP* PSFs are computed near the edge of the detector field of view and include the effect of jitter and instrument optics in the worst case scenario (G. Sei-

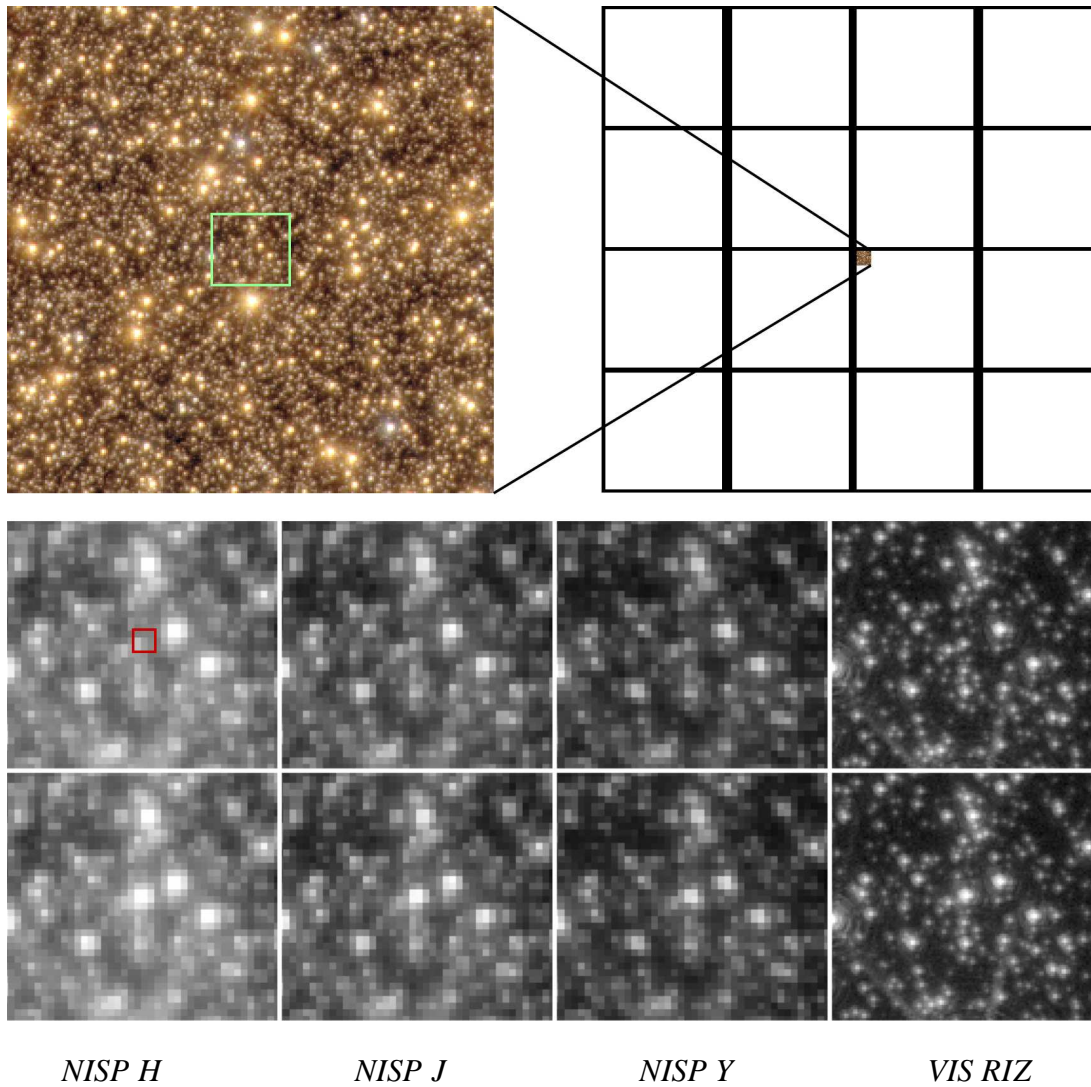


Figure 5.2 – *Top left*: Example of a simulated false-colour composite image of a typical star-field from the *Euclid MaB μ LS* simulation, with colours assigned as red–*NISP H*, green–*NISP J* and blue–*VIS RIZ*, each with a logarithmic stretch. The light green box surrounds the region that is shown zoomed-in in lower panels. The image covers 77×77 arcsec, equivalent to $1/64$ of a single *NISP* detector, of which there are 16. These are shown to the right. *Top right*: Approximate representation of the *NISP* instrument ‘paw-print’. The white areas show active detector regions, while black areas show the gaps between detectors. In the corner of one of the detectors is shown the size of a simulated image relative to the detectors. (Caption continued on next page)

Figure 5.2 – (Continued) *Bottom panels*: The bottom panels show a small image region surrounding a microlensing event (located at the center), the top row showing images at baseline and the bottom row showing images at peak magnification $\mu = 224$. Panels from right to left show *NISP H*, *J*, *Y*, and *VIS RIZ* images, respectively. The small red box shows the aperture that was used to compute photometry in the *NISP* images; the *VIS* aperture is a similar size but different shape. At peak, the event saturates in both *NISP H* and *VIS RIZ* images, but not in *NISP J* and *Y* images.

del, private communication). The *VIS* PSF is similarly computed (M. Cropper, private communication). Figure 5.2 shows an example of a simulated, colour-composite image of a field with a microlensing event at its centre. The brighter stars in the image are red-clump giants in the bulge, except for those which are distinctly bluer/whiter, which are \sim F-stars in the disc. The fainter, resolved stars are turn-off and upper-main-sequence stars in the bulge. The figure also shows an approximate representation of the scale of the *NISP* instrument, which is constructed from 4×4 HgCdTe infrared arrays, each of 2048×2048 pixels covering 10×10 arcmin, for a total detector area of 0.47 deg^2 ; the gaps between detectors are approximately to scale. We do not include these gaps in the simulation and assume the instrument is a single 8192×8192 -pixel detector. The lower section of Figure 5.2 shows a set of zoomed-in image sections, centered on the microlensing event at peak and at baseline, in each of the *NISP* and *VIS* bands. Note the diffraction spikes and Airy rings in the *VIS* images, especially those due to the bright star just out of frame below center; spikes due to the out-of-frame star can just about be made out in the *NISP* images also. Such spikes and rings can significantly affect photometry of faint sources. Figure 5.3 shows the lightcurve of the simulated event that occurs in the example image, including the points that are lost to saturation. The event peaks at magnification $\mu = 224$ and saturates over the peak in both *H*-band and *VIS* images, but not in *J*- and *Y*-band images. For the sake of computational efficiency only a small image segment, just bigger than the largest aperture, is simulated in standard operation.

$$M_1 = 0.4M_\odot \quad M_p = 100M_\oplus \quad a = 3.86\text{AU} \quad \Delta\chi^2 = 107679$$

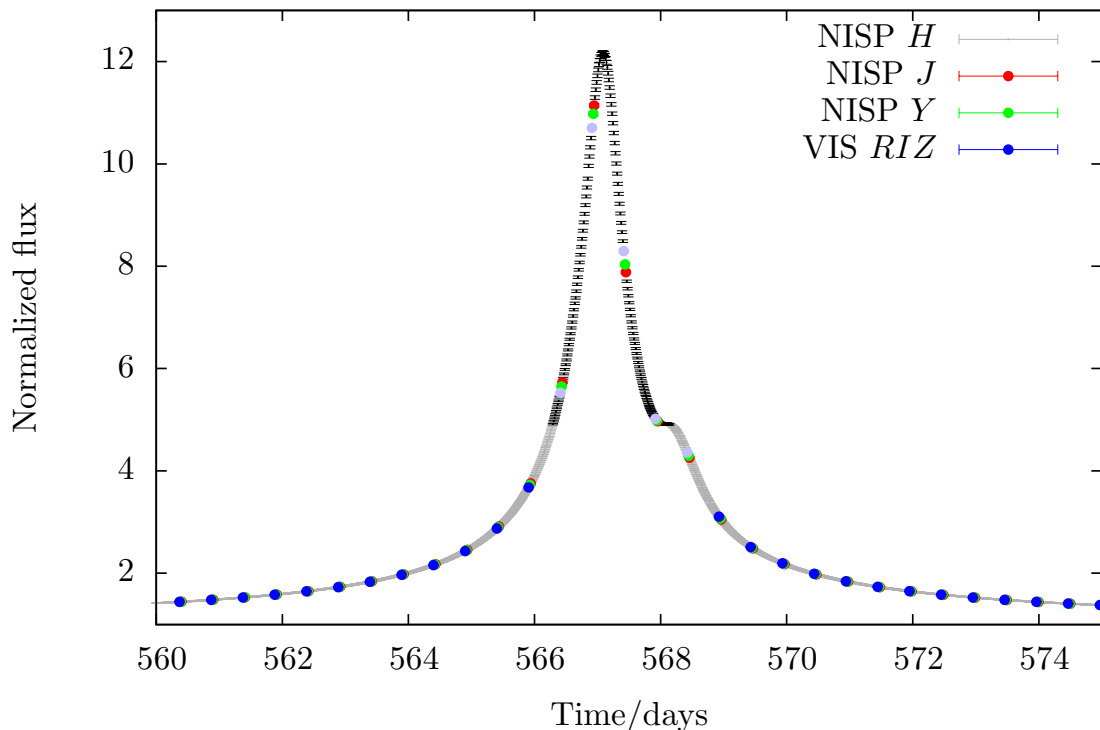


Figure 5.3 – Lightcurve of the simulated event shown in Figure 5.2, with all fluxes scaled to H -band. Grey, red, green and blue show data from $NISP H$, J , Y and $VIS RIZ$, respectively. Saturated H -band data points are shown in black, and saturated RIZ -band data points are shown in light blue. The event reaches a peak magnification of ~ 224 , but the normalized flux only increases by a factor of ~ 12 because the source ($H = 20.3$) is blended with a brighter star at the edge of the aperture and a much brighter star ~ 5 $NISP$ -pixels away, as well as the lens ($H = 21.6$) and fainter stars. At baseline, the source contributes just 5 percent of the total flux. Some of the event parameters are shown above the figure: M_1 is the host-star mass; $\Delta\chi^2$ is introduced in the next section.

5.2.5 Planet detections

To determine whether a planet is detected in a microlensing event we use a simple $\Delta\chi^2$ test, where $\Delta\chi^2$ is the difference in χ^2 between the best-fitting single-lens model and the best-fitting planetary model, which we assume to be the true underlying model that was used to simulate the event. We require that $\Delta\chi^2 > 160$, which corresponds to a

$\sigma > 12.6$ detection of the planet. We choose this value in order to aid comparison with other simulations (Bennett and Rhie 2002, Gaudi et al., unpublished). $\Delta\chi^2 > 160$ is also the value adopted by the *WFIRST* science definition team for their calculations of the exoplanet figure of merit (Green et al. 2011). In Appendix A we show that this choice is conservative with regards to the comparison between single and planetary models, but also argue that this may not be the case for the exclusion of possible false positives.

In order to allow fair comparisons between the different bands that *Euclid* can observe in, we also require that the contribution to $\Delta\chi^2$ from the primary observing band is at least half of the total. This condition ensures that the primary band provides most of the information about the planet and excludes events where a planet is detected but most of the data is lost (due to saturation, for example).

Figure 5.4 shows some example lightcurves from the simulation. The lightcurves show planet detections with varying degrees of significance, ranging from a detection that barely passed the cut (lightcurve (a), $\Delta\chi^2 = 168$) to a very significant detection (lightcurve (e), $\Delta\chi^2 = 1327$). Note however, that many events will have much higher $\Delta\chi^2$ than this, up to $\Delta\chi^2 \approx 10^{6-7}$. The example lightcurves also cover a range of host and planet masses; the event with the lowest-mass planet is event (e), which has a planet mass $M_p = 0.03M_\oplus$ and is strongly detected with $\Delta\chi^2 = 1327$. Note that due to a small bug in the observation scheduling module of *MaBμLS*, observations in *Y* and *RIZ* start and finish a day late. This should not significantly affect the results, but will be corrected in future versions of the simulator.

5.3 Expected yields

In this section we discuss preliminary results from our application of the *MaBμLS* simulator to the *Euclid* mission. Unless otherwise noted, we present the results assuming that each lens star in the simulation is orbited by a single planet of mass M_p with semimajor axis in the range $0.03 < a < 30$ AU.

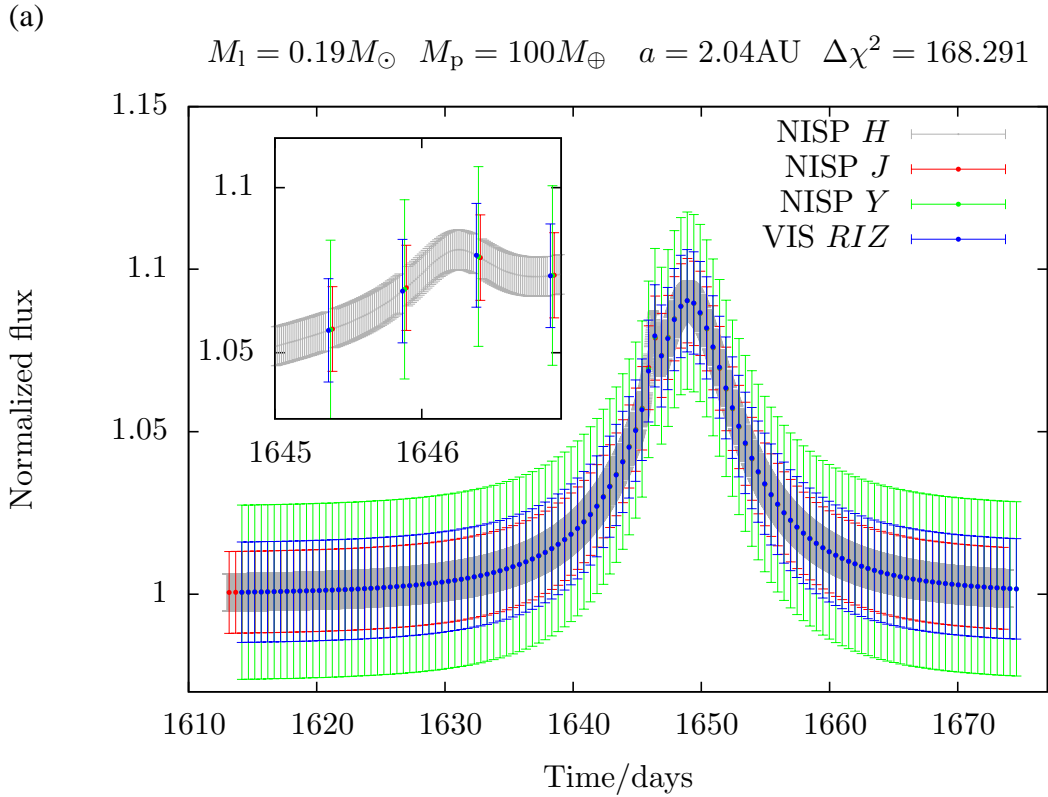


Figure 5.4 – Example lightcurves from the *MaB μ LS* simulation of *Euclid*, continued on later pages. Only 1 season of data is shown for each lightcurve. Error bars show the $1\text{-}\sigma$ photometric uncertainty, but data points are not scattered for clarity. Moving sequentially from (a) to (e) the $\Delta\chi^2$ for each lightcurve increases. Lightcurve (a) is only just classified as a detection with $\Delta\chi^2 = 168$. Some event parameters are shown above each plot, including the planet mass. The planet masses range from $M_p = 0.03M_\oplus$ for (e) (which has the highest $\Delta\chi^2$ of these examples) to $M_p = 100M_\oplus$ for (a). In all cases except (b) the inset shows a small region of the lightcurve around the planetary deviation; for (b) the 1-season lightcurve is shown in the inset.

Figure 5.5 shows the expected number of planet detections N_{det} plotted against planet mass, using our default assumption that there is one planet of mass M_p and semimajor axis $0.03 < a < 30$ AU per star. The value that is actually plotted on the y-axis, $N_{\text{det}}/f(M_p)$, takes into account our ignorance of the planetary mass function $f(M_p)$. In all plots, except Figures 5.6 and 5.7, $f(M_p)$ is defined to be the expected number of planets of mass M_p orbiting a star with semimajor axis $0.03 < a < 30$ AU;

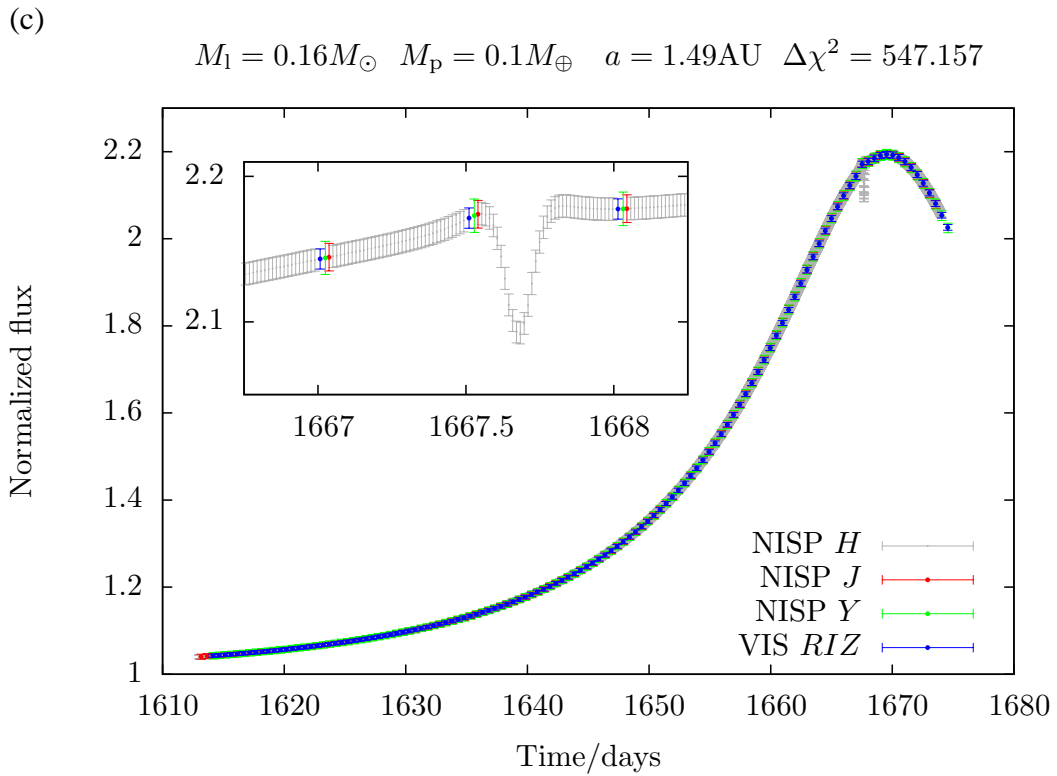
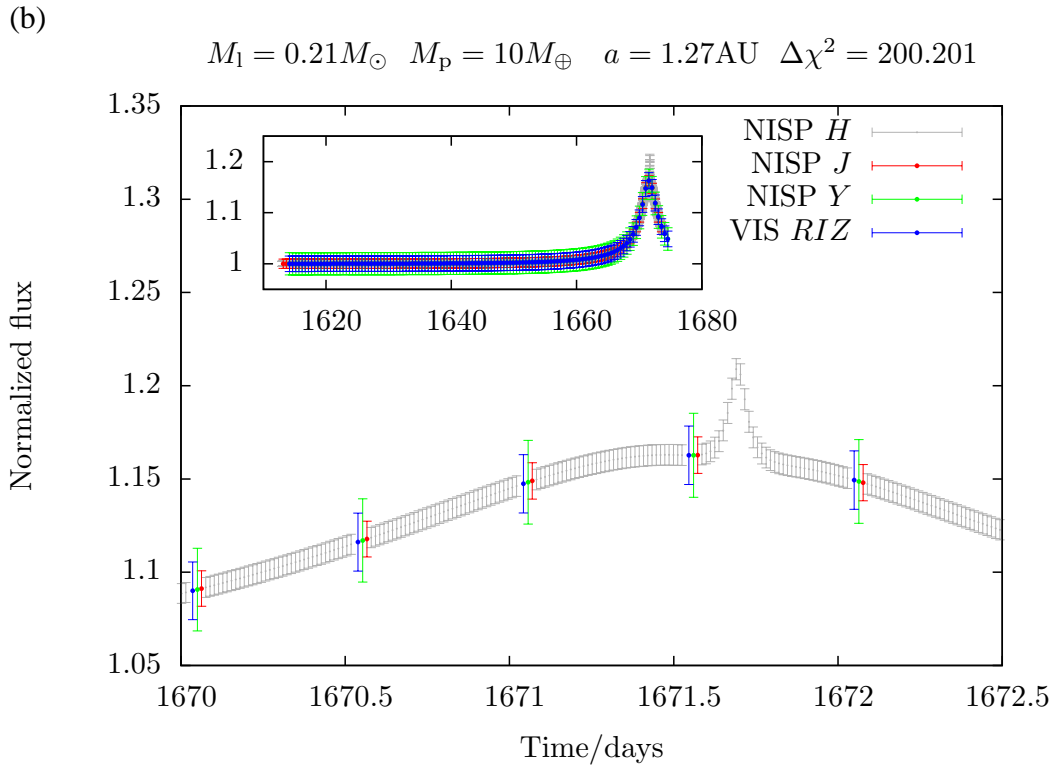
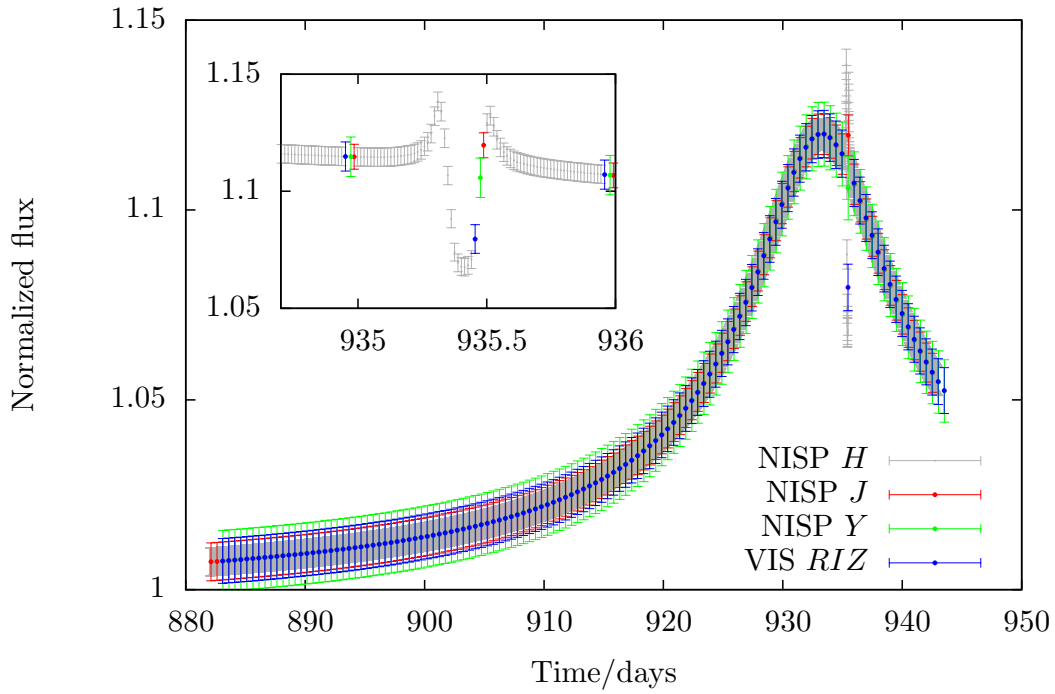


Figure 5.4 – Continued.

(d)

$$M_1 = 0.88M_\odot \quad M_p = 1M_\oplus \quad a = 2.92\text{AU} \quad \Delta\chi^2 = 1009.71$$



(e)

$$M_1 = 0.44M_\odot \quad M_p = 0.03M_\oplus \quad a = 9.15\text{AU} \quad \Delta\chi^2 = 1327.25$$

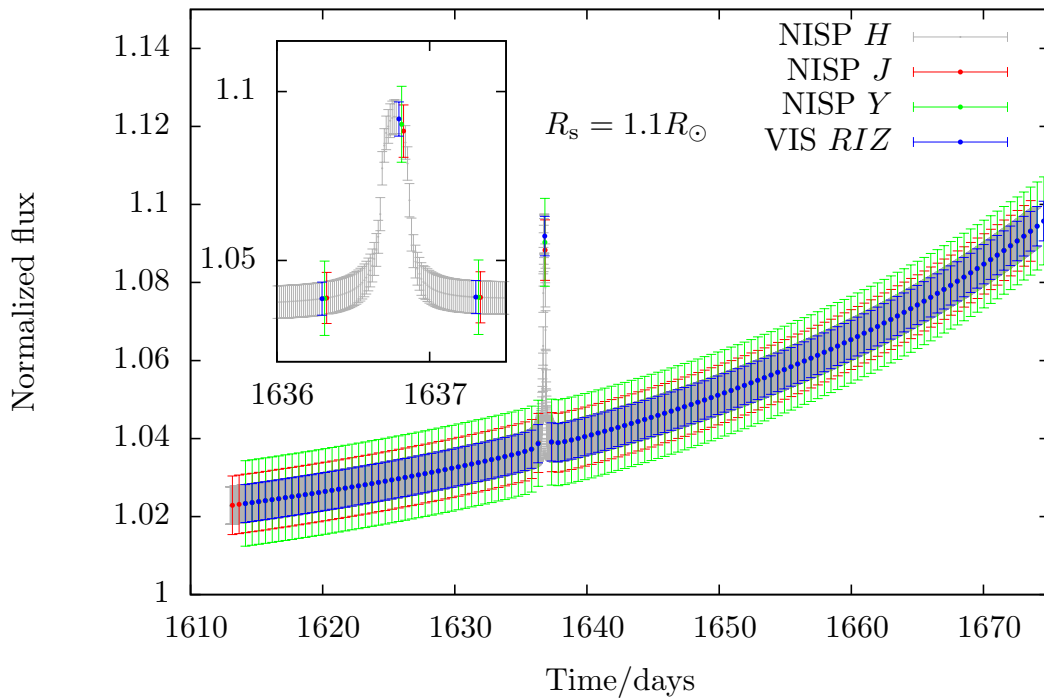


Figure 5.4 – Continued.

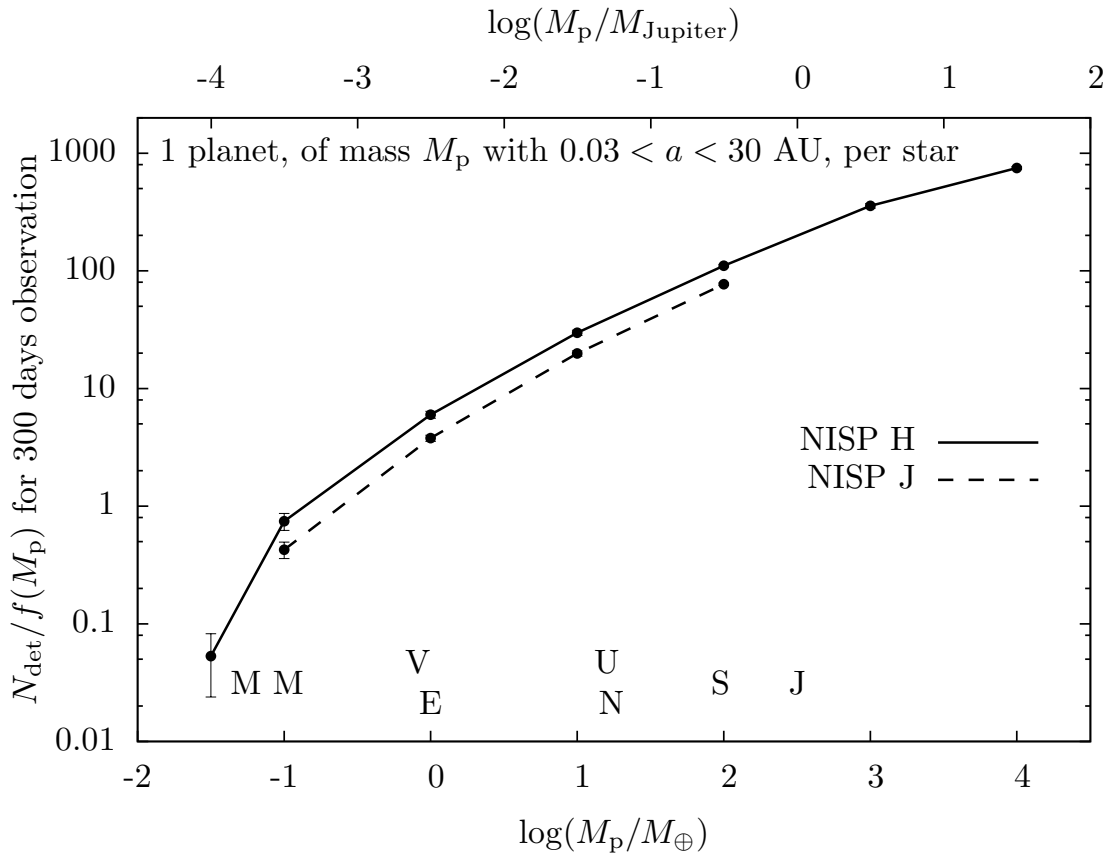


Figure 5.5 – Number of planets detected in a 300-day survey by *Euclid*, plotted against planet mass M_p , assuming one planet of mass M_p per star with semimajor axis $0.03 \leq a < 30$ AU. The solid line shows the yield for a survey with H as the primary band and the dashed line shows the yield for a survey with J as the primary band. The masses of Solar System planets are indicated by letters.

the mass functions used in the other figures will be described in due course. The error bars on all plots show the uncertainty due to the finite number of events that we simulate. This does not include a ~ 5 -percent systematic uncertainty resulting from the calculation of the overall event rate using source and lens catalogues. Neither does it include any contribution to the error due to uncertainties in the Besançon model parameters or models. This implies that the prediction of the total expected yield contains significant uncertainty, but that comparisons between simulations should be good to the errors quoted.

The plot in Figure 5.5 shows results of simulations with the primary observing bands, H and J . Of the bands available to *Euclid*, the H -band is the most effective band with which to perform a planetary microlensing survey, with yields ~ 50 percent higher than those expected for the J -band. Should our default assumptions apply, a 10-month microlensing survey by *Euclid*, primarily observing in H -band, should be expected to detect ~ 200 Jupiter-mass planets, ~ 110 Saturn-mass planets, ~ 40 Neptune-mass planets, ~ 6 Earth-mass planets and ~ 0.75 Mars-mass planets. *Euclid* can detect planets with masses less than Mars mass, but with low efficiency.

Recent measurements of planet abundances using several techniques have shown that our default assumptions about the abundance of planets are quite unrealistic. Multiple studies have suggested that the number of planets increases with decreasing planet mass (Cumming et al. 2008; Johnson et al. 2010; Sumi et al. 2010; Howard et al. 2011; Mayor et al. 2011) and that planets are not distributed logarithmically in semimajor axis (Cumming et al. 2008). This picture is also supported by planet population synthesis models (Mordasini et al. 2009a,b; Ida and Lin 2008b). In Figure 5.6 we attempt to improve our yield estimates by using a simple two-parameter power-law planetary mass function

$$f(M_p) \equiv \frac{d^2N}{d \log M_p d \log a} = f_{\bullet} \left(\frac{M_p}{M_{\bullet}} \right)^{\alpha}, \quad (5.3)$$

where $f(M_p)$ is now the number of planets of mass M_p per decade of planet mass per decade of semimajor axis per star and where f_{\bullet} is the planet abundance (in $\text{dex}^{-2} \text{star}^{-1}$) at some mass M_{\bullet} about which the mass function pivots. Here, α is the slope of the mass function, with negative values implying increasing planetary abundance with decreasing planetary mass. For simplicity, and because there are no measurements of the slope of the planetary semimajor axis distributions in the regime probed by microlensing, we assume that $dN/d \log a$ is constant.

We use two estimates of the mass-function parameters based on measurements made using both RV and microlensing data sets. The first, more conservative mass function (in terms of the yield of low-mass planets) uses the mass-function slope $\alpha = -0.31 \pm 0.20$ measured by Cumming et al. (2008) from planets with periods

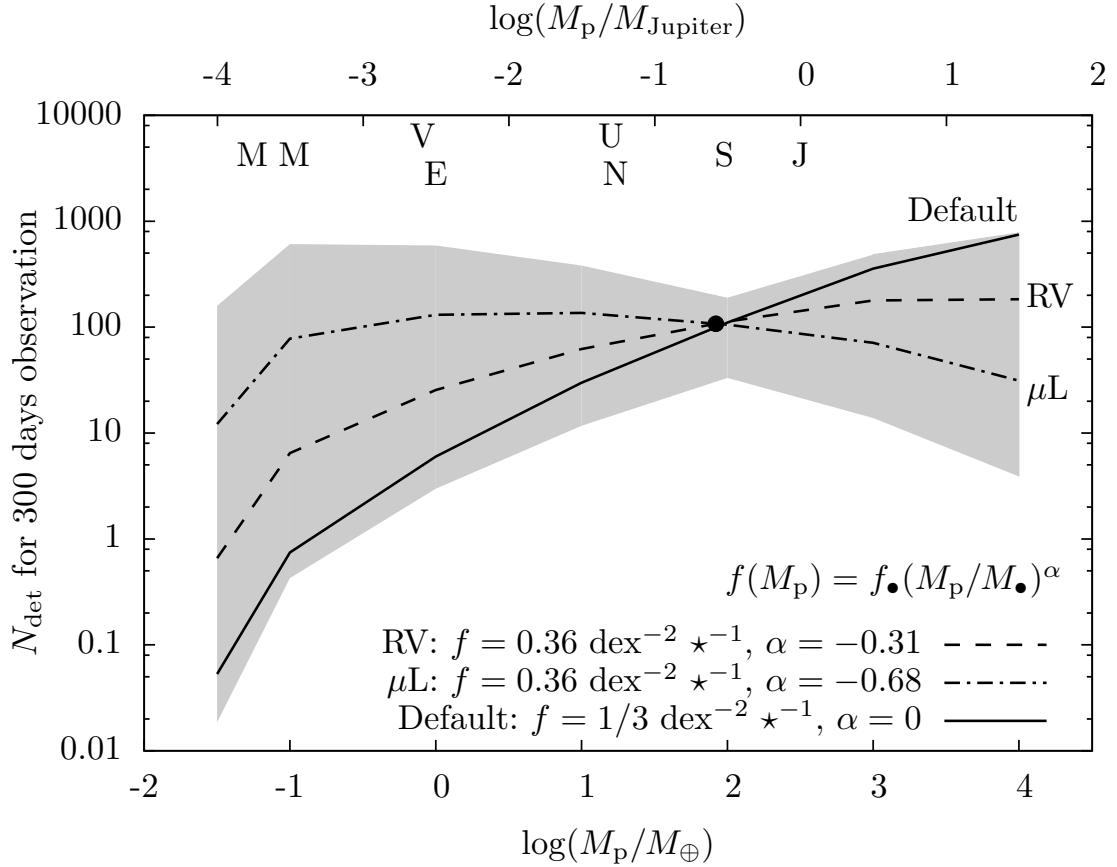


Figure 5.6 – Predictions of the planet yield based on recent estimates of the planet abundance and planet-mass distribution. The solid line shows our default logarithmic prior of one planet per decade of mass and semimajor axis per star. The dashed line (labelled RV) shows the expected yield using an extrapolation of the mass-function slope measured by Cumming et al. (2008) using RV data combined with a normalization measured by Gould et al. (2010) from microlensing data. The dot-dashed line (labelled μL) shows the expected yield using the same Gould et al. (2010) normalization, but using a mass-function slope measured by Sumi et al. (2010) from microlensing data. The circle shows the point about which the empirical mass functions are pivoted, while the grey shaded region shows the region enclosed when the parameters f_{\bullet} and α are changed by 1σ from both the RV and microlensing mass-function parameters. More details are given in the text. The masses of Solar System planets are denoted by letters.

in the range $T = 2\text{--}2000$ d, detected via radial velocities. For the normalization we use $f_{\bullet} = 0.36 \pm 0.15$ at $M_{\bullet} \approx 80M_{\oplus}$, measured by Gould et al. (2010) from high-magnification microlensing events observed by MicroFUN. Gould et al. (2010) argue that this value is consistent with the abundance and semimajor axis distribution measured by Cumming et al. (2008), extrapolated to orbits with $a \approx 2.5$ AU. We note that the host stars studied by Cumming et al. (2008) typically have higher masses than those that are probed by microlensing. We call the combination of the Cumming et al. (2008) slope and Gould et al. (2010) normalization, the RV mass function. The second mass function we consider uses the same Gould et al. (2010) normalization, but a slope $\alpha = 0.68 \pm 0.20$ measured by Sumi et al. (2010) from 10 microlensing planet detections and assuming a reasonable detection efficiency as a function of planet mass. We call this the microlensing mass function.

Figure 5.6 plots the yields that would be expected for three mass functions: the two determined empirically and described above, and for comparison, our default assumption of a logarithmic mass function ($\alpha = 0$) with one planet per 3 decades of a ($f_{\bullet} = 1/3 \text{ dex}^{-2} \text{ star}^{-1}$ at any value of M_{\bullet}). The shaded regions in the plot enclose the range of expected yields possible within 1σ of all the input mass-function parameters (e.g., $-0.88 < \alpha < -0.11$; the $1\text{-}\sigma$ upper limit of the RV slope nearly coincides with the $1\text{-}\sigma$ lower limit of the microlensing slope, so the degree of uncertainty essentially covers the entire range).

Perhaps the most important thing that Figure 5.6 highlights is the degree of uncertainty that is involved in predicting the yields of planet surveys. There remain a number of sources of uncertainty we have not considered, such as that from the choice of semimajor axis distribution. Even at the pivot point of the mass functions, anchored by measurements at $M_p \approx 100M_{\oplus}$, the uncertainty in expected yield is a factor of three. At low planet masses the uncertainty is greater than three orders of magnitude.

It seems reasonable, however, to assume that the planet abundance increases towards lower masses. If this is indeed the case, the expected yield of low-mass planets will exceed that of our default assumptions, possibly by an order of magnitude or more.

We choose to continue using the default assumptions throughout the rest of the chapter in order to remain conservative. This conservatism is appropriate as we have to extrapolate the empirical mass functions over a significant range. However, should the empirical mass functions be correct, planet yields will be sufficient for the measurement of abundance statistics down to Mars mass ($0.1M_{\oplus}$) or Mercury mass ($0.05M_{\oplus}$) for the RV and microlensing mass-function parameters, respectively. The negative slope of the mass functions does imply lower yields for planets with masses larger than the pivot mass, but even the steep slope of the microlensing mass function predicts yields greater than 10 dex^{-2} planets over the entire planetary mass regime ($M_p < 13M_{\text{Jupiter}}$). In fact, the mass-function slope measured through microlensing almost exactly cancels the detection efficiency slope, leaving a relatively flat yield curve above Mars mass, which peaks at Earth mass with $N_{\text{det}} \approx 120 \text{ dex}^{-2}$. This number means that *Euclid* would detect approximately 60 planets with mass in the range $M_p = 0.56\text{--}1.8M_{\oplus}$ (half a decade surrounding $M_p = 1M_{\oplus}$) and semimajor axis in the range $a = 1\text{--}10 \text{ AU}$, if this mass function were assumed.

5.3.1 The M_p - a diagram

We have discussed the ability of our simulated survey to probe the planetary mass function, but a perhaps more important goal of such a survey is to explore the planet mass–semimajor axis (M_p - a) plane where planet formation models predict a lot of structure (e.g., Ida and Lin 2004; Mordasini et al. 2009a). Figure 5.7 plots contours of planet detection yields for the simulated survey in the M_p - a plane, assuming there is one planet per host at a given point in the plane. The positions of planet detections to date, by all detection methods (RV, transits, direct detection, timing and microlensing) are also shown, as well as candidate planets detected by *Kepler* (Borucki et al. 2011), which have been plotted by assuming the planetary mass-radius relation, $M_p = (R_p/R_{\oplus})^{2.06}M_{\oplus}$, which is used by Lissauer et al. (2011). It is clear that microlensing surveys probe a different region of the M_p - a plane to all other detection

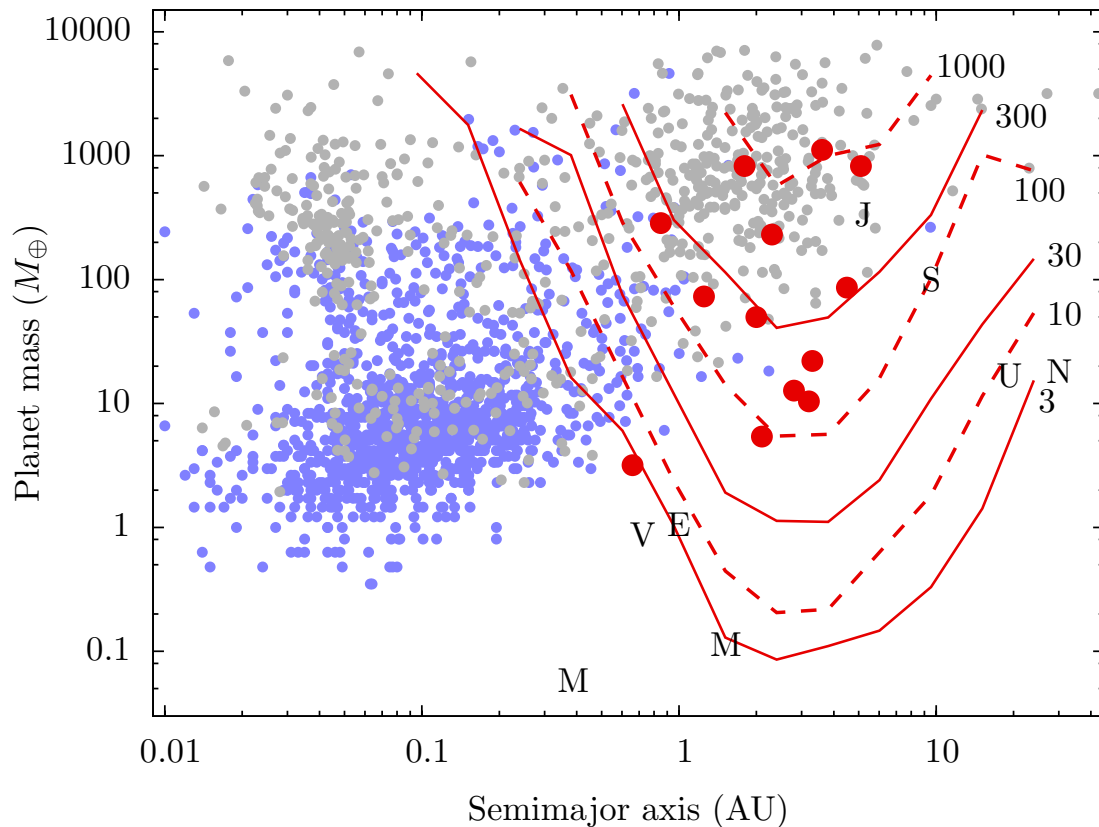


Figure 5.7 – Red lines show the expected yield of a 300-day *Euclid* survey with 60 days of observations per year, plotted against planet mass and semimajor axis, assuming one planet per star at each point in the planet mass–semimajor axis plane. The grey points show planets detected by all methods up to 17th October 2011 (Schneider et al. 2011), and light blue points show candidate planets from the *Kepler* mission, with masses calculated using the mass-radius relation of Lissauer et al. (2011). The red points show planets detected via microlensing to date.

methods, covering planets in orbits ~ 0.3 –10 AU. The peak sensitivity of the simulated *Euclid* survey is at a semimajor axis $a \approx 2$ –3 AU, in good agreement with previous simulations of space-based microlensing surveys (Bennett and Rhie 2002, Gaudi et al., unpublished). The planets *Euclid* is sensitive to lie in wider orbits than those detectable by *Kepler*, and stretch to much lower masses than can be detected by RV in this semimajor axis range, reaching down to Mars mass. The range of semimajor axis

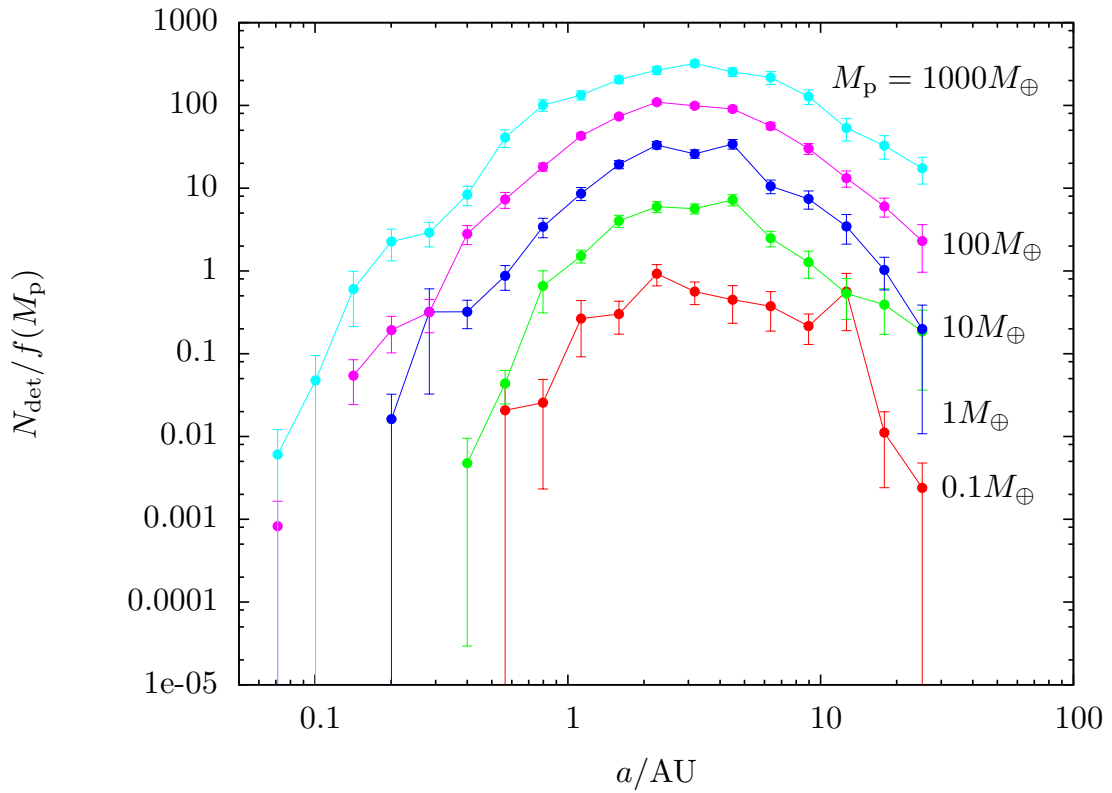


Figure 5.8 – Predictions of the planet yield as a function of semimajor axis a .

probed by *Euclid* decreases with decreasing mass, from ~ 0.3 to more than 20 AU for Jupiter-mass planets, down to ~ 1 –10 AU for Earth-mass planets and ~ 1.5 –4 AU for Mars-mass planets. There will be a significant degree of overlap between *Euclid* and full-mission *Kepler* detections at separations $0.3 \lesssim a \lesssim 1$ AU. Similarly, at masses larger than $M_p \gtrsim 50M_\oplus$, there will be overlap with RV surveys over a wide range of semimajor axes. Both overlaps will facilitate comparisons between the data sets of each technique. It should be noted however, that the host populations probed by each technique are different, as we will see in the next section.

Figure 5.8 plots the expected yields for various planet masses as a function of semimajor axis a , using our default assumptions. The peak sensitivity of *Euclid* is to planets with semimajor axis $a \approx 2$ –3 AU. The sensitivity is within an order of magnitude of the peak in the range $0.5 \lesssim a \lesssim 20$ AU. Should the mass function of

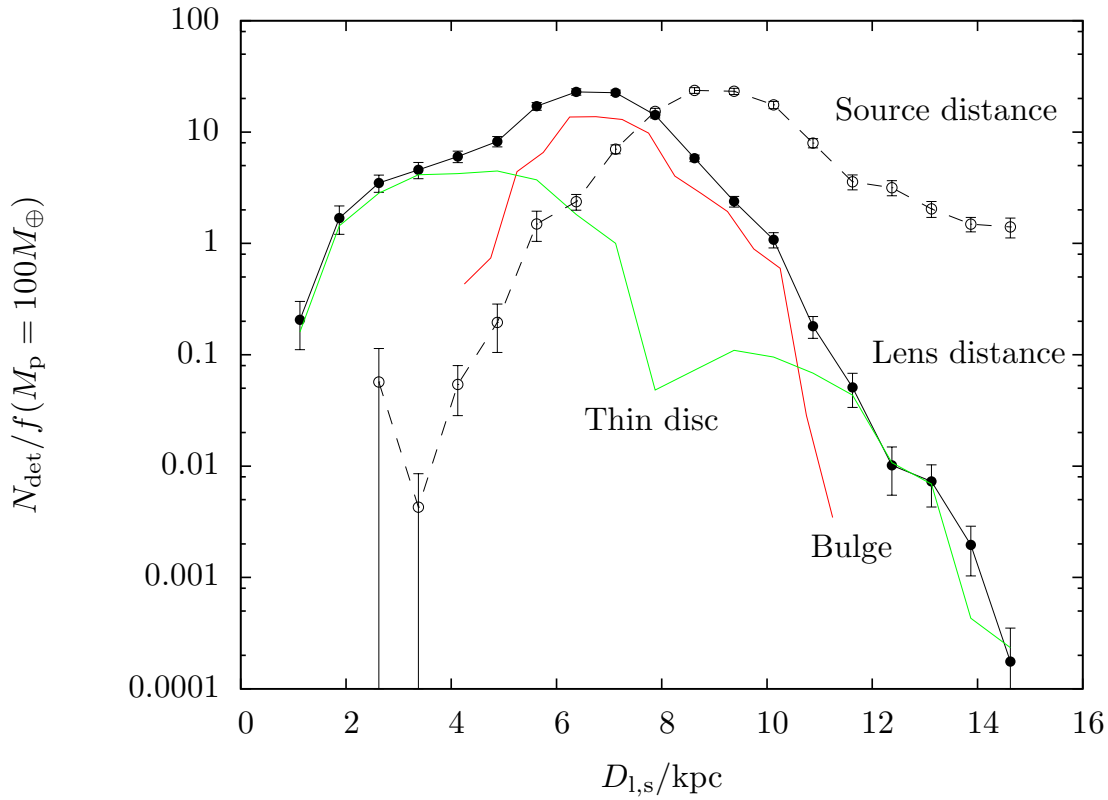


Figure 5.9 – Predictions of the $100\text{-}M_{\oplus}$ planet yield as a function of lens (solid lines) and source (dashed line) distances, D_l and D_s , respectively. The red and green lines show the contributions due to bulge and thin disc lenses, respectively; thick disc and halo lenses contribute the remainder, which is small.

planets resemble the microlensing mass function we use in Figure 5.6, each of the curves shown in Figure 5.8 would lie somewhere between the curves for $10\text{-}M_{\oplus}$ and $100\text{-}M_{\oplus}$ planets, suggesting that it would be possible to measure the semimajor axis distribution over the range $0.3 \lesssim a \lesssim 30$ AU for planets down to Earth or possibly even Mars mass.

5.3.2 The host-star populations

Figure 5.9 plots the distribution of $100\text{-}M_{\oplus}$ planet detections as a function of lens and source distances, D_l and D_s , respectively. The contribution of thin-disc and bulge

populations to the yields is also plotted. Thick disc and stellar halo lens yields have not been plotted as at no point are they dominant. However, near the Galactic centre it should be noted that stellar halo lenses have a higher yield than the thin disc due to the disc hole (see Section 5.2.1). Most of the host stars are near-side bulge stars between $5.5 < D_1 < 8$ kpc. Beyond this, the number of lenses with detected planets drops-off exponentially with increasing distance, dropping by four orders of magnitude from $D_1 \sim 9$ to 15 kpc. The steepness of this fall is partly caused by the truncation of the source distribution at 15 kpc. Though the majority of lenses are in the bulge, a substantial number reside in the near disc. The contribution of planet detections by each component is 60, 30, 3 and 7 percent for the bulge, thin disc, thick disc and stellar halo populations, respectively. The distribution of planetary host stars probed by *Euclid* is very different to that probed by any other technique. For example, most of *Euclid*'s host stars are M-dwarfs in the bulge, whereas most of *Kepler*'s host stars are FGK-dwarfs in the disc (Howard et al. 2011). Unlike the lens stars, the majority of source stars reside in the far bulge, with a small fraction in the far disc. Very few near disc stars act as sources due to the low optical depth to sources on the near side of the bulge.

5.4 Discussion

We have developed *MaB μ LS*, an all-purpose microlensing simulator with a particular focus on exoplanetary microlensing. Using the Besançon Galaxy model (Robin et al. 2003) and comprehensive image simulations, it is the first microlensing simulator to generate blending and event parameter distributions in a self-consistent manner. The Marshall et al. (2006) three-dimensional dust model, combined with the use of evolutionary tracks and stellar atmosphere models, enables realistic comparisons of the performance of microlensing surveys that observe in different pass-bands in the optical and infrared.

As an example of *MaB μ LS*'s use, we have simulated a 300-day planetary mi-

cro lensing survey by the *Euclid* space-craft. We show that of the *J*- and *H*-bands available to *Euclid*,³ a survey primarily conducted in *H* will perform best, detecting ~ 6 Earth-mass planets during the survey, compared to ~ 4 for the *J*-band survey, both assuming there is one Earth-mass planet per star with semimajor axis between 0.03 and 30 AU. Using perhaps more realistic assumptions of the planetary mass function, *Euclid* could expect to detect of the order of 100 Earth-mass planets and a similar number of Mars-mass planets. Such low-mass planets in the orbits probed by *Euclid* (0.5–10 AU) are inaccessible to any other planet detection technique, including microlensing surveys from the ground.

MaB μ LS is still under active development, but is already a powerful tool for the optimization of microlensing surveys. *Euclid* has only just been selected by ESA, and the mission and its surveys will enter a more intensive process of development in the coming few years; *MaB μ LS* will play a major role in the design and optimization of a *Euclid* microlensing survey. There are also exciting possibilities for the use of *MaB μ LS* in planetary detection efficiency calculations for current ground-based surveys. However, we devote the rest of this chapter to a discussion of some of the current limitations of the simulator and our plans to develop it in the context of the *Euclid* mission.

5.4.1 The Besançon model

The Besançon model has been in development for over 25 years (Robin and Creze 1986) and is by this point a highly sophisticated model of the Galaxy. This development is not complete and the model will continue to be refined as ever more data on the Galaxy becomes available. The version of the model we have used in this chapter includes an improved model of the Galactic bulge but with parameters that have since been updated (Robin et al. 2011). This active development, independent of *MaB μ LS*, is extremely valuable, enabling *MaB μ LS* to incorporate the latest understanding of the Galaxy without any need to update the simulator itself.

³Surveys with *NISP Y* and *VIS RIZ* as the primary band have not yet been simulated.

The continuing development of the Besançon model reflects our still relatively limited understanding of the Galaxy. This is especially the case when it comes to the bulge, where the interpretation of observations is extremely challenging due to the multiple stellar populations and large amounts of dust along the line of sight. Studies of the triaxial bulge/bar exemplify this, with different investigators reporting bar angles ranging from 10 to 40° (e.g., Picaud and Robin 2004; Rattenbury et al. 2007; Benjamin et al. 2005) and the evidence is building for more than one structure (e.g., Babusiaux and Gilmore 2005; Nishiyama et al. 2005; Cabrera-Lavers et al. 2007). Such uncertainties in structures and their parameters must propagate through our simulations and on into our absolute yields in a way that is difficult to quantify. Nevertheless, the Besançon model is the most self-consistent Galactic model to be used in microlensing simulations to date. This will be reflected in comparative studies such as the survey optimization we plan to perform.

5.4.2 Systematics

For the simulations presented here we have assumed a somewhat arbitrary value of the amplitude of systematic photometry errors that can be expected with *Euclid* data. Preliminary examination of the simulations suggests that our results could be quite sensitive to this choice, as in many cases the photometric noise is dominated by the systematic component and not photon noise. This warrants that we look more closely at the effect of systematics in future work. It is very important to investigate how expected yields will vary with differing amplitudes of systematic error, as the value we use may be a significant overestimate. Certainly, the tight control of systematics required by *Euclid* for galaxy-shape measurements should mean that *Euclid* will be one of the best-characterized optical observatories ever built (*Euclid* red book). To what degree this control will translate to crowded field photometry, however, is not yet clear.

5.4.3 Planet mass measurements

In this work we have presented estimates of the expected planet detection yield for a *Euclid* microlensing survey. While space-based microlensing offers significantly higher yields per unit time than do ground-based observations, this is not the only motivation for space-based observations. A standard planetary microlensing event does not automatically imply a measurement of planet mass or semimajor axis, only the planet-star mass ratio and the projected star-planet separation in units of the Einstein radius r_E . As discussed in Chapter 2, to measure the planet mass we must measure the lens mass, either by detecting subtle, higher-order effects in the microlensing lightcurve, such as microlensing parallax (e.g., Gould 2000a; An et al. 2002), or directly detecting the lens star (Alcock et al. 2001a; Kozłowski et al. 2007). Without these the mass can only be determined probabilistically (e.g., Dominik 2006; Beaulieu et al. 2006). The projected separation in physical units can be determined if the lens mass and distance are known (as well as the source distance, which it is possible to estimate from its colour and magnitude). Determining the semimajor axis will require the detection of orbital motion (Bennett et al. 2010; Skowron et al. 2011), but this will only be possible in a subset of events (see Chapter 3).

For a survey by *Euclid* we expect parallax measurements to be rare. Parallax effects are strongest in long microlensing events lasting a substantial fraction of a year due to the acceleration of the Earth (Gould 1992), but *Euclid*'s seasons will be too short to constrain or detect a parallax signal in most events (Smith et al. 2005). However, thanks to the high-resolution imaging capabilities of the *VIS* instrument, lens detection should be routine (Bennett et al. 2007). In events where the light of the lens is detected, the lens mass and distance can be determined by combining measurements of the angular Einstein radius θ_E (which gives a mass-distance relation, see Equation 2.7) with a main-sequence mass-luminosity relation. Measurement of θ_E should be possible in most events, either from finite-source effects in the lightcurve or by measuring the relative lens-source proper motion as the pair separate (Bennett et al. 2007).

It is also possible to estimate the lens mass and distance from measurements of its colour and magnitude (Bennett et al. 2007). From a single epoch of *NISP* and *VIS* images, this will likely not be possible. However, over each season at least 100 images will be taken in each *VIS* and *NISP* band, which will be randomly dithered. These can be stacked to form a much deeper, higher-resolution image in each band. From these images it should be possible to isolate the source (whose brightness is known from the lightcurve) from any blended light. After subtracting the source, if the remaining light is due to the lens, its mass can be estimated from its colour and magnitude. The planet mass can then be determined, as the planet-host mass ratio is known from the lightcurve. However, if either the source or lens has a luminous companion, estimating the lens mass will be more difficult (Bennett et al. 2007).

We do not attempt to estimate the number of planet detections with mass measurements in this work, but note that the image simulations we have developed provide the necessary tools to perform this calculation. In future work, to get an accurate estimate of the uncertainties on measured planet parameters, we will stack simulated images that have been dithered and attempt to extract from them measurements of the lens colour and magnitude and the lens-source proper motion. We will combine these with estimates of the lightcurve parameter uncertainties from Markov Chain Monte Carlo fits to the lightcurve data in order to fully estimate the uncertainty on the planet mass and projected separation in physical units. These calculations will allow a full determination of planetary microlensing figures of merit, such as the one defined by the *WFIRST* Science Definition Team (Green et al. 2011).

5.4.4 Survey optimization

The survey we simulate in this work has not been optimized. There are many factors that can be varied to increase planet yields, such as the choice of target fields, the number of target fields and the strategy with which they are observed. However, planet yields are not the only measure of the scientific yield of the survey. For example,

planetary-mass measurements without the need for additional follow-up observations are an important goal of the *Euclid* microlensing survey, and so any assessment of the relative performance of different possible surveys must also evaluate performances in this respect. Figures of merit will be used to quantify the optimization process.

6

Summary and future work

In Chapter 3 we simulated microlensing lightcurves by orbiting-binary lenses in order to determine the fraction of binary-lens lightcurves that are affected by orbital motion. This was done by fitting the lightcurves with static binary-lens models. Those that were poorly fit by the static model were counted as orbital motion detections. We corrected for systematic false-positive detections by also fitting the lightcurves of static-binary lenses. We found that for a continuous-monitoring survey without intensive follow-up of high-magnification events, the orbital motion detection efficiency ϵ_{OM} for planetary events with caustic crossings is $\epsilon_{\text{OM}} = 0.061 \pm 0.010$, consistent with observational results; for planetary events without caustic crossings $\epsilon_{\text{OM}} = 0.0130 \pm 0.0055$. Similarly for stellar binaries, we found $\epsilon_{\text{OM}} = 0.098 \pm 0.011$ for events with caustic crossings and $\epsilon_{\text{OM}} = 0.048 \pm 0.006$ for events without caustic crossings.

We also investigated how various microlensing parameters affect the orbital motion detectability. We found that the orbital motion detection efficiency increases as the binary mass ratio and event timescale increase, and as the impact parameter and lens distance decrease. For planetary caustic-crossing events, the detection efficiency is highest at relatively large values of semimajor axis ~ 4 AU, due to the large size of the resonant caustic at this orbital separation. Effects due to the orbital inclination are small and appear to only significantly affect smooth stellar binary events.

We find that, as suggested by Gaudi (2009), it is possible to classify many orbital

motion events into one of two classes. The first class, *separational* events, typically show large effects due to subtle changes in resonant caustics, caused by changes in the projected binary separation. The second class, *rotational* events, typically show much smaller effects which are due to the magnification patterns of close lenses exhibiting large changes in angular orientation over the course of an event. These changes typically cause only subtle changes to the lightcurve.

In Chapter 4 we studied rapidly-rotating lenses (RRLs), having found examples of detectable binary lenses orbiting with a period similar to their microlensing timescale in the previous chapter. That these events are detectable is remarkable because the strength of binary-lens features decreases rapidly as the orbital separation decreases. Yet, we show both analytically and numerically that it is possible to detect repeating features in the lightcurve of binary microlenses that complete several orbits during the microlensing event. We use a simulation to estimate the rate of RRL events for a ground-based and space-based microlensing survey to be $0.32f_b$ and $7.8f_b$ events per year, respectively, assuming year-round monitoring and where f_b is the binary fraction. We also detail how RRL event parameters can be quickly estimated from their lightcurves, and suggest a method to model RRL events using timing measurements of lightcurve features. Modelling RRL lightcurves will yield the lens orbital period and possibly measurements of all orbital elements including the inclination and eccentricity. Measurement of the period from the lightcurve allows a mass-distance relation to be defined, which, when combined with a measurement of microlens parallax or finite-source effects, can yield a mass measurement to a two-fold degeneracy. It may be possible to remove this degeneracy, even with only relatively weak limits on finite-source effects or on the microlensing parallax.

In Chapter 5 we develop a microlensing simulator: the Manchester-Besançon microLensing Simulator, or *MaBμLS*. By drawing on the Besançon population synthesis Galactic model and performing detailed image simulations, this simulator is one of the most comprehensive microlensing simulators yet developed. Synthetic images are created by using a detailed set of detector parameters and a numerical or analytic point

spread function. Microlensing events, together with stars drawn from the Besançon model, are added to the image and photometry performed. *MaBμLS* can simulate microlensing surveys conducted by a combination of observatories on the ground and in space, observing in different pass-bands and with a potentially complex observing strategy. The simulator has been designed to be modular, so that the user can define their own lightcurve-generator and detection-criteria functions in order to study different phenomena.

We have demonstrated the use of *MaBμLS* by applying it to the recently selected *Euclid* space mission. A microlensing survey has been proposed as an additional science program on the mission. We show that such a survey will detect ~ 6 Earth-mass planets if there is one such planet per star with a semimajor axis in the range $a = 0.03\text{--}30$ AU. If instead of this we assume that the planetary mass function follows values recently measured, of the order of 60 Earth-mass planets ($0.6\text{--}1.8M_{\oplus}$) should be detected, along with similar numbers of all other planet masses.

6.1 Future work

At the time of writing Chapter 3 there was only one event where orbital motion had been used to obtain a measurement of orbital parameters (Bennett et al. 2010). This event was clearly a special event containing signatures of two planets as well as orbital motion signatures, and at the time it was certainly possible that such an event was a fluke. However, since that time two more events have yielded fairly strong Keplerian orbital parameter constraints (Skowron et al. 2011; Shin et al. 2011), suggesting that such measurements should be possible in a reasonable fraction of events. The amount of work needed to model such events is significant because the full orbital motion parameter space is large. It is possible that an ‘assay by simulation’ of orbital motion events, following an approach similar to that taken in Chapter 3, may contribute to the understanding of the parameter space. The rationale is as follows: rather than fitting the simulated events with static-binary models, one would fit them with full

Keplerian models. This time it would not be the degree of agreement between models that was of interest, but the uncertainty in the parameters that could be derived. A Markov Chain Monte Carlo minimizer would be the most appropriate tool to estimate the uncertainties, as in many cases there may be broad, shallow and/or degenerate χ^2 minima. The results of this simulation would hopefully be a map of the parameter space suggesting where strong orbital constraints could be obtained. However, it is not clear if such an endeavor would succeed in producing sufficient significant results to reward the required work.

In Chapter 4 we showed that there was a reasonable chance that RRLs would be detected, either in archival data, or in data that will be collected in the near future. The best chance of detecting RRLs would appear to be in OGLE-IV data. OGLE-IV began alerting microlensing events this year and the list of alerts has exceeded 1500, i.e., OGLE-IV is detecting over two and a half times the number of events that OGLE-III was detecting. Also, certain fields are now sampled with a much higher cadence. After a few years of routine operation, once the OGLE-IV baseline has been built-up, a search for RRL events in conjunction with a search for parallax and xallarap events similar to those by Smith et al. (2002a) and Poindexter et al. (2005) would likely produce interesting results.

Perhaps the most promising line of future work will be the exploitation of *MaB μ LS*. The simulations we have presented are effectively preliminary results; we are awaiting an updated set of parameters for *Euclid*, following the announcement of its selection early in October 2011, in order to run full simulations comparing each of the available band-passes and investigating the effects of systematics. There is also a small amount of work needed to implement simulations of mass measurements by direct detection of the lens and to begin performing figure of merit simulations. However, all the tools for this are ready, they just need to be brought together.

A potentially valuable extension to *MaB μ LS* would be to make it an end-to-end simulator. At present *MaB μ LS* has the capability to produce realistic images, but it skips over perhaps the most crucial phase of the production of lightcurves: crowded

field photometry. *MaB μ LS* currently simulates aperture photometry, but it would produce more realistic results, together with many of the systematic errors, if it were to run standard crowded field photometry (CFP) routines on the simulated images. Such a development will almost certainly be needed to perform realistic simulations of ground-based surveys. However, it would come at considerable computational cost, due to the additional image processing. That said, it is likely that the additional realism would be well worth the additional expense.

6.2 Wider impact

In Chapters 3 and 4 we have focused on the somewhat specialized topic of orbital motion in microlensing, a relatively rarely-detected effect. However, by making possible the measurement of the semimajor axis and other orbital parameters, orbital motion detection can enable the like-for-like comparison of microlensing planet detections with those made by radial velocities and other methods. In fact, through the measurement of orbital motion signatures, Skowron et al. (2011) recently predicted the radial velocity signature of a binary microlens, which falls within the sensitivity range of current radial velocity instruments. This makes possible the first independent test of a microlensing detection and interpretation. The application of this process to other events will prove invaluable in tying together the disconnected parameter spaces of each planet detection technique, therefore allowing a more complete picture of the distribution of planetary systems to be developed.

In Chapter 5 we have developed a powerful tool for optimizing an exoplanetary microlensing survey by *Euclid*. Such a survey will probe the distribution of cold, low-mass planets at the position of the snow-line and beyond, completing the census of Earth-mass planets that *Kepler* has begun. The combined data sets of each method, with large numbers of detected planets, will allow theories of planet formation and evolution to be tested to an unprecedented degree. An understanding of these processes and the planetary systems that they form will ultimately lead to a much better

understanding of the number and types of planets that can potentially harbour life, which in turn will contribute to estimates of the abundance of life in the universe.

Appendix A

On the choice of detection criteria

In this appendix we discuss the choice of $\Delta\chi^2$ threshold for planet detections in Chapter 5, though much of the discussion also applies to the choice of threshold used in Chapter 3. In Chapter 5, we are concerned with determining if a planetary microlensing signature can be said to be detected.

The problem at hand is one of model selection: do we prefer the simpler single-lens model (model S), or do we prefer the more complicated planetary model (model B – for binary)? We can evaluate this quantitatively in a Bayesian framework, using our lightcurve data and our prior knowledge about the models and their parameters (see Gregory 2005, for a review). The posterior probability we assign to model S given the data D and background information I , $P(S|D, I)$, is by Bayes theorem

$$P(S|D, I) = \frac{P(D|S, I)P(S|I)}{P(D|I)}, \quad (\text{A.1})$$

where $P(D|S, I)$ is the probability of the data given the model, i.e., the likelihood, $P(S|I)$ is the prior probability we assign to the model and $P(D|I)$ is the evidence. A similar expression can be written for the posterior probability we assign to model B , $P(B|D, I)$.

To compare our two models we can take the ratio of their posterior probabilities, the Bayes factor,

$$\frac{P(B|D, I)}{P(S|D, I)} = \frac{P(D|B, I)P(B|I)}{P(D|S, I)P(S|I)}, \quad (\text{A.2})$$

where the evidence has cancelled out. If this ratio is large, then we favour the binary-lens model to that of the single lens. We may take the ratio of prior probabilities $P(B, I)/P(S|I)$ to be of the order of one, i.e., the lens is roughly as likely to be orbited by a planet as it is not to be. This leaves us with the ratio of likelihoods to be calculated.

The likelihood of model S , which has the set of parameters $\vec{\theta}_S$, is

$$P(D|S, I) = \int P(D|\vec{\theta}_S, S, I)P(\vec{\theta}_S|S, I)d\vec{\theta}_S, \quad (\text{A.3})$$

where $P(D|\vec{\theta}_S, S, I)$ is the likelihood of the set of parameters $\vec{\theta}_S$, $P(\vec{\theta}_S|S, I)$ is the prior probability of the parameters, and the integral marginalizes over the range of each parameter. A similar expression can be written for the likelihood of model B , $P(D|B, I)$, marginalized over the parameters $\vec{\theta}_B$.

The likelihood is related to the χ^2 for model S as

$$P(D|\vec{\theta}_S, S, I) \propto \exp\left(-\frac{\chi_S^2(\vec{\theta}_S)}{2}\right), \quad (\text{A.4})$$

where $\chi_S^2(\vec{\theta}_S)$ is the χ^2 of the single-lens model with parameters $\vec{\theta}_S$ and where the terms hidden by the proportionality sign depend only on the data. A similar expression can be written for $P(D|\vec{\theta}_B, B, I)$. The hidden data terms are equal for both models and can be taken outside the integral in Equation A.3 and will cancel each other in Equation A.2.

Before deciding on the priors of each parameter, we note that the single-lens model is a special case of the binary-lens model, with the parameters q (the mass ratio) and s (the projected separation) equal to zero and the source trajectory angle α becoming completely degenerate;¹ the other parameters of the model are identical. Also, in most cases the source radius ρ_* (in units of the Einstein radius) is almost completely degenerate in the single-lens model but not in the binary-lens model. If we choose uninformative, uniform priors (or logarithmic where necessary) on the common free parameters of the models, then the prior for each parameter can be taken outside of the integral in Equation A.3 to be cancelled in Equation A.2. We can also choose uninformative, uniform priors for the remaining four parameters of the binary-lens model s ,

¹ α should not be confused with the mass-function slope.

q , α and ρ_* to take them outside the integral. The priors

$$P(\log s|B, I) = \frac{1}{2 - (-1)}, \quad P(\log q|B, I) = \frac{1}{0 - (-8)}, \quad (\text{A.5})$$

$$P(\log \rho_*|B, I) = \frac{1}{-1 - (-7)} \quad \text{and} \quad P(\alpha|B, I) = \frac{1}{2\pi}, \quad (\text{A.6})$$

are suitably uninformative, i.e., $0.1 \leq s \leq 100$, $10^{-8} \leq q \leq 1$, $0 \leq \alpha < 2\pi$ and $10^{-7} \leq \rho_* \leq 0.1$.

We can now write down the ratio of posteriors

$$\frac{P(B|D, I)}{P(S|D, I)} = \frac{\frac{1}{288\pi} \int e^{-\chi_B^2/2} d\vec{\theta}_B}{\int e^{-\chi_S^2/2} d\vec{\theta}_S}. \quad (\text{A.7})$$

If we assume that the likelihood functions for both models are well described by multivariate Gaussians and that the parameters are uncorrelated, we can approximate the marginalized likelihood (Equation A.3) as

$$P(D|S, I) \approx \left(\prod_{i=0}^N \sqrt{2\pi\sigma_i} \right) \exp\left(-\frac{\chi_{S,\min}^2}{2}\right), \quad (\text{A.8})$$

(see, e.g., Gregory 2005) where σ_i is the uncertainty on the i^{th} parameter of $\vec{\theta}_S$ and $\chi_{S,\min}^2$ is the χ^2 of the best-fitting single-lens model, and similarly for $P(D|B, I)$. From here on we will drop the ‘min’ subscript and all usage of χ^2 that follows will assume that it is the χ^2 of the best-fitting model. We will return to the assumption of no correlation later.

It is reasonable to assume that the uncertainties on the common parameters of each model will be of similar magnitude, (though the uncertainty of these parameters in the binary-lens model will be slightly larger due to the additional freedom afforded by each additional free parameter). The uncertainties on the common parameters then cancel, and we are left with

$$\frac{P(B|D, I)}{P(S|D, I)} \approx \frac{(2\pi)^2 \sigma_{\log s} \sigma_{\log q} \sigma_\alpha \sigma_{\log \rho_*} e^{-\chi_B^2/2}}{288\pi e^{-\chi_S^2/2}} \quad (\text{A.9})$$

$$\approx \frac{\pi}{72} \sigma_{\log s} \sigma_{\log q} \sigma_\alpha \sigma_{\log \rho_*} \exp\left(-\frac{\Delta\chi^2}{2}\right), \quad (\text{A.10})$$

where $\Delta\chi^2 = \chi_S^2 - \chi_B^2$. As $\Delta\chi^2$ can become very large, it is helpful to take logs of both sides of Equation A.10

$$\Delta L \approx \frac{\Delta\chi^2}{2} + \ln \sigma_{\log s} + \ln \sigma_{\log q} + \ln \sigma_\alpha + \ln \sigma_{\log \rho_*} - 3.1, \quad (\text{A.11})$$

where $\Delta L = \ln P(B|D, I) - \ln P(S|D, I)$; note the order of the subtraction is opposite to that of $\Delta\chi^2$. So, if $\Delta L \gtrsim 3$ or so, i.e., the ratio of posterior probabilities is greater than 10^3 or so, then the binary-lens model is favoured. In fact, if we want to be conservative and require that the binary model be ‘strongly favoured’ we should require $\Delta L > 10$ (Jeffreys 1961; Robert et al. 2009).

Equation A.11 implies that for a fixed $\Delta\chi^2$ we will be *less* likely to believe a detection the *smaller* the error bars on its parameters are. This is to be expected. We should be suspicious of a model if the parameters need very fine tuning to produce only a weak signal. Assuming that the uncertainties on each parameter were equal, even for $\Delta\chi^2 = 100$, which is below our adopted threshold, the uncertainty would have to be $< 10^{-4}$ on each parameter in order to warrant suspicion about the detection. This seems to be unlikely for planetary microlensing events.

At this point it is worth investigating some examples. Figures A.1 and A.2 show two example lightcurves of $\Delta\chi^2 \approx 100$ from an earlier simulation of the *Euclid* mission using a version of *MaBμLS* that did not include image simulations. Figure A.1 involves a Mars-mass planet, and the planetary deviation is very localized. Figure A.2 involves a $100-M_\oplus$ planet with a deviation that covers a significant fraction of the lightcurve, but with an amplitude less than the uncertainty in individual data points. We performed a Markov Chain Monte Carlo (MCMC) minimization using the method of Doran and Müller (2004) on each of the lightcurves in order to evaluate the uncertainties on the event parameters.

The results of the MCMC minimization are shown in Figure A.3. It is clear that these $\Delta\chi^2 \approx 100$ detections provide measurements of the mass ratio and projected separation of the planets, though the uncertainties in these measurements are significantly larger than those for a much stronger detection such as that shown in Figure A.4. The

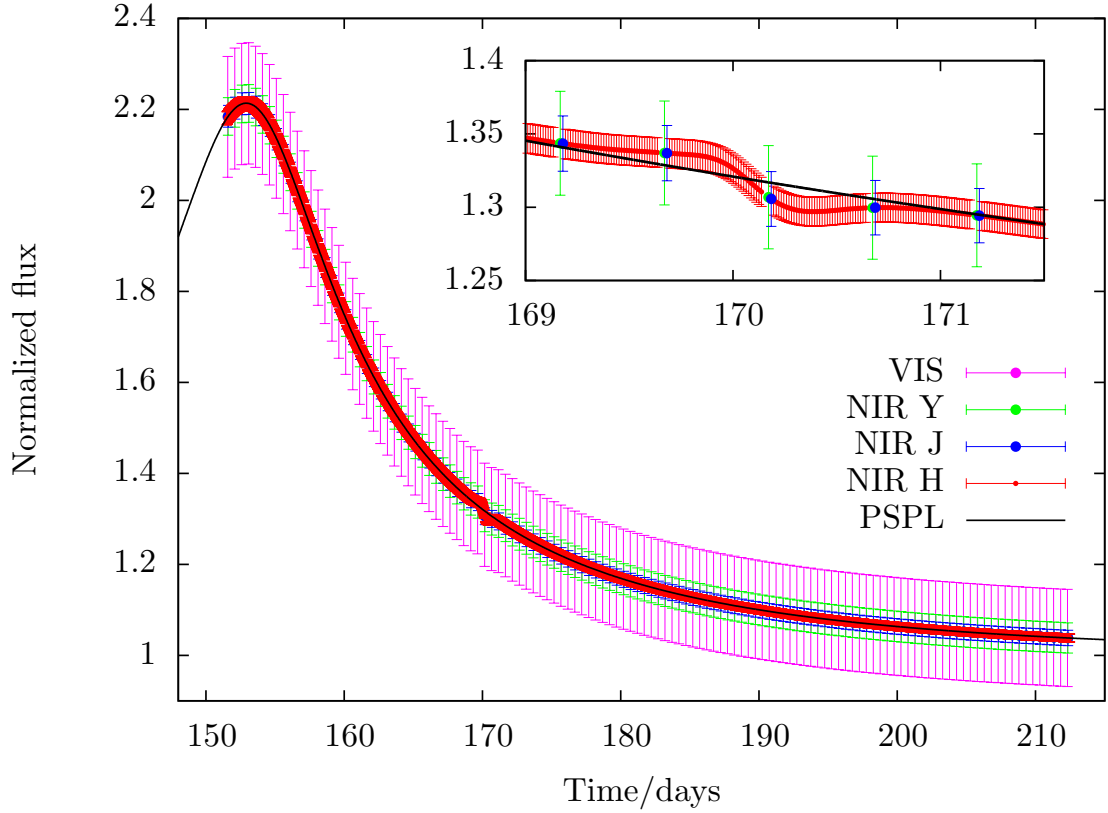


Figure A.1 – Lightcurve of a $0.1-M_{\oplus}$ planet orbiting a $0.14-M_{\odot}$ star at 0.68 AU, which is detected with $\Delta\chi^2 = 103$. The planet causes a ~ 2 -day deviation in the wing of the host star’s microlensing event, which has an amplitude similar to the accuracy of the primary H -band photometry. Different coloured points with error bars show photometric data points and their uncertainties in different bands, magenta showing data in the broad visual-band (VIS) and green, blue and red showing data in the near infrared Y -, J - and primary H -band respectively. The black line shows the best-fitting point-lens model. The inset figure shows a close-up of the planetary deviation, with VIS data points removed for clarity. Fluxes in each band have been scaled to that of the H -band. All other lightcurve examples in this Appendix will follow the same conventions, unless otherwise stated. The events shown in this chapter were generated in a previous version of *MaB μ LS* which did not use image simulations.

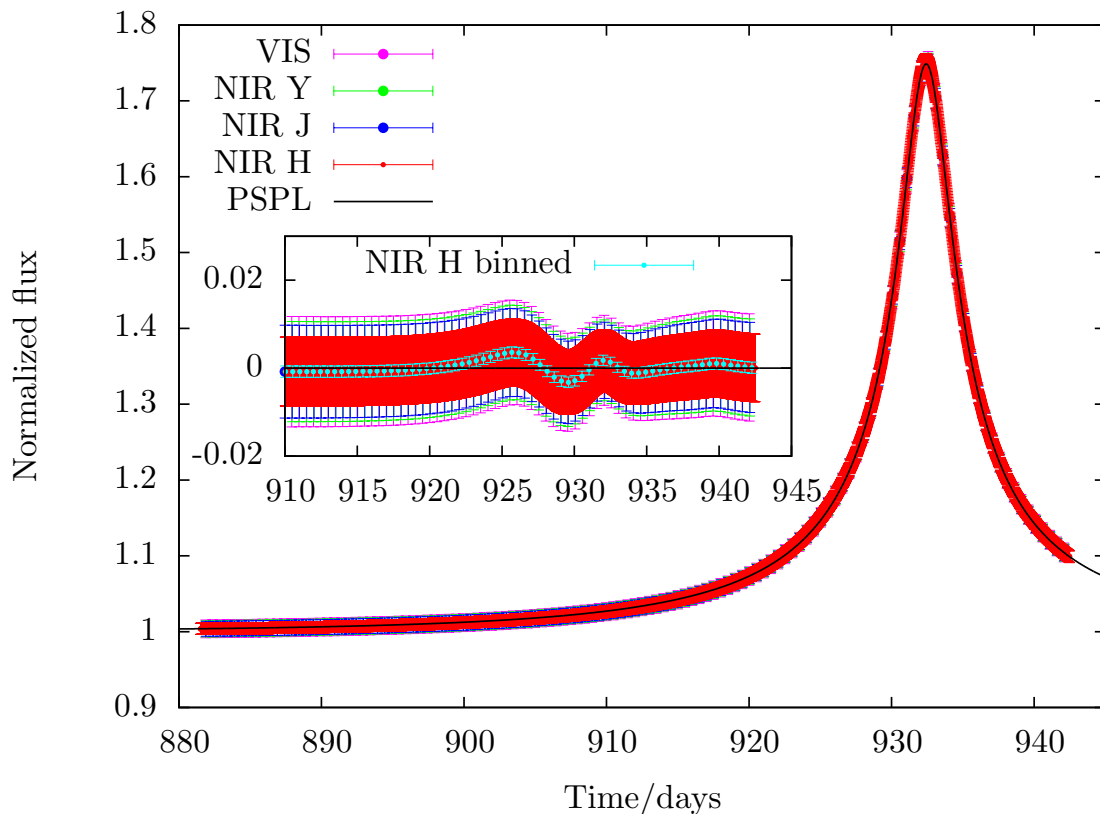


Figure A.2 – A $\Delta\chi^2 = 102$ detection of a $100-M_{\oplus}$ planet orbiting a $0.21-M_{\odot}$ star at 1.3 AU. The inset shows the residual with respect to the best-fit point-lens model. The deviation, which covers most of the event, is clearly detectable in the binned H -band residuals, shown with cyan points.

ΔL values for each of the examples are:

- $0.1-M_{\oplus}$ planet (top left of Figure A.3): $\Delta L = 32.1$,
- $100-M_{\oplus}$ planet (top right): $\Delta L = 35.9$,
- $10-M_{\oplus}$ planet (bottom left): $\Delta L = 29400$,

where we have taken the errors on each parameter to be the projected uncertainties (i.e. the square root of the variance of the parameter values of points in the MCMC run). In each case the binary-lens interpretation is strongly favoured. However, it can be seen that in some cases the parameters are correlated. Correlations will reduce ΔL , because

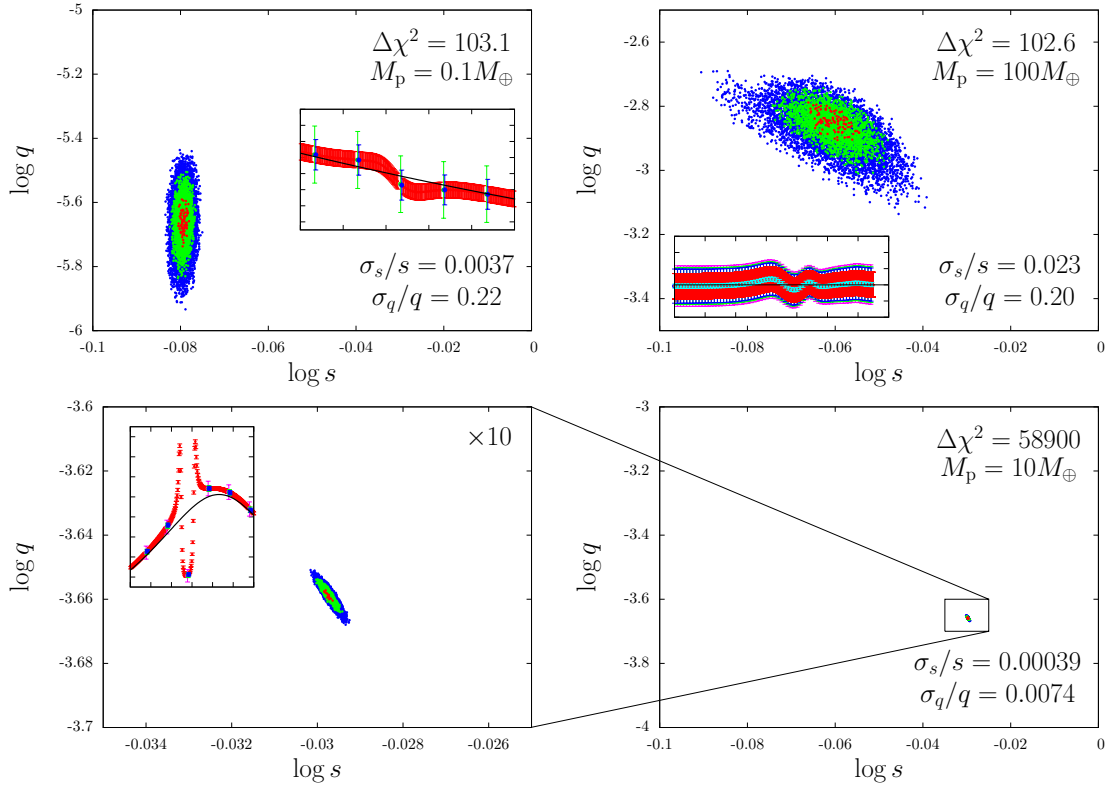


Figure A.3 – Results of an optimized Markov Chain Monte Carlo (MCMC) routine used to model the lightcurves of the example events shown in Figures A.1 (top left-hand panel) and A.2 (top right-hand panel). The red, green and blue points fill in 1-, 2- and 3- σ error ellipses in the $\log q$ - $\log s$ plane, respectively. The inset panels show the planetary deviation being modelled. The bottom right-hand panel shows the results of an MCMC minimization for a much stronger $\Delta\chi^2 = 58900$ detection, the lightcurve for which is shown in Figure A.4. These three panels are shown at the same scale, with a range in $\log s$ of 0.1 and a range in $\log q$ of 1. The bottom left-hand panel zooms in by a factor of ten on the error ellipse for the strong detection.

the error ellipses will fill a smaller fraction of the space allowed by the priors than is suggested by their projected errors. However, even for the $\Delta\chi^2$ cases we show, the correlations would have to be extremely strong to reduce ΔL to 10. This suggests that a $\Delta\chi^2$ threshold of 100 or even lower may be sufficient to define a planet detection.

We have derived an approximate expression for the Bayes factor of a model se-

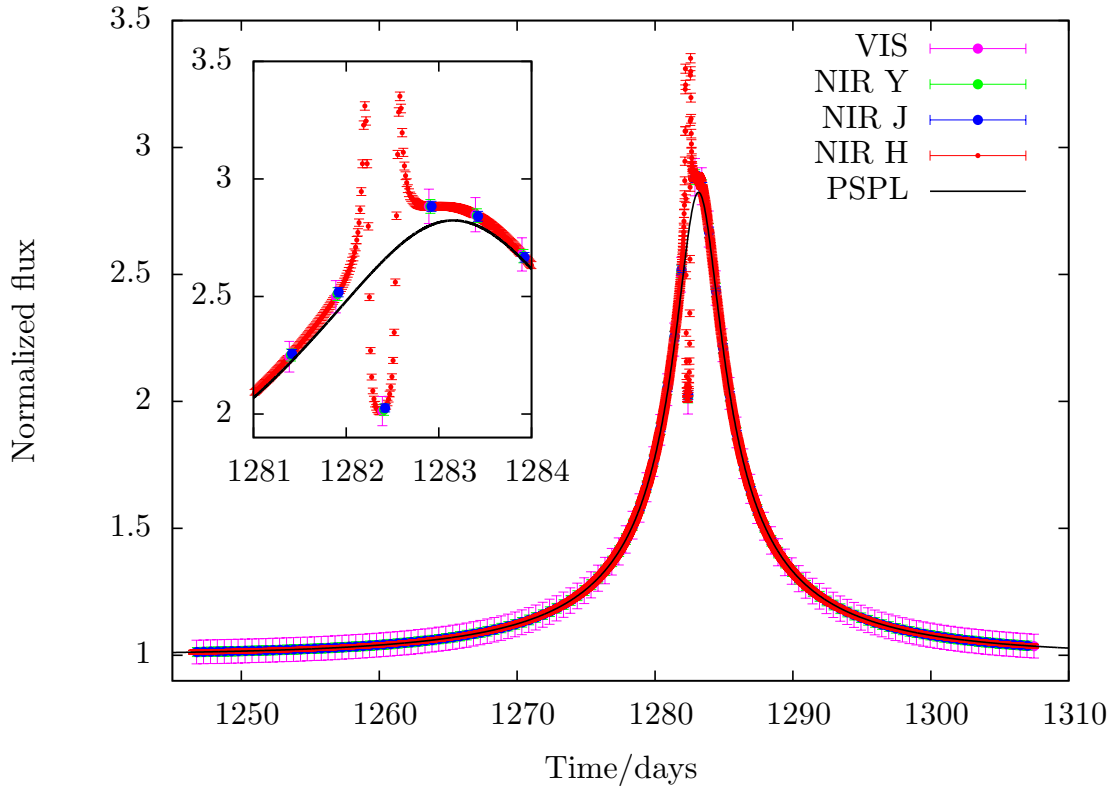


Figure A.4 – A strong, $\Delta\chi^2 = 58900$, detection of a $10-M_{\oplus}$ planet orbiting a $0.14-M_{\odot}$ star at 0.82 AU.

lection problem between a binary- and a single-lens model of a microlensing event. The uncertainties of the binary-lens model parameters for two low- χ^2 example events, suggest a $\Delta\chi^2$ threshold of 100 would be sufficient to claim detection of a planet, and that even lower thresholds may be possible. However, while we have shown that a binary-lens interpretation is strongly favoured over a single-lens model, we have not shown that it is preferred over any other plausible models, such as a binary-source star being lensed, or a blended irregular or long-period variable star. These are not simulated in our model so it is easy to rule them out, but in the real data this will not be so easy. Each of these types of potential false positive event may or will occur and some of their lightcurves will pass the simple $\Delta\chi^2$ cut we have used here. The $\Delta\chi^2$ cut will not be the only cut that planet detections will have to pass. In future work it will be important to model these cuts as well.

References

- H. A. Abt. Normal and abnormal binary frequencies. *ARA&A*, 21:343–372, 1983.
- C. Afonso, J. N. Albert, J. Andersen, R. Ansari, É. Aubourg, P. Bareyre, J. P. Beaulieu, G. Blanc, X. Charlot, F. Couchot, C. Coutures, R. Ferlet, P. Fouqué, J. F. Glicenstein, B. Goldman, A. Gould, D. Graff, M. Gros, J. Haissinski, C. Hamadache, J. de Kat, T. Lasserre, L. Le Guillou, É. Lesquoy, C. Loup, C. Magneville, J. B. Marquette, É. Maurice, A. Maury, A. Milsztajn, M. Moniez, N. Palanque-Delabrouille, O. Perdereau, L. Prévot, Y. R. Rahal, J. Rich, M. Spiro, P. Tisserand, A. Vidal-Madjar, L. Vigroux, and S. Zylberajch. Limits on Galactic dark matter with 5 years of EROS SMC data. *A&A*, 400:951–956, March 2003.
- C. Alard. Image subtraction using a space-varying kernel. *A&AS*, 144:363–370, June 2000.
- C. Alard and R. H. Lupton. A Method for Optimal Image Subtraction. *ApJ*, 503:325–331, August 1998.
- M. D. Albrow, J.-P. Beaulieu, J. A. R. Caldwell, M. Dominik, B. S. Gaudi, A. Gould, J. Greenhill, K. Hill, S. Kane, R. Martin, J. Menzies, R. M. Naber, K. R. Pollard, P. D. Sackett, K. C. Sahu, P. Vermaak, R. Watson, A. Williams, H. E. Bond, and I. M. van Bemmell. Detection of Rotation in a Binary Microlens: PLANET Photometry of MACHO 97-BLG-41. *ApJ*, 534:894–906, May 2000.
- C. Alcock, R. A. Allsman, D. Alves, T. S. Axelrod, D. Baines, A. C. Becker, D. P. Bennett, A. Bourke, A. Brakel, K. H. Cook, B. Crook, A. Crouch, J. Dan, A. J. Drake, P. C. Fragile, K. C. Freeman, A. Gal-Yam, M. Geha, J. Gray, K. Griest, A. Gurtierrez, A. Heller, J. Howard, B. R. Johnson, S. Kaspi, M. Keane, O. Kovo, C. Leach, T. Leach, E. M. Leibowitz, M. J. Lehner, Y. Lipkin, D. Maoz, S. L. Marshall, D. McDowell, S. McKeown, H. Mendelson, B. Messenger, D. Minniti, C. Nelson, B. A. Peterson, P. Popowski, E. Pozza, P. Purcell, M. R. Pratt, J. Quinn, P. J. Quinn, S. H.

- Rhie, A. W. Rodgers, A. Salmon, O. Shemmer, P. Stetson, C. W. Stubbs, W. Sutherland, S. Thomson, A. Tomaney, T. Vandehei, A. Walker, K. Ward, and G. Wyper. Binary Microlensing Events from the MACHO Project. *ApJ*, 541:270–297, September 2000a.
- C. Alcock, R. A. Allsman, D. Alves, T. S. Axelrod, D. P. Bennett, K. H. Cook, K. C. Freeman, K. Griest, J. Guern, M. J. Lehner, S. L. Marshall, B. A. Peterson, M. R. Pratt, P. J. Quinn, A. W. Rodgers, C. W. Stubbs, and W. Sutherland. First Observation of Parallax in a Gravitational Microlensing Event. *ApJL*, 454:L125–L128, December 1995.
- C. Alcock, R. A. Allsman, D. R. Alves, T. S. Axelrod, A. C. Becker, D. P. Bennett, K. H. Cook, N. Dalal, A. J. Drake, K. C. Freeman, M. Geha, K. Griest, M. J. Lehner, S. L. Marshall, D. Minniti, C. A. Nelson, B. A. Peterson, P. Popowski, M. R. Pratt, P. J. Quinn, C. W. Stubbs, W. Sutherland, A. B. Tomaney, T. Vandehei, and D. Welch. The MACHO Project: Microlensing Results from 5.7 Years of Large Magellanic Cloud Observations. *ApJ*, 542:281–307, October 2000b.
- C. Alcock, R. A. Allsman, D. R. Alves, T. S. Axelrod, A. C. Becker, D. P. Bennett, K. H. Cook, A. J. Drake, K. C. Freeman, M. Geha, K. Griest, S. C. Keller, M. J. Lehner, S. L. Marshall, D. Minniti, C. A. Nelson, B. A. Peterson, P. Popowski, M. R. Pratt, P. J. Quinn, C. W. Stubbs, W. Sutherland, A. B. Tomaney, T. Vandehei, and D. Welch. Direct detection of a microlens in the Milky Way. *Nature*, 414:617–619, December 2001a.
- C. Alcock, R. A. Allsman, D. R. Alves, T. S. Axelrod, A. C. Becker, D. P. Bennett, K. H. Cook, A. J. Drake, K. C. Freeman, M. Geha, K. Griest, M. J. Lehner, S. L. Marshall, D. Minniti, C. A. Nelson, B. A. Peterson, P. Popowski, M. R. Pratt, P. J. Quinn, C. W. Stubbs, W. Sutherland, A. B. Tomaney, T. Vandehei, and D. Welch. The MACHO Project: Microlensing Detection Efficiency. *ApJS*, 136:439–462, October 2001b.
- J. H. An. Gravitational lens under perturbations: symmetry of perturbing potentials with invariant caustics. *MNRAS*, 356:1409–1428, February 2005.
- J. H. An, M. D. Albrow, J.-P. Beaulieu, J. A. R. Caldwell, D. L. DePoy, M. Dominik, B. S. Gaudi, A. Gould, J. Greenhill, K. Hill, S. Kane, R. Martin, J. Menzies, R. W. Pogge, K. R. Pollard, P. D. Sackett, K. C. Sahu, P. Vermaak, R. Watson, and A. Williams. First Microlens Mass Measurement: PLANET Photometry of EROS BLG-2000-5. *ApJ*, 572:521–539, June 2002.

- C. Babusiaux and G. Gilmore. The structure of the Galactic bar. *MNRAS*, 358:1309–1319, April 2005.
- V. Batista, A. Gould, S. Dieters, S. Dong, I. Bond, J. P. Beaulieu, D. Maoz, B. Monard, G. W. Christie, J. McCormick, M. D. Albrow, K. Horne, Y. Tsapras, M. J. Burgdorf, S. Calchi Novati, J. Skottfelt, J. Caldwell, S. Kozłowski, D. Kubas, B. S. Gaudi, C. Han, D. P. Bennett, J. An, The MOA Collaboration, F. Abe, C. S. Botzler, D. Douchin, M. Freeman, A. Fukui, K. Furusawa, J. B. Hearnshaw, S. Hosaka, Y. Itow, K. Kamiya, P. M. Kilmartin, A. Korpela, W. Lin, C. H. Ling, B. S. Makita, K. Masuda, Y. Matsubara, N. Miyake, Y. Muraki, M. Nagaya, K. Nishimoto, K. Ohnishi, T. Okumura, Y. C. Perrott, N. Rattenbury, T. Saito, D. J. Sullivan, T. Sumi, W. L. Sweatman, P. J. Tristram, E. von Seggern, P. C. M. Yock, The PLANET Collaboration, S. Brilliant, J. J. Calitz, A. Cassan, A. Cole, K. Cook, C. Coutures, D. Dominis Prester, J. Donatowicz, J. Greenhill, M. Hoffman, F. Jablonski, S. R. Kane, N. Kains, J.-B. Marquette, R. Martin, E. Martioli, P. Meintjes, J. Menzies, E. Pedretti, K. Pollard, K. C. Sahu, C. Vinter, J. Wambsganss, R. Watson, A. Williams, M. Zub, The FUN Collaboration, W. Allen, G. Bolt, M. Bos, D. L. DePoy, J. Drummond, J. D. Eastman, A. Gal-Yam, E. Gorbikov, D. Higgins, J. Janczak, S. Kaspi, C.-U. Lee, F. Mallia, A. Maury, L. A. G. Monard, D. Moorhouse, N. Morgan, T. Natusch, E. O. Ofek, B.-G. Park, R. W. Pogge, D. Polishook, R. Santallo, A. Shporer, O. Spector, G. Thornley, J. C. Yee, The MiNDSTeP Consortium, V. Bozza, P. Browne, M. Dominik, S. Dreizler, F. Finet, M. Glittrup, F. Grundahl, K. Harpsøe, F. V. Hessman, T. C. Hinse, M. Hundertmark, U. G. Jørgensen, C. Liebig, G. Maier, L. Mancini, M. Mathiasen, S. Rahvar, D. Ricci, G. Scarpetta, J. Southworth, J. Surdej, F. Zimmer, The RoboNet Collaboration, A. Allan, D. M. Bramich, C. Snodgrass, I. A. Steele, and R. A. Street. MOA-2009-BLG-387Lb: a massive planet orbiting an M dwarf. *A&A*, 529:A102–A118, May 2011.
- J. P. Beaulieu, D. P. Bennett, V. Batista, A. Cassan, D. Kubas, P. Fouqué, E. Kerrins, S. Mao, J. Miralda-Escudé, J. Wambsganss, B. S. Gaudi, A. Gould, and S. Dong. EUCLID: Dark Universe Probe and Microlensing Planet Hunter. In V. Coudé Du Foresto, D. M. Gelino, & I. Ribas, editor, *Pathways Towards Habitable Planets*, volume 430 of *Astronomical Society of the Pacific Conference Series*, pages 266–271, October 2010.
- J.-P. Beaulieu, D. P. Bennett, P. Fouqué, A. Williams, M. Dominik, U. G. Jørgensen,

- D. Kubas, A. Cassan, C. Coutures, J. Greenhill, K. Hill, J. Menzies, P. D. Sackett, M. Albrow, S. Brilliant, J. A. R. Caldwell, J. J. Calitz, K. H. Cook, E. Corrales, M. Desort, S. Dieters, D. Dominis, J. Donatowicz, M. Hoffman, S. Kane, J.-B. Marquette, R. Martin, P. Meintjes, K. Pollard, K. Sahu, C. Vinter, J. Wambsganss, K. Woller, K. Horne, I. Steele, D. M. Bramich, M. Burgdorf, C. Snodgrass, M. Bode, A. Udalski, M. K. Szymański, M. Kubiak, T. Więckowski, G. Pietrzyński, I. Soszyński, O. Szewczyk, Ł. Wyrzykowski, B. Paczyński, F. Abe, I. A. Bond, T. R. Britton, A. C. Gilmore, J. B. Hearnshaw, Y. Itow, K. Kamiya, P. M. Kilmartin, A. V. Korpela, K. Masuda, Y. Matsubara, M. Motomura, Y. Muraki, S. Nakamura, C. Okada, K. Ohnishi, N. J. Rattenbury, T. Sako, S. Sato, M. Sasaki, T. Sekiguchi, D. J. Sullivan, P. J. Tristram, P. C. M. Yock, and T. Yoshioka. Discovery of a cool planet of 5.5 Earth masses through gravitational microlensing. *Nature*, 439:437–440, January 2006.
- J. W. Beletic, R. Blank, D. Gulbransen, D. Lee, M. Loose, E. C. Piquette, T. Sprafke, W. E. Tennant, M. Zandian, and J. Zino. Teledyne Imaging Sensors: infrared imaging technologies for astronomy and civil space. In *Society of Photo-Optical Instrumentation Engineers (SPIE) Conference Series*, volume 7021 of *Presented at the Society of Photo-Optical Instrumentation Engineers (SPIE) Conference*, August 2008.
- R. A. Benjamin, E. Churchwell, B. L. Babler, R. Indebetouw, M. R. Meade, B. A. Whitney, C. Watson, M. G. Wolfire, M. J. Wolff, R. Ignace, T. M. Bania, S. Bracker, D. P. Clemens, L. Chomiuk, M. Cohen, J. M. Dickey, J. M. Jackson, H. A. Kobulnicky, E. P. Mercer, J. S. Mathis, S. R. Stolovy, and B. Uzpen. First GLIMPSE Results on the Stellar Structure of the Galaxy. *ApJL*, 630:L149–L152, September 2005.
- D. P. Bennett. The Detection of Terrestrial Planets via Gravitational Microlensing: Space vs. Ground-based Surveys. In J. Beaulieu, A. Lecavelier Des Etangs, & C. Terquem, editor, *Extrasolar Planets: Today and Tomorrow*, volume 321 of *Astronomical Society of the Pacific Conference Series*, pages 59–67, December 2004.
- D. P. Bennett. An Efficient Method for Modeling High-magnification Planetary Microlensing Events. *ApJ*, 716:1408–1422, June 2010.
- D. P. Bennett. The Microlensing Planet Search Program of the WFIRST Mission. In *American Astronomical Society Meeting Abstracts #217*, volume 43 of *Bulletin of the American Astronomical Society*, page 318.01, January 2011.

- D. P. Bennett, J. Anderson, I. A. Bond, A. Udalski, and A. Gould. Identification of the OGLE-2003-BLG-235/MOA-2003-BLG-53 Planetary Host Star. *ApJL*, 647:L171–L174, August 2006.
- D. P. Bennett, J. Anderson, and B. S. Gaudi. Characterization of Gravitational Microlensing Planetary Host Stars. *ApJ*, 660:781–790, May 2007.
- D. P. Bennett, I. A. Bond, A. Udalski, T. Sumi, F. Abe, A. Fukui, K. Furusawa, J. B. Hearnshaw, S. Holderness, Y. Itow, K. Kamiya, A. V. Korpela, P. M. Kilmartin, W. Lin, C. H. Ling, K. Masuda, Y. Matsubara, N. Miyake, Y. Muraki, M. Nagaya, T. Okumura, K. Ohnishi, Y. C. Perrott, N. J. Rattenbury, T. Sako, T. Saito, S. Sato, L. Skuljan, D. J. Sullivan, W. L. Sweatman, P. J. Tristram, P. C. M. Yock, M. Kubiak, M. K. Szymański, G. Pietrzyński, I. Soszyński, O. Szewczyk, Ł. Wyrzykowski, K. Ulaczyk, V. Batista, J. P. Beaulieu, S. Brilliant, A. Cassan, P. Fouqué, P. Kervella, D. Kubas, and J. B. Marquette. A Low-Mass Planet with a Possible Sub-Stellar-Mass Host in Microlensing Event MOA-2007-BLG-192. *ApJ*, 684:663–683, September 2008.
- D. P. Bennett and S. H. Rhie. Detecting Earth-Mass Planets with Gravitational Microlensing. *ApJ*, 472:660–664, November 1996.
- D. P. Bennett and S. H. Rhie. Simulation of a Space-based Microlensing Survey for Terrestrial Extrasolar Planets. *ApJ*, 574:985–1003, August 2002.
- D. P. Bennett, S. H. Rhie, S. Nikolaev, B. S. Gaudi, A. Udalski, A. Gould, G. W. Christie, D. Maoz, S. Dong, J. McCormick, M. K. Szymański, P. J. Tristram, B. Macintosh, K. H. Cook, M. Kubiak, G. Pietrzyński, I. Soszyński, O. Szewczyk, K. Ulaczyk, Ł. Wyrzykowski, The OGLE Collaboration, D. L. DePoy, C. Han, S. Kaspi, C.-U. Lee, F. Mallia, T. Natusch, B.-G. Park, R. W. Pogge, D. Polishook, The μ FUN Collaboration, F. Abe, I. A. Bond, C. S. Botzler, A. Fukui, J. B. Hearnshaw, Y. Itow, K. Kamiya, A. V. Korpela, P. M. Kilmartin, W. Lin, J. Ling, K. Masuda, Y. Matsubara, M. Motomura, Y. Muraki, S. Nakamura, T. Okumura, K. Ohnishi, Y. C. Perrott, N. J. Rattenbury, T. Sako, T. Saito, S. Sato, L. Skuljan, D. J. Sullivan, T. Sumi, W. L. Sweatman, P. C. M. Yock, The MOA Collaboration, M. Albrow, A. Allan, J.-P. Beaulieu, D. M. Bramich, M. J. Burgdorf, C. Coutures, M. Dominik, S. Dieters, P. Fouqué, J. Greenhill, K. Horne, C. Snodgrass, I. Steele, Y. Tsapras, F. t. PLANET, RoboNet Collaborations, B. Chaboyer, A. Crocker, and S. Frank. Masses and Orbital Constraints for the OGLE-2006-BLG-109Lb,c Jupiter/Saturn Analog Planetary System. *ApJ*, 713:837–855, April

2010.

- P. Bergeron, F. Wesemael, and A. Beauchamp. Photometric Calibration of Hydrogen- and Helium-Rich White Dwarf Models. *PASP*, 107:1047–1054, November 1995.
- O. Bienayme, A. C. Robin, and M. Creze. The mass density in our Galaxy. *A&A*, 180: 94–110, June 1987.
- J. Binney and S. Tremaine. *Galactic Dynamics: Second Edition*. Princeton University Press, 2008.
- N. Bissantz, P. Englmaier, J. Binney, and O. Gerhard. The microlensing optical depth of the COBE bulge. *MNRAS*, 289:651–659, August 1997.
- R. D. Blandford, M. P. Haynes, J. P. Huchra, L. Hillenbrand, S. J. Battel, L. Bildsten, J. E. Carlstrom, D. M. Elmegreen, J. Frieman, F. A. Harrison, T. M. Heckman, R. C. Kennicutt, Jr., J. I. Lunine, C. E. Max, D. McCammon, S. M. Ritz, J. Toomre, S. D. Tremaine, M. S. Turner, N. deGrasse Tyson, P. A. Vanden Bout, A. T. Young, D. C. Shapero, M. H. Moloney, B. L. Sponberg, R. L. Riemer, B. D. Dewhurst, J. C. Lancaster, D. B. Lang, T. Thorowgood, C. Chamberlain, C. Gruber, C. J. Knutson, L. Coates-Fogle, and B. Dolan. *New Worlds, New Horizons in Astronomy and Astrophysics*. National Academies Press, 2010.
- A. F. Boden, A. I. Sargent, R. L. Akeson, J. M. Carpenter, G. Torres, D. W. Latham, D. R. Soderblom, E. Nelan, O. G. Franz, and L. H. Wasserman. Dynamical Masses for Low-Mass Pre-Main-Sequence Stars: A Preliminary Physical Orbit for HD 98800 B. *ApJ*, 635:442–451, December 2005.
- A. D. Bolatto and E. E. Falco. The detectability of planetary companions of compact Galactic objects from their effects on microlensed light curves of distant stars. *ApJ*, 436:112–116, November 1994.
- I. A. Bond, A. Udalski, M. Jaroszyński, N. J. Rattenbury, B. Paczyński, I. Soszyński, Ł. Wyrzykowski, M. K. Szymański, M. Kubiak, O. Szewczyk, K. Żebruń, G. Pietrzyński, F. Abe, D. P. Bennett, S. Eguchi, Y. Furuta, J. B. Hearnshaw, K. Kamiya, P. M. Kilmartin, Y. Kurata, K. Masuda, Y. Matsubara, Y. Muraki, S. Noda, K. Okajima, T. Sako, T. Sekiguchi, D. J. Sullivan, T. Sumi, P. J. Tristram, T. Yanagisawa, and P. C. M. Yock. OGLE 2003-BLG-235/MOA 2003-BLG-53: A Planetary Microlensing Event. *ApJL*, 606:L155–L158, May 2004.
- W. J. Borucki, D. G. Koch, G. Basri, N. Batalha, T. M. Brown, S. T. Bryson, D. Caldwell, J. Christensen-Dalsgaard, W. D. Cochran, E. DeVore, E. W. Dunham, T. N.

- Gautier, III, J. C. Geary, R. Gilliland, A. Gould, S. B. Howell, J. M. Jenkins, D. W. Latham, J. J. Lissauer, G. W. Marcy, J. Rowe, D. Sasselov, A. Boss, D. Charbonneau, D. Ciardi, L. Doyle, A. K. Dupree, E. B. Ford, J. Fortney, M. J. Holman, S. Seager, J. H. Steffen, J. Tarter, W. F. Welsh, C. Allen, L. A. Buchhave, J. L. Christiansen, B. D. Clarke, S. Das, J.-M. Désert, M. Endl, D. Fabrycky, F. Fressin, M. Haas, E. Horch, A. Howard, H. Isaacson, H. Kjeldsen, J. Kolodziejczak, C. Kulesa, J. Li, P. W. Lucas, P. Machalek, D. McCarthy, P. MacQueen, S. Meibom, T. Miquel, A. Prsa, S. N. Quinn, E. V. Quintana, D. Ragozzine, W. Sherry, A. Shporer, P. Tenenbaum, G. Torres, J. D. Twicken, J. Van Cleve, L. Walkowicz, F. C. Witteborn, and M. Still. Characteristics of Planetary Candidates Observed by Kepler. II. Analysis of the First Four Months of Data. *ApJ*, 736:19–41, July 2011.
- A. P. Boss. Giant planet formation by gravitational instability. *Science*, 276:1836–1839, 1997.
- A. P. Boss. Rapid Formation of Super-Earths around M Dwarf Stars. *ApJL*, 644:L79–L82, June 2006.
- A. P. Boss. Formation of Giant Planets by Disk Instability on Wide Orbits Around Protostars with Varied Masses. *ApJ*, 731:74–87, April 2011.
- R. R. Bourassa, R. Kantowski, and T. D. Norton. The Spheroidal Gravitational Lens. *ApJ*, 185:747–756, November 1973.
- V. Bozza. Perturbative analysis in planetary gravitational lensing. *A&A*, 348:311–326, August 1999.
- V. Bozza. Caustics in special multiple lenses. *A&A*, 355:423–432, March 2000a.
- V. Bozza. Secondary caustics in close multiple lenses. *A&A*, 359:1–8, July 2000b.
- V. Bozza. Microlensing with an advanced contour integration algorithm: Green’s theorem to third order, error control, optimal sampling and limb darkening. *MNRAS*, 408:2188–2200, November 2010.
- D. M. Bramich. A new algorithm for difference image analysis. *MNRAS*, 386:L77–L81, May 2008.
- A. Buchalter and M. Kamionkowski. Rates for Parallax-shifted Microlensing Events from Ground-based Observations of the Galactic Bulge. *ApJ*, 482:782–791, June 1997.
- A. Buchalter, M. Kamionkowski, and R. M. Rich. Rates for Color-shifted Microlensing Events. *ApJ*, 469:676–690, October 1996.

- A. Cabrera-Lavers, P. L. Hammersley, C. González-Fernández, M. López-Corredoira, F. Garzón, and T. J. Mahoney. Tracing the long bar with red-clump giants. *A&A*, 465:825–838, April 2007.
- A. G. W. Cameron. Physics of the primitive solar accretion disk. *Moon and Planets*, 18:5–40, February 1978.
- S. Casertano, M. G. Lattanzi, A. Sozzetti, A. Spagna, S. Jancart, R. Morbidelli, R. Panunzio, D. Pourbaix, and D. Queloz. Double-blind test program for astrometric planet detection with Gaia. *A&A*, 482:699–729, May 2008.
- A. Cassan. An alternative parameterisation for binary-lens caustic-crossing events. *A&A*, 491:587–595, November 2008.
- G. Chabrier. Is Galactic Dark Matter White? *ApJL*, 513:L103–L106, March 1999.
- A. M. Cherepashchuk, M. V. Sazhin, and I. A. Trifalencov. Effects of Gravitational Microlensing of Binary and Multiple Stars. *Ap&SS*, 229:265–299, July 1995.
- S.-J. Chung. Characterization of the Resonant Caustic Perturbation. *ApJ*, 705:386–390, November 2009.
- S.-J. Chung, C. Han, B.-G. Park, D. Kim, S. Kang, Y.-H. Ryu, K. M. Kim, Y.-B. Jeon, D.-W. Lee, K. Chang, W.-B. Lee, and Y. H. Kang. Properties of Central Caustics in Planetary Microlensing. *ApJ*, 630:535–542, September 2005.
- S.-J. Chung and C.-U. Lee. Properties of the planetary caustic perturbation. *MNRAS*, 411:151–154, February 2011.
- M. Cropper, A. Refregier, P. Guttridge, O. Boulade, J. Amiaux, D. Walton, P. Thomas, K. Rees, P. Pool, J. Endicott, A. Holland, J. Gow, N. Murray, A. Amara, D. Lumb, L. Duvet, R. Cole, J.-L. Augeres, and G. Hopkinson. VIS: the visible imager for Euclid. In *Society of Photo-Optical Instrumentation Engineers (SPIE) Conference Series*, volume 7731 of *Society of Photo-Optical Instrumentation Engineers (SPIE) Conference Series*, July 2010.
- A. Cumming, R. P. Butler, G. W. Marcy, S. S. Vogt, J. T. Wright, and D. A. Fischer. The Keck Planet Search: Detectability and the Minimum Mass and Orbital Period Distribution of Extrasolar Planets. *PASP*, 120:531–554, May 2008.
- T. Currie. On the Semimajor Axis Distribution of Extrasolar Gas Giant Planets: Why Hot Jupiters are Rare Around High-Mass Stars. *ApJL*, 694:L171–L176, April 2009.
- R. M. Cutri, M. F. Skrutskie, S. van Dyk, C. A. Beichman, J. M. Carpenter, T. Chester, L. Cambresy, T. Evans, J. Fowler, J. Gizis, E. Howard, J. Huchra, T. Jarrett, E. L.

- Kopan, J. D. Kirkpatrick, R. M. Light, K. A. Marsh, H. McCallon, S. Schneider, R. Stiening, M. Sykes, M. Weinberg, W. A. Wheaton, S. Wheelock, and N. Zacarias. *2MASS All Sky Catalog of point sources*. NASA/IPAC Infrared Science Archive, June 2003.
- G. D’Angelo, R. H. Durisen, and J. J. Lissauer. *Giant Planet Formation*, pages 319–346. Univ. of Arizona press, 2011.
- R. Di Stefano and A. A. Esin. Blending of Light in Gravitational Microlensing Events. *ApJL*, 448:L1–L4, July 1995.
- M. Dominik. Improved Routines for the Inversion of the Gravitational Lens Equation for a Set of Source Points. *A&AS*, 109:597–610, March 1995.
- M. Dominik. A robust and efficient method for calculating the magnification of extended sources caused by gravitational lenses. *A&A*, 333:L79–L82, May 1998a.
- M. Dominik. Galactic microlensing with rotating binaries. *A&A*, 329:361–374, January 1998b.
- M. Dominik. The binary gravitational lens and its extreme cases. *A&A*, 349:108–125, September 1999.
- M. Dominik. Stochastic distributions of lens and source properties for observed galactic microlensing events. *MNRAS*, 367:669–692, April 2006.
- M. Dominik. Adaptive contouring - an efficient way to calculate microlensing light curves of extended sources. *MNRAS*, 377:1679–1688, June 2007.
- M. Dominik. Planetary mass function and planetary systems. *MNRAS*, 411:2–8, February 2011.
- M. Dominik, K. Horne, A. Allan, N. J. Rattenbury, Y. Tsapras, C. Snodgrass, M. F. Bode, M. J. Burgdorf, S. N. Fraser, E. Kerins, C. J. Mottram, I. A. Steele, R. A. Street, P. J. Wheatley, and Ł. Wyrzykowski. ARTEMiS (Automated Robotic Terrestrial Exoplanet Microlensing Search): A possible expert-system based cooperative effort to hunt for planets of Earth mass and below. *Astronomische Nachrichten*, 329:248–251, March 2008.
- M. Dominik, U. G. Jørgensen, N. J. Rattenbury, M. Mathiasen, T. C. Hinse, S. Calchi Novati, K. Harpsøe, V. Bozza, T. Anguita, M. J. Burgdorf, K. Horne, M. Hundertmark, E. Kerins, P. Kjærgaard, C. Liebig, L. Mancini, G. Masi, S. Rahvar, D. Ricci, G. Scarpetta, C. Snodgrass, J. Southworth, R. A. Street, J. Surdej, C. C. Thöne, Y. Tsapras, J. Wambsganss, and M. Zub. Realisation of a fully-deterministic

- microlensing observing strategy for inferring planet populations. *Astronomische Nachrichten*, 331:671–691, July 2010.
- M. Dominik and K. C. Sahu. Astrometric Microlensing of Stars. *ApJ*, 534:213–226, May 2000.
- S. Dong, I. A. Bond, A. Gould, S. Kozłowski, N. Miyake, B. S. Gaudi, D. P. Bennett, F. Abe, A. C. Gilmore, A. Fukui, K. Furusawa, J. B. Hearnshaw, Y. Itow, K. Kamiya, P. M. Kilmartin, A. Korpela, W. Lin, C. H. Ling, K. Masuda, Y. Matsubara, Y. Muraki, M. Nagaya, K. Ohnishi, T. Okumura, Y. C. Perrott, N. Rattenbury, T. Saito, T. Sako, S. Sato, L. Skuljan, D. J. Sullivan, T. Sumi, W. Sweatman, P. J. Tristram, P. C. M. Yock, The MOA Collaboration, G. Bolt, G. W. Christie, D. L. DePoy, C. Han, J. Janczak, C.-U. Lee, F. Mallia, J. McCormick, B. Monard, A. Maury, T. Natusch, B.-G. Park, R. W. Pogge, R. Santallo, K. Z. Stanek, The μ FUN Collaboration, A. Udalski, M. Kubiak, M. K. Szymański, G. Pietrzyński, I. Soszyński, O. Szewczyk, Ł. Wyrzykowski, K. Ulaczyk, and The OGLE Collaboration. Microlensing Event MOA-2007-BLG-400: Exhuming the Buried Signature of a Cool, Jovian-Mass Planet. *ApJ*, 698:1826–1837, June 2009a.
- S. Dong, D. L. DePoy, B. S. Gaudi, A. Gould, C. Han, B.-G. Park, R. W. Pogge, A. Udalski, O. Szewczyk, M. Kubiak, M. K. Szymański, G. Pietrzyński, I. Soszyński, Ł. Wyrzykowski, and K. Żebruń. Planetary Detection Efficiency of the Magnification 3000 Microlensing Event OGLE-2004-BLG-343. *ApJ*, 642:842–860, May 2006.
- S. Dong, A. Gould, A. Udalski, J. Anderson, G. W. Christie, B. S. Gaudi, The OGLE Collaboration, M. Jaroszyński, M. Kubiak, M. K. Szymański, G. Pietrzyński, I. Soszyński, O. Szewczyk, K. Ulaczyk, Ł. Wyrzykowski, The μ FUN Collaboration, D. L. DePoy, D. B. Fox, A. Gal-Yam, C. Han, S. Lépine, J. McCormick, E. Ofek, B.-G. Park, R. W. Pogge, The MOA Collaboration, F. Abe, D. P. Bennett, I. A. Bond, T. R. Britton, A. C. Gilmore, J. B. Hearnshaw, Y. Itow, K. Kamiya, P. M. Kilmartin, A. Korpela, K. Masuda, Y. Matsubara, M. Motomura, Y. Muraki, S. Nakamura, K. Ohnishi, C. Okada, N. Rattenbury, T. Saito, T. Sako, M. Sasaki, D. Sullivan, T. Sumi, P. J. Tristram, T. Yanagisawa, P. C. M. Yock, T. Yoshioika, The PLANET/Robo Net Collaborations, M. D. Albrow, J. P. Beaulieu, S. Brilliant, H. Calitz, A. Cassan, K. H. Cook, C. Coutures, S. Dieters, D. D. Prester, J. Donatowicz, P. Fouqué, J. Greenhill, K. Hill, M. Hoffman, K. Horne, U. G. Jørgensen, S. Kane, D. Kubas, J. B. Marquette, R. Martin, P. Meintjes, J. Menzies, K. R. Pol-

- lard, K. C. Sahu, C. Vinter, J. Wambsganss, A. Williams, M. Bode, D. M. Bramich, M. Burgdorf, C. Snodgrass, I. Steele, V. Doublier, and C. Foellmi. OGLE-2005-BLG-071Lb, the Most Massive M Dwarf Planetary Companion? *ApJ*, 695:970–987, April 2009b.
- M. Doran and C. M. Müller. Analyse this! A cosmological constraint package for CMBEASY. *Journal of Cosmology and Astroparticle Physics*, 9:003, September 2004.
- F. Dubath, M. A. Gasparini, and R. Durrer. Microlensing modulation by quadrupole variation. *Phys. Rev. D*, 75(2):024015–024021, January 2007.
- A. Duquennoy and M. Mayor. Multiplicity among solar-type stars in the solar neighbourhood. II - Distribution of the orbital elements in an unbiased sample. *A&A*, 248:485–524, August 1991.
- J. Einasto. Galactic mass modeling. In W. B. Burton, editor, *The Large-Scale Characteristics of the Galaxy*, volume 84 of *IAU Symposium*, pages 451–458, 1979.
- A. Einstein. Erklärung der Perihelionbewegung der Merkur aus der allgemeinen Relativitätstheorie. *Sitzungsber. preuss.Akad. Wiss.*, 47:831–839, 1915.
- A. Einstein. Lens-Like Action of a Star by the Deviation of Light in the Gravitational Field. *Science*, 84:506–507, December 1936.
- H. Erdl and P. Schneider. Classification of the multiple deflection two point-mass gravitational lens models and application of catastrophe theory in lensing. *A&A*, 268:453–471, February 1993.
- Euclid payload manager. Euclid Payload Definition Document. *esa*, 4, September 2009.
- D. A. Fischer, G. W. Marcy, R. P. Butler, S. S. Vogt, G. Laughlin, G. W. Henry, D. Abouav, K. M. G. Peek, J. T. Wright, J. A. Johnson, C. McCarthy, and H. Isaacson. Five Planets Orbiting 55 Cancri. *ApJ*, 675:790–801, March 2008.
- D. J. Fixsen, J. D. Offenberg, R. J. Hanisch, J. C. Mather, M. A. Nieto-Santisteban, R. Sengupta, and H. S. Stockman. Cosmic-Ray Rejection and Readout Efficiency for Large-Area Arrays. *PASP*, 112:1350–1359, October 2000.
- H. T. Freudenreich. A COBE Model of the Galactic Bar and Disk. *ApJ*, 492:495–510, January 1998.
- B. S. Gaudi. Oral presentation at 13th Microlensing Workshop, Paris, January 2009.
- B. S. Gaudi. *Microlensing by Exoplanets*, pages 79–110. University of Arizona Press,

- 2010.
- B. S. Gaudi, M. D. Albrow, J. An, J.-P. Beaulieu, J. A. R. Caldwell, D. L. DePoy, M. Dominik, A. Gould, J. Greenhill, K. Hill, S. Kane, R. Martin, J. Menzies, R. M. Naber, J.-W. Pel, R. W. Pogge, K. R. Pollard, P. D. Sackett, K. C. Sahu, P. Vermaak, P. M. Vreeswijk, R. Watson, and A. Williams. Microlensing Constraints on the Frequency of Jupiter-Mass Companions: Analysis of 5 Years of PLANET Photometry. *ApJ*, 566:463–499, February 2002.
- B. S. Gaudi, D. P. Bennett, A. Udalski, A. Gould, G. W. Christie, D. Maoz, S. Dong, J. McCormick, M. K. Szymański, P. J. Tristram, S. Nikolaev, B. Paczyński, M. Kuźbiak, G. Pietrzyński, I. Soszyński, O. Szewczyk, K. Ulaczyk, Ł. Wyrzykowski, D. L. DePoy, C. Han, S. Kaspi, C.-U. Lee, F. Mallia, T. Natusch, R. W. Pogge, B.-G. Park, F. Abe, I. A. Bond, C. S. Botzler, A. Fukui, J. B. Hearnshaw, Y. Itow, K. Kamiya, A. V. Korpela, P. M. Kilmartin, W. Lin, K. Masuda, Y. Matsubara, M. Motomura, Y. Muraki, S. Nakamura, T. Okumura, K. Ohnishi, N. J. Rattenbury, T. Sako, T. Saito, S. Sato, L. Skuljan, D. J. Sullivan, T. Sumi, W. L. Sweatman, P. C. M. Yock, M. D. Albrow, A. Allan, J.-P. Beaulieu, M. J. Burgdorf, K. H. Cook, C. Coutures, M. Dominik, S. Dieters, P. Fouqué, J. Greenhill, K. Horne, I. Steele, Y. Tsapras, B. Chaboyer, A. Crocker, S. Frank, and B. Macintosh. Discovery of a Jupiter/Saturn Analog with Gravitational Microlensing. *Science*, 319:927–, 2008.
- B. S. Gaudi and A. Gould. Detection Rates for Close Binaries via Microlensing. *ApJ*, 482:83–88, June 1997.
- B. S. Gaudi, R. M. Naber, and P. D. Sackett. Microlensing by Multiple Planets in High-Magnification Events. *ApJL*, 502:L33–L37, July 1998.
- B. S. Gaudi and A. O. Petters. Gravitational Microlensing near Caustics. I. Folds. *ApJ*, 574:970–984, August 2002a.
- B. S. Gaudi and A. O. Petters. Gravitational Microlensing near Caustics. II. Cusps. *ApJ*, 580:468–489, November 2002b.
- B. S. Gaudi and P. D. Sackett. Detection Efficiencies of Microlensing Data Sets to Stellar and Planetary Companions. *ApJ*, 528:56–73, January 2000.
- L. Girardi, G. Bertelli, A. Bressan, C. Chiosi, M. A. T. Groenewegen, P. Marigo, B. Salasnich, and A. Weiss. Theoretical isochrones in several photometric systems. I. Johnson-Cousins-Glass, HST/WFPC2, HST/NICMOS, Washington, and ESO Imaging Survey filter sets. *A&A*, 391:195–212, August 2002.

- P. Goldreich and S. Tremaine. Disk-satellite interactions. *ApJ*, 241:425–441, October 1980.
- A. Gould. Extending the MACHO search to about 10×6 solar masses. *ApJ*, 392:442–451, June 1992.
- A. Gould. MACHO velocities from satellite-based parallaxes. *ApJL*, 421:L75–L78, February 1994a.
- A. Gould. Proper motions of MACHOs. *ApJL*, 421:L71–L74, February 1994b.
- A. Gould. A Natural Formalism for Microlensing. *ApJ*, 542:785–788, October 2000a.
- A. Gould. Measuring the Remnant Mass Function of the Galactic Bulge. *ApJ*, 535:928–931, June 2000b.
- A. Gould. Hexadecapole Approximation in Planetary Microlensing. *ApJ*, 681:1593–1598, July 2008.
- A. Gould and N. Andronov. Complete Parallax and Proper-Motion Solutions for Halo Binary-Lens Microlensing Events. *ApJ*, 516:236–242, May 1999.
- A. Gould, S. Dong, B. S. Gaudi, A. Udalski, I. A. Bond, J. Greenhill, R. A. Street, M. Dominik, T. Sumi, M. K. Szymański, C. Han, W. Allen, G. Bolt, M. Bos, G. W. Christie, D. L. DePoy, J. Drummond, J. D. Eastman, A. Gal-Yam, D. Higgins, J. Janczak, S. Kaspi, S. Kozłowski, C.-U. Lee, F. Mallia, A. Maury, D. Maoz, J. McCormick, L. A. G. Monard, D. Moorhouse, N. Morgan, T. Natusch, E. O. Ofek, B.-G. Park, R. W. Pogge, D. Polishook, R. Santallo, A. Shporer, O. Spector, G. Thornley, J. C. Yee, μ FUN Collaboration, M. Kubiak, G. Pietrzyński, I. Soszyński, O. Szewczyk, Ł. Wyrzykowski, K. Ulaczyk, R. Poleski, OGLE Collaboration, F. Abe, D. P. Bennett, C. S. Botzler, D. Douchin, M. Freeman, A. Fukui, K. Furusawa, J. B. Hearnshaw, S. Hosaka, Y. Itow, K. Kamiya, P. M. Kilmartin, A. Korpela, W. Lin, C. H. Ling, S. Makita, K. Masuda, Y. Matsubara, N. Miyake, Y. Muraki, M. Nagaya, K. Nishimoto, K. Ohnishi, T. Okumura, Y. C. Perrott, L. Philpott, N. Rattenbury, T. Saito, T. Sako, D. J. Sullivan, W. L. Sweatman, P. J. Tristram, E. von Seggern, P. C. M. Yock, MOA Collaboration, M. Albrow, V. Batista, J. P. Beaulieu, S. Brilliant, J. Caldwell, J. J. Calitz, A. Cassan, A. Cole, K. Cook, C. Coutures, S. Dieters, D. Dominis Prester, J. Donatowicz, P. Fouqué, K. Hill, M. Hoffman, F. Jablonski, S. R. Kane, N. Kains, D. Kubas, J.-B. Marquette, R. Martin, E. Martioli, P. Meintjes, J. Menzies, E. Pedretti, K. Pollard, K. C. Sahu, C. Vinter, J. Wambsganss, R. Watson, A. Williams, M. Zub, PLANET Collabora-

- tion, A. Allan, M. F. Bode, D. M. Bramich, M. J. Burgdorf, N. Clay, S. Fraser, E. Hawkins, K. Horne, E. Kerins, T. A. Lister, C. Mottram, E. S. Saunders, C. Snodgrass, I. A. Steele, Y. Tsapras, RoboNet Collaboration, U. G. Jørgensen, T. Anguita, V. Bozza, S. Calchi Novati, K. Harpsøe, T. C. Hinse, M. Hundertmark, P. Kjærgaard, C. Liebig, L. Mancini, G. Masi, M. Mathiasen, S. Rahvar, D. Ricci, G. Scarpetta, J. Southworth, J. Surdej, C. C. Thöne, and MiNDSTeP Consortium. Frequency of Solar-like Systems and of Ice and Gas Giants Beyond the Snow Line from High-magnification Microlensing Events in 2005-2008. *ApJ*, 720:1073–1089, September 2010.
- A. Gould and C. Gaucherel. Stokes’s Theorem Applied to Microlensing of Finite Sources. *ApJ*, 477:580–584, March 1997.
- A. Gould and A. Loeb. Discovering planetary systems through gravitational microlenses. *ApJ*, 396:104–114, September 1992.
- A. Gould, A. Udalski, D. An, D. P. Bennett, A.-Y. Zhou, S. Dong, N. J. Rattenbury, B. S. Gaudi, P. C. M. Yock, I. A. Bond, G. W. Christie, K. Horne, J. Anderson, K. Z. Stanek, D. L. DePoy, C. Han, J. McCormick, B.-G. Park, R. W. Pogge, S. D. Poindexter, I. Soszyński, M. K. Szymański, M. Kubiak, G. Pietrzyński, O. Szewczyk, Ł. Wyrzykowski, K. Ulaczyk, B. Paczyński, D. M. Bramich, C. Snodgrass, I. A. Steele, M. J. Burgdorf, M. F. Bode, C. S. Botzler, S. Mao, and S. C. Swaving. Microlens OGLE-2005-BLG-169 Implies That Cool Neptune-like Planets Are Common. *ApJL*, 644:L37–L40, June 2006.
- J. Green, P. Schechter, C. Baltay, R. Bean, D. Bennett, R. Brown, C. Conselice, M. Donahue, S. Gaudi, T. Lauer, S. Perlmutter, B. Rauscher, J. Rhodes, T. Roellig, D. Stern, T. Sumi, A. Tanner, Y. Wang, E. Wright, N. Gehrels, R. Sambruna, and W. Traub. Wide-Field InfraRed Survey Telescope (WFIRST) Interim Report. *ArXiv e-prints*, August 2011.
- P. C. Gregory. *Bayesian Logical Data Analysis for the Physical Sciences: A Comparative Approach with ‘Mathematica’ Support*. Cambridge University Press, 2005.
- K. Griest. Galactic microlensing as a method of detecting massive compact halo objects. *ApJ*, 366:412–421, January 1991.
- K. Griest and W. Hu. Effect of binary sources on the search for massive astrophysical compact halo objects via microlensing. *ApJ*, 397:362–380, October 1992.
- K. Griest and N. Safizadeh. The Use of High-Magnification Microlensing Events in

- Discovering Extrasolar Planets. *ApJ*, 500:37–50, June 1998.
- C. Hamadache, L. Le Guillou, P. Tisserand, C. Afonso, J. N. Albert, J. Andersen, R. Ansari, É. Aubourg, P. Bareyre, J. P. Beaulieu, X. Charlot, C. Coutures, R. Ferlet, P. Fouqué, J. F. Glicenstein, B. Goldman, A. Gould, D. Graff, M. Gros, J. Haissinski, J. de Kat, É. Lesquoy, C. Loup, C. Magneville, J. B. Marquette, É. Maurice, A. Maury, A. Milsztajn, M. Moniez, N. Palanque-Delabrouille, O. Perdureau, Y. R. Rahal, J. Rich, M. Spiro, A. Vidal-Madjar, L. Vigroux, and S. Zylberajch. Galactic Bulge microlensing optical depth from EROS-2. *A&A*, 454:185–199, July 2006.
- C. Han. Properties of Planetary Caustics in Gravitational Microlensing. *ApJ*, 638:1080–1085, February 2006.
- C. Han. Microlensing Detections of Moons of Exoplanets. *ApJ*, 684:684–690, September 2008.
- C. Han. Distinguishing Between Planetary and Binary Interpretations of Microlensing Central Perturbations Under the Severe Finite-Source Effect. *ApJL*, 691:L9–L12, January 2009a.
- C. Han. Microlensing Zone of Planets Detectable Through the Channel of High-Magnification Events. *ApJ*, 691:452–457, January 2009b.
- C. Han, H.-Y. Chang, J. H. An, and K. Chang. Properties of microlensing light curve anomalies induced by multiple planets. *MNRAS*, 328:986–992, December 2001.
- C. Han, S.-J. Chung, D. Kim, B.-G. Park, Y.-H. Ryu, S. Kang, and D. W. Lee. Gravitational Microlensing: A Tool for Detecting and Characterizing Free-Floating Planets. *ApJ*, 604:372–378, March 2004.
- C. Han and A. Gould. Statistics of Microlensing Optical Depth. *ApJ*, 449:521–526, August 1995a.
- C. Han and A. Gould. The Mass Spectrum of MACHOs from Parallax Measurements. *ApJ*, 447:53–61, July 1995b.
- C. Han and A. Gould. Einstein Radii from Binary-Source Lensing Events. *ApJ*, 480:196–202, May 1997.
- C. Han and A. Gould. Stellar Contribution to the Galactic Bulge Microlensing Optical Depth. *ApJ*, 592:172–175, July 2003.
- C. Han and W. Han. On the Feasibility of Detecting Satellites of Extrasolar Planets via Microlensing. *ApJ*, 580:490–493, November 2002.
- C. Han and Y.-G. Kim. Comparison of the Two Follow-up Observation Strategies for

- Gravitational Microlensing Planet Searches. *ApJ*, 546:975–979, January 2001.
- C. Han, S.-H. Park, and Y.-S. Lee. Distribution of caustic-crossing intervals for Galactic binary-lens microlensing events. *MNRAS*, 314:59–64, May 2000.
- S. J. Hardy and M. A. Walker. Parallax effects in binary microlensing events. *MNRAS*, 276:L79–L82, October 1995.
- M. Haywood, A. C. Robin, and M. Creze. The evolution of the Milky Way disc. II. Constraints from star counts at the galactic poles. *A&A*, 320:440–459, April 1997.
- J. B. Hearnshaw, F. Abe, I. A. Bond, A. C. Gilmore, Y. Itow, K. Kamiya, K. Masuda, Y. Matsubara, Y. Muraki, C. Okada, N. J. Rattenbury, T. Sako, M. Sasaki, D. J. Sullivan, and P. C. M. Yock. The MOA 1.8-metre alt-az Wide-field Survey Telescope and the MOA Project. In W. Sutantyo, P. W. Premadi, P. Mahasena, T. Hidayat, & S. Mineshige, editor, *The 9th Asian-Pacific Regional IAU Meeting*, page 272, January 2006.
- T. J. Henry and D. W. McCarthy, Jr. The mass-luminosity relation for stars of mass 1.0 to 0.08 solar mass. *AJ*, 106:773–789, August 1993.
- E. Hog, I. D. Novikov, and A. G. Polnarev. MACHO photometry and astrometry. *A&A*, 294:287–294, February 1995.
- J. A. Holtzman, A. M. Watson, W. A. Baum, C. J. Grillmair, E. J. Groth, R. M. Light, R. Lynds, and E. J. O’Neil, Jr. The Luminosity Function and Initial Mass Function in the Galactic Bulge. *AJ*, 115:1946–1957, May 1998.
- A. W. Howard, G. W. Marcy, S. T. Bryson, J. M. Jenkins, J. F. Rowe, N. M. Batalha, W. J. Borucki, D. G. Koch, E. W. Dunham, T. N. Gautier, III, J. Van Cleve, W. D. Cochran, D. W. Latham, J. J. Lissauer, G. Torres, T. M. Brown, R. L. Gilliland, L. A. Buchhave, D. A. Caldwell, J. Christensen-Dalsgaard, D. Ciardi, F. Fressin, M. R. Haas, S. B. Howell, H. Kjeldsen, S. Seager, L. Rogers, D. D. Sasselov, J. H. Steffen, G. S. Basri, D. Charbonneau, J. Christiansen, B. Clarke, A. Dupree, D. C. Fabrycky, D. A. Fischer, E. B. Ford, J. J. Fortney, J. Tarter, F. R. Girouard, M. J. Holman, J. A. Johnson, T. C. Klaus, P. Machalek, A. V. Moorhead, R. C. Morehead, D. Ragozzine, P. Tenenbaum, J. D. Twicken, S. N. Quinn, H. Isaacson, A. Shporer, P. W. Lucas, L. M. Walkowicz, W. F. Welsh, A. Boss, E. Devore, A. Gould, J. C. Smith, R. L. Morris, A. Prsa, and T. D. Morton. Planet Occurrence within 0.25 AU of Solar-type Stars from Kepler. *ArXiv e-prints*, March 2011.
- K.-H. Hwang, A. Udalski, C. Han, Y.-H. Ryu, I. A. Bond, J.-P. Beaulieu, M. Dominik,

- K. Horne, A. Gould, B. S. Gaudi, M. Kubiak, M. K. Szymański, G. Pietrzyński, I. Soszyński, O. Szewczyk, K. Ulaczyk, Ł. Wyrzykowski, The OGLE Collaboration, F. Abe, C. S. Botzler, J. B. Hearnshaw, Y. Itow, K. Kamiya, P. M. Kilmartin, K. Masuda, Y. Matsubara, M. Motomura, Y. Muraki, S. Nakamura, K. Ohnishi, C. Okada, N. Rattenbury, T. Saito, T. Sako, M. Sasaki, D. J. Sullivan, T. Sumi, P. J. Tristram, J. N. Wood, P. C. M. Yock, T. Yoshioka, The MOA Collaboration, M. Albrow, D. P. Bennett, D. M. Bramich, S. Brilliant, J. A. R. Caldwell, J. J. Calitz, A. Cassan, K. H. Cook, E. Corrales, C. Coutures, M. Desort, S. Dieters, D. Dominis, J. Donatowicz, P. Fouqué, J. Greenhill, K. Harpsøe, K. Hill, M. Hoffman, U. G. Jørgensen, S. Kane, D. Kubas, R. Martin, J.-B. Marquette, P. Meintjes, J. Menzies, K. Pollard, K. Sahu, I. Steele, C. Vinter, J. Wambsganss, A. Williams, K. Woller, M. Burgdorf, C. Snodgrass, M. Bode, The Planet/RoboNet Collaboration, D. L. Depoy, C.-U. Lee, B.-G. Park, R. W. Pogge, and The μ FUN Collaboration. OGLE-2005-BLG-153: Microlensing Discovery and Characterization of a Very Low Mass Binary. *ApJ*, 723: 797–802, November 2010.
- S. Ida and D. N. C. Lin. Toward a Deterministic Model of Planetary Formation. I. A Desert in the Mass and Semimajor Axis Distributions of Extrasolar Planets. *ApJ*, 604:388–413, March 2004.
- S. Ida and D. N. C. Lin. Toward a Deterministic Model of Planetary Formation. IV. Effects of Type I Migration. *ApJ*, 673:487–501, January 2008a.
- S. Ida and D. N. C. Lin. Toward a Deterministic Model of Planetary Formation. V. Accumulation Near the Ice Line and Super-Earths. *ApJ*, 685:584–595, September 2008b.
- K. Ioka, R. Nishi, and Y. Kan-Ya. Kepler Rotation Effects on the Binary-Lens Microlensing Events. *Progress of Theoretical Physics*, 102:983–1000, November 1999.
- F. James and M. Roos. Minuit - a system for function minimization and analysis of the parameter errors and correlations. *Computer Physics Communications*, 10:343–367, December 1975.
- J. Janczak, A. Fukui, S. Dong, L. A. G. Monard, S. Kozłowski, A. Gould, J. P. Beaulieu, D. Kubas, J. B. Marquette, T. Sumi, I. A. Bond, D. P. Bennett, F. Abe, K. Furusawa, J. B. Hearnshaw, S. Hosaka, Y. Itow, K. Kamiya, A. V. Korpela, P. M. Kilmartin, W. Lin, C. H. Ling, S. Makita, K. Masuda, Y. Matsubara, N. Miyake, Y. Muraki, M. Nagaya, T. Nagayama, K. Nishimoto, K. Ohnishi, Y. C. Perrott, N. J. Rattenbury, T. Sako, T. Saito, L. Skuljan, D. J. Sullivan, W. L. Sweatman, P. J.

- Tristram, P. C. M. Yock, The MOA Collaboration, J. H. An, G. W. Christie, S.-J. Chung, D. L. DePoy, B. S. Gaudi, C. Han, C.-U. Lee, F. Mallia, T. Natusch, B.-G. Park, R. W. Pogge, The μ FUN Collaboration, T. Anguita, S. Calchi Novati, M. Dominik, U. G. Jørgensen, G. Masi, M. Mathiasen, The MiNDSTEp Collaboration, V. Batista, S. Brilliant, A. Cassan, A. Cole, E. Corrales, C. Coutures, S. Dieters, P. Fouqué, J. Greenhill, and The PLANET Collaboration. Sub-Saturn Planet MOA-2008-BLG-310Lb: Likely to be in the Galactic Bulge. *ApJ*, 711:731–743, March 2010.
- M. Jaroszynski. Binary Lenses in OGLE-II 1997-1999 Database. A Preliminary Study. *Acta Astronomica*, 52:39–60, March 2002.
- M. Jaroszynski, J. Skowron, A. Udalski, M. Kubiak, M. K. Szymanski, G. Pietrzynski, I. Soszynski, K. Zebrun, O. Szewczyk, and Ł. Wyrzykowski. Binary Lenses in OGLE-III EWS Database. Season 2004. *Acta Astronomica*, 56:307–332, December 2006.
- M. Jaroszynski, A. Udalski, M. Kubiak, M. Szymanski, G. Pietrzynski, I. Soszynski, K. Zebrun, O. Szewczyk, and Ł. Wyrzykowski. Binary Lenses in OGLE-III EWS Database. Seasons 2002-2003. *Acta Astronomica*, 54:103–128, June 2004.
- M. Jaroszynski, A. Udalski, M. Kubiak, M. K. Szymanski, G. Pietrzynski, I. Soszynski, K. Zebrun, O. Szewczyk, and Ł. Wyrzykowski. Mass Estimates for Some of the Binary Lenses in OGLE-III Database. *Acta Astronomica*, 55:159–175, June 2005.
- H. Jeffreys. *Theory of Probability: Third Edition*. Oxford University Press, 1961.
- J. A. Johnson, A. W. Howard, G. W. Marcy, B. P. Bowler, G. W. Henry, D. A. Fischer, K. Apps, H. Isaacson, and J. T. Wright. The California Planet Survey. II. A Saturn-Mass Planet Orbiting the M Dwarf Gl 649. *PASP*, 122:149–155, February 2010.
- M. Kamionkowski. Microlensing by stars. *ApJL*, 442:L9–L12, March 1995.
- E. Kerins, A. C. Robin, and D. J. Marshall. Synthetic microlensing maps of the Galactic bulge. *MNRAS*, 396:1202–1210, June 2009.
- S.-L. Kim, B.-G. Park, C.-U. Lee, I.-S. Yuk, C. Han, T. O’Brien, A. Gould, J. W. Lee, and D.-J. Kim. Technical specifications of the KMTNet observation system. In *Society of Photo-Optical Instrumentation Engineers (SPIE) Conference Series*, volume 7733 of *Society of Photo-Optical Instrumentation Engineers (SPIE) Conference Series*, July 2010.
- K. Konno and Y. Kojima. Asymmetry in Microlensing-Induced Light Curves. *Progress*

- of *Theoretical Physics*, 101:885–901, April 1999.
- S. Kozłowski. *Gravitational Microlensing in the Milky Way with the Hubble Space Telescope and OGLE-III*. PhD thesis, JBCA, University of Manchester, Manchester UK, 2007.
- S. Kozłowski, P. R. Woźniak, S. Mao, and A. Wood. The First Direct Detection of a Gravitational μ -Lens toward the Galactic Bulge. *ApJ*, 671:420–426, December 2007.
- D. Kubas, A. Cassan, J. P. Beaulieu, C. Coutures, M. Dominik, M. D. Albrow, S. Bril-lant, J. A. R. Caldwell, D. Dominis, J. Donatowicz, C. Fendt, P. Fouqué, U. G. Jørgensen, J. Greenhill, K. Hill, J. Heinmüller, K. Horne, S. Kane, J. B. Marquette, R. Martin, J. Menzies, K. R. Pollard, K. C. Sahu, C. Vinter, J. Wambsganss, R. Wat-son, A. Williams, and C. Thurl. Full characterization of binary-lens event OGLE-2002-BLG-069 from PLANET observations. *A&A*, 435:941–948, June 2005.
- G. P. Kuiper. On the Origin of the Solar System. *Proceedings of the National Academy of Science*, 37:1–14, January 1951.
- C. J. Lada. Stellar Multiplicity and the Initial Mass Function: Most Stars Are Single. *ApJL*, 640:L63–L66, March 2006.
- R. Laureijs, J. Amiaux, S. Arduini, J. . Auguères, J. Brinchmann, R. Cole, M. Cropper, C. Dabin, L. Duvet, A. Ealet, and et al. Euclid Definition Study Report. *ArXiv e-prints*, October 2011.
- C.-H. Lee, A. Riffeser, S. Seitz, and R. Bender. Finite-Source Effects in Microlensing: A Precise, Easy to Implement, Fast, and Numerically Stable Formalism. *ApJ*, 695: 200–207, April 2009.
- C. Leinert, S. Bowyer, L. K. Haikala, M. S. Hanner, M. G. Hauser, A.-C. Levasseur-Regourd, I. Mann, K. Mattila, W. T. Reach, W. Schlosser, H. J. Staude, G. N. Toller, J. L. Weiland, J. L. Weinberg, and A. N. Witt. The 1997 reference of diffuse night sky brightness. *A&AS*, 127:1–99, January 1998.
- S. Liebes. Gravitational Lenses. *Physical Review*, 133:835–844, February 1964.
- C. Liebig and J. Wambsganss. Detectability of extrasolar moons as gravitational mi-crolenses. *A&A*, 520:A68–A81, September 2010.
- D. N. C. Lin, P. Bodenheimer, and D. C. Richardson. Orbital migration of the planetary companion of 51 Pegasi to its present location. *Nature*, 380:606–607, April 1996.
- J. J. Lissauer. Timescales for planetary accretion and the structure of the protoplanetary

- disk. *Icarus*, 69:249–265, February 1987.
- J. J. Lissauer, D. Ragozzine, D. C. Fabrycky, J. H. Steffen, E. B. Ford, J. M. Jenkins, A. Shporer, M. J. Holman, J. F. Rowe, E. V. Quintana, N. M. Batalha, W. J. Borucki, S. T. Bryson, D. A. Caldwell, J. A. Carter, D. Ciardi, E. W. Dunham, J. J. Fortney, T. N. Gautier, III, S. B. Howell, D. G. Koch, D. W. Latham, G. W. Marcy, R. C. Morehead, and D. Sasselov. Architecture and Dynamics of Kepler’s Candidate Multiple Transiting Planet Systems. *ApJS*, 197:8–34, November 2011.
- S. Mao. Introduction to Gravitational Microlensing. *ArXiv e-prints*, November 2008.
- S. Mao and B. Paczyński. Gravitational microlensing by double stars and planetary systems. *ApJL*, 374:L37–L40, June 1991.
- S. Mao and B. Paczyński. Mass Determination with Gravitational Microlensing. *ApJ*, 473:57–64, December 1996.
- G. W. Marcy and R. P. Butler. A Planetary Companion to 70 Virginis. *ApJL*, 464:L147–L151, June 1996.
- D. J. Marshall, A. C. Robin, C. Reylé, M. Schultheis, and S. Picaud. Modelling the Galactic interstellar extinction distribution in three dimensions. *A&A*, 453:635–651, July 2006.
- F. Masset and M. Snellgrove. Reversing type II migration: resonance trapping of a lighter giant protoplanet. *MNRAS*, 320:L55–L59, February 2001.
- M. Mayor, M. Marmier, C. Lovis, S. Udry, D. Ségransan, F. Pepe, W. Benz, J. Bertaux, F. Bouchy, X. Dumusque, G. Lo Curto, C. Mordasini, D. Queloz, and N. C. Santos. The HARPS search for southern extra-solar planets XXXIV. Occurrence, mass distribution and orbital properties of super-Earths and Neptune-mass planets. *ArXiv e-prints*, September 2011.
- M. Mayor and D. Queloz. A Jupiter-mass companion to a solar-type star. *Nature*, 378:355–359, November 1995.
- H. Mizuno. Formation of the Giant Planets. *Progress of Theoretical Physics*, 64:544–557, August 1980.
- C. Mordasini, Y. Alibert, and W. Benz. Extrasolar planet population synthesis. I. Method, formation tracks, and mass-distance distribution. *A&A*, 501:1139–1160, July 2009a.
- C. Mordasini, Y. Alibert, W. Benz, and D. Naef. Extrasolar planet population synthesis. II. Statistical comparison with observations. *A&A*, 501:1161–1184, July 2009b.

- G. E. Morfill. Physics and Chemistry in the Primitive Solar Nebula. In R. Lucas, A. Omont, & R. Stora, editor, *Birth and the Infancy of Stars*, page 693, 1985.
- M. Nagasawa, S. Ida, and T. Bessho. Formation of Hot Planets by a Combination of Planet Scattering, Tidal Circularization, and the Kozai Mechanism. *ApJ*, 678: 498–508, May 2008.
- T. Naylor. An optimal extraction algorithm for imaging photometry. *MNRAS*, 296: 339–346, May 1998.
- R. J. Nemiroff and W. A. D. T. Wickramasinghe. Finite source sizes and the information content of macho-type lens search light curves. *ApJL*, 424:L21–L23, March 1994.
- R.G. Newcombe. Interval estimation for the difference between independent proportions: Comparison of eleven methods. *Statistics in Medicine*, 17(8):873–890, 1998a.
- R.G. Newcombe. Two-sided confidence intervals for the single proportion: Comparison of seven methods. *Statistics in Medicine*, 17(8):857–872, 1998b.
- S. Nishiyama, T. Nagata, D. Baba, Y. Haba, R. Kadowaki, D. Kato, M. Kurita, C. Nagashima, T. Nagayama, Y. Murai, Y. Nakajima, M. Tamura, H. Nakaya, K. Sugitani, T. Naoi, N. Matsunaga, T. Tanabé, N. Kusakabe, and S. Sato. A Distinct Structure inside the Galactic Bar. *ApJL*, 621:L105–L108, March 2005.
- H. C. Ohanian. The caustics of gravitational 'lenses'. *ApJ*, 271:551–555, August 1983.
- B. Paczyński. Gravitational microlensing by the galactic halo. *ApJ*, 304:1–5, May 1986.
- B. Paczyński. Gravitational Microlensing in the Local Group. *ARA&A*, 34:419–460, 1996.
- B. Paczyński. Binary Source Parallax Effect in Gravitational Micro-lensing. *ArXiv Astrophysics e-prints*, November 1997.
- B.-G. Park, D. L. DePoy, B. S. Gaudi, A. Gould, C. Han, R. W. Pogge, F. Abe, D. P. Bennett, I. A. Bond, S. Eguchi, Y. Furuta, J. B. Hearnshaw, K. Kamiya, P. M. Kilmartin, Y. Kurata, K. Masuda, Y. Matsubara, Y. Muraki, S. Noda, K. Okajima, N. J. Rattenbury, T. Sako, T. Sekiguchi, D. J. Sullivan, T. Sumi, P. J. Tristram, T. Yanagisawa, and P. C. M. Yock. MOA 2003-BLG-37: A Bulge Jerk-Parallax Microlens Degeneracy. *ApJ*, 609:166–172, July 2004.
- S. J. Peale. Expectations from a Microlensing Search for Planets. *Icarus*, 127:269–289, June 1997.

- S. J. Peale. Probability of Detecting a Planetary Companion during a Microlensing Event. *ApJ*, 552:889–911, May 2001.
- S. J. Peale. Comparison of a Ground-based Microlensing Search for Planets with a Search from Space. *AJ*, 126:1595–1603, September 2003.
- O. Pejcha and D. Heyrovský. Extended-Source Effect and Chromaticity in Two-Point-Mass Microlensing. *ApJ*, 690:1772–1796, January 2009.
- S. Picaud and A. C. Robin. 3D outer bulge structure from near infrared star counts. *A&A*, 428:891–903, December 2004.
- S. Poindexter, C. Afonso, D. P. Bennett, J.-F. Glicenstein, A. Gould, M. K. Szymański, and A. Udalski. Systematic Analysis of 22 Microlensing Parallax Candidates. *ApJ*, 633:914–930, November 2005.
- J. B. Pollack, O. Hubickyj, P. Bodenheimer, J. J. Lissauer, M. Podolak, and Y. Greenzweig. Formation of the Giant Planets by Concurrent Accretion of Solids and Gas. *Icarus*, 124:62–85, November 1996.
- P. Popowski, K. Griest, C. L. Thomas, K. H. Cook, D. P. Bennett, A. C. Becker, D. R. Alves, D. Minniti, A. J. Drake, C. Alcock, R. A. Allsman, T. S. Axelrod, K. C. Freeman, M. Geha, M. J. Lehner, S. L. Marshall, C. A. Nelson, B. A. Peterson, P. J. Quinn, C. W. Stubbs, W. Sutherland, T. Vandehei, D. Welch, and MACHO Collaboration. Microlensing Optical Depth toward the Galactic Bulge Using Clump Giants from the MACHO Survey. *ApJ*, 631:879–905, October 2005.
- D. Raghavan, H. A. McAlister, T. J. Henry, D. W. Latham, G. W. Marcy, B. D. Mason, D. R. Gies, R. J. White, and T. A. ten Brummelaar. A Survey of Stellar Families: Multiplicity of Solar-type Stars. *ApJS*, 190:1–42, September 2010.
- S. Rahvar and M. Dominik. Planetary microlensing signals from the orbital motion of the source star around the common barycentre. *MNRAS*, 392:1193–1204, January 2009.
- N. J. Rattenbury, I. A. Bond, J. Skuljan, and P. C. M. Yock. Planetary microlensing at high magnification. *MNRAS*, 335:159–169, September 2002.
- N. J. Rattenbury, S. Mao, T. Sumi, and M. C. Smith. Modelling the Galactic bar using OGLE-II red clump giant stars. *MNRAS*, 378:1064–1078, July 2007.
- S. Refsdal. The gravitational lens effect. *MNRAS*, 128:295–306, 1964.
- S. Refsdal. On the possibility of determining the distances and masses of stars from the gravitational lens effect. *MNRAS*, 134:315–319, 1966.

- C. Reylé, D. J. Marshall, A. C. Robin, and M. Schultheis. The Milky Way's external disc constrained by 2MASS star counts. *A&A*, 495:819–826, March 2009.
- C. Reylé and A. C. Robin. Early galaxy evolution from deep wide field star counts. II. First estimate of the thick disc mass function. *A&A*, 373:886–894, July 2001.
- S. H. Rhie. How Cumbersome is a Tenth Order Polynomial?: The Case of Gravitational Triple Lens Equation. *ArXiv Astrophysics e-prints*, February 2002.
- C. P. Robert, N. Chopin, and J. Rousseau. Harold Jeffreys's theory of probability revisited. *Statistical Science*, 24(2):141–172, 2009.
- A. Robin and M. Creze. Stellar populations in the Milky Way - A synthetic model. *A&A*, 157:71–90, March 1986.
- A. C. Robin, D. J. Marshall, M. Schultheis, and C. Reyle. submitted, 2011.
- A. C. Robin, C. Reylé, S. Derrière, and S. Picaud. A synthetic view on structure and evolution of the Milky Way. *A&A*, 409:523–540, October 2003.
- Y.-H. Ryu, C. Han, K.-H. Hwang, R. Street, A. Udalski, T. Sumi, A. Fukui, J.-P. Beaulieu, A. Gould, M. Dominik, F. Abe, D. P. Bennett, I. A. Bond, C. S. Botzler, K. Furusawa, F. Hayashi, J. B. Hearnshaw, S. Hosaka, Y. Itow, K. Kamiya, P. M. Kilmartin, A. Korpela, W. Lin, C. H. Ling, S. Makita, K. Masuda, Y. Matsubara, N. Miyake, Y. Muraki, K. Nishimoto, K. Ohnishi, Y. C. Perrott, N. Rattenbury, T. Saito, L. Skuljan, D. J. Sullivan, D. Suzuki, W. L. Sweatman, P. J. Tristram, K. Wada, P. C. M. Yock, The MOA Collaboration, M. K. Szymański, M. Kubiak, G. Pietrzyński, R. Poleski, I. Soszyński, O. Szewczyk, Ł. Wyrzykowski, K. Ulaczyk, The OGLE Collaboration, M. Bos, G. W. Christie, D. L. Depoy, A. Gal-Yam, B. S. Gaudi, S. Kaspi, C.-U. Lee, D. Maoz, J. McCormick, B. Monard, D. Moorhouse, R. W. Pogge, D. Polishook, Y. Shvartzvald, A. Shporer, G. Thornley, J. C. Yee, The μ FUN Collaboration, M. D. Albrow, V. Batista, S. Brilliant, A. Cassan, A. Cole, E. Corrales, C. Coutures, S. Dieters, P. Fouqué, J. Greenhill, J. Menzies, The PLANET Collaboration, A. Allan, D. M. Bramich, P. Browne, K. Horne, N. Kains, C. Snodgrass, I. Steele, Y. Tsapras, The RoboNet Collaboration, V. Bozza, M. J. Burgdorf, S. Calchi Novati, S. Dreizler, F. Finet, M. Glittrup, F. Grundahl, K. Harpsøe, F. V. Hessman, T. C. Hinse, M. Hundertmark, U. G. Jørgensen, C. Liebig, G. Maier, L. Mancini, M. Mathiasen, S. Rahvar, D. Ricci, G. Scarpetta, J. Skottfelt, J. Surdej, J. Southworth, J. Wambsganss, F. Zimmer, and The MiNDSTeP Collaboration. OGLE-2009-BLG-092/MOA-2009-BLG-137: A Dramatic Repeating Event with the Second Perturbation Predicted by Real-time

- Analysis. *ApJ*, 723:81–88, November 2010.
- V. S. Safronov. *Evolutsiia doplanetnogo oblaka (English transl.: Evolution of the Protoplanetary Cloud and Formation of Earth and the Planets)*. NASA Tech. Transl. F-677, Jerusalem: Israel Sci. Transl. 1972), 1969.
- T. Sako, T. Sekiguchi, M. Sasaki, K. Okajima, F. Abe, I. A. Bond, J. B. Hearnshaw, Y. Itow, K. Kamiya, P. M. Kilmartin, K. Masuda, Y. Matsubara, Y. Muraki, N. J. Rattenbury, D. J. Sullivan, T. Sumi, P. Tristram, T. Yanagisawa, and P. C. M. Yock. MOA-cam3: a wide-field mosaic CCD camera for a gravitational microlensing survey in New Zealand. *Experimental Astronomy*, 22:51–66, October 2008.
- G. Schaller, D. Schaerer, G. Meynet, and A. Maeder. New grids of stellar models from 0.8 to 120 solar masses at $Z = 0.020$ and $Z = 0.001$. *A&AS*, 96:269–331, December 1992.
- P. L. Schechter, M. Mateo, and A. Saha. DOPHOT, a CCD photometry program: Description and tests. *PASP*, 105:1342–1353, November 1993.
- J. Schneider, C. Dedieu, P. Le Sidaner, R. Savalle, and I. Zolotukhin. Defining and cataloging exoplanets: the exoplanet.eu database. *A&A*, 532:A79, August 2011.
- P. Schneider, J. Ehlers, and E. E. Falco. *Gravitational Lenses*. Gravitational Lenses, XIV, 560 pp. 112 figs.. Springer-Verlag Berlin Heidelberg New York. Also Astronomy and Astrophysics Library, 1992.
- P. Schneider and A. Weiss. The two-point-mass lens - Detailed investigation of a special asymmetric gravitational lens. *A&A*, 164:237–259, August 1986.
- T. Schramm and R. Kayser. A simple imaging procedure for gravitational lenses. *A&A*, 174:361–364, March 1987.
- M. Schweitzer, R. Bender, R. Katterloher, F. Eisenhauer, R. Hofmann, R. Saglia, R. Holmes, O. Krause, H.-W. Rix, J. Booth, P. Fagrelus, J. Rhodes, S. Seshadri, A. Refregier, J. Amiaux, J.-L. Augueres, O. Boulade, C. Cara, A. Amara, S. Lilly, E. Atad-Ettdgui, A.-M. di Giorgio, L. Duvet, C. Kuehl, and M. Syed. NIP: the near infrared imaging photometer for Euclid. In *Society of Photo-Optical Instrumentation Engineers (SPIE) Conference Series*, volume 7731 of *Society of Photo-Optical Instrumentation Engineers (SPIE) Conference Series*, July 2010.
- I.-G. Shin, A. Udalski, C. Han, A. Gould, M. Dominik, P. Fouqué, M. Kubiak, M. K. Szymański, G. Pietrzyński, I. Soszyński, K. Ulaczyk, Ł. Wyrzykowski, The OGLE Collaboration, D. L. DePoy, S. Dong, B. S. Gaudi, C.-U. Lee, B.-G. Park, R. W.

- Pogge, The μ FUN Collaboration, M. D. Albrow, A. Allan, J. P. Beaulieu, D. P. Bennett, M. Bode, D. M. Bramich, S. Brilliant, M. Burgdorf, H. Calitz, A. Cassan, K. H. Cook, E. Corrales, C. Coutures, N. Desort, S. Dieters, D. Dominis Prester, J. Donatowicz, S. N. Fraser, J. Greenhill, K. Hill, M. Hoffman, K. Horne, U. G. Jørgensen, S. R. Kane, D. Kubas, J. B. Marquette, R. Martin, P. Meintjes, J. Menzies, C. Mottram, T. Naylor, K. R. Pollard, K. C. Sahu, C. Snodgrass, I. Steele, C. Vinter, J. Wambsganss, A. Williams, K. Woller, and The PLANET/RoboNet Collaborations. OGLE-2005-BLG-018: Characterization of Full Physical and Orbital Parameters of a Gravitational Binary Lens. *ApJ*, 735:85, July 2011.
- J. Skowron, M. Jaroszynski, A. Udalski, M. Kubiak, M. K. Szymanski, G. Pietrzynski, I. Soszynski, O. Szewczyk, Ł. Wyrzykowski, and K. Ulaczyk. Binary Lenses in OGLE III EWS Database. Season 2005. *Acta Astronomica*, 57:281–299, December 2007.
- J. Skowron, A. Udalski, A. Gould, S. Dong, L. A. G. Monard, C. Han, C. R. Nelson, J. McCormick, D. Moorhouse, G. Thornley, A. Maury, D. M. Bramich, J. Greenhill, S. Kozłowski, I. Bond, R. Poleski, Ł. Wyrzykowski, K. Ulaczyk, M. Kubiak, M. K. Szymanski, G. Pietrzynski, I. Soszynski, B. S. Gaudi, J. C. Yee, L. -. Hung, R. W. Pogge, D. L. DePoy, C. -. Lee, B. -. Park, W. Allen, F. Mallia, J. Drummond, G. Bolt, A. Allan, P. Browne, N. Clay, M. Dominik, S. Fraser, K. Horne, N. Kains, C. Mottram, C. Snodgrass, I. Steele, R. A. Street, Y. Tsapras, F. Abe, D. P. Bennett, C. S. Botzler, D. Douchin, M. Freeman, A. Fukui, K. Furusawa, F. Hayashi, J. B. Hearnshaw, S. Hosaka, Y. Itow, K. Kamiya, P. M. Kilmartin, A. Korpela, W. Lin, C. H. Ling, S. Makita, K. Masuda, Y. Matsubara, Y. Muraki, T. Nagayama, N. Miyake, K. Nishimoto, K. Ohnishi, Y. C. Perrott, N. Rattenbury, T. Saito, L. Skuljan, D. J. Sullivan, T. Sumi, D. Suzuki, W. L. Sweatman, P. J. Tristram, K. Wada, P. C. M. Yock, J. -. Beaulieu, P. Fouque, M. D. Albrow, V. Batista, S. Brilliant, J. A. R. Caldwell, A. Cassan, A. Cole, K. H. Cook, C. Coutures, S. Dieters, D. Dominis Prester, J. Donatowicz, S. R. Kane, D. Kubas, J. -. Marquette, R. Martin, J. Menzies, K. C. Sahu, J. Wambsganss, A. Williams, and M. Zub. Binary microlensing event OGLE-2009-BLG-020 gives a verifiable mass, distance and orbit predictions. *ArXiv e-prints*, January 2011.
- M. C. Smith, V. Belokurov, N. W. Evans, S. Mao, and J. H. An. The nature of parallax microlensing events towards the Galactic bulge. *MNRAS*, 361:128–140, July 2005.
- M. C. Smith, S. Mao, and B. Paczyński. Acceleration and parallax effects in gravita-

- tional microlensing. *MNRAS*, 339:925–936, March 2003.
- M. C. Smith, S. Mao, and P. Woźniak. Parallax microlensing events in the OGLE II data base toward the Galactic bulge. *MNRAS*, 332:962–970, June 2002a.
- M. C. Smith, S. Mao, P. Woźniak, A. Udalski, M. Szymański, M. Kubiak, G. Pietrzyński, I. Soszyński, and K. Żebruń. Optical gravitational lensing experiment: OGLE-1999-BUL-19 - the first multipeak parallax event. *MNRAS*, 336:670–684, October 2002b.
- M. C. Smith, P. Woźniak, S. Mao, and T. Sumi. Blending in gravitational microlensing experiments: source confusion and related systematics. *MNRAS*, 380:805–818, September 2007.
- M. D. Snellgrove, J. C. B. Papaloizou, and R. P. Nelson. On disc driven inward migration of resonantly coupled planets with application to the system around GJ876. *A&A*, 374:1092–1099, August 2001.
- P. B. Stetson. DAOPHOT - A computer program for crowded-field stellar photometry. *PASP*, 99:191–222, March 1987.
- D. J. Stevenson and J. I. Lunine. Rapid formation of Jupiter by diffuse redistribution of water vapor in the solar nebula. *Icarus*, 75:146–155, July 1988.
- T. Sumi. Extinction map of the Galactic centre: OGLE-II Galactic bulge fields. *MNRAS*, 349:193–204, March 2004.
- T. Sumi, F. Abe, I. A. Bond, R. J. Dodd, J. B. Hearnshaw, M. Honda, M. Honma, Y. Kan-ya, P. M. Kilmartin, K. Masuda, Y. Matsubara, Y. Muraki, T. Nakamura, R. Nishi, S. Noda, K. Ohnishi, O. K. L. Petterson, N. J. Rattenbury, M. Reid, T. Saito, Y. Saito, H. Sato, M. Sekiguchi, J. Skuljan, D. J. Sullivan, M. Takeuti, P. J. Tristram, S. Wilkinson, T. Yanagisawa, and P. C. M. Yock. Microlensing Optical Depth toward the Galactic Bulge from Microlensing Observations in Astrophysics Group Observations during 2000 with Difference Image Analysis. *ApJ*, 591:204–227, July 2003.
- T. Sumi, D. P. Bennett, I. A. Bond, A. Udalski, V. Batista, M. Dominik, P. Fouqué, D. Kubas, A. Gould, B. Macintosh, K. Cook, S. Dong, L. Skuljan, A. Cassan, F. Abe, C. S. Botzler, A. Fukui, K. Furusawa, J. B. Hearnshaw, Y. Itow, K. Kamiya, P. M. Kilmartin, A. Korpela, W. Lin, C. H. Ling, K. Masuda, Y. Matsubara, N. Miyake, Y. Muraki, M. Nagaya, T. Nagayama, K. Ohnishi, T. Okumura, Y. C. Perrott, N. Rattenbury, T. Saito, T. Sako, D. J. Sullivan, W. L. Sweatman, P. J. Tristram, P. C. M.

- Yock, The MOA Collaboration, J. P. Beaulieu, A. Cole, C. Coutures, M. F. Duran, J. Greenhill, F. Jablonski, U. Marboeuf, E. Martioli, E. Pedretti, O. Pejcha, P. Rojo, M. D. Albrow, S. Brilliant, M. Bode, D. M. Bramich, M. J. Burgdorf, J. A. R. Caldwell, H. Calitz, E. Corrales, S. Dieters, D. Dominis Prester, J. Donatowicz, K. Hill, M. Hoffman, K. Horne, U. G. Jørgensen, N. Kains, S. Kane, J. B. Marquette, R. Martin, P. Meintjes, J. Menzies, K. R. Pollard, K. C. Sahu, C. Snodgrass, I. Steele, R. Street, Y. Tsapras, J. Wambsganss, A. Williams, M. Zub, The PLANET Collaboration, M. K. Szymański, M. Kubiak, G. Pietrzyński, I. Soszyński, O. Szewczyk, Ł. Wyrzykowski, K. Ulaczyk, The OGLE Collaboration, W. Allen, G. W. Christie, D. L. DePoy, B. S. Gaudi, C. Han, J. Janczak, C.-U. Lee, J. McCormick, F. Mallia, B. Monard, T. Natusch, B.-G. Park, R. W. Pogge, R. Santallo, and The μ FUN Collaboration. A Cold Neptune-Mass Planet OGLE-2007-BLG-368Lb: Cold Neptunes Are Common. *ApJ*, 710:1641–1653, February 2010.
- T. Sumi, K. Kamiya, D. P. Bennett, I. A. Bond, F. Abe, C. S. Botzler, A. Fukui, K. Furusawa, J. B. Hearnshaw, Y. Itow, P. M. Kilmartin, A. Korpela, W. Lin, C. H. Ling, K. Masuda, Y. Matsubara, N. Miyake, M. Motomura, Y. Muraki, M. Nagaya, S. Nakamura, K. Ohnishi, T. Okumura, Y. C. Perrott, N. Rattenbury, T. Saito, T. Sako, D. J. Sullivan, W. L. Sweatman, P. J. Tristram, A. Udalski, M. K. Szymański, M. Kubiak, G. Pietrzyński, R. Poleski, I. Soszyński, Ł. Wyrzykowski, K. Ulaczyk, and Microlensing Observations in Astrophysics (MOA) Collaboration. Unbound or distant planetary mass population detected by gravitational microlensing. *Nature*, 473:349–352, May 2011.
- T. Sumi, P. R. Woźniak, A. Udalski, M. Szymański, M. Kubiak, G. Pietrzyński, I. Soszyński, K. Żebruń, O. Szewczyk, Ł. Wyrzykowski, and B. Paczyński. Microlensing Optical Depth toward the Galactic Bulge Using Bright Sources from OGLE-II. *ApJ*, 636:240–260, January 2006.
- G. A. Tikhov. Sur la déviation des rayons lumineux dans le champ de gravitation des étoiles. *Izvestiya Glavnoy Astronomicheskoy Observatorii v Pulkove*, 16, 1938.
- P. Tisserand, L. Le Guillou, C. Afonso, J. N. Albert, J. Andersen, R. Ansari, É. Aubourg, P. Bareyre, J. P. Beaulieu, X. Charlot, C. Coutures, R. Ferlet, P. Fouqué, J. F. Glicenstein, B. Goldman, A. Gould, D. Graff, M. Gros, J. Haissinski, C. Hamadache, J. de Kat, T. Lasserre, É. Lesquoy, C. Loup, C. Magneville, J. B. Marquette, É. Maurice, A. Maury, A. Milsztajn, M. Moniez, N. Palanque-Delabrouille, O. Perdereau, Y. R. Rahal, J. Rich, M. Spiro, A. Vidal-Madjar, L. Vi-

- groux, S. Zylberajch, and The EROS-2 Collaboration. Limits on the Macho content of the Galactic Halo from the EROS-2 Survey of the Magellanic Clouds. *A&A*, 469: 387–404, July 2007.
- A. B. Tomaney and A. P. S. Crotts. Expanding the Realm of Microlensing Surveys with Difference Image Photometry. *AJ*, 112:2872–2895, December 1996.
- Y. Tsapras, R. Street, K. Horne, C. Snodgrass, M. Dominik, A. Allan, I. Steele, D. M. Bramich, E. S. Saunders, N. Rattenbury, C. Mottram, S. Fraser, N. Clay, M. Burgdorf, M. Bode, T. A. Lister, E. Hawkins, J. P. Beaulieu, P. Fouqué, M. Albrow, J. Menzies, A. Cassan, and D. Dominis-Prester. RoboNet-II: Follow-up observations of microlensing events with a robotic network of telescopes. *Astronomische Nachrichten*, 330:4–11, January 2009.
- D. Tytler. Chapter 7. In Beichman, C. A., editor, *A Road Map for the Exploration of Neighboring Planetary Systems*, 1996.
- A. Udalski. The Optical Gravitational Lensing Experiment. Real Time Data Analysis Systems in the OGLE-III Survey. *Acta Astronomica*, 53:291–305, December 2003.
- A. Udalski. The Optical Gravitational Lensing Experiment (OGLE): Bohdan’s and Our Great Adventure. In K. Z. Stanek, editor, *Astronomical Society of the Pacific Conference Series*, volume 403 of *Astronomical Society of the Pacific Conference Series*, pages 110–128, March 2009.
- A. Udalski. Status of the OGLE-IV survey. In Bozza, V. and Calchi Novati, S. and Mancini, L. and Scarpetta, G., editor, *XV International Conference on Gravitational Microlensing: Conference Book*, XV International Conference on Gravitational Microlensing: Conference Book, page 19, February 2011.
- A. Udalski, M. Jaroszyński, B. Paczyński, M. Kubiak, M. K. Szymański, I. Soszyński, G. Pietrzyński, K. Ulaczyk, O. Szewczyk, Ł. Wyrzykowski, G. W. Christie, D. L. DePoy, S. Dong, A. Gal-Yam, B. S. Gaudi, A. Gould, C. Han, S. Lépine, J. McCormick, B.-G. Park, R. W. Pogge, D. P. Bennett, I. A. Bond, Y. Muraki, P. J. Tristram, P. C. M. Yock, J.-P. Beaulieu, D. M. Bramich, S. W. Dieters, J. Greenhill, K. Hill, K. Horne, and D. Kubas. A Jovian-Mass Planet in Microlensing Event OGLE-2005-BLG-071. *ApJL*, 628:L109–L112, August 2005.
- A. Udalski, M. Kubiak, and M. Szymanski. Optical Gravitational Lensing Experiment. OGLE-2 – the Second Phase of the OGLE Project. *Acta Astronomica*, 47:319–344, July 1997.

- S. Udry and N. C. Santos. Statistical Properties of Exoplanets. *ARA&A*, 45:397–439, September 2007.
- D. A. VandenBerg, P. A. Bergbusch, and P. D. Dowler. The Victoria-Regina Stellar Models: Evolutionary Tracks and Isochrones for a Wide Range in Mass and Metallicity that Allow for Empirically Constrained Amounts of Convective Core Overshooting. *ApJS*, 162:375–387, February 2006.
- D. Veras, J. R. Crepp, and E. B. Ford. Formation, Survival, and Detectability of Planets Beyond 100 AU. *ApJ*, 696:1600–1611, May 2009.
- M. Vietri and J. P. Ostriker. The statistics of gravitational lenses - Apparent changes in the luminosity function of distant sources due to passage of light through a single galaxy. *ApJ*, 267:488–510, April 1983.
- M. A. Walker. Microlensed Image Motions. *ApJ*, 453:37–39, November 1995.
- J. Wambsganss. Discovering Galactic planets by gravitational microlensing: magnification patterns and light curves. *MNRAS*, 284:172–188, January 1997.
- J. Wambsganss. *Gravitational Microlensing*, pages 453–540. Gravitational Lensing: Strong, Weak and Micro, Saas-Fee Advanced Courses, Volume 33. ISBN 978-3-540-30309-1. Springer-Verlag Berlin Heidelberg, 2006, p. 453, 2006.
- J. Wambsganss, H. J. Witt, and P. Schneider. Gravitational microlensing - Powerful combination of ray-shooting and parametric representation of caustics. *A&A*, 258: 591–599, May 1992.
- W. R. Ward. Protoplanet Migration by Nebula Tides. *Icarus*, 126:261–281, April 1997.
- Edwin B. Wilson. Probable inference, the law of succession, and statistical inference. *Journal of the American Statistical Association*, 22(158):209–212, 1927.
- H. J. Witt. Investigation of high amplification events in light curves of gravitationally lensed quasars. *A&A*, 236:311–322, September 1990.
- H. J. Witt and S. Mao. Can lensed stars be regarded as pointlike for microlensing by MACHOs? *ApJ*, 430:505–510, August 1994.
- H. J. Witt and S. Mao. On the Minimum Magnification Between Caustic Crossings for Microlensing by Binary and Multiple Stars. *ApJL*, 447:L105–L108, July 1995.
- P. R. Woźniak. Difference Image Analysis of the OGLE-II Bulge Data. I. The Method. *Acta Astronomica*, 50:421–450, December 2000.
- P. R. Woźniak and B. Paczyński. Microlensing of Blended Stellar Images. *ApJ*, 487:

55–60, September 1997.

- J. T. Wright, O. Fakhouri, G. W. Marcy, E. Han, Y. Feng, J. A. Johnson, A. W. Howard, D. A. Fischer, J. A. Valenti, J. Anderson, and N. Piskunov. The Exoplanet Orbit Database. *PASP*, 123:412–422, April 2011.
- Ł. Wyrzykowski, S. Kozłowski, J. Skowron, V. Belokurov, M. C. Smith, A. Udalski, M. K. Szymański, M. Kubiak, G. Pietrzyński, I. Soszyński, O. Szewczyk, and K. Żebruń. The OGLE view of microlensing towards the Magellanic Clouds - I. A trickle of events in the OGLE-II LMC data. *MNRAS*, 397:1228–1242, August 2009.
- Ł. Wyrzykowski, S. Kozłowski, J. Skowron, A. Udalski, M. K. Szymański, M. Kubiak, G. Pietrzyński, I. Soszyński, O. Szewczyk, K. Ulaczyk, and R. Poleski. The OGLE view of microlensing towards the Magellanic Clouds - III. Ruling out subsolar MA-CHOs with the OGLE-III LMC data. *MNRAS*, 413:493–508, May 2011.
- Ł. Wyrzykowski, A. Udalski, S. Mao, M. Kubiak, M. K. Szymanski, G. Pietrzynski, I. Soszynski, and O. Szewczyk. The Optical Gravitational Lensing Experiment. Variable Baseline Microlensing Events in the Galactic Bulge. *Acta Astronomica*, 56:145–169, June 2006.
- X. Yuan, X. Cui, X. Gong, D. Wang, Z. Yao, X. Li, H. Wen, Y. Zhang, R. Zhang, L. Xu, F. Zhou, L. Wang, Z. Shang, and L. Feng. Progress of Antarctic Schmidt Telescopes (AST3) for Dome A. In *Society of Photo-Optical Instrumentation Engineers (SPIE) Conference Series*, volume 7733 of *Society of Photo-Optical Instrumentation Engineers (SPIE) Conference Series*, July 2010.
- Z. Zheng and A. Gould. Superluminal Caustics of Close, Rapidly Rotating Binary Microlenses. *ApJ*, 541:728–733, October 2000.